Investigations of Hypervelocity Impact Physics

Andrew Jonathan Thurber

Dissertation submitted to the faculty of the Virginia Polytechnic Institute and State University in partial fulfillment of the requirements for the degree of

Doctor of Philosophy
In
Mechanical Engineering

Javid Bayandor
Francine Battaglia
Walter F. O'Brien
Jamshid A. Samareh
Wayne A. Scales

July 23, 2014
Blacksburg, VA

Keywords: hypervelocity impact, orbital debris, finite element, shock

Investigations of Hypervelocity Impact Physics

Andrew J. Thurber

ABSTRACT

Spacecraft and satellites in orbit are under an increasing threat of impact from orbital debris and naturally occurring meteoroids. While objects larger than 10 cm are routinely tracked and avoided, collisions inevitably occur with smaller objects at relative velocities exceeding 10 km/s. Such hypervelocity impacts (HVI) create immense shock pressures and can melt or vaporize aerospace materials, even inducing brief plasmas at higher speeds. Sacrificial shields have been developed to protect critical components from damage under these conditions, but the response of many materials in such an extreme event is still poorly understood.

This work presents the summary of computational analysis methods to quantify the relevant physical mechanisms at play in a hypervelocity impact. Strain rate-dependent behavior was investigated using several models, and fluid material descriptions were used to draw parallels under high shear rate loading. The production and expansion of impact plasmas were modeled and compared to experimental evidence. Additionally, a parametric study was performed on a multitude of possible material candidates for sacrificial shield design, and new shielding configurations were proposed.

A comparison of material models indicated that the Johnson-Cook and Steinberg-Cochran-Guinan-Lund metallic formulations yielded the most consistent results with the lowest deviation from experimental measures in the strain rate regime of interest. Both meshless Lagrangian and quasi-Eulerian meshed schemes approximated the qualitative and quantitative characteristics of HVI debris clouds with average measurable errors under 5%. While the meshless methods showed better resolution of interfaces and small details, the meshed methods were shown to converge faster under several metrics with fewer regions of spurious instability.

Additionally, a new technique was introduced using hypothetical viscous fluids to approximate debris cloud behavior, which showed good correlation to experimental results when such models were constructed using the shear rates seen in hypervelocity impacts. Formulations using non-Newtonian fluids showed additional capability in approximating solid behavior, both quantitatively and qualitatively. Such fluid models are significant, in that they reproduced the qualitative and quantitative characteristics of evolving debris clouds with better fidelity than purely hydrodynamic models using inviscid fluids. This indicates that while inertial effects can dominate overdriven shock phenomena, neglecting shear forces invariably introduces errors; such forces can instead be simplistically approximated via viscous models. The viscous approximation also allowed for a successful scaling analysis using dimensionless Pi terms, which was unfeasible using solid constitutive relations.

Attempts to model plasma dynamics saw success in the simulation of a laser ablation-driven flyer plate by using a hot gas with solid initial conditions; similar strategies were used to analyze plasma production in hypervelocity impacts with reasonable correlation to experimental measurements. Lastly, the analysis of bumper material candidates showed that metals with a low density such as beryllium and magnesium yield a higher specific energy and momentum reduction of incident projectiles with lower weight requirements than a similarly constructed bumper using aluminum. Investigations of bumpers using a combination of materials and variations in microstructure showed promise in increasing weight-normalized efficacy. Through these computational models, the parameters which influence damage and debris in hypervelocity impacts are more critically understood.

ACKNOWLEDGEMENTS

I'd firstly like to say thank you to my advisor, Professor Javid Bayandor, for his constant support and encouragement. Your excitement and energy toward research translates directly to your students, and it has been an honor to be a part of the CRASH Lab's early years at Virginia Tech.

I'd also like to thank the members of my defense committee, Professor Battaglia, Professor O'Brien, Dr. Samareh, and Professor Scales, for your insight and criticism. Our discussions always proved fruitful to my research, and you were always willing to help me understand new concepts and applications.

I'd like to thank the members of the CRASH Lab, including Aaron Siddens, Matt Satterwhite, Andrew Costain, Scott Perino, and Yangkun Song. In coursework and research alike, my efforts were always complemented by knowledgeable and insightful help, and our camaraderie helped motivate large portions of this work.

Lastly, I'd like to say thank you to my parents for your continued love and support. I could not have done this without you.

CONTENTS

List of Tables

List of Figures

Nomenclature

A, B	=	strain rate hardening parameters	(MPa)
C	=	strain hardening coefficient	-
C_0	=	speed of sound	(m/s)
S_{1-3}	=	slope coefficients	-
T^*	=	normalized temperature	(K)
T_{room}	=	room temperature	(K)
T_{melt}	=	melting temperature	(K)
a	=	first order volume correction to γ_0	-
e	=	specific internal energy	(Mbar/cc)
m	=	thermal softening power exponent	-
n	=	strain hardening power exponent	-
γ_0	=	Gruneisen gamma	-
ε_p	=	equivalent plastic strain	(s^{-1})
$\dot{\varepsilon_p}$	=	equivalent plastic stain rate	(s^{-1})
σ	=	equivalent stress response	(MPa)
σ_y	=	yield stress	(MPa)
σ_p	=	effective plastic stress	(MPa)
σ_t	=	thermally activated plastic stress	(MPa)

1 INTRODUCTION

1.1 Background and Motivation

Spacecraft and orbital structures are at risk of impact with interplanetary micrometeorites and man-made debris. As human exploration of space evolves, higher quantities of orbital debris are created which increase the likelihood of impact with vital space structures. While debris mitigation strategies using active reduction have been proposed, the current debris environment remains fraught with dangerous particles. The largest objects are routinely tracked and actively avoided by spacecraft, but millions of objects smaller than 1 cm exist in orbit, which are difficult to track accurately [1]. While these smaller objects have lower masses than their tracked counterparts, the relative velocities between such debris and vital spacecraft components can be upwards of 10 km/s, giving them extreme kinetic energies.

The impact energy in such hypervelocity impacts (HVI) creates shock pressures well in excess of material strengths, causing unconventional failure modes as seen in Figure 1, where the incident projectile energy has created a large impact crater while shock pressures induced significant levels of rear spallation and shock induced fracture. Impacts in the low hypervelocity regime create shock driven spall, while higher speeds can melt and vaporize aerospace alloys. The highest velocities shock materials into a brief plasma state, which can cause electrostatic discharges and damage electronic components. Such impacts have traditionally been called hydrodynamic, since the strength of materials has been considered negligible [2], but the true role that material strength plays has not been fully studied. Kinetic energy is transformed into extreme temperatures and pressures over the course of a few nanoseconds, meaning that the impact physics can be treated as essentially adiabatic [3].

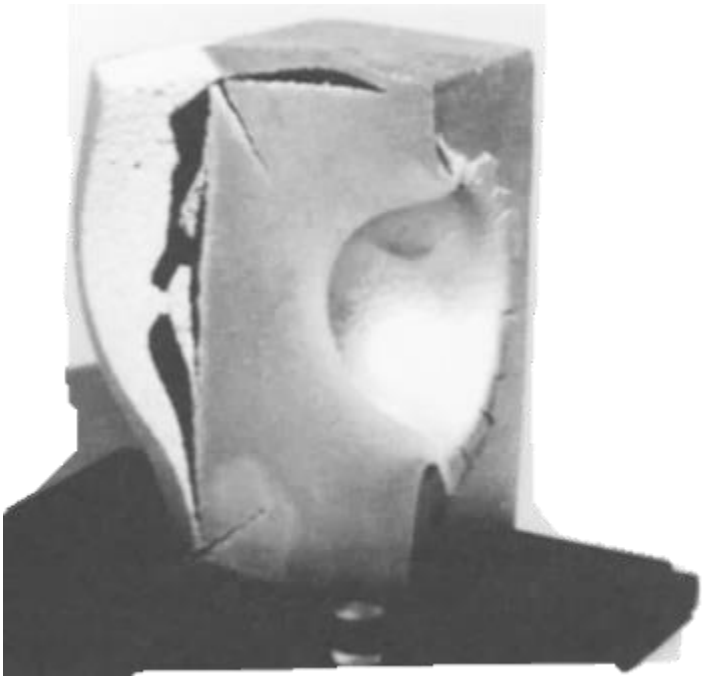

Figure 1. Sectioned specimen showing impact crater, fracture, and spallation in a thick aluminum target after hypervelocity impact [4].

Due to the immense kinetic energy of particles traveling in the hypervelocity regime, inertial effects dominate the onset of damaging effects and many materials behave fluidically, even if minor levels of melt occur [5]. However, stiffness and shear effects can contribute to projectile resistance and evolution of the debris cloud in non-negligible magnitudes. Shock pressures are coupled with sliding interfaces and large amounts of shear deformation, leading to combined levels of compression, shear, and tensile shock pressures at free surfaces. The rate at which these processes occur varies significantly as the impact event progresses, leading to heavily strain rate-dependent behavior.

Despite these complex coupled processes, traditional HVI analysis has been mostly experimental, with more recent computational models yielding somewhat simplistic results. The rate-dependence, significance of shear stresses, and multiphysics have not been quantified in previous studies. The physics of shock induced phase change and plasma formation are poorly understood, and experimental studies are primarily performed to assess shielding performance as needed. The motivation of this work is thus to further characterize the physics of HVI through computational analysis and develop effective

modeling strategies for hypervelocity phenomena. By providing a more complete description of HVI mechanics and establishing predictive computational techniques, HVI threats can be more rapidly characterized and effective shielding mechanisms can be designed with lower time and cost requirements.

1.2 Objectives

This work uses computational modeling techniques to characterize the physical mechanisms at play in hypervelocity impact events. To more fully understand the physics present in hypervelocity impact, several simulations are presented which explore the individual parameters of HVI more fundamentally. Using a combination of meshed and meshless finite element algorithms, impact processes are directly modeled and analyzed, and the role that shock pressures, shear forces, and energy transfer play are individually investigated.

Trends in fragmentation and debris are analyzed from various materials and projectile shapes and compared to experimentally studied impacts. Additionally, the strain rate behavior of materials is analyzed, and the strain rate dependence of fluid mechanics is used to draw parallels with high strain rate solid deformation. The level to which shear and shear rate contribute is investigated using purely fluid interactions with viscous forces varied incrementally, before more comprehensive models are shown with viscous to inertial ratios approaching those seen in solid impact events. The interactions of strain rate-dependent metallic models are reformulated in the context of Newtonian and non-Newtonian fluids, and the capability of such models in capturing the relevant energetic profiles is demonstrated. Laser ablation and shaped charge impact are also modeled to illustrate unique techniques used in overcoming the challenges in simulating the multiphysics interactions inherent to HVI. The possible creation of plasma discharges is modeled using the techniques developed for laser ablation studies. Lastly, a parametric study is performed on several material candidates for bumper shielding, and several promising findings are recommended for further experimental characterization.

Several commercially available tools have been used to model physical processes with high shock pressures, large deformations, and evolving domains. The shock physics

community has extensively used SALE-3D from Los Alamos [6] or more recently Sandia's CTH [7] with Eulerian schemes to conservatively evaluate shock phenomena. The presented work has investigated Century Dynamics/Ansys AutoDyn [8], Dassault Systemes Abaqus/Explicit [9], and most prominently LSTC's Ls-Dyna [10], which grew from Lawrence Livermore's Dyna3D code [11]. Simulation results are from Ls-Dyna unless otherwise specified, but in the interest of clarity, the implemented numerical methods are described and formulated with their originally published nomenclature, rather than Ls-Dyna specific references.

1.3 Summary of Contributions

This work has made significant contributions to the understanding of hypervelocity impact physics and high strain rate, high pressure phenomena in the following ways:

- **Fluidic strain rate dependency** – by analyzing the strain rate-dependent behavior of metals, the plastic deformation was considered to be roughly analogous to fluid shear. Several fluid approximations were then created to reformulate the high strain rate behavior of such materials with good agreement. Both Newtonian and non-Newtonian fluid models successfully recreated the impact response of metallic substances under the loading conditions of HVI.
- **Mechanical plasma modeling** – studies were performed to model the laser ablation-acceleration of an aluminum disk by using compressible gas dynamics for the plasma. When the strategy was applied to impact-induced plasmas, the resultant material expansion rates compared well to experimental values.
- **Parametric bumper evaluation** – several metals were evaluated at varying thicknesses for their capability in defeating incident projectiles traveling at velocities of 7 km/s. The resulting parametric evaluation of bumper materials identifies key candidates for improved orbital debris shielding relative to a currently used baseline.

1.4 Reader's Guide

An understanding of hypervelocity impact risk and the computational models presented in this work requires an understanding of the physical characteristics of HVI and the debris environment, the mechanical theories used to describe material response, and the numerical algorithms implemented for effective modeling. This chapter has summarized the motivation for further HVI studies and the objectives and contributions of this work.

Chapter 2 details the risk of orbital debris and micrometeorites, as well as environment models and future projections for risk levels. Experimental studies of HVI are summarized, with a focus on early research into debris protection strategies and shielding. Physical mechanisms with similarities to HVI are presented last, focusing on weapons which use HVI physics and laser ablation processes using plasma production.

Chapter 3 reviews theories and approximations to materials under HVI conditions, beginning with a derivation of the basic equations in shock physics and a comparison of shock-capturing equations of state. Competing constitutive relations for metals are then presented, with a quantitative study demonstrating the limited range of applicability for some models. A review of Newtonian and non-Newtonian fluid theories is then presented, followed by a description of composite mechanics and the relevant approximations to composite failure. Studies into plasma production from HVI are lastly presented, with a description of current models and gaps in the literature.

Chapter 4 details the numerical techniques used in this study, beginning with the finite element method and the variations on shell and solid elements which were used. More advanced arbitrary Lagrangian Eulerian schemes are then presented, followed by a brief derivation of smoothed particle hydrodynamics and its variations. The algorithms used in time step control and stability are then presented, followed by a discussion of numerical accuracy and the need for verification and validation.

Chapter 5 is the largest section of this work, detailing the computational models of HVI phenomena which were constructed. Initial efforts using computational methods are

briefly reviewed, followed by a discussion of their limitations. More advanced techniques are then presented with applications to HVI debris cloud modeling, and the accuracy of such models is analyzed. The fluid characteristics of HVI are then discussed, followed by an analysis of hydrodynamic material modeling; viscous and non-Newtonian formulations of solid behavior are then derived and compared to solid behavior, followed by a dimensionless analysis. The response of composite structures under HVI loading is then analyzed, and the introduction of a volume-fraction based equation of state is seen to increase the accuracy of numerical predictions. The behavior of plasmas is analyzed by first modeling a laser ablation-driven flyer plate using a non-ionized gas material description; this strategy is then extended to HVI plasma production by converting high energy portions of solid into a hot, dense gas. A parametric study is lastly performed, comparing various candidate materials for implementation in bumper shields; variations in microstructure and material layering are also analyzed.

Chapter 6 summarizes the findings of this work and details the contributions and improvements which can be introduced for more effective shielding design. Several new areas of research and desired experimental results are also discussed, with a focus on the need for further physical characterization.

Appendix A discusses the comparison of material theories and computational methods in more detail, and contains several large figures and tables which are unsuitable for the main body. Appendix B discusses the methods undertaken in code verification, with figures and tables describing the convergence study for each numerical method. Appendix C presents several figures of debris clouds and material deformation which are impractical for inclusion in the body of the text.

2 PHYSICAL PHENOMENA

2.1 Orbital Debris and Micrometeorite Risk

The risk of impact to spacecraft and structures in orbit was initially due to natural meteoroids in solar orbit which crossed the orbital path of the Earth. As more materials were placed in space, the risk shifted such that man-made objects and fragments became a larger danger, and impact with debris was significantly more probable than with naturally occurring micrometeoroids [12]. While the total flux of debris is now significantly higher than the meteoroid flux in many orbits, impact events with naturally occurring meteoroids is still a concern, as these higher velocity collisions can have significantly different damage mechanisms.

2.1.1 Man-made Orbital Debris

Man-made orbital debris ranges in size from the micron regime to a few massive objects over 100 cm, with velocities spanning between approximately 1 km/s to over 15 km/s, averaging approximately 8 km/s [13]. Most of this debris is made of small metallic fragments from orbiting structures, but some is also composed of orbiting solid rocket exhaust and flecks of paint [14]. Traditionally, risk from debris impacts have been modeled assuming an object density of 2.8 g/cm^3, since aluminum fragments are a common threat. An interesting variation on this trend is a significant population of the LEO debris field composed of liquid sodium-potassium coolant from the nuclear cores of radar ocean reconnaissance satellites (RORSATs) launched by the Soviet Union [15]. While the droplets' average density of approximately 1 g/cm^3 is lower than most orbital debris, droplets exceeding 4 cm in diameter are not uncommon, and predictive models showed that this unique debris type could possibly account for over 20% of the debris larger than 5 mm in diameter between 600 and 1200 km altitude [16].

Kessler and Cour-Palais wrote on the evolution of debris over time [17] and described a "Kessler Syndrome" in which the debris environment can pass a critical threshold, after which the rate of new debris production exceeds the rate of orbital decay. This causes runaway growth in the debris environment leading to a permanently

inhospitable zone in space. More recent analysis indicates that this threshold may have already been surpassed in limited altitudes, and suggestions have been made that active debris removal is essential for the continued usage of several altitudes [18].

The rate at which orbital debris progresses has changed since the initial assessment of a Kessler Syndrome, as several high profile events have drastically increased fragment levels over the historical rate. Most prominently, China conducted an anti-satellite missile test in 2007, destroying a Fengyun 1C weather satellite in polar orbit. This destruction created over 150,000 debris particles over 1 cm in size, and was the single largest man-made debris generating event in the history of space exploration [13]. After two years, only 50 of these tracked objects had decayed from orbit, and the debris from the Chinese missile test constituted over 20% of the entire debris population over 10 cm in size. Following this explosion and the accidental collision between the Iridium 33 and Cosmos 2251 satellites, projections maintained that the active removal of 5 large objects per year would prevent the further runaway growth of debris from collisions [19].

2.1.2 Micrometeorites

The risk of impact from larger meteoroids shows an inverse square relationship; that is, the flux of meteoroids through a given area is roughly inversely proportional to the square of a meteoroid's radius [20]. This means that while the risk of impact with small objects can be quite high, the risk of a larger object creating catastrophic damage is significantly smaller. The size of such naturally occurring meteoroids varies from a few microns in diameter to over 10 cm, however, the risk of impact with such large objects is over two orders of magnitude lower than orbital debris impact risk [21]. The risk is roughly comparable between the two impact types for objects smaller than 1 mm. Unlike orbital debris, however, velocities of solar system meteoroids relative to the Earth span from approximately 10 km/s resulting from purely gravitational acceleration, to over 72 km/s [20].

Risk from impacts with stream meteoroids such as the Perseids or Leonids can be anticipated, since they follow heliocentric orbits which intersect with the Earth's path around the Sun at regular intervals. Additionally, such meteoroids have a maximum

expected velocity due to their orbital path. Impacts with sporadic meteors are less predictable, however, and the velocities of such non-orbiting objects can be a cause for alarm [22].

While mechanical damage is the primary concern in orbital debris impacts, the small size and significantly higher velocity of meteoroid impacts means that electrostatic discharge from plasma formation is significantly more damaging than physical deformation. Plasma generation from impacts has been found to scale roughly with velocity to the fourth power, such that the risk of electrical damage from impacts exceeding 70 km/s is cause for significant concern [23].

2.2 Experimental Characterization and Design

The risk of damage to space structures from micrometeorites was known as early as the 1940's, when Whipple proposed a double bumper shielding design for lightweight protection [24]. While a monolithic shield must be sufficiently thick to defeat incident projectiles without fracture or spall, a double bumper design uses a sacrificial outer layer to induce projectile breakup and melt, and then utilizes the spacing between shields to allow the debris to spread until the damage to the interior layer is minimal. As the debris environment has evolved and mission constraints have changed, hypervelocity impact characterization and shielding designs have steadily improved.

2.2.1 Hypervelocity Testing and Ballistic Limit Equations

While the micrometeorite environment wasn't fully understood, part of the Apollo program involved extensive hypervelocity impact testing of shielding designs [25]. Since no orbital debris existed at that time, meteoroids were accepted to be the primary threat, and the Service Module and Command Module were designed to withstand impacts from projectiles with a standard density of 0.5 g/cm^3 at velocities over 11 km/s. Impact tests were conducted using a significantly larger and denser projectile, with a 0.16 cm aluminum impactor at approximately 7 km/s using a two-stage light gas gun.

To analytically characterize the threat from hypervelocity impacts, a series of penetration equations dubbed "ballistic limit equations" were developed, which define the

penetration threshold for incident objects over a range of velocities and sizes [26]. The size and velocity regime is divided into sections based on expected material response, and particles larger than the critical size are expected to puncture through the shield. This is visible in Figure 2, where the advantage of a double bumper shield over a monolithic shield is evident.

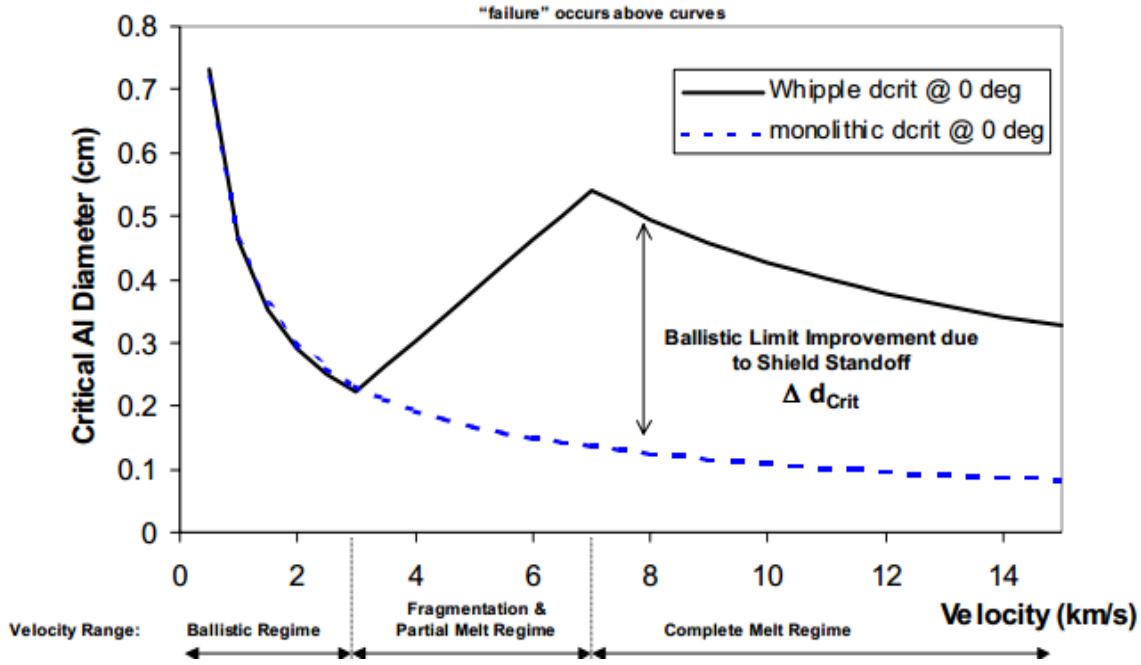

Figure 2. Graph of ballistic limit curves for a single and double plate shield [27].

The Cour-Palais ballistic limit equations were developed as part of the Apollo program, but as man-made debris began to supersede meteoroids as the primary threat, the 0.16 cm projectile sizing dated the usefulness of the existing methods. To remedy this, the equations were modified using tests of 1.3 cm diameter projectiles by Christiansen in 1991 as part of shielding design for the International Space Station [28]. The modified equations were integrated into the NASA code BUMPER for rapid design of shielding configurations [29].

As manufacturing processes for composite materials improved, significant attention was devoted to the hypervelocity impact response and feasibility of using such lightweight materials for structural shielding. Early hypervelocity impact tests of nylon and aluminum cylinders impacting composite laminates showed that using composites as a

bumper shield produced long flakes and quantities of debris significantly in excess of the initial projectile [30]. Later impact experiments showed that using Kevlar or carbon fiber reinforced polymers as a rear sheet in a double bumper shield offers minimal advantages over an aluminum shielding design [31], but further studies concluded that using composites as an intermediate shield between the bumper and rear sheet offered significant improvements over a double bumper shield of equal weight [32]. Consequently, ballistic limit equations have been extended to define effective regimes for multi-shock shielding designs with composite components in various configurations [27].

2.2.2 Variations in Shielding

Honeycomb sandwich panels are attractive for implementation in space structures, since the internal reinforcement provides additional rigidity with relatively little increase in weight. As a shielding strategy, the internal honeycomb was theorized to provide additional protection from oblique HVI, as the panels would interfere with incident debris; preliminary research suggested the addition of a honeycomb increased impact energy absorption [33], but later work demonstrated that the "channeling" of debris could cause further damage than a shield with no honeycomb [34]. It was found that as impacts occurred near normal incidence, the spallation and spread of debris was actually hindered by the honeycomb structure, such that a larger amount of debris was concentrated within one cell, increasing the energy and momentum transfer in a small area. While the likelihood of this effect causing a significant decrease in shielding efficacy was debated for some time, further honeycomb testing and simulation showed increased damage to the secondary bumper directly caused by the honeycomb channeling [35]. Despite these findings, composite panels with aluminum honeycomb are still used in current MMOD shielding designs.

Several studies on mitigating debris produced by the impact event itself have examined the rear ejecta distribution from a variety of shielding designs [36]. The use of a thin aluminum mesh, a fiberglass fabric layer, and a thin Kevlar layer all provided a significant reduction in rear ejecta over a standard bumper, and such designs add little weight to the overall shield structure. Ballistic limit equations were developed for such

mesh double bumper shields, and a steel mesh shield is currently used on the Russian FGB module in the International Space Station [37].

2.3 Other HVI Phenomena

While this work has aimed to computationally model hypervelocity impacts from orbital debris impacting bumper shields, there are other industrial and military processes which produce some of the unique physics present in HVI. These were investigated and simulated as an attempt to more thoroughly describe the computational challenges and strategies in modeling HVI physics.

2.3.1 Shaped Charges and Explosively Formed Penetrators

When an explosive device is contained within a hollow conical or hemispherical shell, the resultant explosion can drive the shell liner at speeds well in excess of the traditional detonation velocity of the high explosive, as seen in Figure 3. The detonation energy of a high explosive is released perpendicular to the explosive's surface; for explosives with hollow conical or hemispherical shapes, this produces a confluence of detonation waves which can greatly increase the propulsive shock energy locally over that which may be achieved in other orientations. Known as the Munroe effect [38], this geometric modification to explosive designs revolutionized warfare during World War II, as it enabled effective anti-tank weaponry to be deployable by infantry and aircraft.

When this effect is used with a thin conical liner, a jet of semi-molten material is produced which is effective usually over short distances, due to jet instabilities; this configuration is called a shaped charge. With a thicker hemispherical liner, the device is called an explosively formed penetrator (EFP) because the ductile liner is formed into a solid projectile capable of traveling large distances with no breakup. Shaped charges are capable of far more armor penetration than an EFP, but generally result in much less energy and momentum transfer. The standard shaped charge design has been intensely studied and refined, such that modern shaped charge devices are capable of propelling dense metals at hypervelocity speeds over limited ranges, with tip velocities for copper and tantalum shaped charges exceeding 8 km/s [39].

Simulations were conducted to model an experiment in which tantalum lined shaped charges were detonated into large billets of titanium armor plating. These are presented in Appendix A, where the scenario is used to compare differing metallic constitutive relations.

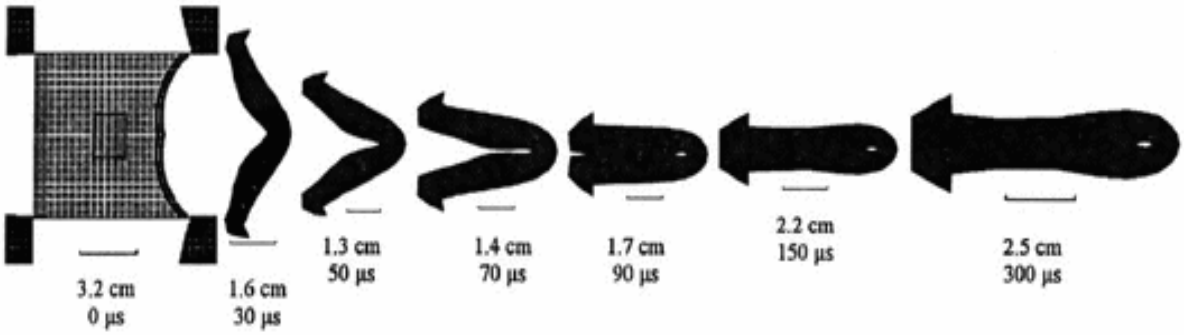

Figure 3. The Munroe effect shaping a hemispherical liner into a projectile [40].

2.3.2 Laser Ablation and Shock Peening

Advances in laser technology have allowed the use of incident radiation to precisely remove material through phase change processes. Laser ablation is the process of using pulsed or continuous beams to induce evaporation or plasma creation on a surface, resulting in expansion and removal of the heated material. Such ablative processes have been used in manufacturing and cleaning, but also more recently in propulsion, as low mass objects are intensely accelerated by the expansion of the resultant high pressure plasma [41].

This is also used as a surface treatment in laser shock peening, as high energy pulsed lasers are used to induce a high pressure plasma; the resulting shock pressures and plasma expansion create residual stresses within the target material which can be tailored to increase fatigue resistance and resist cracking. The high shock pressures and plasma formation dynamics are an essential part of these laser processes, and show similarities to hypervelocity impacts. A laser ablation-propelled aluminum disk is modeled in Section 5.5, after which the plasma modeling methodology is extended to small particles impacting semi-infinite targets at speeds in the hypervelocity regime.

3 MATERIAL THEORIES

3.1 Shock Physics and Equations of State

A shock wave is a rapid rise in energy, corresponding to an increase in pressure, density, and temperature taking place over the course of a few mean free path lengths. Shocks are created from wave superposition if a pressure disturbance moves greater than the medium's speed of sound (e.g. supersonic projectiles in air), and can result from dispersion effects in materials with nonlinear pressure-density relations, as faster wave components coincide with earlier generated slower waves (as seen in solids). A planar shock propagating in a tube is shown in Figure 4, in which the state of the material after the shock has been changed from the initial conditions, and variables U and e represent velocity and specific energy, respectively, where U_s is the velocity of the shock front. This classical description is known as a Riemann problem, for the mathematician who first derived solutions to conservation laws with piecewise constant properties and a discontinuity [42].

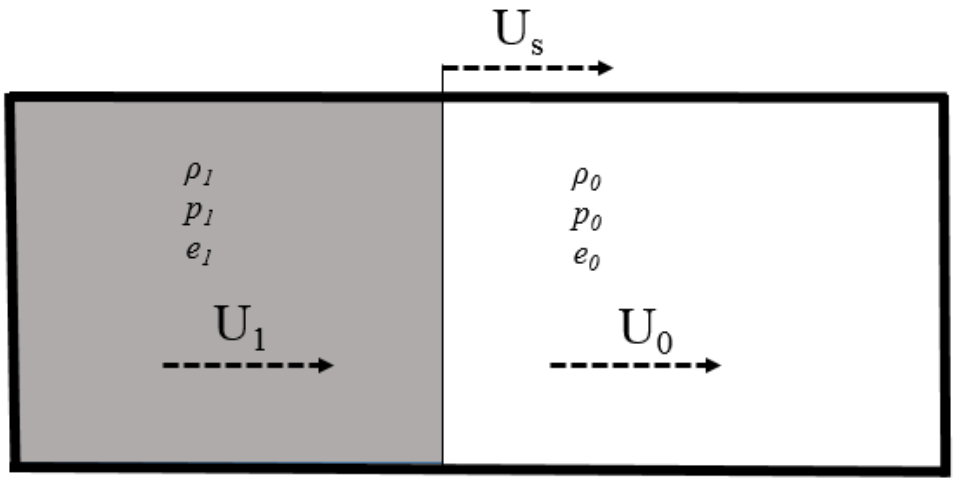

Figure 4. Shock tube depiction.

3.1.1 Rankine-Hugoniot Jump Conditions and Rayleigh Line

If no motion is assumed in the pre-shock region ($U_0=0$), conservation of mass across the shock requires that in a finite time interval,

$$\rho_0 U_s = \rho_1 (U_S - U_1) \tag{1}$$

During the same time interval, the change in momentum is due entirely to the mass which has been accelerated from an initial state of rest to the new velocity U_1, which must equal the impulse from the change in pressure, such that conservation of momentum dictates

$$p_1 - p_0 = \rho_1 (U_S - U_1) U_1 = \rho_0 U_s U_1 \tag{2}$$

where the result of Eq. (1) has been substituted. Lastly, the increase in specific internal and kinetic energy of the shocked mass during this time interval must balance with the work done by the pressure change, and the conservation of energy across the shock is

$$p_1 v_1 = (e_1 - e_0)\rho_0 U_s + \frac{1}{2}\rho_0 U_S {U_1}^2 \tag{3}$$

These equations are known as the Rankine-Hugoniot jump conditions, after the 19th century scientists who derived them separately [43].

Experimental observation has revealed that most solids have a linear relationship between shock velocity and particle velocity (we rename U_1 to U_p), such that

$$U_s = C_0 + S U_p \tag{4}$$

where C_0 is the material speed of sound and S is the experimentally determined U_s-U_p slope. This relation is known as the shock Hugoniot, and represents the possible peak states achievable under shock loading. Using the conservation of momentum and energy equations above, this linear relationship becomes a curve in the p-V plane, representing an adiabatic relationship, shown in Figure 5 relative to specific volume. However, shocks are inherently non-equilibrium conditions, and the Hugoniot is not a path that shocked material follows in the p-V plane. Rather, the initial and final states are on the equilibrium isentrope,

but the path is a straight line known as the Rayleigh line. Thus, by knowing the shock velocity and particle velocity of a material under shock loading, a single point on the Hugoniot curve can be established. By measuring this U_s-U_p relationship over multiple shock magnitudes, the full Hugoniot curve for a material can be characterized which, through the Rankine-Hugoniot relations, yields a series of *p*-*V* values, corresponding to a piecewise equation of state for the shock process. While this is sufficient to describe ideal shock behavior, the full evolution of state variables through shock and release requires further assumptions for a physically accurate equation of state.

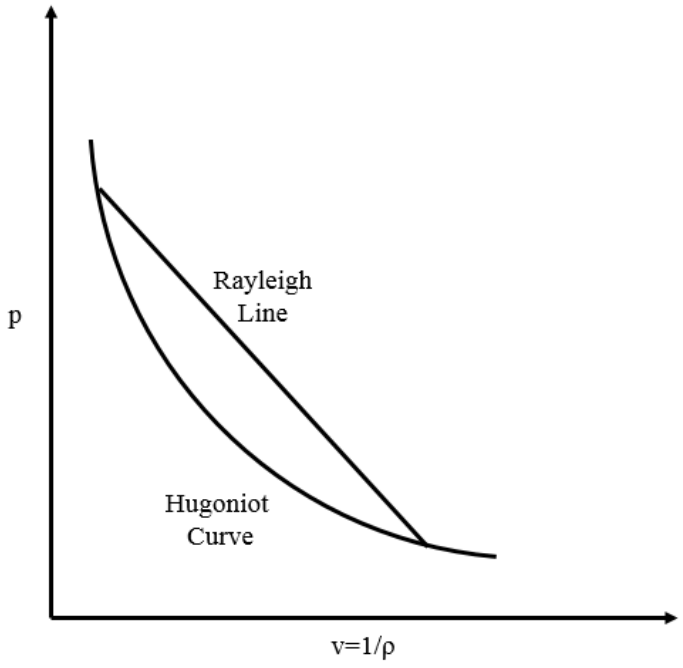

Figure 5. Shock Hugoniot and Rayleigh line.

3.1.2 SESAME Tabulated Values

Los Alamos National Laboratories has investigated high pressure shock phenomena for several decades as a consequence of funded projects in nuclear weapons analysis and high shock/high strain rate material modeling. As a result, U_s-U_p relations and their associated *p*-*V*-*e* space have been experimentally determined for hundreds of materials, resulting in a large dataset of tabulated values which can be used in equation of

state modeling. This compendium of experimentally determined shock data has been dubbed the SESAME EOS [44], despite not containing a true equation for the determination of shock and release states.

3.1.3 Polynomial Equation of State

Since the *p-V-e* relationship of real materials is nonlinear, the generalized approximation to such behavior with no theoretical basis is a simple polynomial, relating

$$P = c_0 + c_1\mu + c_2\mu^2 + c_3\mu^3 + (c_4 + c_5\mu + c_6\mu^2)E$$

where

$$\mu = \frac{\rho}{\rho_0} = \frac{V_0}{V} - 1 \tag{5}$$

the three quantities via a cubic term in adiabatic volume and a quadratic volume relationship to energy, as seen in Eq. (5).

The constants of such an equation must be experimentally determined, though this simplistic form is useful in two approximations: setting C_0 to the material speed of sound and forcing all other constants to 0 simulates incompressibility, while setting constants c_4 and c_5 to the gas ratio of specific heats creates the classic equation of state for a compressible gamma-law gas, described by

$$p = \rho(\gamma - 1)e \tag{6}$$

Additionally, the polynomial form lends itself well to nonlinear fits of experimental data, and was used to construct a continuous function from a series of SESAME values for comparison to the Mie-Gruneisen EOS.

3.1.4 Mie-Gruneisen Equation of State

Theoretical work by Gruneisen into solid state mechanics determined that changing the volume of a solid crystal lattice affected the vibrational properties of the lattice and thus, the temperature [45]. The extension of this model is that at 0K, the pressure of a solid is directly related to its energy via the Gruneisen gamma (γ_0). Based partly on Gruneisen's solid state work and partly on the work of Gustav Mie in high temperature interatomic potentials, the Mie-Gruneisen equation of state represents an off-Hugoniot condition for determining the shocked and post-shocked states of real materials. The third-order slope corrected form of the Mie-Gruneisen EOS allows for a nonlinear shock velocity/particle velocity relationship and defines the pressure under compression as

$$P = \frac{C^2\rho_0\mu\left[1+\left(1-\frac{\gamma_0}{2}\right)\mu-\frac{a}{2}\mu^2\right]}{\left[1-(S_1-1)\mu-S_2\frac{\mu^2}{\mu+1}-S_3\frac{\mu^2}{(\mu+1)^2}\right]^2}+(\gamma_0+a\mu)E \tag{7}$$

Under tension, the material response is governed by the simplified form shown in Eq. (8) where the pressure is defined by

$$P = C^2\rho_0\mu+(\gamma_0+a\mu)E \tag{8}$$

where

$$\mu = \frac{\rho}{\rho_0} = \frac{V_0}{V} - 1$$

When modeling fluid dynamics with SPH, it has become somewhat commonplace to use an artificial equation of state similar to that introduced by Monaghan [46]. Such a relationship allows for the calculation of bulk flow properties as well as a modification of the fluid's speed of sound in order to satisfy conditions of incompressibility. However, as HVI is not an incompressible interaction, fluid analogues have not been modeled with this simplifying assumption.

Experimental impact studies in Al 6061 were performed generating shock pressures up to 500 GPa using impact velocities which exceeded 16 km/s [47]; these studies indicated that the linear U_s-U_p relationship extends possibly further than this regime, and that the compressive response predicted by the Mie-Gruneisen EOS are still valid at such speeds. Care must be taken near these impact speeds, however, since flyer plate studies in aluminum suggest that shock pressures in excess of 600 GPa will induce a state of total melt, and approach majority vaporization [48]. As the Mie-Gruneisen model was derived from solid state assumptions, strong shocks resulting in a total melt scenario will not by accurately predicted.

3.1.5 Jones-Wilkins-Lee

An empirical equation of state defining the shock and expansion of high explosives was initially proposed by Jones and Miller [49], and subsequently expanded to a more complete adiabatic form by Wilkins [50], basing his work on spherical experiments and small degrees of material expansion. Lee, *et. al* expanded this work further [51] by using cylindrically capable assumptions of larger deformation to satisfy thermodynamic conditions at extreme levels of expansion. The resultant Jones-Wilkins-Lee (JWL) equation of state has since seen wide implementation in computations involving high explosives [52], and constants have been determined for a wide variety of explosive materials. In the current study, the JWL EOS is used for modeling the explosive propellant in the tantalum shaped charge validation studies presented in Appendix A. In the JWL EOS, the pressure is defined as

$$P = A\left[1 - \frac{\omega}{R_1\left(\frac{V}{V_0}\right)}\right]e^{-R_1\left(\frac{V}{V_0}\right)} + B\left[1 - \frac{\omega}{R_2\left(\frac{V}{V_0}\right)}\right]e^{-R_2\left(\frac{V}{V_0}\right)} + \omega E\frac{V_0}{V} \tag{9}$$

3.2 Metallic Constitutive Models

Since impact occurs at kilometers per second and higher, HVI deforms materials at incredibly high strain rates and creates pressures well in excess of standard material strengths. While shock pressures are calculated by the aforementioned equation of state, material responses to shock phenomena are determined by the appropriate material constitutive relations. Due to the modification of material strength with changes in temperature, a temperature-dependent material model capable of high strain rates is necessary.

3.2.1 Steinberg-Cochran-Guinan-Lund Model

A semi-empirical model was proposed by Steinberg, Cochran, and Guinan (SCG) [53] which assumes that strain rate effects on the yield strength and shear modulus of metals approach an asymptotic limit under strong shocks exceeding 10 GPa. The initial strain rate-independent model was designed to be valid at strain rates exceeding 10^5 s^{-1}, and has been successfully implemented in a variety of hydrocodes for modeling the response of metals and non-metallic materials [54] under high pressure shock loading and high strain rates.

In the initially formulated rate-independent SCG model, the yield stress is given as a function of shear by

$$\sigma_y = \sigma_{y0}(\varepsilon_p)\frac{G(p,T)}{G_0} \tag{10}$$

where the shear modulus is pressure and temperature dependent, with the temperature defined by energetic terms. This shear modulus and corresponding terms are defined by

$$G(p,T) = G_0\left[1 + A\frac{p}{\eta^{1/3}} - B(T-300)\right]$$

$$A = \frac{1}{G_0}\frac{\partial G}{\partial p}$$

$$B = \frac{1}{G_0}\frac{\partial G}{\partial T} \tag{12}$$

$$\eta = \frac{V_0}{V}$$

where temperature is defined based on energetic considerations as the difference between current energy and the energy along the zero Kelvin isotherm (E_c) divided by the material's specific heat: $T = (E - E_c)/c_p$. Reference conditions are assumed to be 300K and atmospheric pressure. Melting is characterized through a modified form of the Lindemann melting law [55], based on crystal lattice vibrational instabilities and derived via the energetically defined temperature. Work hardening is incorporated through a Bauschinger model initially defined for uranium by Cochran and Guinan [56]. Damage under strong shocks is incorporated as a spall threshold, defined as an evolution of microcracks through a continuum where a damage variable *D(x,t)* is given as a function of the volume *V* of microcracks in a given area *A*.

$$D(x,t) = \int_0^t \frac{dV}{A}, \;\; dV > 0 \tag{11}$$

As tensile stress exceeds the spall strength (Σ) of a material, relevant material properties such as the shear modulus and yield strength are multiplied by a damage function *F* defined by

$$F = 1 - (D/D_0)^{2/3} \tag{13}$$

which equals zero at total fracture, creating a region of zero strength where spall occurs.

While this rate-independent model accounts for pressure and temperature dependence of material response including work hardening, spall, and pressure-dependent melting, it fails to accurately predict elastic precursors in several materials such as tungsten [57], and cannot represent shock smearing and precursor decay. To address these shortcomings, the model was extended by Steinberg and Lund [58] into lower strain rates through the introduction of a thermally activated yield stress term, such that the total yield stress is

$$\sigma_y = \left[\sigma_T\left(\dot{\varepsilon_p}, T\right) + \sigma_A(\varepsilon_p)\right]\frac{G(p,T)}{G_0} \tag{14}$$

and the strain rate is related to the yield strength and temperature through

$$\dot{\varepsilon_p} = \left\{\frac{1}{C_1} exp\left[\frac{2U_k}{kT}\left(1 - \frac{\sigma_T}{\sigma_p}\right)^2\right] + \frac{C_2}{\sigma_T}\right\}^{-1} \tag{15}$$

where σ_p is the Peierls stress, $U_k$is the energy to form a kink in a Peierls-type dislocation segment, k is Boltzmann's constant, and C_1 and C_2 are constants derived from the dislocation density, the Burgers' vector, and the Debye frequency. The resultant rate-dependent Steinberg-Cochran-Guinan-Lund (SCGL) model has a theoretically derived form with empirically determined constants, and has been validated for a variety of materials at strain rates from 10^{-4} to 10^{6} s^{-1} as well as temperatures up to melt. Constants for the rate-independent and rate-dependent forms are given in Table and Table, respectively.

3.2.2 Johnson-Cook Model

Contrary to the theoretically derived SCGL constitutive relations, Johnson and Cook derived their material model by performing a series of experiments at multiple strain rates, temperatures, and pressures and then fitting the data to a decoupled rate-dependent/rate-independent equation. The Johnson-Cook (JC) [59] material model is an empirical relation that has seen success in modelling rapid deformation, and was used to characterize the response of aluminum in the presented HVI simulations. The JC model expresses von Mises flow stress as shown in Eq. (16), where

$$\sigma = \left[A + B\left(\varepsilon_p\right)^n\right]\left[1 + C\ln\left(\frac{\dot{\varepsilon}_p}{\dot{\varepsilon}_0}\right)\right]\left[1 - (T^*)^m\right]$$
$$T^* = \frac{T - T_{room}}{T_{melt} - T_{room}} \tag{16}$$

where the constants *A, B, C, n, m,* and T_{melt} are experimentally determined. It is apparent that at ambient temperature and strain rate equal to the reference rate, this relationship reduces to

$$\sigma = A + B\left(\varepsilon_p\right)^n \tag{17}$$

which is a yield stress with a standard power law relationship for strain hardening, commonly used in quasistatic material analysis [60]. This allows the JC stress relation to accurately predict a wide range of strain rates from approximately 10^{-2} to 10^5 s^{-1}, however, the use of appropriate modeling constants is essential. Constants *A, B,* and *n* determined from high strain rate dynamic testing will not be appropriate for a quasistatic modeling effort. While the value of $\dot{\varepsilon}_0$ can be estimated to non-dimensionalize the value of the logarithmic parameter, the appropriate value is that which corresponds to the test apparatus strain rate order of magnitude. Using dynamic testing constants for quasistatic response will significantly overpredict the static response, while quasistatic constants will underpredict high strain rate behavior [61]. These limitations notwithstanding, the JC material model can effectively account for the response of metals to high stresses and strain

rates, even as the temperature approaches melting. The stress formulation decouples the effects of strain rate and temperature dependency, however, which has caused an overprediction of yield stresses when these effects are dependent on one another, such as when elevated temperatures increase the coefficient of strain rate hardening [62]. The JC strength model accounts for the temperature, pressure, and strain rate dependence of plastic deformation, but not the presence of dynamic failure or fracture. Since the brittle and ductile behavior of materials is also dependent on these variables, the model was extended with a temperature and strain rate-dependent fracture model [63] where damage is defined by

$$D = \sum \frac{\Delta\varepsilon}{\varepsilon^f} \tag{18}$$

where the increment of plastic strain relative to the equivalent strain at fracture ε^f increases the value of dimensionless damage D until total failure occurs at D=1. The generalized strain at fracture is formulated with rate and temperature effects similar in form to the JC strength, given as

$$\varepsilon^f = \left[D_1 + D_2 exp D_3 \left(\frac{\sigma_m}{\bar{\sigma}}\right)\right]\left[1 + D_4 ln\left(\frac{\dot{\varepsilon}_p}{\dot{\varepsilon}_0}\right)\right][1 + D_5 T^*] \tag{19}$$

where σ_m is the average of the three normal stresses, $\bar{\sigma}$ is the von Mises equivalent stress, and $D_{1\text{-}5}$ are experimentally determined constants. The JC damage formulation has an advantage in that the temperature and strain rate forms are identical to those in the JC stress relation, thereby making a self-consistent relationship between stress and strain. By relying on continuum assumptions and purely empirical constants, this damage model is simpler than microstructure nucleation and growth models [64] while still retaining an accurate rate-dependent form for a variety of metals.

3.2.3 Zerilli-Armstrong Dislocation Model

Zerilli and Armstrong (ZA) proposed a rate-dependent model [65] for metals based on simplified dislocation mechanics of body centered cubic (bcc) and face centered cubic (fcc) materials. The yield stress is decoupled into a thermally activated portion, an athermal grain size dependency, and an athermal portion with strain rate dependency. The flow stress is expressed differently for fcc and bcc metals since the strain hardening of fcc metals is highly dependent on temperature and strain rate, while the coupled temperature and strain rate term influences bcc metals more strongly through a modification of yield stress. These stresses are formulated as

$$\sigma_{y,bcc} = \sigma_a + C_1 \exp(-C_3 T + C_4 T \, ln \, \dot{\varepsilon}) + C_5 \varepsilon^n + k d^{-\frac{1}{2}} \tag{20}$$

$$\sigma_{y,fcc} = \sigma_a + C_2 \varepsilon^{\frac{1}{2}} \exp(-C_3 T + C_4 T \, ln \, \dot{\varepsilon}) + k d^{-\frac{1}{2}} \tag{21}$$

where the plastic strain hardening effect on bcc metals is assumed to have a power law form with exponent *n*, and the microstructural stress intensity *k* divided by the square root of the average grain diameter *d* is decoupled from the thermal components of the stress. Constants *n*, *k*, and $C_{1\text{-}5}$ are experimentally determined.

3.2.4 Mechanical Threshold Stress Model

Follansbee and Kocks [66] assumed the flow stress of copper was dependent on an internal mechanical threshold subject to thermal, mechanical, and grain effects. The stress response was formulated as

$$\sigma_y(\varepsilon_p, \dot{\varepsilon}, T) = \sigma_a + (S_i \sigma_i + S_e \sigma_e) \frac{\mu(p,T)}{\mu_0} \tag{22}$$

where σ_a is the athermal stress contribution, σ_i is the thermal dislocation stress, σ_e is the contribution from strain hardening, the two factor of *S* are scaling constants dependent on strain rate and temperature, and μ is the pressure and temperature dependent shear modulus, with μ_0 defined at 0K and ambient pressure.

3.2.5 Elastic-Plastic-Hydrodynamic Model

The generalized elastic-plastic-hydrodynamic (EPH) constitutive relation represents the von Mises yield criteria with a bilinear form based on radial return plasticity [67] with pressure hardening effects. The yield strength is given as

$$\sigma_y = \sigma_0 + E_h \varepsilon_p + (a_1 + p a_2)\max(p, 0)$$
$$E_h = \frac{E_t E}{E - E_t} \tag{23}$$

where E_t is the tangent modulus, a_1 and a_2 are the linear and quadratic pressure hardening coefficients, respectively, and pressure is taken as positive in compression. Under tensile loading, the pressure hardening term disappears, creating a simplistic bilinear stress-strain relationship with hardening parameter β=1. In addition to the bilinear form shown above with given constants, a series of plastic strains and corresponding stresses can be defined to generate an arbitrary σ-ε function. Additionally, a spall criteria similar in form to that described for the SCGL model is implemented; as tensile stresses approach the spall strength of the material, a logical void is created and separation occurs.

3.2.6 Summary and Comparison

While rate dependence has been recognized in a variety of metals for decades, technology has only allowed for accurate experimental characterization of high pressure and high strain rate mechanical behavior in the past few decades. Rate-sensitive constitutive relations have thus seen extensive research since the 1980's, yielding several computationally useful models with varying degrees of theoretical and empirical contributions. All of the aforementioned solid material models contain terms to account for strain rate dependence as well as varying degrees of pressure and temperature dependence, with the exception of the EPH model, which contains only a limited pressure-hardening term. As such, proper characterization of the model constants should ideally predict an accurate material response over a wide range of strain rates including those approached in the HVI regime ($> 10^6$ s^{-1}).

To directly evaluate the comparative accuracy of these models, two simulations were constructed; a Taylor bar to deform tantalum at medium (~10^4 s^{-1}) strain rates, and a shaped charge for the high (>10^6 s^{-1}) strain rate regime. The model details and images are confined to the appendix for brevity, but the percent error results are presented graphically in Figure 6 for quantitative comparisons of deformed radius and height for the Taylor bar, and jet tip velocity and penetration depth for the shaped charge. It is immediately apparent that the JC and SCG models show the lowest overall errors in both strain rate regimes of interest; the EPH and MTS models meanwhile predict the highest overall error. As a result, the JC model was primarily used for all simulations presented in this work, with the SCG model used for comparison, as well as in materials for which JC constants have not been fully developed.

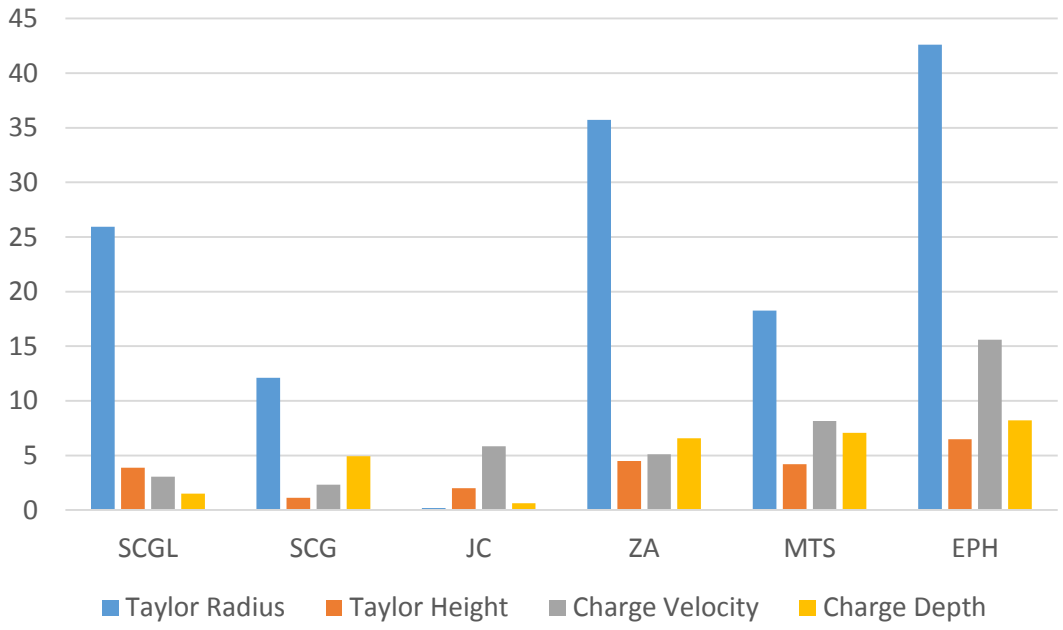

Figure 6. Comparison of percent errors predicted by six material models.

3.3 Fluid Models

Under the extreme pressures, elevated temperatures, and rapid strain rates in a hypervelocity impact, materials exhibit behaviors quite dissimilar to those seen in quasistatic regimes. Many metals can exhibit largely fluid behaviors, even when conditions allow the material to remain mostly solid; to quantify this effect and explore the role of shear strength in hypervelocity impact, several models were constructed in which the metals involved are instead modeled as fluids. Multiple fluid formulations were used corresponding to Newtonian fluids, Bingham plastics, and generalized Herschel-Bulkley non-Newtonian fluids.

3.3.1 Newtonian Fluids

A Newtonian fluid is defined by viscous stresses which are linearly proportional to the flow rate, resulting in a constant definition of viscosity. Using the nomenclature of the solid mechanics formulations, deviatoric stresses are calculated as a function of shear strain rate [68] expressed in Eq. (24) as

$$\sigma'_{ij} = \mu \dot{\varepsilon}'_{ij} \tag{24}$$

where μ is the dynamic viscosity, $\dot{\varepsilon}'_{ij}$ is the deviatoric strain rate, and hydrostatic stresses are calculated via the corresponding equation of state.

3.3.2 Bingham Plastic

A Bingham plastic is a fluid with a linear relationship between shear stress and flow rate after an initial threshold stress has been overcome [69]. Under increasing levels of applied stress, this results in an initial elasticity followed by a standard viscous plasticity. Mathematically, the response to post-yielding flow is expressed as

$$\sigma'_{ij} = \sigma_0 + \mu \dot{\varepsilon}'_{ij} \tag{25}$$

where no shear is allowed if the threshold stress is not exceeded ($\dot{\varepsilon}'_{ij}=0$ if $\sigma'_{ij} < \sigma_0$).

3.3.3 Generalized Herschel-Bulkley Fluid

A generalized model for non-Newtonian fluids was proposed by Herschel and Bulkley [70] which allows for shear thinning and thickening as well as a Bingham-type elasticity. In contrast to the Newtonian model, the viscosity is also allowed to be a function of the strain rate, which contains a power-law modification as seen in Eq. (26)

$$\sigma'_{ij} = \sigma_0 + m\left(\dot{\varepsilon}'_{ij}\right)^n \tag{26}$$

where m is a generalized viscous term and n is the flow index. If $n>1$, the fluid is shear thickening, and shear thinning behavior is modeled with $n<1$.

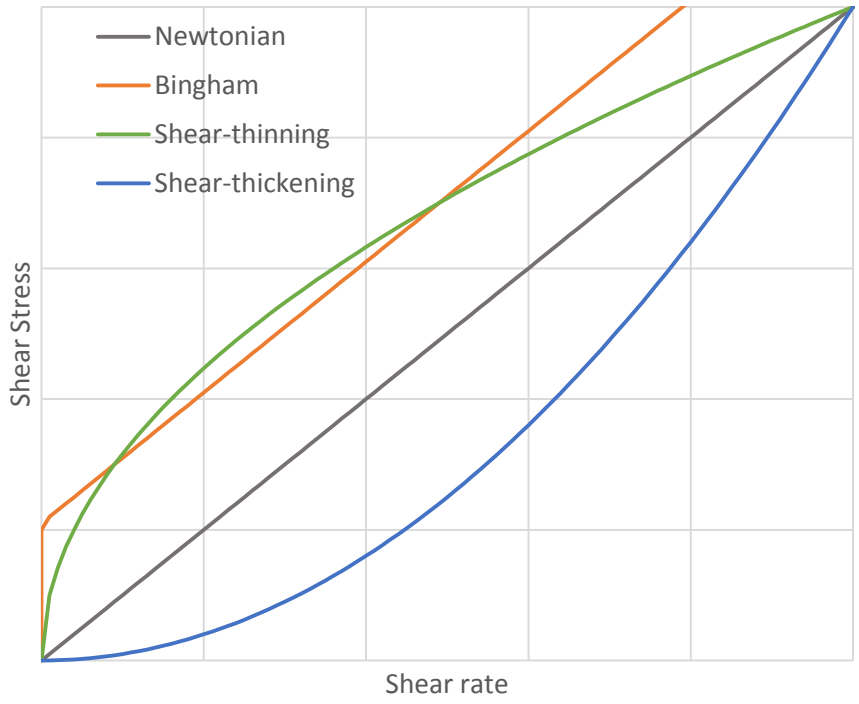

Figure 7. Shear stress vs. shear rate for 4 fluid models.

3.4 Composite Models

The composite materials of significant interest to the aerospace community are generally composed of an isotropic matrix with directional reinforcements from strong fibers. Ceramic matrix and metal matrix composites have been used frequently in applications with high thermal loads and ablative or frictional effects [71], while polymer matrix composites are more popular for structural applications without high temperature applications. Carbon fiber reinforced polymers (CFRP) are popular in both woven and uniaxial laminated configurations for their high strength to weight ratios, and woven aramid-epoxy composites (often made of Kevlar®) have been used in impact-resistant armor and shielding applications requiring strong through-thickness protection [72].

To analyze such microstructured anisotropic materials in the context of macro-scale continuum mechanics, some variation of Classical Lamination Theory (CLT) is usually employed, within which the assembly of a limited number of lamina (individual layers) into a full laminate (bonded plate of multiple layers) is homogenized into one effective plate with anisotropic properties [73]. This approximation significantly reduces the unknown variables in predicting material response and allows for closed-form solutions for several load cases. In doing so, CLT requires the assumptions of thin plates (thickness < ~10x length, width) and transverse displacements significantly smaller than the transverse thickness. It also requires the same assumptions as classical plate theory via the Kirchoff Hypothesis, and assumptions of perfect bonding. The Kirchoff Hypothesis used in plate approximations states that the plate (and lamina) normals must remain straight, do not stretch or deviate in length, and always make a right angle to the total plate's neutral plane [74]. The assumption of perfect bonding requires that the lamina do not separate from one another; the interlaminar bond is assumed to be infinitesimal (i.e. no gap or bonding thickness), idealized in strength, such that the strength of the bond is always equal to the strength of the total laminate, and impossible to shear, such that lamina cannot slip or deform laterally with respect to one another.

These conditions are appropriate for the prediction of elastic deformation and quasistatic stress analysis, but under impact loading with the expectation of large transverse

deformation, fiber and matrix damage, and through-thickness shear and perforation, the assumptions simply do not hold.

3.4.1 Fiber and Matrix Fracture, Delamination

For purposes of increased manufacturing yields and ease, the polymer matrix used in most aerospace composites is a thermosetting epoxy, which is mechanically quite weak. The primary strength of a fiber-reinforced composite is the strength of the fibers themselves; as such, the most immediately apparent mode of composite failure is via the fracture of fiber reinforcements. When a single fiber breaks under excessive loading, the stress is redistributed to the surrounding region, which is often incapable of carrying the new load, leading to a sudden catastrophic failure.

The matrix of a composite is also a load-bearing component, and the damage induced between fibers can lead to further crack propagation and ultimate failure. In uniaxial composites, tensile forces which approach orientations transverse to the fiber direction create stresses which are opposed almost entirely by the strength of the matrix. To circumvent this catastrophic scenario, laminates are usually constructed with at least 2 lamina orientations [73], but manufacturing defects or stress-induced damage between fibers and between lamina can lead to a coalescence of matrix cracks resulting in a reduction in shear strength and delamination.

Under impact and through-thickness damage, laminated composite materials can suffer through-thickness weakening and damage without intra-laminar breakage, exhibiting a unique phenomenon of delamination. That is, the layers which provide the material strength separate from one another, eliminating orthotropic constraints and creating a through-thickness-dependent strength profile. CLT-based material models have traditionally encountered drastic errors when modeling such damage [75], so the preferred modeling methodology uses a fully 3D representation or a quasi-3D material definition without a CLT-type interlaminar smoothing. Each orientation of anisotropic materials can then be presented individually, with coupling between layers modeled directly as a physical separation threshold.

3.4.2 Failure Models for Computational Analysis

Chang and Chang [76] defined three failure criteria for transversely isotropic composites with local stress concentrations where a damage parameter is defined by $0 \leq F \leq 1$. Once the damage criteria is reached, the material is considered failed, and has no mathematical strength. The matrix cracking failure criteria is defined under conditions of shear and transverse tensile loading by

$$F_m = \left(\frac{\sigma_2}{E_2}\right)^2 + \bar{\sigma}_{12} \tag{27}$$

where σ_2 is the tensile stress in the transverse direction, E_2 is the elastic modulus in the transverse direction, and $\bar{\sigma}_{12}$ is the in-plane shear stress. The compression failure criteria includes contributions from tensile, shear, and compressive forces, and is defined by

$$F_c = \left(\frac{\sigma_2}{2E_{12}}\right)^2 + \left[\left(\frac{C_2}{2E_{12}}\right)^2 - 1\right]\frac{\sigma_2}{C_2} + \bar{\sigma}_{12} \tag{28}$$

where E_{12} is the shear modulus between the longitudinal and transverse directions and C_2 is transverse compressive stress. The criteria for fiber breakage contain a similar weighted quadratic stress form in the longitudinal direction, with the damage parameter defined under conditions of tension and shear as

$$F_f = \left(\frac{\sigma_1}{E_1}\right)^2 + \bar{\sigma}_{12} \tag{29}$$

Tsai and Wu [77] treated fiber compression and tensile failure in a similar fashion, but developed alternate rules for matrix cracking under tensile and compressive forces to follow

$$F_m = \left(\frac{{\sigma_2}^2}{E_1E_2}\right) + {\bar{\sigma}_{12}}^2 + \left(\frac{C_2 - \sigma_2}{E_1E_2}\right) \tag{30}$$

The quadratic power introduced in each failure criteria have no physical basis in either continuum theory or micromechanics; it was introduced because a quadratic fit to experimental data introduced significantly less error [78]. Both the Tsai-Wu and Chang-Chang failure models have seen success in crash and impact modeling, primarily for thin shell finite elements. The extension of these strength and damage parameters into 3D elements is allowable, but the relevant out of plane properties must be defined separately. Additionally, both damage models were formulated for plates using assumptions of perfect bonding, so delamination damage is not implicitly included.

These failure models show adequate predictive capabilities in the quasistatic and lower dynamic regimes, but the lack of an equation of state underpredicts the shock loading pressure response. The anisotropic shock response of composite structures was studied at the micromechanical level by researchers at the Ernst-Mach Institute (EMI) [79], and later by Vignjevic and colleagues via flyer plate tests [80]; qualitative damage levels predicted by these anisotropic equations of state were acceptable, but the errors in wave propagation speed and larger scale material response were significant. The procedures used by both groups to experimentally derive parameters lacked a concrete methodology, and the present validity of composite equations of state is largely inconclusive.

3.5 Impact Plasma Dynamics

Plasmas are comprised of energetic, ionized gas, but for traditional plasma models to hold, Chen [81] suggests that the quasi-neutral gas must also have a large number of particles, be free from large electric potentials, and have a low collision frequency. At various stages in an impact event, these criteria do not necessarily hold. Under the initial shock dynamics which create a plasma from HVI, the collision frequency is quite high, such that purely mechanical hydrodynamic forces can dominate electromagnetic ones. As the plasma expands and rarifies, continuum dynamics lose relevance and the condition of a "large number" of particles within a relevant volume is no longer valid. Nonetheless, investigations have shown that HVI does produce somewhat ionized plasma discharges under various conditions [82], and it is prudent to examine the effect computationally.

3.5.1 Experimental Investigations into HVI Plasmas

The intense shock pressures seen in HVI have been known to generate plasma discharges for decades, as preliminary investigations were performed as part of the Apollo program [83]. In sufficiently small micrometeoroids, the kinetic energy of the incident particle is entirely converted upon impact into energy used for phase change (vaporization energy) and ionization energy [84]. The electrostatic discharge and electromagnetic pulse (EMP) associated with impact plasma generation have been suggested as a root cause of electrical anomalies in several missions during heightened meteor activity. The geostationary Olympus spacecraft experienced a variety of electrical malfunctions during peak activity of the Perseid meteor shower in 1993 [85]; though no direct measurements of impact with any foreign object were detected, there was no other theorized cause of the electrostatic discharge which occurred. The Jason-1 satellite, by contrast, experienced a detectable momentum shift in correlation with electrical disturbances during peak Perseid activity in 2004 [86], leading researchers to conclude that an impact event was the primary cause for such an electrostatic discharge.

Experimental characterization of impact plasmas is notoriously difficult, especially at macroscopic scales. A series of experiments was conducted in which 0.9 mm thick Ti-6Al/4V flyer plates with radius 8.5 mm were propelled by a three-stage light gas gun at speeds of 9.5-11 km/s into an indium target [87]; while a suite of RF detectors was used for the characterization of resultant plasma discharges, the final results were inconclusive, with average signal quality being within background noise levels. The authors postulated that the target material and the launch velocities were likely insufficient to produce measurable quantities of electrostatic discharge from plasma formation, despite the fact that indium was chosen as a target material due to its relatively low ionization energy and that impacts in the 10 km/s range have been known to produce shock-induced plasmas.

Studies using micron-scale particles have generally seen better success at plasma generation and detection. A series of experiments performed at the University of Kent used electrostatic generators to propel particles of iron, aluminum, and boron carbide into targets of various materials at speeds ranging from 1 to nearly 90 km/s [88]. This method proved

suitable for detection of RF emissions, and the authors recommended such electrostatic repulsion methods for future HVI experimentation.

3.5.2 Modeling Concerns

Within a high density, ionized plasma, moving magnetic fields induce currents in the conductive gas, which in turn create new forces affecting fluid dynamics; the new motion of the charged constituents then changes the electromagnetic forces once again, such that the fluid mechanics and evolving magnetic fields are coupled. The conservation equations of such a plasma are thus a combination of the Navier-Stokes fluid dynamics equations and the Maxwell equations of electromagnetism, which must be solved simultaneously. The dynamics of these coupled differential equations form the field of magnetohydrodynamics (MHD), which has been extended to tokamak fusion models, interstellar nebulas, and stellar fusion processes [89]. Computational MHD algorithms are still a subject of intense research, and algorithms are still under development for the treatment of dense shock-driven plasmas [90].

In the initial phases of impact plasma formation, the density is quite high ($\sim 10^{23}$ m^{-3}) and the electromagnetic forces are largely superseded by the mechanical forces typical of such a high pressure, high temperature fluid [91]. While direct detection methods have relied on the detection of radio frequency (RF) signals resulting from electromagnetic interactions, a direct simulation of the magnetic forces via MHD is unnecessary for the simulation of the mechanical effects of an impact plasma. As such, the electromagnetic forces have been excluded from the present modeling efforts, and only the mechanical contributions from impact plasmas have been modeled.

3.5.3 Uncertainties in Impact Plasma Characterization

Despite extensive experimental efforts and increasing records of electrical disturbances in spacecraft, the true physics of impact plasma production remain relatively unknown. Predictions of impact plasmas with respect to any given impact event remain wildly unreliable [87], and computational methods estimating levels of ionization and electrostatic effects are still largely based on simplistic models such as 1D particle in cell

(PIC) calculations. Nonetheless, a correlation between impact speed and resultant plasma mass has been observed [88], leading researchers to conclude that peak impact pressures also correlate with plasma production. The time-dependence and rate of such production remain uncharacterized, requiring computational models of such plasma characterization to rely on basic physical assumptions.

4 NUMERICAL METHODS

4.1 Finite Element Methods

The chosen shape functions for finite element algorithms may exactly recreate the numerical order and consistency of the studied problem, but for 3D dynamic analysis, this is usually only the case in simplistic elements in which the problem and discretization completely satisfy Euler-Lagrange discretization equations, such as a simple beam deformation [92]. Under the conditions of HVI, all computational methods must be regarded as an approximation only, as the full physics of the interaction are impossible to describe exactly through numerical procedures. A comprehensive treatment of the finite element method (FEM) including shape functions, weak forms of differential equations, and time integration schemes in explicit analysis is outside the scope of the current work. For a review of relevant algorithms and their development, the reader is encouraged to read the procedural work by Bathe [93]. The specific element formulations used are detailed below, as well as aspects of their numerical formulation which deviate significantly from traditional FEM procedure. The Lagrangian particle method of smoothed particle hydrodynamics is derived in more detail, as it is less commonly used in computational analysis of explicit dynamics.

4.1.1 Shell Element Variations and Shape Functions

To briefly invoke a colloquial description, the introduction of 3D shell formulations has been a blessing and a curse. That is, while such algorithms have been beneficial for computational efficiency, they have invariably been detrimental for the accurate formulation of fundamental theories [94]. Under constraints of realistic 3D deformation, shell elements can only aspire to be rough approximations of true material behavior. However, many structural bodies of engineering interest involve skin-type elements which are quite thin with respect to reinforcing bodies. By using shell formulations, the following advantages are possible:

- A reduction in total number of required equations via a reduction in total out of plane nodes

- Possible elimination of timestep-dependence on element thickness via the through-thickness reduction to 2D
- Selectively-reduced equations possible for certain materials and design constraints, further increasing computational speed

Yet the aforementioned improvements can have serious mathematical drawbacks dependent on model parameters, such that

- Stress wave propagation is impossible through the thickness of shell elements, creating S-wave disparities in 3D material formulations
- Selectively-reduced integration algorithms create so-called "hourglassing" via zero-energy modes, in which the deformation of an element may be unphysical and be a net zero contributor to total strain energy
- Usage of shells for "thin" 3D structures may lead to inaccurate kinematic constraints and overestimates for strain energy and other relevant parameters

Based on explicit constraints defined initially by Hughes, *et. al* [95], Hughes and Liu proposed an explicit 3D shell formulation [96] which was also extended into axisymmetric and 2D formulations with a reduced-integration Lagrangian framework [97]. These were analyzed by later researchers [98] who found that while the Hughes-Liu shells predict acceptable results in plane strain assumptions, their prediction of through thickness shear was inconsistent with true equilibrium conditions. A more efficient alternative is the 3D Belytschko-Lin-Tsay shell [99], which uses an optimized quadrature algorithm to predict results consistent with the Hughes-Liu shell using less than $1/6^{th}$ the computational effort.

4.1.2 Solid Element Formulations

The hexahedral solid "brick" element is the workhorse of 3D finite element algorithms. Using 8 nodes within each corner and Gaussian integration, stresses and strains are integrated in all three dimensions without relying on the mid-plane assumptions and integration point simplifications seen in shell elements. The traditional fully-integrated solid element has disadvantages however, in that increased strain leading to elevated

Poisson effects can result in bending modes being disallowed [100]. Additionally, if deviatoric stresses are significantly smaller than hydrostatic pressure, no physical basis for resisting hourglass modes is possible. Instead, a selectively reduced element is used [101], which both reduces the order of the integration matrix, saving computational cost, and also significantly reduces hourglass modes from shear locking.

In addition to the hexahedral solid element, pentahedral "prism" elements and tetrahedral elements are implementable in explicit dynamics. The integration of such nodal configurations often contributes an unphysical stiffness to calculations and directly increases inaccuracies; the presented meshes using solid elements were designed to eliminate the need for these entirely.

4.1.3 EFG and XFEM: Limited Modifications

In linear analysis using finite elements, it is often the case that the computational time for the solution of assembled equations is trivial compared to the time required for initial mesh generation procedures. While 2D and 3D solid elements are demonstrably robust and accurate, complex geometries require care to prevent under-integrated elements and increasingly small time steps. To counter some of the limitations of more traditional Lagrangian finite element formulations based on shape function integration across fixed nodes, Nayroles *et al.* developed an element-free formulation based on moving least-squares interpolants [102]. The method requires only a generation of nodes within the domain of interest (often quasi-randomly placed) coupled with a consistent boundary treatment; a mesh of finite elements is not needed for the development of proper Galerkin equations. This initial algorithm was extended by Belytschko *et al.* [103] to form what was termed the element-free Galerkin (EFG) method. Nodal connectivity is established through the aforementioned interpolants, but the domain is still discretized in a number of cells over which integration is performed.

This method was designed to couple the stability and consistency of solid formulations, but be applicable to mesh-free scenarios. In practice, however, the usage of cells and nodal connectivity limits the practical usage. While large deformations can be approximated more accurately than with more traditional solid formulations, the nodal

neighbors are invariant, and only deformations involving compression, extension, and continuous shear are reproducible. Problems involving penetration, separation, and evolving boundaries or free surfaces see little to no improvement under EFG discretization.

Explicit finite element methods are used for dynamic loading conditions involving time varying loading conditions such as impact, shock, and combined tensile, compressive, and shear loading. Such compounded loading conditions inherently introduce numerical discontinuities, which require special treatment if a diverging solution is to be avoided. A crack represents such a discontinuity, as it is a discontinuous increase in displacement, representing a mathematically infinite value of strain. Such discontinuities have been resolved by local mesh refinement around the crack path [104], but this introduces a mesh-dependent solution which can vary from the true physics of the problem. An alternative approach incorporates the Partition of Unity method [105] to create an enriched field of nodes with additional degrees of freedom to map the crack geometry and modify the finite element shape function with an additional Heaviside term for mathematical treatment of the discontinuity. This Extended Finite Element Method (X-FEM) [106] has seen success in modeling 2D crack propagation, and has been modified to implicitly model 3D cracks and branching. Unfortunately, the crack separation which is possible through X-FEM requires an initially continuous mesh, and allows for progressive separation through an extending crack front. In the condition of spall, shock pressures create a tensile regime which exceeds material strength, creating a dynamic expansion of material which varies in density and strength and ultimately fails; this scenario is difficult to resolve with X-FEM since the failure happens suddenly and completely. Additionally, X-FEM methods are subject to the deformation constraints of standard 2D and 3D elements, and cannot track the massive deformation present in HVI.

For these reasons, the EFG and X-FEM method were deemed unsuitable for modeling of shock, deformation, and debris induced through HVI.

4.2 Arbitrary Lagrangian Eulerian Schemes

Generally speaking, in a Lagrangian reference frame, objects of interest are discretized into elements which define only the geometry of the original part, and these elements move and deform as the material reacts to displacements and forces. By contrast, an Eulerian reference frame discretizes an area of interest into stationary cells while relevant material properties are advected through the mesh. A deforming cube depicts the differences between these schemes in Figure 8. Lagrangian schemes satisfy conservation of mass by definition, and follow interfaces between regions exactly as any mesh encompasses only the geometry of the relevant entity. However, under large deformations, the original elements can become warped and distorted so as to prevent mathematical convergence [94]. Eulerian algorithms use stationary meshes which allow for extensive distortion of the original material with no convergence issues; this also means that the resolution of relevant properties and geometrical features is a function of the initial mesh size, and interfaces can become difficult to track. Arbitrary Lagrangian-Eulerian (ALE) schemes attempt to rectify these issues by combining the advantages of each method; in practice, however, this is done in several fundamentally different ways. Within LS-DYNA, ALE algorithms allow a deformed Lagrangian part to use an Eulerian grid for remapping distorted elements; materials are also advected through a deformable moving mesh, with interfaces reconstructed at regular intervals. In addition to the aforementioned algorithms within LS-DYNA, modern advancements of Godunov's work [107] in using Riemann problems to capture shock discontinuities have seen recent popularity due to their accuracy and self-consistent formulation; it is expected that these improved algorithms will soon be available in commercial codes.

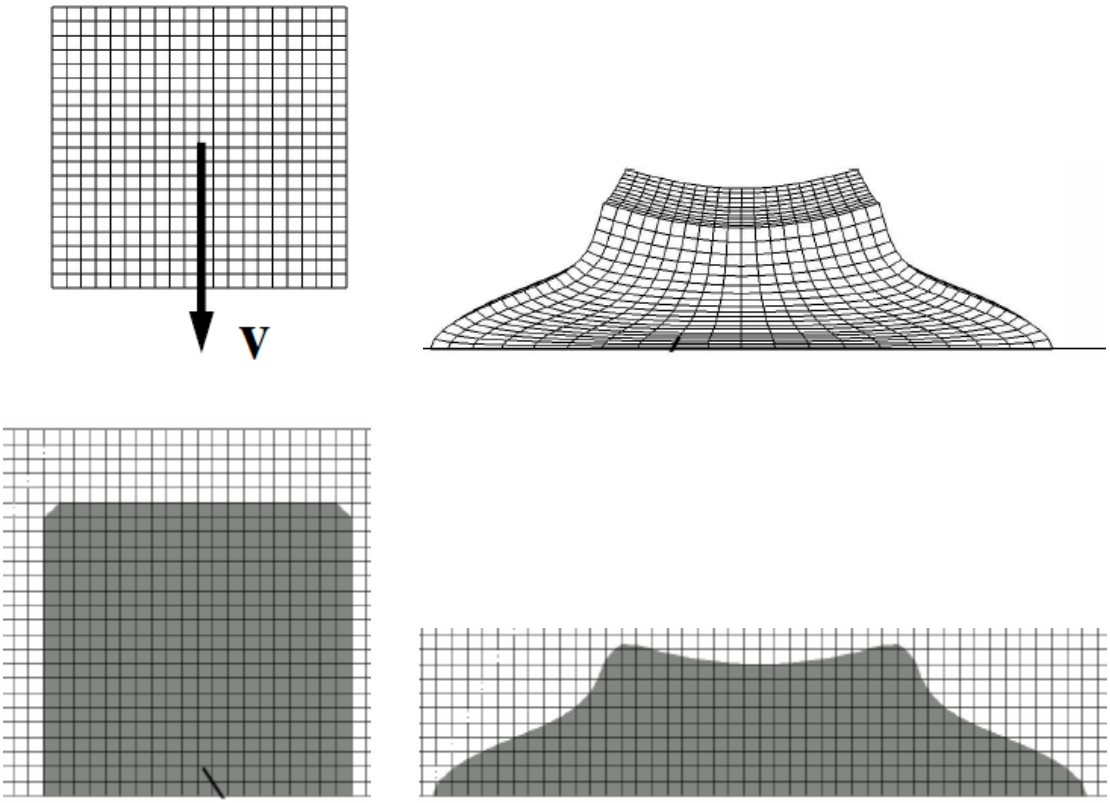

Figure 8. A Lagrangian scheme (top) compared with an Eulerian description of the same deformation (bottom).

4.2.1 Lagrangian Mesh Remapping

The Lagrangian remap algorithm of ALE uses the Eulerian advection scheme purely to alleviate the distortion possible in Lagrangian finite elements. The Lagrangian mesh is allowed to follow prescribed constraints, and as the elements deform past a given threshold, the advection algorithm begins performing minute adjustments of the mesh, advecting the relevant material conditions through the updated discretization as necessary [108]. This increases accuracy in two ways: by preventing excessive mesh distortion, the fidelity of the result is increased in the Lagrangian frame, but secondly, the advection scheme is second order accurate, providing an improvement over manually remeshed simulations. The cost of remeshing is often much larger than the cost of the Lagrangian calculation which creates deformation, however, the increase in model fidelity can be

drastic. After a Lagrangian deformation time step is completed, the advection step begins by analyzing the deformed mesh. If remeshing is necessary, the boundary nodes are moved before the interior nodes, and the element variables are then transported through the new mesh as necessary. This algorithm can provide significant improvements in accuracy, but is limited to deformations which retain the fundamental characteristics of the initial Lagrangian domain. Large deformations which change the overall element distribution can increase the computational cost of the remeshing algorithm until the advection calculations fail to converge. As an example, a cylinder may deform into a conical shape and be accurately remeshed, but if the central node of the upper surface is axially deformed downward approaching a hollow tube, the remeshing algorithm will invariably reduce the timestep until no solution is possible. The Lagrangian remap form of ALE algorithms is thus of little use to HVI computations, as the evolving domains and extensive fragmentation can drive such algorithms past their practical usability.

4.2.2 Multimaterial Advection Schemes

In contrast to the mesh remap ALE scheme, the multi-material ALE formulation (MMALE) is primarily Eulerian with a Lagrangian interface reconstruction step. The advection mesh itself is also allowed to move and deform, representing a Lagrangian domain, within which an Eulerian mesh and material description hold. In LS-DYNA, shock capturing Eulerian methods are available using SALE-type first-order donor cell algorithms [109] and second-order van Leer [110] implementations. While the donor cell algorithm is monotonic and conservative, it can be highly dissipative under shocks. This means that while numerical discontinuities are avoided, the resultant material behavior is unnecessarily smoothed over a large number of neighboring cells in 3D. The donor cell algorithm can be somewhat dispersive as well (i.e. transient material response is communicated slower than mass flux) but these variations are largely damped out by the dissipative smoothing. The far more useful algorithm is the van Leer implementation, which constructs a piecewise linear field from a series of constant value cells, then maps the values from the constructed field onto the new mesh configuration. This advection method conserves total internal energy and momentum, but not kinetic energy. Instead,

kinetic energy which is dissipated as a result of the advection algorithm is converted to internal energy.

4.2.3 Modern Godunov Methods

In researching variations on control volume schemes, Godunov [107] developed a modification to the classical Riemann problem [111] which allows finite volume methods to effectively capture shock discontinuities at control volume boundaries. Based on integral conservations laws, his method involved an initial assumption of piecewise continuous distributions of shock solutions at any given time *n*; the actual distribution could follow a constant, linear, quadratic, or higher distribution, so long as it remained continuous. From these distributions, first, second, or third order formulations are constructed to solve the Riemann problem at the interface between two control volumes. After the solution of the Riemann problem across every interface, the new state of the control volume is calculated from the average of each neighboring contribution at time *n+1*. This method saw limited popularity upon its initial formulation, but after van Leer revisited the algorithm [112] and Caramana, et. al reformulated the scheme for total energy conservation [113], a new field of shock hydrodynamics modeling grew to investigate Lagrangian and ALE implementations of conservative Godunov methods [114]. The primary advantage of modern Godunov methods over classical ALE schemes is that energy is conserved implicitly and the artificial viscosity is thermodynamically consistent, meaning that shock discontinuities are not only numerically stable, but also physically accurate. Modifications to these algorithms have been investigated by the author, but are not yet suitable to model 3D impact scenarios [115].

4.3 Smoothed Particle Hydrodynamics

In order to model the extreme deformation and explosive interactions seen in HVI, many computational discretization methods are tested beyond design constraints and fail to converge. Traditional finite element techniques are suitable for many interactions of continuous media, but when analyzing the rapidly evolving domains present under hypervelocity conditions, mesh warping and entanglement can prevent effective calculation past limited timescales [116]. Even meshed schemes with adaptive mesh

refinement and element erosion/deletion can prove insufficient, as post-impact debris is often deleted, and highly deformed shapes are truncated [117]. However, meshless Lagrangian schemes such as Smoothed Particle Hydrodynamics (SPH) allow severe deformation without numerical discontinuities. SPH has been used to successfully model both solid deformation [118] and fluid dynamics [46], and is thus an excellent method to model a high energy phenomenon which displays characteristics of both.

The SPH method was initially formulated independently by Lucy [119] and Gingold and Monaghan [120] to model star movements within evolving galaxies. The method was later expanded to continuum mechanics as the equations of fluid motion were discretized [121]. This was shortly followed by a generalized discretization of solid mechanics by Libersky and Petschek [118]. In continuum mechanics, the method discretizes a continuous medium into a number of particles with interacting sub-domains. Each particle has a center of mass, a particle volume within radius *r*, and a smoothing length *h*. The strength and range of a particle's influence are dictated by a smoothing kernel function, *W*, and smoothing length, *h*, respectively, with the interaction strength equal to zero at a radius over 2*h* from the center.

4.3.1 Kernel and Particle Approximation

The kernel approximation of a function $f(x)$ over a sub-domain of influence can be written as:

$$\lim_{h\to 0} W(x-x',h) = \delta(x-x') \tag{31}$$

where:

$$\langle f(x)\rangle = \int W(x-x',h) f(x') d\,x' \tag{32}$$

$$\int W(x-x',h) d\,x' = 1 \tag{33}$$

These constraints on the proposed smoothing kernel have addressed continuous functions, but are not yet appropriate for a series of discrete particles. Eq. (32) can be written as a summation over a series of discrete points as depicted in Eq. (34) as

$$\langle f(x_i)\rangle \approx \sum_{j=1}^{n} f_j(x_j)\, W\big(x_i - x_j, h\big)\frac{m_j}{\rho_j} \tag{34}$$

Thus the total influence seen by one particle is the summation of effects from all neighboring particles. The effect of Eq. (34) can be seen in Figure 9, where the overlapping Kernel functions are summed at any given point, creating a smooth distribution.

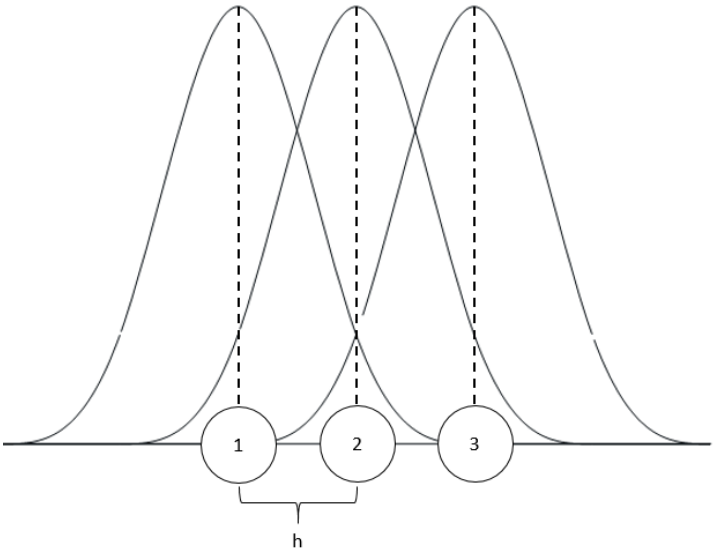

Figure 9. Kernel function overlap visualization.

The Kernel function itself is generally similar to a Gaussian distribution and can be selected from a variety of functions. The present study uses the Cubic B-spline, a piecewise continuous function described by Eq. (35).

$$W(v,h) = C\begin{cases} 1 - \frac{3}{2}v^2 + \frac{3}{4}v^3 & v \le 1 \\ \frac{1}{4}(2-v)^3 & 1 < v \le 2 \\ 0 & 2 < v \end{cases} \tag{35}$$

where C is a normalization constant dependent on the number of dimensions and v represents the normalized coefficients, given as

$$v = \left|x_i - x_j\right|/h \tag{36}$$

In accordance with the improved methods of previous studies, the smoothing length parameter has been left variable to obtain a more realistic representation of HVI behavior [122]. This allows for the solver to adjust the smoothing length on a particle-by-particle basis, which enhances accuracy considerably when large deformations and variations in particle spacing are present.

4.3.2 Equations of Motion

Particle behavior is derived from the conservation laws of fluid dynamics [9]. The discretized forms of mass, momentum, and energy conservation are shown in Eq. (37), where *i* represents a given particle and *j* is any neighboring particle.

$$\begin{aligned} \frac{d\rho_i}{dt} &= \rho_i \sum_j \frac{m_j}{\rho_j}\left(U_i^\beta - U_j^\beta\right) W_{ij,\beta} \\ \frac{dU_i^\alpha}{dt} &= -\sum_j m_j \left(\frac{\sigma_i^{x\beta}}{\rho_i^2} + \frac{\sigma_j^{x\beta}}{\rho_j^2}\right) W_{ij,\beta} \\ \frac{dE_i}{dt} &= \frac{\sigma_i^{x\beta}}{\rho_i^2} \sum_j m_j \left(U_i^x - U_j^\beta\right) W_{ij,\beta} \end{aligned} \tag{37}$$

These equations fail to account for dissipative terms, and can allow large unphysical oscillations near shock waves. With high velocity particles possessing infinitesimal surface areas, each particle can create false impact pressures and shockwaves. A Monaghan-type artificial viscous pressure term represented by Π was implemented to smooth the shockwave between particles as opposed to treating them individually [123].

$$\frac{d\rho_i}{dt} = -\sum_j m_j\left(U_i^\beta - U_j^\beta\right) W_{ij,\beta}$$

$$\frac{dU_i^\alpha}{dt} = -\sum_j m_j \left(\frac{\sigma_i^{x\beta}}{\rho_i^2} + \frac{\sigma_j^{x\beta}}{\rho_j^2} + \Pi_{\mathrm{ij}}\right) W_{ij,\beta} \tag{38}$$

$$\frac{dE_i}{dt} = \sum_j m_j\left(U_i^\alpha - U_j^\alpha\right)\left(\frac{\sigma_i^{x\beta}}{\rho_i^2} + \frac{\Pi_{\mathrm{ij}}}{2}\right) W_{ij,\beta}$$

This term is defined and further described during the discussions of numerical stability in section 4.4.3.

4.3.3 SPH Variations

The above formulation assumes that the smoothing function is symmetric, and that the same weighting interaction from particle *i* to particle *j* is exerted by particle *j* on particle *i*. While this does enhance stability under certain loading conditions, it is not a requirement for mathematical consistency and can even be a detriment in rare scenarios [124]. Removing this constraint, the particle approximation to the weak form of conservation of momentum is expressed in a more general form as

$$\frac{dU_i^\alpha}{dt} = \sum_j m_j \left(\frac{\sigma_i^{x\beta}}{\rho_i^2} W_{ij,\beta} - \frac{\sigma_j^{x\beta}}{\rho_j^2} W_{ji,\beta}\right) \tag{39}$$

and the condition that $W_{ij,\beta} = W_{ji,\beta}$ is not enforced.

Additionally, it is possible that materials and domains with different densities and different discretization intervals will interact. In the conditions of a domain with varying particle spacing, the mass and density assigned to closely packed entities will necessarily vary from those approximating larger volumes. Under such conditions, the symmetric and generalized particle approximations can predict inappropriate interaction terms. To remedy this, the generalized approximation is modified further to reflect appropriate mass-weighting, such that the momentum equation becomes

$$\frac{dU_i^\alpha}{dt} = \sum_j m_j \left(\frac{\sigma_i^{x\beta}}{\rho_i \rho_j} W_{ij,\beta} - \frac{\sigma_j^{x\beta}}{\rho_j \rho_i} W_{ji,\beta} \right) \tag{40}$$

which is sometimes referred to as a fluid formulation, due to the robustness when calculating free surfaces and interactions from particles on unstructured configurations.

Under certain loading conditions, tensile forces and accelerations between SPH particles are improperly represented by the B-spline kernel function; when this occurs, numerical separation is possible in which the particles separate without sufficient stresses to cause material failure [125]. This "tensile instability" results from an interaction between the chosen material model and the kernel function which creates a zero or negative modulus, leading stresses to amplify deformations. An alternate SPH formulation was proposed to correct this issue, in which the kernel around a particle is no longer Eulerian in nature, but defined in a Lagrangian reference frame. This means that rather than the support kernel defining a fixed region around a node through time, it covers the same set of points through time as defined by the initial configuration. While this Total Lagrangian formulation allows for tensile forces with no risk of instability, the fixed support eliminates the dynamic neighbor search which makes SPH useful for large deformation problems.

The four discussed SPH variations are compared to each other under a problem of plastic deformation in Appendix A, where the possible shortcomings of each are discussed. Unless otherwise stated, the generalized form in Eq. (39) was used for all presented simulations.

4.3.4 SPH Boundary Condition Treatment

A single SPH particle with no neighbors on one side is mathematically a free surface. Using standard FEA boundary methods, such as constraining movement in one or all directions, can create instabilities, as the standard support for a domain of *2h* ensures that insufficient quantities of fixed particles contribute an inadequate support kernel to interior nodes. Additionally, a reflected or slip boundary condition requires defining an adequate level of particles outside the domain of interest. Instead, a self-consistent method of using "ghost" particles was implemented [126], in which virtual particles are initialized opposite the boundary to perfectly counteract the kinematics of the boundary particles, creating a perfect Neumann boundary condition using the internal SPH formulation.

4.4 Algorithms for Coupling and Stability

4.4.1 Contact algorithms

While SPH particles allow for much larger deformations than meshed methods, the computational cost associated with a large domain can become excessive. In particular, a uniform particle spacing in all directions is recommended for accuracy; this means that modeling thin structures with sufficient through-thickness resolution can force a prohibitively large number of particles in thicker directions. It is therefore prudent to combine SPH and other finite elements in the same simulation, such that the benefits of both methods can be combined. A simple way of creating numerical communication between SPH nodes and finite elements is via a standard FEM contact algorithm, treating the SPH particles as if they were FEM nodes.

The most straightforward manner for contact between FEM elements is the nodal penalty method [10], in which penetrating "slave" nodes induce an artificial spring force within the "master" element which is compatible with the finite element stiffness matrix. This force resists further penetration of the offending surface, and creates a tied deformation between the incident node and the element. This is a more robust approach than the more general kinematic constraint method [95], and ensures that momentum is exactly conserved.

In practice, this is a sufficient algorithm for low velocity contact between deformable bodies, and some interactions at higher speeds if the impact surface is mathematically rigid. At higher speeds, however, the standard penalty approach is insufficient to capture an accurate estimation of proper constraints; the penalty formulation assumes that material strengths and stiffness dominate the interaction, which is inaccurate as impact velocities exceed the ballistic regime. At speeds approaching those seen in hypervelocity impacts, it is necessary to adjust the penalty constraints in a manner similar to that used in modeling dissimilar material interfaces. Within this so-called "soft" constraint algorithm, an additional stiffness is defined based on the masses of the penetrating nodes and the surrounding nodes of the master surface [127]. This was defined initially to model the contact of materials with highly dissimilar stiffness, such as contact between steel and foam, but the mass-weighted approach generates a significant improvement in penetration detection at ballistic speeds and higher.

4.4.2 Hybrid Elements

In improvement over the master-slave contact algorithms was suggested by Sauer [128], via the introduction of hybrid elements which contain FEA nodes coupled to meshless particles. In this way, the SPH particles near the hybrid FEA elements interact with the interior particles via the kernel function, identical to SPH-SPH interactions; the forces are then translated to the element's integration points, such that the nodal reaction forces are transmitted to any other FEA elements which border the hybrid element. This two-way communication between the methods improves momentum transmission between the domains and reduces reflected transient waves. By using the internal kinematics of each numerical method, this hybrid technique shows improved accuracy over the previous master-slave or tied transmission methods, and is the preferred algorithm when using both SPH and FEA for a single domain.

4.4.3 Artificial Viscosity

As previously discussed, a shock is a rapid rise in energy with a width of only a few mean free paths; on the grid resolution of standard numerical applications, this is represented as a discontinuous jump between two states. While coarse resolutions can smooth over this condition, mesh refinement leads to increasingly discontinuous solutions with unphysical oscillations following the shock. Richtmyer and von Neumann [129] formulated a pressure term consistent with finite difference and finite element methods to damp these oscillations and smooth the discontinuity. This artificial viscosity term is formulated as

$$q = \alpha\rho(v_1 - v_0)^2 + \beta\rho C_0(v_1 - v_0) \tag{41}$$

or equivalently

$$q = \alpha\rho(\dot{\varepsilon})^2 + \beta\rho C_0|\dot{\varepsilon}| \tag{42}$$

where α and β are constants which define the level of damping desired, $\dot{\varepsilon}$ is the strain rate, v is the nodal velocity, and C_0 is the speed of sound. Ideally, the artificial viscosity should be as small as possible to still retain an accurate result; in practice, however, minimal artificial viscosity for shocks replicates the jump discontinuity more sharply, but at the cost of unwanted resonance.

During the derivation of SPH equations in section 4.3.2, the artificial viscous pressure term was introduced, but never explicitly defined; formulated by Monaghan and Gingold [123], the term appears as

$$\Pi_{ij} = \frac{2}{\rho_i\rho_j}\left(\beta\mu_{ij}C_{ij} + \alpha{\mu_{ij}}^2\right)$$

where (43)

$$\mu_{ij} = h_{ij}\frac{(v_i - v_j)(x_i - x_j)}{(x_i - x_j)^2 + \eta^2}$$

Artificial viscosity is only active in compression ($(v_i - v_j)(x_i - x_j) < 0$), and the extra term in the denominator is designed to prevent division by 0, defined by $\eta = 0.01{h_{ij}}^2$. This can readily be seen as the particle discretization of the von-Neumann-Richtmyer artificial viscosity above, with a quadratic term for shock smoothing and a linear term to damp spurious oscillations and excessive turbulence in the momentum field. Traditionally the constants that have been recommended for use are $\alpha = 1.5,\ \beta = 0.06$. This typically produces minimal numerical damping of flows in the linear term, and acceptable smoothing of shocks in the quadratic term without excessive resonance, however, stronger shocks may require adjustment of these constants.

4.4.4 Time Step Stability Criteria

In an explicit numerical scheme, partial differential equations of space and time are solved simultaneously. As the solution marches forward in time, the relevant spatial derivatives only yield stable solutions with a sufficiently small time step. As initially seen by Courant, Friedrichs, and Lewy [130], the stability of the solution requires that the speed of information not traverse an entire spatial step faster than one time step (i.e. the time step must be sufficiently small so that information cannot reach the next node before the next integration step is performed). They suggested a reduction factor of 0.9, such that the maximum time step with the Courant-Friedrichs-Lewy (CFL) factor is

$$\delta t \leq CFL * Max\left(\frac{v}{\Delta x}\right) = Min\left(\frac{\Delta x}{v}\right) CFL \tag{44}$$

where the smallest inter-nodal distance and largest velocity can be used for a global time step which guarantees stability.

For SPH, the time step criteria follows the standard form using minimum distance and information speed, defined with the CFL multiplier as

$$\delta t = Min\left(\frac{h_i}{C_i + v_i}\right) CFL \tag{45}$$

But since C_i is the adiabatic sound speed, the standard CFL condition of 0.9 is often insufficient to prevent numerical discontinuities in the presence of overdriven shocks. The artificial viscosity is designed to damp such effects, but in practice, a CFL condition of 0.5 or lower is often necessary for stability. This is of course dependent on the constants applied to the artificial viscosity, the material model used, contact/coupling options, and several other factors.

4.5 Discussion and Summary

While physical experiments recreate the true physics of interest, computational methods can only produce results reflective of the underlying algorithms and input conditions. This means that any trends, improvements, or suggestions based on computational analysis are subject to more scrutiny than empirically determined research, and that the code results must be demonstrably self-consistent and mathematically predictable (verification), and reasonably accurate with respect to experimental results (validation).

For simple computational schemes, a test problem with an analytically provable answer is often used for code verification, where the internal mathematics are tested to demonstrably recreate the initial function. As codes become more complex, verification can be performed on each individual component if the source code is known; using the above algorithms as an example, a verification might consist of testing the time step control, artificial viscosity, and spatial discretization separately, using functions similar to each algorithms original form. In commercial codes this is impossible, since the exact discretization method is often not available via the source code. It is often sufficient to then demonstrate code consistency via a convergence study; if a known test problem is modeled with increasing computational accuracy, the code should converge toward a single solution. If this is not the case, such a computational scheme cannot be described as predictive, since results diverge from a single consistent value. Since the source code was not available for LS-Dyna, a convergence study was performed using both the ALE and SPH formulations, and is presented in the appendix; both methods converged toward a single solution across multiple measures using the case of an extreme impact scenario. However, convergence

alone does not imply accuracy; while the SPH models showed monotonic convergence, the accuracy of SPH simulations can vary greatly under multiphysics loading conditions, and instabilities have been observed under combined tensile and shear loads [124].

If code verification indicates that the mathematical approximations are convergent and self-consistent, code validation requires that the physical approximations reasonably predict the original mechanics of interest. For simplistic scenarios such as Newtonian trajectory calculations, mathematical models can be constructed to exactly recreate the physics of interest such that the experimental error converges toward zero as accuracy is increased. In physical processes with significantly more mathematical complexity, physical approximations may only be valid over limited regimes; refinement of the mathematical discretization can only decrease error if such approximations remain accurate. In the presented work, validation was performed using debris cloud experiments, measurements of damage in impacted specimens, and measurements of velocity and deformation in several calibration models detailed in the appendix. The validation of several material models was then used as a criteria for their continued use.

5 COMPUTATIONAL MODELS

A comparison of the aforementioned solid constitutive models was done at moderate (10^4 s^{-1}) and high ($>10^5$ s^{-1}) strain rates using a tantalum Taylor bar impact test and a tantalum shaped charge, detailed in Appendix A. The results showed that the rate-dependent JC model predicted the lowest average error in both strain rate regimes, tending to overpredict material deformation in the moderate strain rate regime, and underpredict damage in the higher regime. The SCG model presented the second lowest average error, but as it was formulated for high strain rates alone, it tended to underpredict deformation in lower strain rates. The rate-dependent SCGL form displayed greater errors in both regimes, despite the strain rate corrections. The ZA model greatly overpredicted the moderate strain rate response, giving the highest error of the rate-dependent models, and underpredicted the high strain rate response with higher errors than the JC model in both cases. When using the MTS model, lower strain rate response was excessively stiff, and the underpredictions represented an error comparable with the SCGL model; at high strain rates the response was more appropriate and error was comparable to the SCG model. The simplified EPH model performed the poorest in both strain rate regimes.

The rate-dependent JC model was used in the following computational models when constants were available, and the SCG/SCGL model was used when JC calibration experiments were not found in the literature. This is both due to their lower experimental error in the comparison models, as well as the large number of materials for which they have been formulated. The ZA and MTS models have seen success in modeling metallic deformation, but experiments have not been performed to calibrate constants for many structural and aerospace materials, while the JC and SCG/SCGL constitutive relations have been well researched.

The vast majority of the SCGL properties used were taken from a compendium published by Steinberg in 1996 [131] summarizing decades of research in strain rate dependency and shock dynamics. Certain alloys were not studied as extensively by the LLNL group which contributed to the report, and consequently rate-dependent parameters were acquired from other sources, if available. If such data was unavailable in a literature

search, the rate-independent SCG model was used. Some modifications to Ti 6Al/4V properties were taken from experimental studies performed by Kanel *et al.* [132], and spall properties of magnesium alloy AZ31B were adjusted using earlier work from the same research group [133]. The data used in the following models is summarized in the appendix.

5.1 Initial Computational Modeling Efforts

5.1.1 Metallic Triple Bumper Shield

Studies were done on two experimental scenarios to analyze the general behavior of the multi-bumper shielding concept commonly used. To simulate the damage of a metal Whipple shield under hypervelocity impact loading, a model was constructed to replicate the conditions of a triple bumper shield test analyzed by Groenenboom [134] following previous investigations by Cykowski [135]. In the physical test, a 9.53 mm aluminum sphere impacts three layers of aluminum shielding with increasing thicknesses of 1.12, 1.95, and 3.18 mm at 6.78 km/s and 60° incidence. The impacting sphere was modeled using SPH particles to better replicate the disintegration upon impact, while the plates were modeled with shell finite elements to improve computational time and better show shock propagation through the plate structure. The soft constraint described in section 4.4.1 was required for effective contact between the shell elements and SPH particles. The model setup and results are shown in Figure 10.

The general response of the plate is accurately captured by this somewhat crude formulation, and the damaged areas correspond well to Groenenboom's 2D results within certain bounds. The impactor fragments immediately upon impact, sending shockwaves through the target structures. After penetrating the first bumper with a small hole, the fragmented debris causes greater damage to the second plate due to its larger area, but is mostly defeated by the time particles reach the final barrier. However, a crucial component of the previous simulations that is not captured by these studies is the debris created by the plates themselves. The shell formulation does not allow for sufficient fragmentation to transfer into subsequent plates, meaning the multi-bumper simulation cannot accurately reflect real world conditions. Additionally, the choice of key parameters

in the contact algorithm between impactor and plate was seen to have a large effect on the resultant debris field and damage.

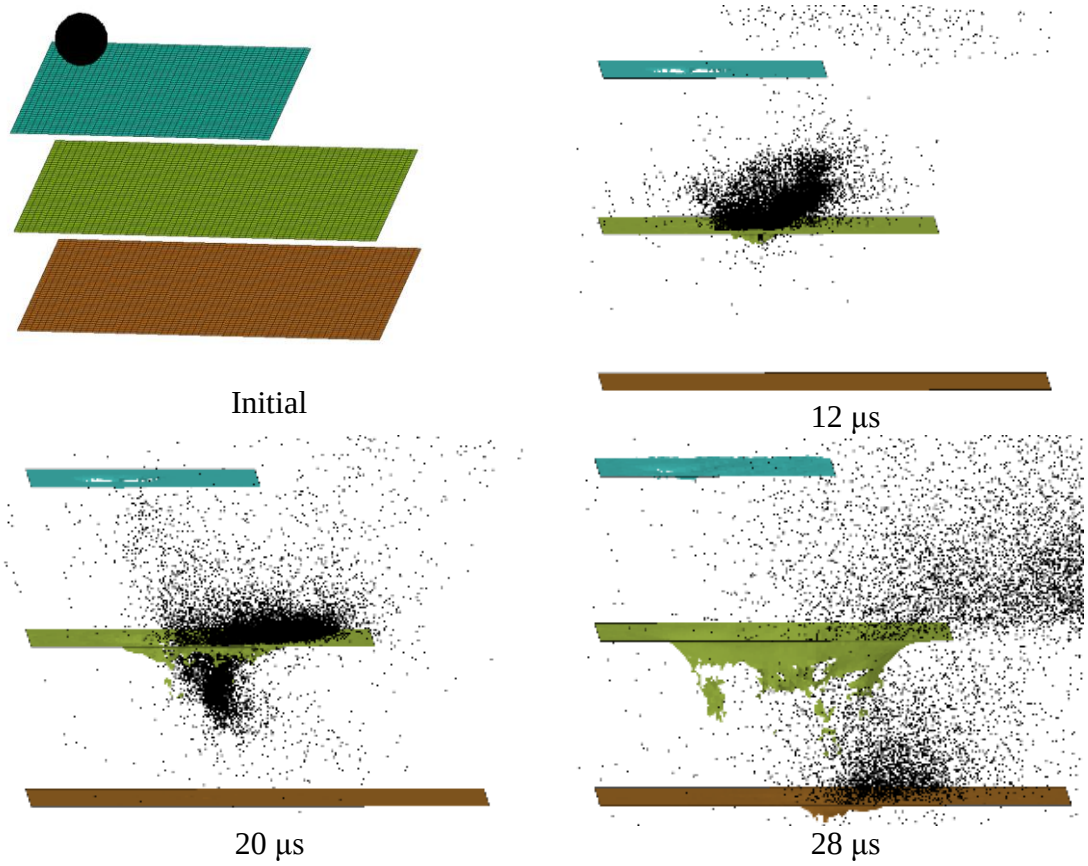

Figure 10. Triple bumper shield damage evolution from SPH impactor.

5.1.2 Composite double bumper shield

Next, a double bumper shield consisting of a metal initial bumper and Kevlar backplate was modeled, to replicate a test performed by Reidel [136] in which a 7 mm Al 2024 sphere at 4.75 km/s impacted a double bumper shield composed of a 2 mm Al 6061 bumper with a 5.7 mm Kevlar backplate. The internal spacing was 15 mm, and the Kevlar backplate was composed of 18 layers of woven 0°/90° fabric with a 62% fiber volume fraction. Material parameters for the continuum formulation were taken from Reidel, with Tsai-Wu failure criteria. Similar to the triple bumper shield, plates were initially modeled with shell elements while the impactor was modeled with SPH particles, seen in Figure 11.

The initial behavior was replicated reasonably well with the aforementioned considerations, but the composite material model used for the backplate failed to account for shock and strain rate effects. The model did converge to an acceptable solution [137], and produced a damage profile similar to that observed experimentally, but this was primarily a consequence of the initial plate slowing impactor particles to acceptable velocities. A significant result of using a shell formulation for the initial bumper plate was a somewhat unphysical debris distribution after impact. The contact algorithm between the SPH particles and shell elements was sufficient for energy and momentum transfer, but failed to include subsequent plate debris, failed to conserve mass and energy, and failed to accurately predict the trajectory of the impacting sphere fragmentation. An improvement to this model was constructed by using SPH particles for both the impactor and the initial bumper plate, which allows for plate debris to be included in the momentum transfer on the rear shield, as well as allowing for a more accurate prediction of initial debris trajectory. A comparison of the debris cloud evolution is shown at two timesteps, as well as the final resultant damage to the Kevlar backplate with von Mises stress criteria in Figure 11. The experimentalists reported a primary damage zone with visible delamination of 11 x 11 cm on the front surface and 7.5 x 12.5 cm on the rear; smaller impacts occurred over a nearly 35 cm diameter from the central perforation on the front face and created regions of isolated delamination up to 12 cm diameter near the rear laminate. Despite the simplicity used, the quantitative damaged zone is remarkably similar to the experimental results, yielding a primary perforation zone of approximately 4 cm diameter, and a damaged delamination zone of approximately 12 cm. While the shell representation of the backplate enabled a low-effort definition of anisotropic strength and properties, the lack of any true thickness can prevent the proper calculation of through-thickness damage. Additionally, the contact algorithm between SPH particles and shell elements requires calibration of interaction constants; improper choices of these parameters can greatly alter the predicted stress levels and failure areas.

If significantly higher masses and velocities were used, the shell representation of the composite material model would fail to represent the shock and damage transfer in a physically accurate manner. The shortcomings of these models led to the abandonment of further attempts to use such a simplistic approach.

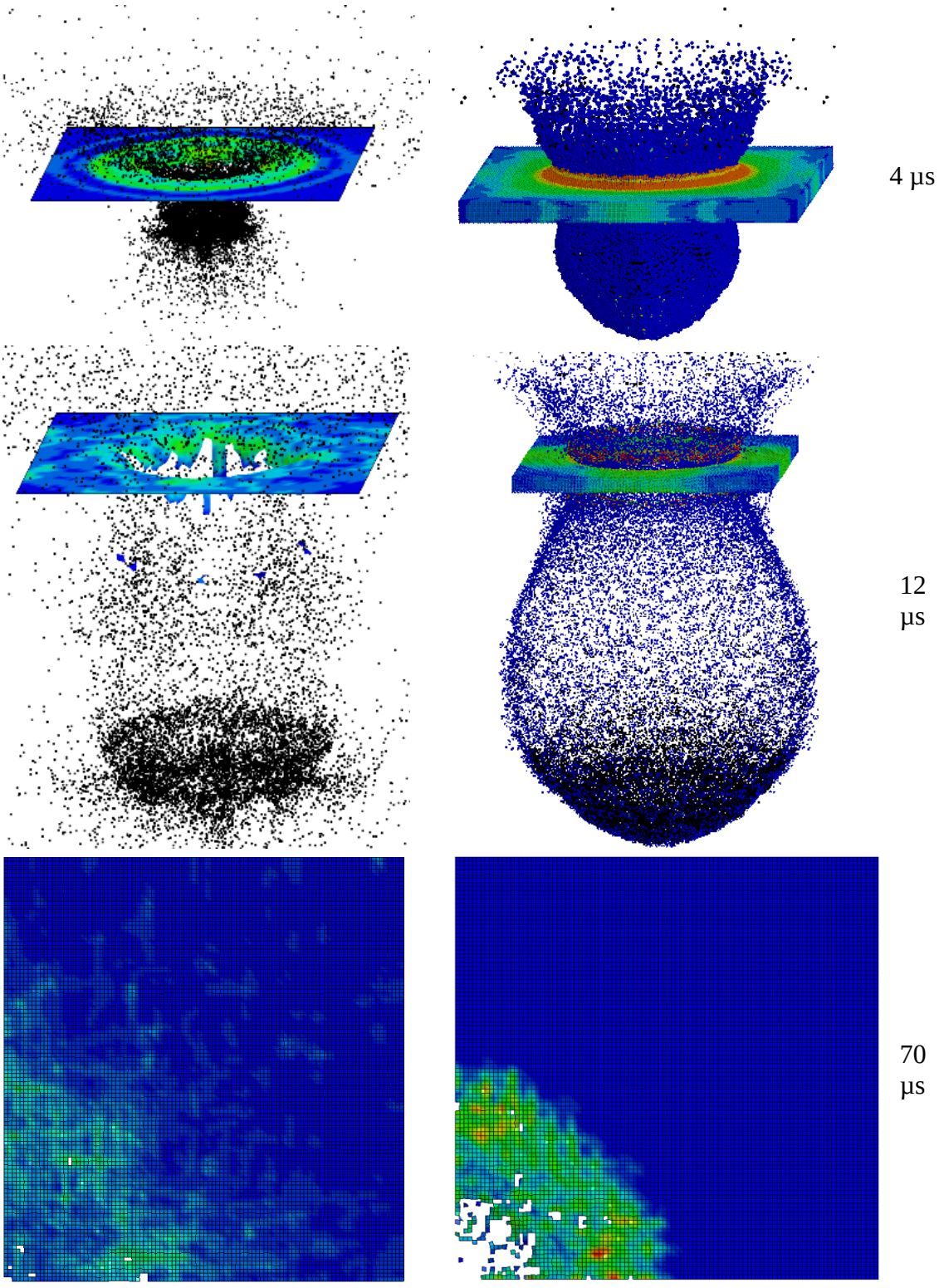

Figure 11. Stress contours of debris cloud evolution using shell bumper (left) and SPH bumper (right) as well as the final damage to the Kevlar backplate (bottom).

5.2 Debris Cloud Modeling

5.2.1 6.64 km/s Impact of Spherical Aluminum

A series of impact tests were performed by A.J. Piekutowski [138] in which Al-2017 spheres of various diameters were propelled into Al-1100, Al-2024, and Al-6061 bumpers at speeds ranging from 3.8 km/s to 7.2 km/s. While quantitative data is limited for the previously mentioned reasons, several high quality radiographs were produced which show the incident projectile immediately before impact, and the debris cloud produced several microseconds after impact. Test 1352 is used for qualitative comparison, in which a 9.53 mm Al-2017 sphere is propelled at 6.64 km/s into a 2.225 mm plate of Al-6061 at normal incidence. Piekutowski identified several critical features within the debris cloud produced by this test: a front hemisphere of denser, partially molten material primarily composed of the impactor, a less dense rear hemisphere of spalled projectile material, a disc-like central division between the two hemispheres composed of spalled solid, an ejecta veil from the impact side of the target, consisting almost entirely of target material, and an expanding debris cloud which extends forward from the impact zone of the target bumper to the disc-like central division.

To simulate this interaction computationally, a model of the impacting ball and a small impact zone of the target plate was created using 363,000 particles and quarter-symmetry. The JC and SCG formulations for Al-2024 were substituted for Al-2017, since the latter material's constants were not available. The two materials have similar chemical composition and material properties, so this substitution is not deemed inadvisable. Constants used for Al-2024 [59] and Al-6061 [139] within the JC and SCG model are given in Table A.47 and Table , respectively. The Mie-Gruneisen EOS constants for all materials used are listed in Table.

The initial impact using the JC model can be seen in Figure 12, where stress contours are plotted separately through projectile and target material. The initial phase of impact shows that while the some of the initial geometry is still present, massive deformation has already begun to occur. The shockwaves visibly propagating backward

through the impacting sphere begin to spall material off the rear, which becomes more pronounced in later stages of impact.

Piekutowski's experimental radiograph is shown in Figure 13, with debris clouds predicted by the JC and SCG models to the top and bottom, respectively. Both methods replicate the qualitative shape to a high degree of accuracy, correctly positioning the disk-like division between front and rear impactor hemispheres.

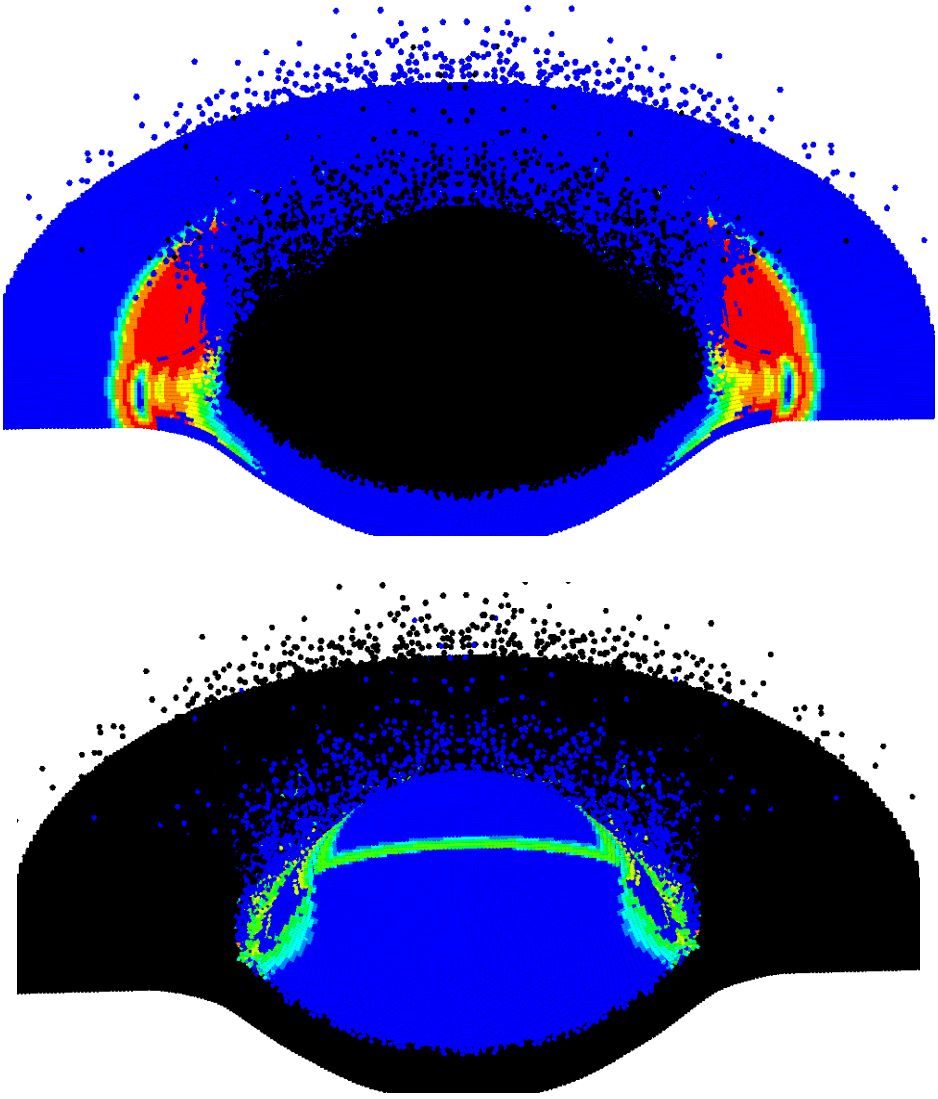

Figure 12. Stress contours through plate material (top) and impactor (bottom) at 1.1 μs

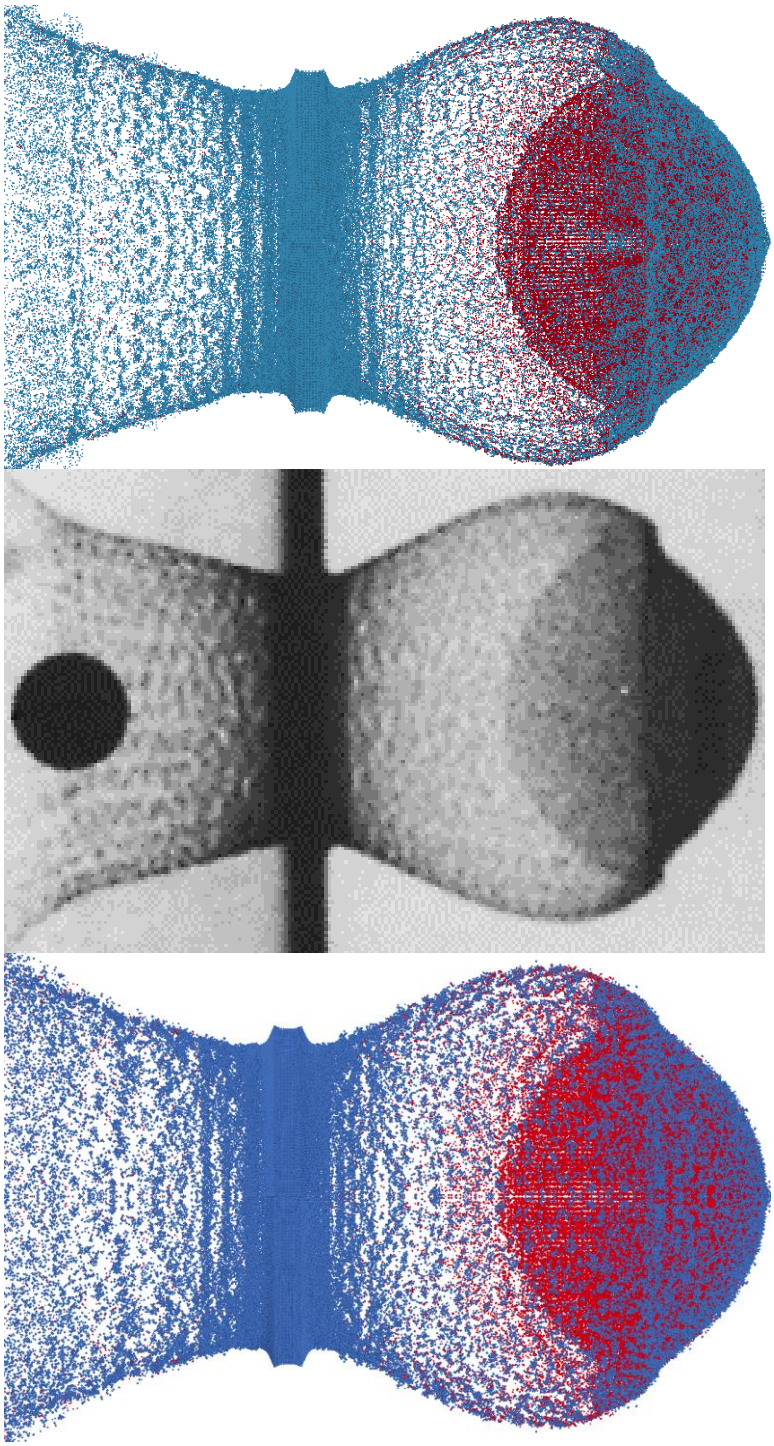

Figure 13. JC simulation (top) and SCG (bottom) compared to experimental radiograph (middle) of aluminum HVI at 6 µs.

Both methods also correctly model the forward hemisphere as a smaller, denser portion of mostly impactor material, and the rear hemisphere as a more finely distributed spall. Similarly, the debris cloud extending from the disk-like division back toward the plate is target material primarily, with the majority of projectile mass still traveling in its initial direction. However, both methods also slightly under predict the angle between the rear debris cloud and the target plate, and create a somewhat rounded interface between the debris cloud and the division between hemispheres. The JC model also creates a more finely distributed debris cloud, with the SCG model predicting larger fragments of plate material. Overall, the qualitative reproduction of both models is excellent.

To compare the two constitutive relations more directly, we can compare selected values of temperature and density, as in Figure 14. In the temperature comparison, the fringe range was selected such that all material in red is above 920 K, which is the liquidus temperature for Al-2024, such that all material in red can be assumed molten, and material in green can be assumed to have been shock heated, but not completely liquid. The JC model predicts a larger molten zone at the tip of the debris hemisphere than the SCG model, and seems to predict higher temperatures overall throughout the debris field.

The fringe range of the density plots was selected to create a cutoff at the density of molten aluminum: 2.375 g/cm^3. Ideally, we would like to assume all material above the cutoff in red is either solid or semisolid, and all material in blue is liquid, but the continuum discretization of SPH is such that it has difficulty discerning between fluid expansion (a true decrease in density) and an increase in the relative motion of spalled solid particles (a finer dust distribution, but not a true change in the density of the dust material). We cannot, therefore conclude that the majority of the impactor material has melted, as would be indicated by the density plot alone. We can conclude, however, that both models predicted the melting of a small portion in the front hemisphere, which agrees with Piekutowski's predictions. We can also see a large number of fragments in the outer debris cloud which are both below the melting point and above the density of liquid aluminum, and can agree with Piekutowski's observations that the front and rear debris fields consist of finely spalled target plate material. While the JC model predicts overall higher temperatures, it

also shows a larger number of these solid density fragments in the outer debris field of the forward plume.

Additionally, when peak shock pressure was predicted at 0.4 μs, the JC model predicts an impact pressure of 2.70 Mbar and peak von-Mises stress at .0047 Mbar, while the SCG model computed peak impact pressure at 2.74 Mbar and von-Mises stresses of .029 Mbar. Ultimately, both material models qualitatively reproduce the debris cloud characteristics to high fidelity, and both produce reasonable predictions for temperature

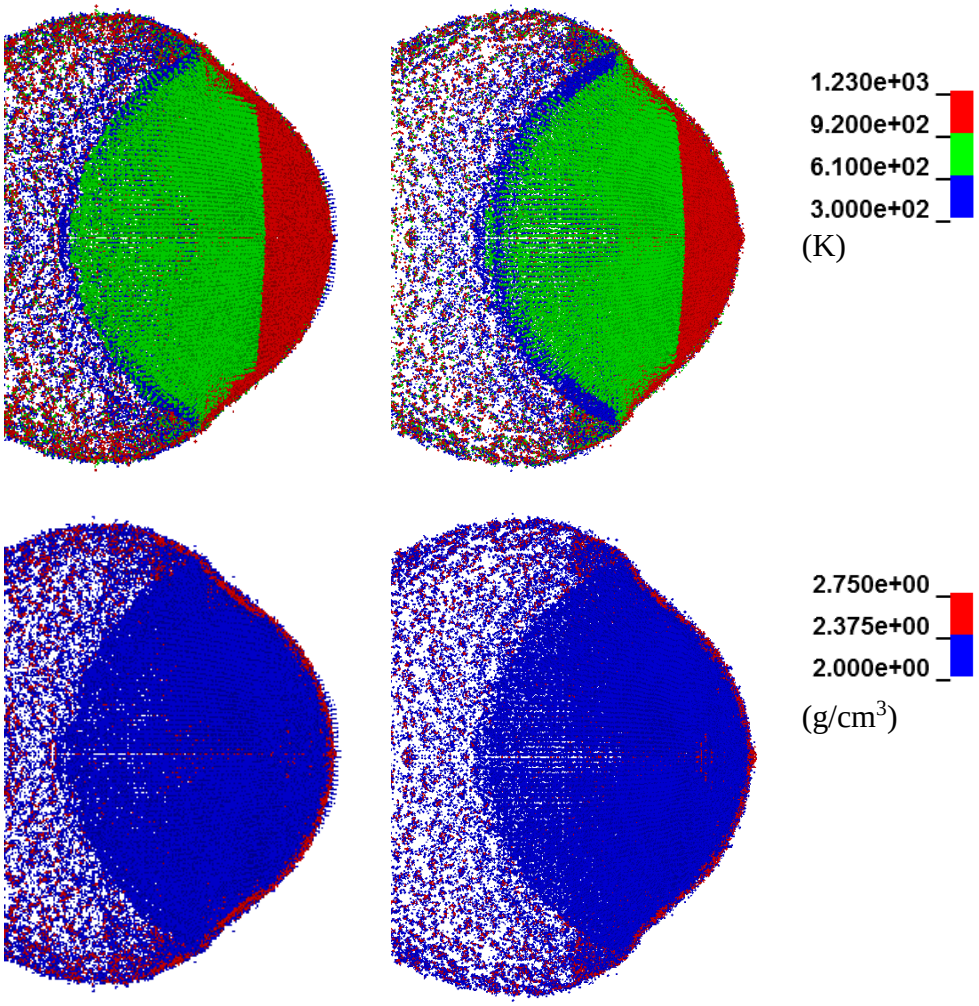

Figure 14. Comparison of temperature (top) and density (bottom) contours between the JC (left) and SCG (right) at 6 μs

distribution through the debris, and peak impact pressures. However, the JC model seems to predict a finer distribution in its debris cloud, as well as overall higher residual temperatures and densities, and significantly lower stresses at failure.

This impact was also modeled using axisymmetric MMALE elements on a grid of varying sizes as a study of ALE convergence properties. The summary of this convergence study is presented in Appendix B, but the debris cloud form and properties are presented below as a validation of axisymmetric MMALE methods in modeling HVI and debris. In contrast to SPH, the ALE models cannot adequately show true fragmentation and debris; since spalled solids expand somewhat uniformly from the original geometry, the Eulerian representation shows a quasi-uniform expansion of the original part without any significantly distinct material separation. Such deviations from the solid density and temperature are thus displayed as contours, using the same fringe ranges as Figure 14.

As seen in Figure 15, the qualitative aspects of the debris cloud are well represented by the ALE formulation as well. Despite the lack of a visual spall representation, the expansion of the rear debris aligns nicely with the experimental radiograph, and while the presence of the "notch" between the fore and aft hemispheres is somewhat more rounded than expected, its position is well placed, and extends nicely into the sloping debris cloud extending from the plate material. The density prediction from the JC model in ALE is similar to the prediction from the SPH models, but the temperature predictions are far lower overall. The region of shock-heated material doesn't extend past the fore hemisphere, which presents the majority of the impactor material as lower temperature spalled solid.

During the suite of experimental studies on debris cloud dynamics, Piekutowski measured the velocity of debris expansion in several directions after impact. As seen in Table 1, both the SPH and axisymmetric ALE formulations calculated the debris cloud properties effectively, with the largest disparity coming from the ALE calculation of radial velocity.

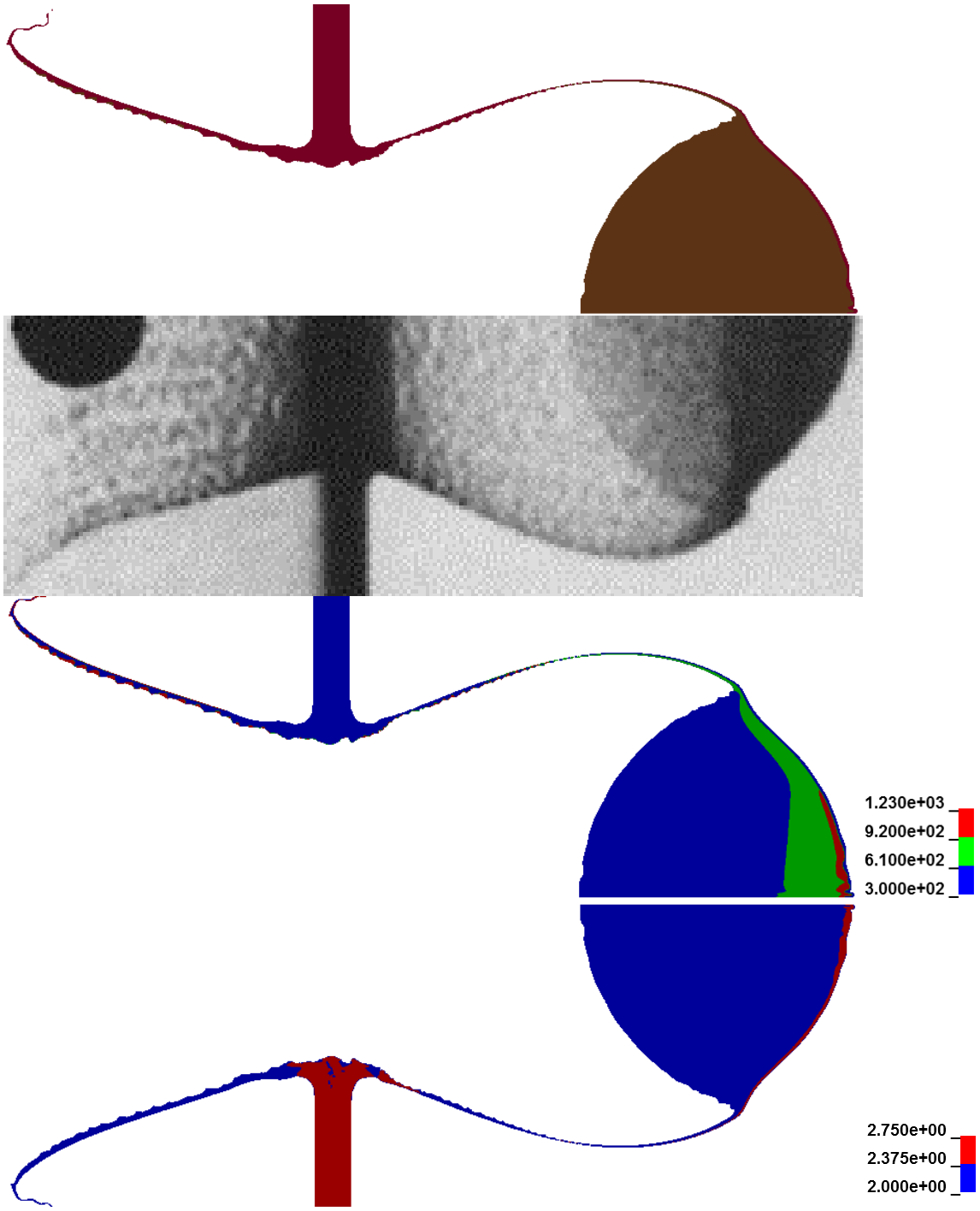

Figure 15. Comparison of MMALE debris clouds with the 6.64 km/s experimental radiograph (top) with contours of temperature and density (bottom).

Table 1. Debris cloud velocity measurements.

Measurement	Experimental	SPH	ALE
Fore Axial Velocity (km/s)	5.97	5.95	5.98
Rear Axial Velocity (km/s)	3.65	3.56	3.79
Notch Radial Velocity (km/s)	0.598	0.621	0.652
Axial % Error	-	-0.34	0.16
Rear % Error	-	-2.46	3.84
Radial % Error	-	3.76	9.03

5.2.2 Spherical Aluminum Debris Trends

The 6.64 km/s impact seen above was selected for model validation due to several unique features seen in the debris cloud which tested minute details in the code; Piekutowski also reported the results of varying bumper shield thicknesses at similar velocities. As a 9.53 mm sphere was propelled into thin and thick plates, the debris cloud morphology showed marked changes as various portions of the shield and projectile underwent spall and melt.

As seen in Figure 16, upon striking a relatively thin shield of 0.8 mm, the incident projectile remained reasonably intact after 6 μs, with a dense, somewhat molten region to the front, and a large expanding region of spall off the rear. The axisymmetric MMALE algorithm has difficulty in showing the thin exterior of the debris cloud and the more detailed features of the semisolid front due to its inability to properly represent material separation. Analysis of the temperature and density contours reveals that this projectile is still largely cool and dense in the fore regime, indicating no large degree of melt and some degree of spall.

An impact with a 1.55 mm plate produced significantly more melt, spall, and expansion, as seen in Figure 17. The expanding debris cloud exhibits a more continuous nature than the 0.8 mm plate impact, and shows a defined “notched” effect similar to the 2.225 mm plate impact. The area of dense material at the front of the debris is significantly smaller than the thinner plate impact, and the majority of the debris is represented by low temperature, low density spall with a small volume of melt at the forefront.

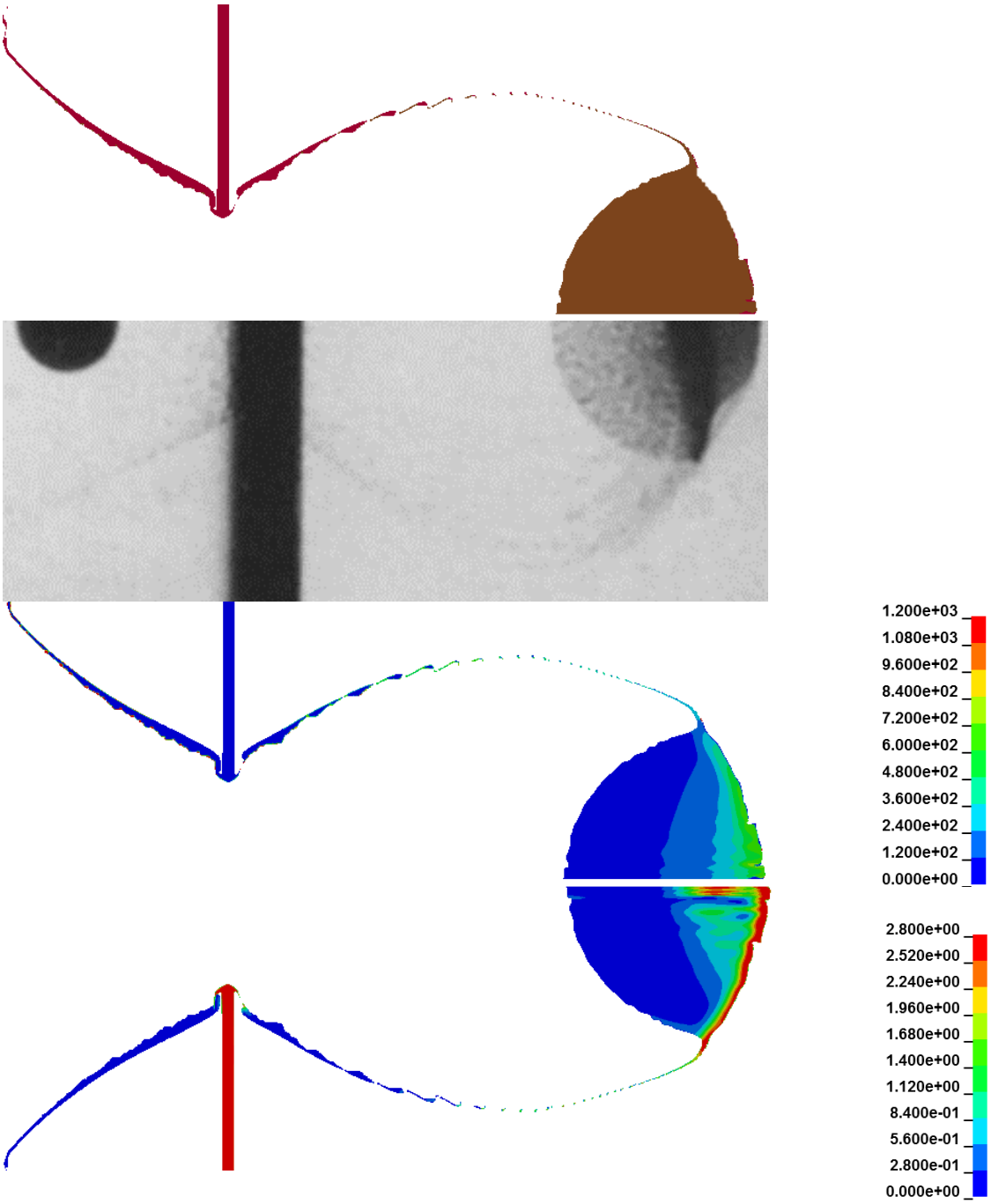

Figure 16. Radiograph and modeled debris cloud (top) at 6 μs with temperature and density contours (bottom) of a 9.53 mm sphere impacting a 0.8 mm plate at 6.68 km/s.

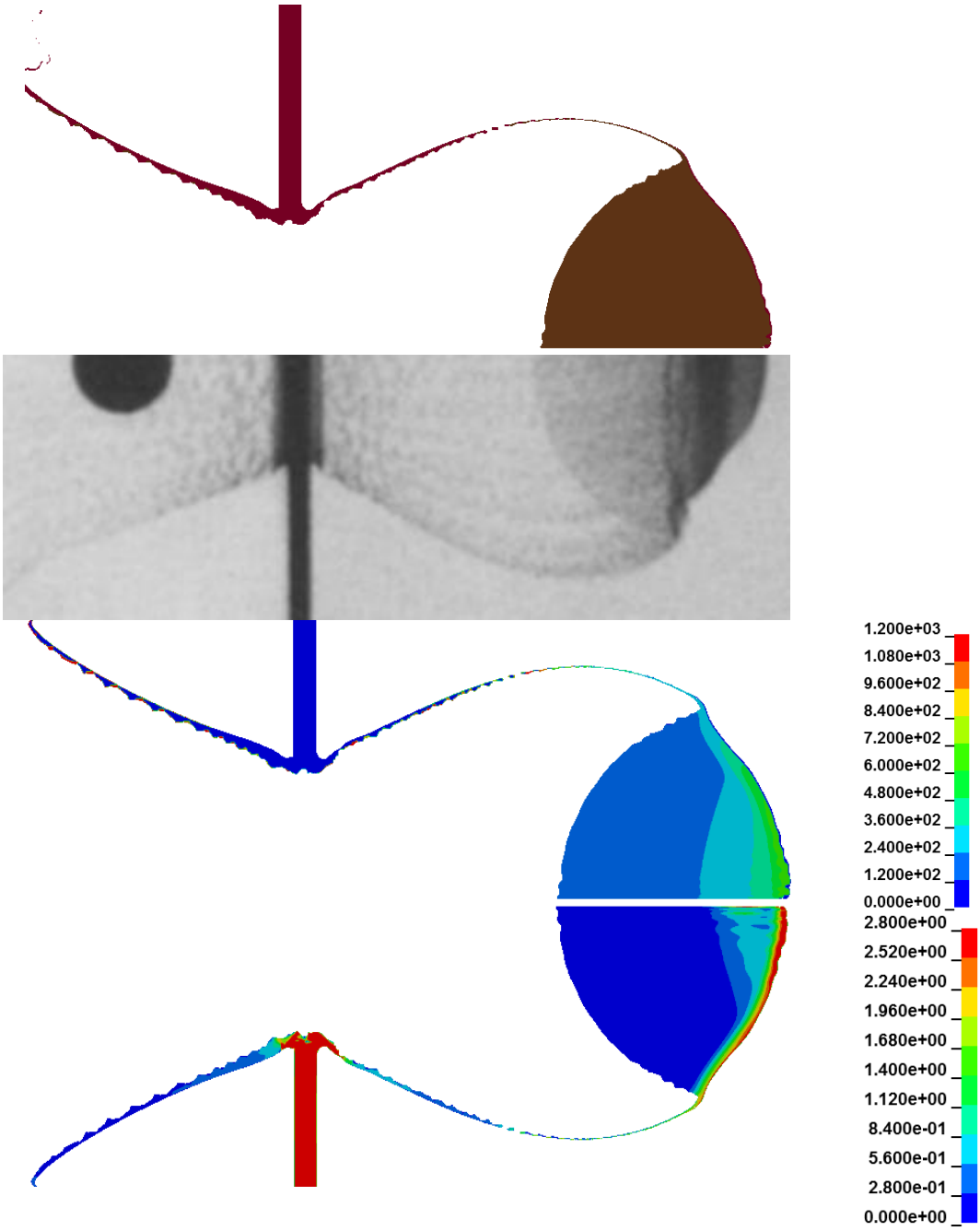

Figure 17. Modeled debris cloud and radiograph (top) at 6 µs with temperature and density contours (bottom) of a 9.53 mm sphere impacting a 1.55 mm plate at 6.71 km/s.

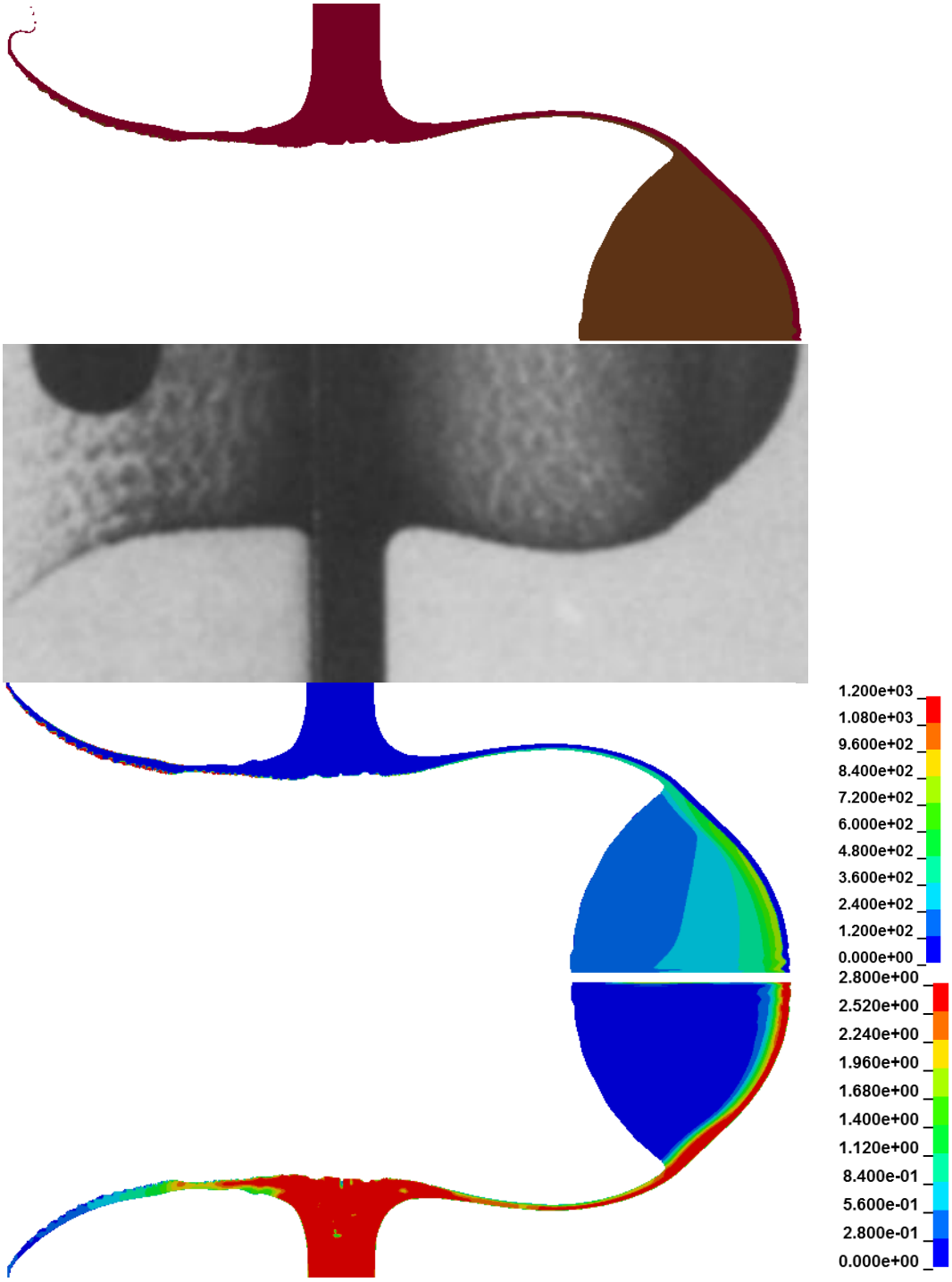

Figure 18. Modeled debris cloud and radiograph (top) at 6 µs with temperature and density contours (bottom) of a 9.53 mm sphere impacting a 4.04 mm plate at 6.68 km/s.

The debris cloud of a 6.68 km/s impact with a 4.04 mm plate shows the most drastic change from this trend, as no disk-like separation between fore and aft exists, seen in Figure 18. The thicker shield has caused a dramatic increase in resistance, creating much larger regions of melt. Because of the increased plate material in the debris cloud, the expanding bubble is significantly denser than the other models, and the average temperature of the debris is higher across all regions. The level of rear spall is somewhat smaller than other debris clouds, and the primary mechanism of deformation seems to be melt.

5.2.3 Non-Spherical Zinc Impacts

Piekutowski also performed experiments using spherical and non-spherical zinc projectiles impacting zinc and aluminum targets [140] near the melt regime in coordination with Sandia National Labs [141]. These were modeled as an additional mode of experimental validation, as well as to demonstrate shock characteristics which can greatly influence debris cloud characteristics and material fragmentation after impact with a bumper shield.

As seen in Figure 19, when a 1.3 cm diameter disk with a thickness of 0.795 mm impacts a zinc plate 0.965 mm thick at 5.01 km/s, the nearly planar shock pressures expel large fragments of the zinc plate in a large columnar debris cloud with a small rounded external debris bubble. Similar to the spall off the rear of the previously shown 6.64 km/s sphere, the disk impact generates shock pressures capable of expelling a significant portion of the disk debris backwards with the rear ejecta. This is evident in the experimental radiograph, and more clearly visible in the modeled debris field. The impacting zinc rod creates a distinctly different debris profile, as seen in the bottom portion of the same figure, with a noticeable pointed front as the majority of the debris expands around it. This is a curious change, since a cylindrical plate and a cylindrical rod share many geometrical aspects, with only a change in the length to diameter ratio.

Analysis of the density profiles of each impact as seen in Figure 20 reveal that while the incident disk was nearly completely destroyed, the rod impact has left a largely solid projectile still traveling at hypervelocity speeds. This is somewhat of a worst case scenario

for bumper shield designs, since the initial impact has not reduced the density or energy of the impactor to a sufficient degree.

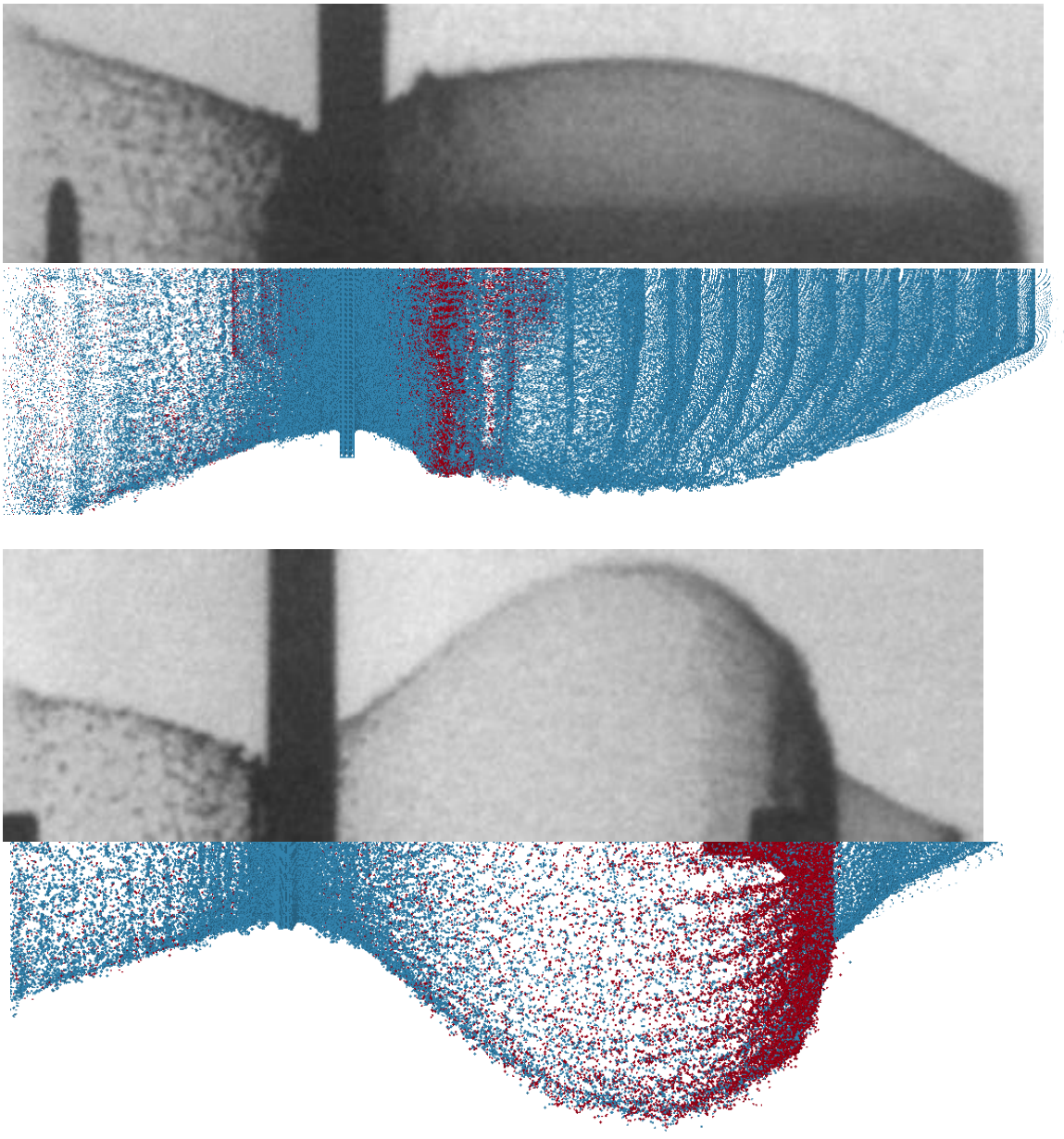

Figure 19. Debris clouds from a zinc disk (top) and rod (bottom) impacting a zinc plate at 5 km/s.

Table 2. Comparison of experimental values to zinc models.

Parameter	Experimental	SPH Model	ALE Model	SPH Error (%)	ALE Error (%)
Disk					
Front Velocity (cm/μs)	0.522	0.538	0.499	3.06	-4.40
Radial Velocity (cm/μs)	0.092	0.098	0.0915	6.52	-0.54
Hole Size (cm)	2.0	2.02	1.985	1.0	-0.75
Rod					
Front Velocity (cm/μs)	0.528	0.543	0.507	2.84	-3.97
Radial Velocity (cm/μs)	0.193	0.192	0.166	-0.51	-13.98
Hole Size (cm)	1.01	1.075	1.004	6.43	-0.59
Sphere					
Front Velocity (cm/μs)	0.471	0.481	0.465	2.12	-1.27
Radial Velocity (cm/μs)	0.284	0.232	0.201	-18.3	-29.22
Hole Size (cm)	1.17	1.178	1.02	0.65	-12.84

The differing debris cloud dynamics are more fully understood when examining the changing shock dynamics of impact, seen in Figure 21. While the flatter plate induces largely planar shock pressures before succumbing to spall and failure, the cylindrical projectile creates a smaller concentrated shock zone, and continues to propel material in the plate as it deforms. The resultant debris is propelled with a small focused shock by the cylinder, whereas the expansion is a wider, more diffuse pattern when impacted by the incident plate. As the ratio between radius and plate thickness reduces, the shock dynamics tend more toward a smaller region of rapid propulsion and less toward a large scale ellipsoid shock profile.

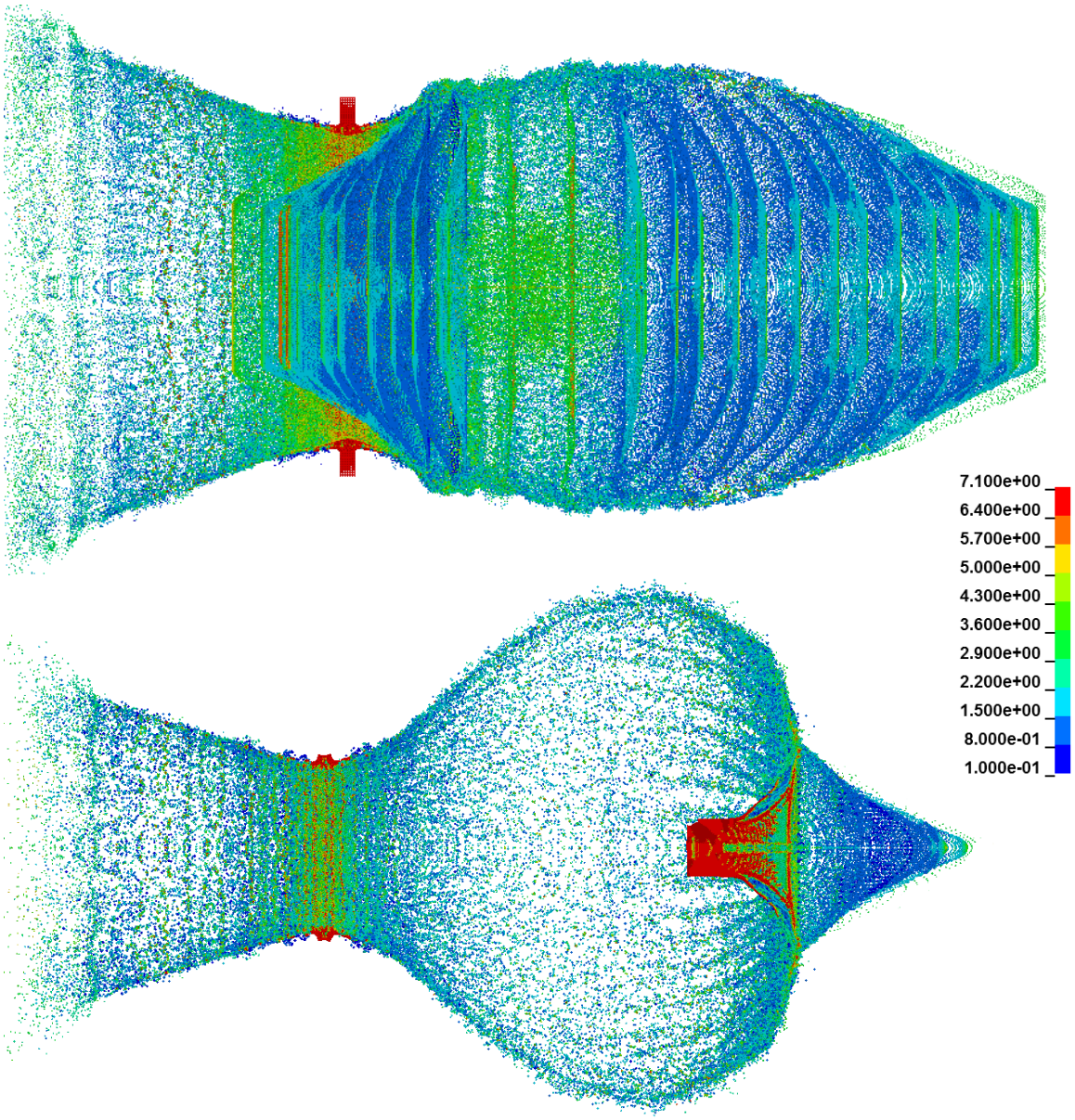

Figure 20. Contours of density (g/cm^3) for the disk (top) and rod (bottom) debris clouds.

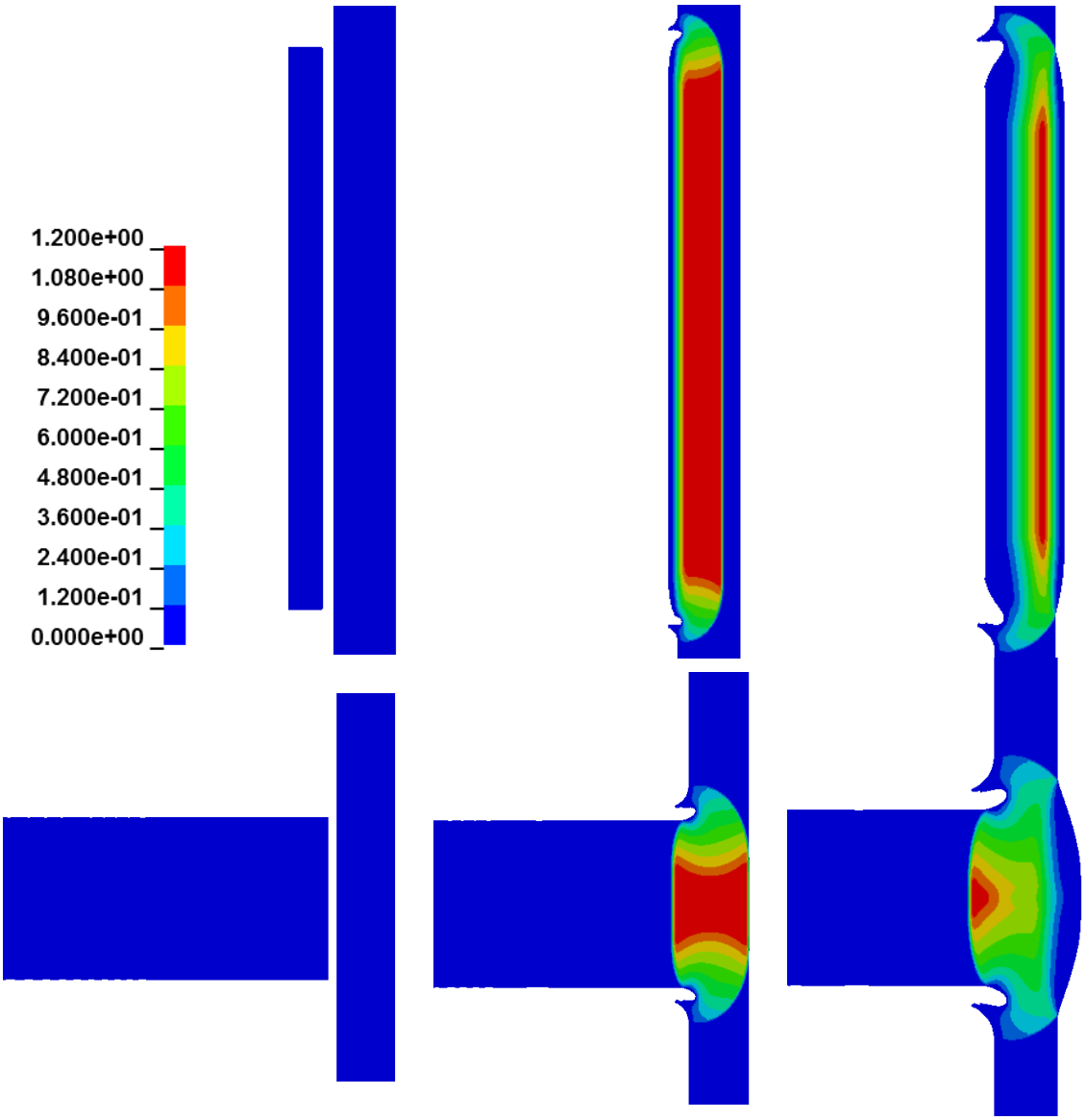

Figure 21. Comparison of shock transfer for a zinc disc (top) and rod (bottom) impacting a plate of identical dimensions at 5 km/s, shown at 0, 2, and 3.5 ns.

5.3 Fluidic Analysis

5.3.1 Fluid Debris Cloud Dynamics

To analyze the ratio between inertial and strength effects, several purely fluidic impacts are presented with steadily increasing viscosity and density held constant. Models were constructed to perform parametric variations on density, but if density is increased identically between plate and impactor, there is no change visibly in the debris field or quantitatively in the shape and velocities of the resultant debris cloud. This is expected, because no change in inertial effects are present; the increased inertial forces at impact are cancelled by increased inertial resistance from the denser plate. The presented models have no experimental baseline, as no experiments have been performed which impact a sheet of fluid with a hypervelocity sphere of fluid. However, since the shock properties of water have been studied extensively, the baseline simulation uses the same initial geometry as the aforementioned aluminum impact, scaled such that the initial velocity recreates the ratio of V_0/C seen in the 6.64 km/s solid impact.

The water sphere and "plate" were modeled using quarter symmetry and a total of 370,000 particles. The aforementioned fluid material model was applied with a density of 1 g/cm3, and viscosity was varied from the .001 Pa*s of water up to 100 Pa*s. Parameters for the shock behavior were taken from Liu and Liu [124] for the water baseline, and were similarly used for all viscous models. While hypervelocity impacts routinely generate a large degree of shock heating, the viscosity in each case was not temperature dependent, and held constant due to a lack of experimental data regarding the degree of shock heating in a viscous fluid at velocities approaching the hypervelocity regime.

An interior cross section of 4 fluid impacts are shown in Figure 22. Qualitatively, increasing the viscosity has the effect of rounding the leading edge of the debris cloud and increasing the amount of target material that is carried forward with the impactor. The increased shear forces decrease the amount of projectile material that remains in a cohesive clump at the forefront of the plume, as the interaction with the surrounding plate material strips larger portions off. Additionally, there is a decrease in the amount of material shocked off the rear of the impactor in the higher viscosity formulations. Increased

viscosity has the effect of "smoothing" the debris cloud initially, until shear forces are so great that their resistance to inertial forces causes material separation, most notably represented in Figure 22d. A higher viscosity also makes a more acute angle between the target and the rear plume, and seems to cause a slight increase in angle between the target plate and the fore debris cloud. Quantitatively, higher viscosities increase the axial deceleration seen by particles near the edges of an incident impactor, as increased shear forces provide larger resistance. While more impactor material is sheared into the surrounding debris cloud, the radial velocities of such material are reduced in higher viscosity interactions. The effects on particles near the center of an impactor are less pronounced, and axial velocities of particles are only slightly reduced with increasing viscosity. Additionally, low viscosity material simulations develop significant eddy formation, while the increased viscosity impacts decrease such rotational motion. This is explored more fully through investigations of strengthless fluid impacts.

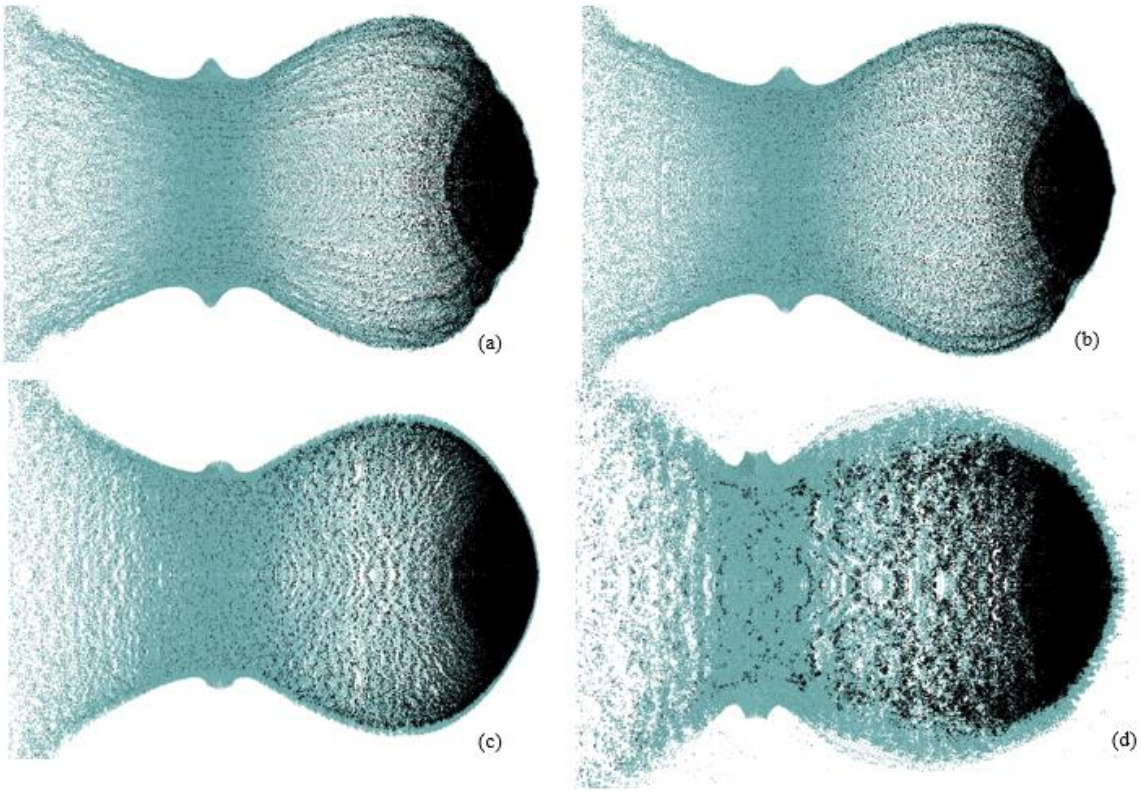

Figure 22. Models of fluid impacts at 25 μs with increasing viscosity: (a) .001 Pa*s (water), (b) 1 Pa*s, (c) 10 Pa*s, and (d) 100 Pa*s

5.3.2 Strengthless Debris Cloud Dynamics

As a contrast to the 6.64 km/s aluminum validation model, a “strengthless” model is also presented to provide closer means of identifying the role shear forces and strength play in defeating incoming debris. This strengthless aluminum model is composed of two fluids, rather than high strain rate solid formulations. The impact speed, density, and EOS constants from aluminum were used, such that the strengthless aluminum scenario models two inviscid fluids impacting with similar inertial effects and shock propagation to those seen in the solid impact.

The strengthless fluid impact was modeled using an identical number of SPH particles in the same geometry, with a null fluid formulation governing material response, and no viscosity. The density and Mie-Gruneisen constants [142] from Al 2024 and Al 6061 were used for the impactor and plate, respectively, such that the only difference between the models is the constitutive equation of the material.

The strengthless fluid has a similar shock profile for the impactor, but generates a markedly different debris cloud. The most apparent difference between the debris generated is the lack of spall. The true solid formulation of aluminum created primarily solid particles of debris as a result of shock pressures exceeding the material’s tensile spall limit. The fluidic formulation, by contrast, has no solid cohesion and thus, no spall criteria. Instead, a continuous stream of shocked matter extends from the forefront of the cloud back to the plate, while the rear plume is equally continuous. Remarkably, the split-hemisphere characteristics which Piekutowski noted in his experiments between fore and aft debris from the impactor are recreated relatively well by this markedly different material formulation. This suggests that inertial effects are primarily responsible for this notching characteristic, rather than material stiffness or shear forces. The impact zone has spread somewhat less to the outer radius of the plate’s particles, compared to the pure metal, and the slope of the debris cloud extending forward from the impact is somewhat steeper.

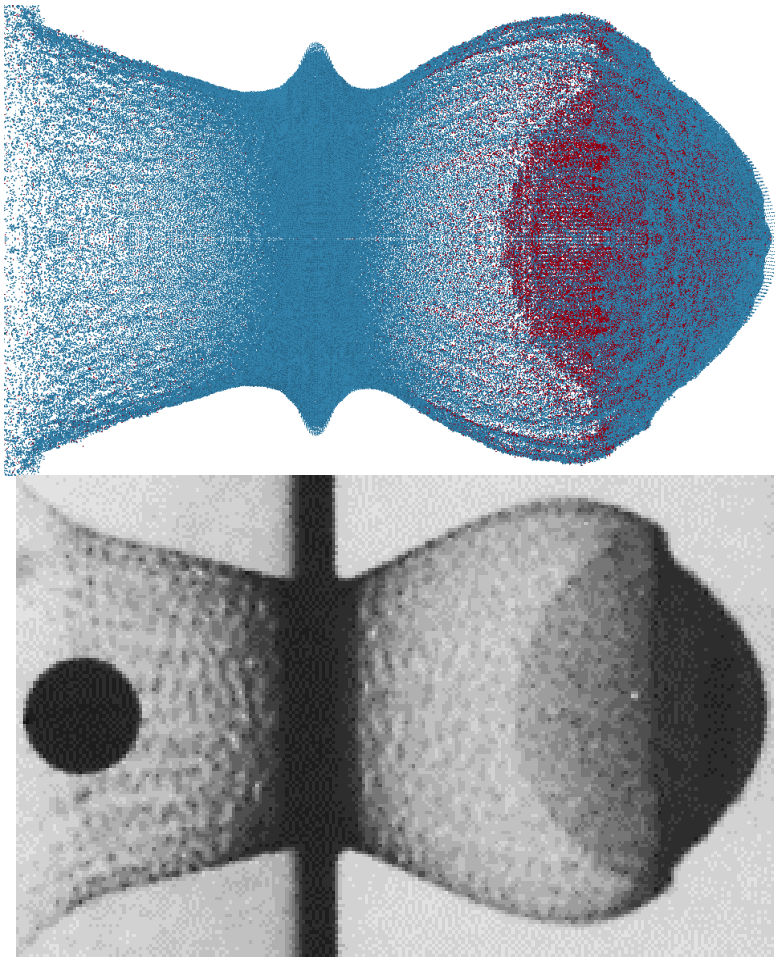

Figure 23. Strengthless fluid model debris cloud (top), comparison to experimental radiograph (bottom).

Overall, by neglecting material strength, the inviscid fluid replicates the experimental debris cloud less effectively than the high strain rate solid formulation, which is to be expected. Furthermore, by accounting for no material stiffness, the fluidic formulation creates structural anomalies which begin as small disturbances, but grow as the debris cloud expands to greatly influence debris behavior. The difference in velocity at the projectile/target interface creates high shear stresses, which result in small eddy formation that grows into larger vortical structures, as seen in Figure 24.

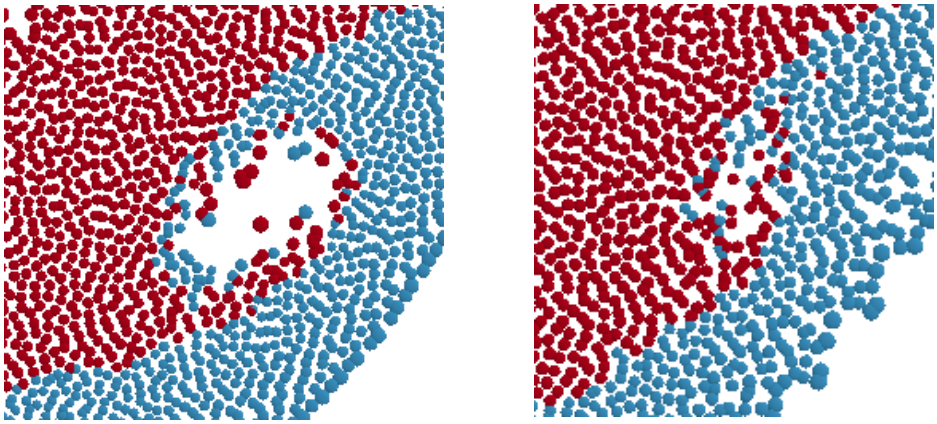

Figure 24. Primary eddy formation in the strengthless formulation (left) vs more random behavior in the solid model (right).

As the projectile penetrates through the target material in the purely fluid model, the interface between objects becomes a high shear rate boundary between two fluids. As it expands, the debris cloud creates a large swirl of particles as shear forces entrain surrounding material from both the projectile and target. By tracking target and projectile particles as they circle the geometric center of motion, a plot of this motion was constructed using four particles for clarity, visible in Figure 25. The JC formulation coupled with the Mie-Gruneisen EOS allows the solid formulation to melt at high enough impact pressures, thus some degree of fluidic motion also occurs at the high pressure and high temperature interface between the two materials.

Nonetheless, the amount of material entrained in the brief swirling motion of molten material is significantly reduced, and most particles undergo shock compression and weakening followed by free expansion with minimal vorticity.

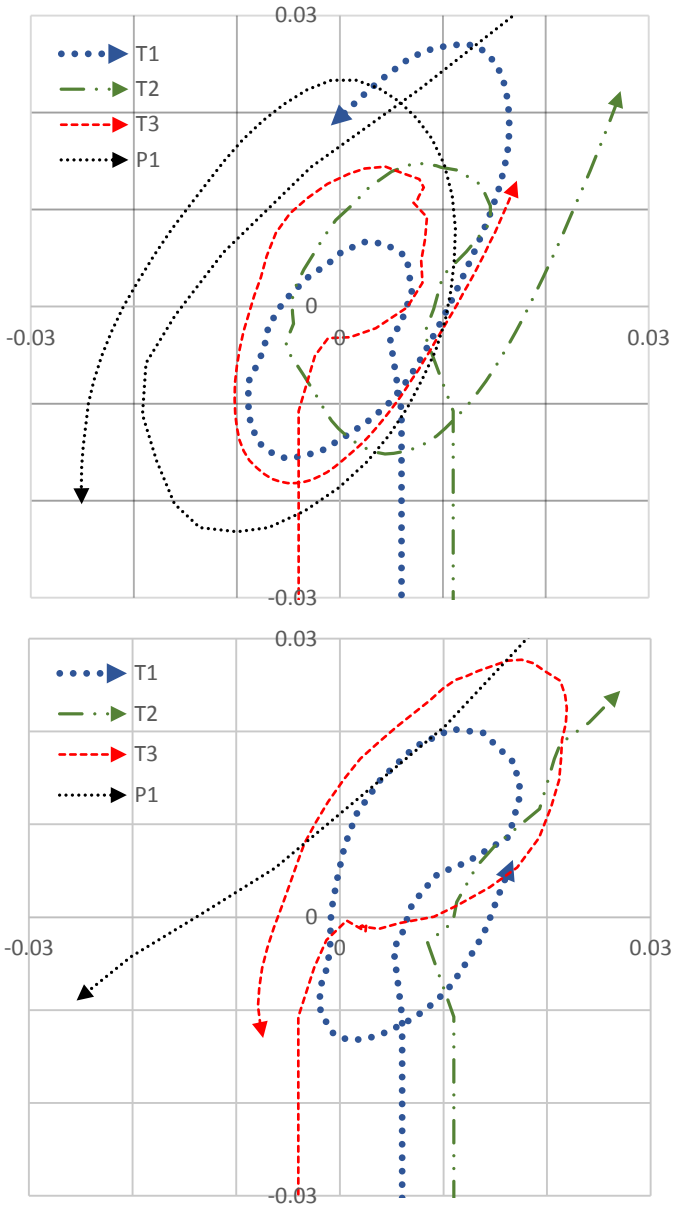

Figure 25. Time history of four particles near the center of the aforementioned eddy for the fluidic formulation (top) vs. the solid model (bottom).

5.3.3 Viscous Fluid Approximation

While the water impact and increased viscosity fluidic impacts are not representative of an experimental test, they lend insight into the role that material strength and shear forces play in impact events. To further establish this role, the strengthless fluid

model of aluminum was modified to have a viscosity of 10^{-5} Mbar-μs (1 Pa-s, or 10^{3} centipoise) while retaining the shock properties of solid aluminum. By contrasting the viscous model with the solid and strengthless formulations, shear effects in HVI can be quantified.

The viscous aluminum model was created using 530,000 particles in quarter symmetry. The Mie-Gruneisen EOS was applied to the impactor and plate using constants for Al-2024 and Al-6061, respectively. Thus the model is representative of the inertial and shock effects of the experimental aluminum impact, while the shear effects are purely fluidic in nature.

As seen in Figure 26, the debris cloud generated by the viscous aluminum formulation is qualitatively more similar to the solid metal simulation and the experimental radiograph than the strengthless model. The characteristic notch pattern and disc-like deviation between fore and aft hemispheres is more easily distinguished, and the overall angles represented by the debris are more similar to the experimental image. In particular, the outward flare of the rear plume is much better represented by the viscous formulation; likewise, the rounding of the fore debris field is more similar to the physical behavior seen in the test image. Unlike the strengthless model which generated a continuous stream of material from the impact zone, the viscous fluid forms into small, distinct droplets characteristic of the fragmentation visible in the solid model. This formation of cohesive droplets makes the formation of the impactor's rear spall somewhat more indistinct, but the general profile of material remains consistent with what is seen in the experimental conditions. Due to the continuous approximation of the fluid, the initiation of these droplets begins much further from the impact zone than in the solid formulation, and the edges of the impact zone distort with the passing shockwave, unlike the solid formulation's relatively stiff outer edge. Nonetheless, the viscous formulation provides a closer qualitative representation of the 6.64 km/s impact than the strengthless formulation.

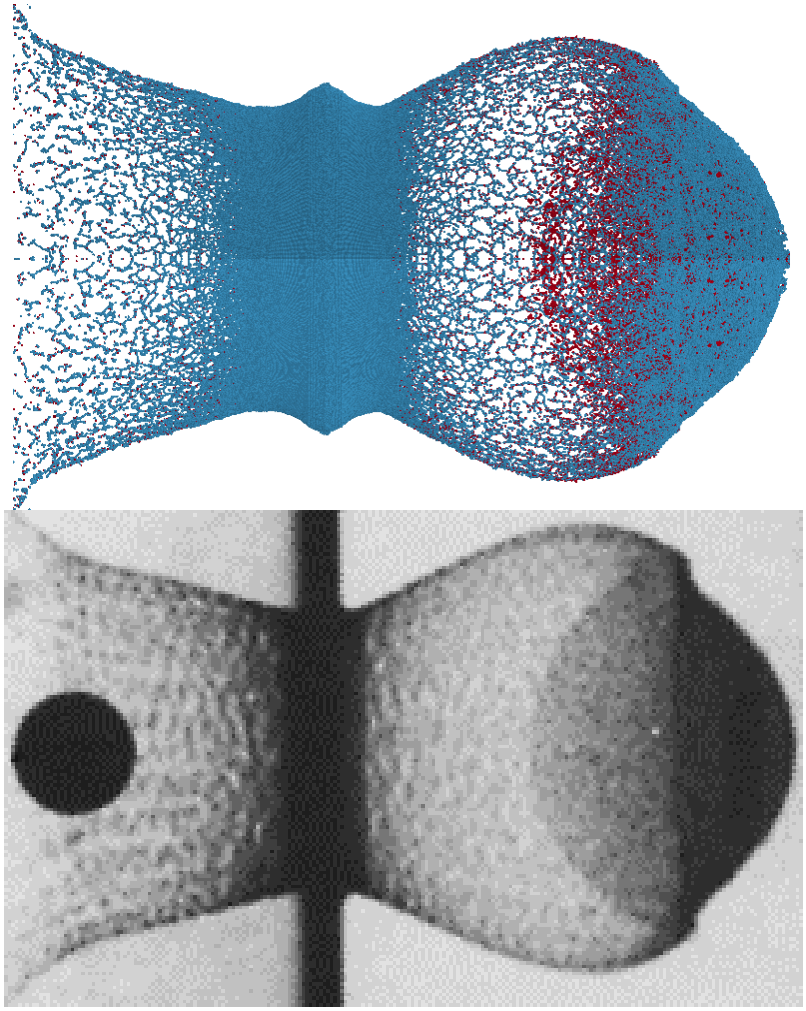

Figure 26. Viscous metal formulation (top) compared to experimental radiograph (bottom) of 6.64 km/s impact at 6 μs.

Quantitatively, the energy transfer between impactor and target material was compared between the solid, strengthless, and viscous formulations, visible in Figure 27. Examination of the kinetic energy reveals a relatively similar trend; as the impactor makes contact with the target, it rapidly accelerates a large portion of target material to several kilometers per second. However, the strengthless formulation over-predicts this contribution of energy, as the fluidic material offers only inertial resistance to this acceleration. The viscous formulation approximates the behavior of the solid formulation significantly better, though it also over-predicts this effect. The plots of internal energy show a similar disparity between the strengthless and solid formulations. As the shock wave passes through the material, the internal energy rises considerably before relaxing to

a post-shocked state. Despite using identical equations of state, the strengthless formulation retains significantly less energy than the solid formulation. The viscous formulation allows for residual energy retention through stresses, and captures this energy release in a closer approximation to the solid formulation. This disparity is most evident in the bottom portion of Figure 27, showing the percent error of the strengthless and viscous formulations relative to the solid formulation. Both fluidic formulations use the exact same densities, shock equations, and number of particles, so it is expected that the initial phases of shock compression in the regime prior to 1 μs should be identical. In examination of both kinetic and internal energy, it is evident that both formulations exhibit a strong degree of error from the solid model, but more importantly, they exhibit the same degree of error. Since neither fluidic model has the initial cohesive strength of the solid model, target plates from both formulations begin to accelerate slightly faster, while the solid formulation initially allows for less significant movement. Around 1 μs, however, the differences between models become much clearer. The errors in kinetic energy imparted to the target decrease below 4% for both formulations, but as the shock spreads and the material expands, the strengthless formulation begins to diverge from the behavior of the solid model, rising above 6% error at 6 μs, and continuing to grow. The viscous formulation more closely approximates this kinetic energy over time, as the error drops from 4% to 2.5% over a period of 4 μs. The difference is more visible in internal energy, as the ability of the strengthless formulation to account for residual energy storage is reduced. While both fluidic formulations show almost no disparity in internal energy around 1 μs, as the shockwave passes and the material expands, the viscous formulation follows the energetic trend of the solid model, with errors in energy no larger than 3%. The strengthless model exhibits errors over 13%, which gradually decrease to 10% at 6 μs. Thus qualitatively and energetically, the viscous model approximates the solid formulation more accurately than a purely hydrodynamic, strengthless formulation. The relative error of the viscous formulation is understandable, since the use of 10^{-5} Mbar-μs viscosity was an initial estimate not meant to exactly approximate the entire behavior of the solid.

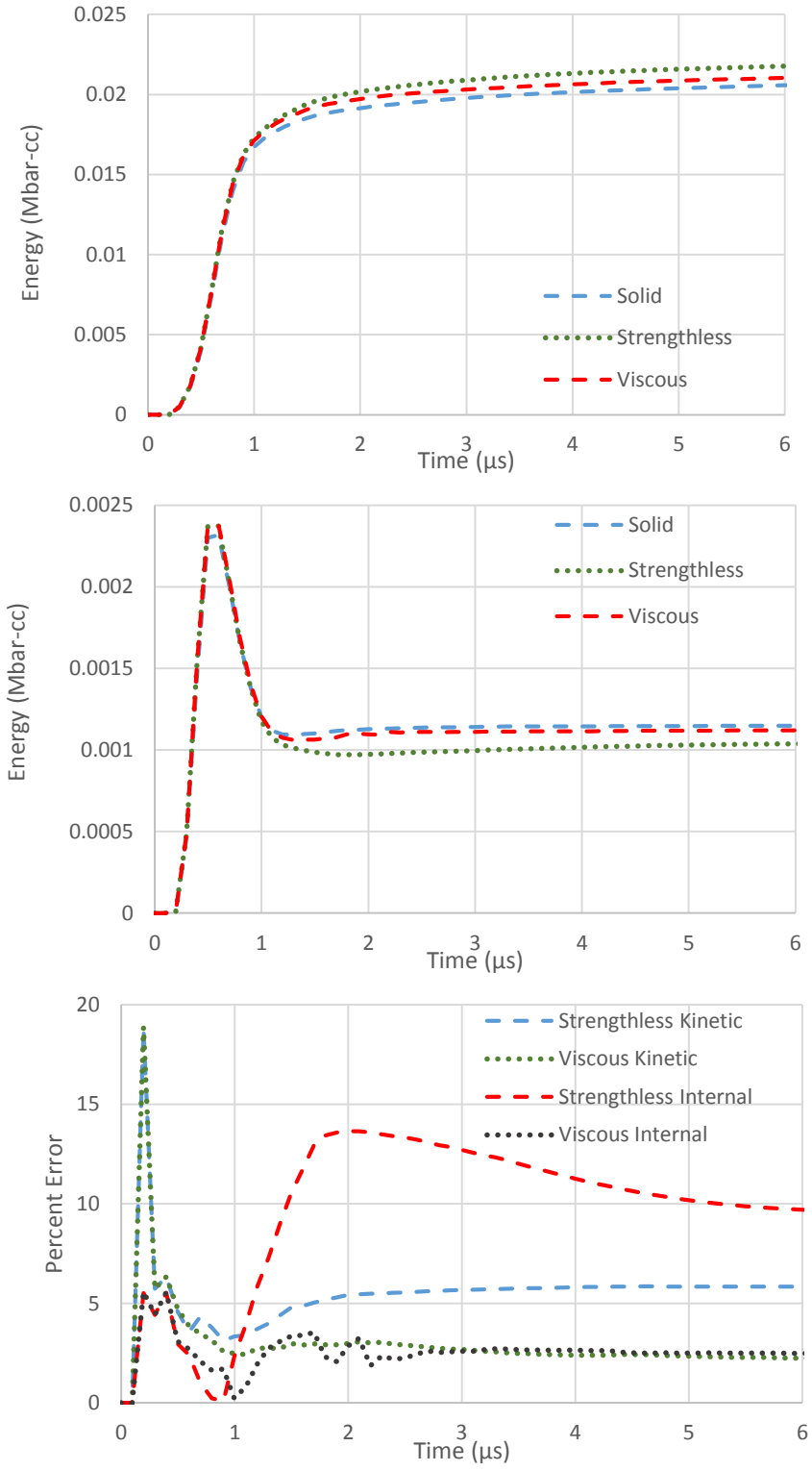

Figure 27. Comparison of kinetic (top) and internal (middle) energy in Mbar-cm^3 transferred from impactor to plate between the strengthless, viscous and solid formulations, along with percent error from solid (bottom).

5.3.4 Rate Dependent Formulations

To continue investigations into the idea that a viscous or non-Newtonian fluid can represent solid strain rate dependent behavior, we examine the stress response of the two discussed metallic models with respect to strain rates. While the Johnson-Cook model was inherently strain-rate dependent from its inception, the SCGL model was initially formulated for purely high strain rate ($>10^6$ s^{-1}) interactions, and then extended into lower strain rate relevance. To compare these two formulations under idealized circumstances, a model was constructed to deform a unit element under the conditions of shear without tensile or compressive forces. The total volume of the element was defined to be uniform with respect to time, while one surface was translated and the opposing surface was held fixed, creating a mathematical representation of pure shear. A four-noded, fully integrated 2D shell was used to force idealized circumstances. The initial and final model geometry are shown in Figure 28.

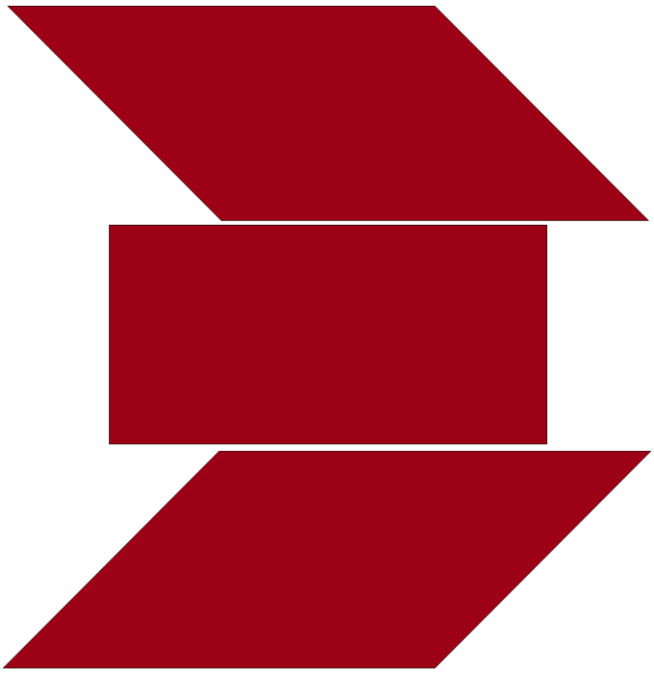

Figure 28. Single element characterization model at 0, 50%, and 100% of termination time.

The results from shear rates varying from 10^{-1} to 10^7 s^{-1} are evident from Figure 29, in which the yield stress predicted by the JC model is clearly increasing with respect to strain rate, while the rate-independent SCG model predicts an initial yield stress

significantly lower than the JC model, but in which the ultimate stress increases more rapidly after yield. This behavior is not unexpected; the SCG rate-invariant model was designed to model strain rates above 10^6 s^{-1}, while the JC model was initially formulated for elevated strain rates (10^3-10^5 s^{-1}), and then extended to lower and higher rates through experimentation and scaling relationships. This means that predictions from the SCG model will generally overpredict low strain rate response at higher strain levels; the JC model by contrast has been known to underpredict the response of materials at strain rates over an order of magnitude higher than the initial formulation intended [143].

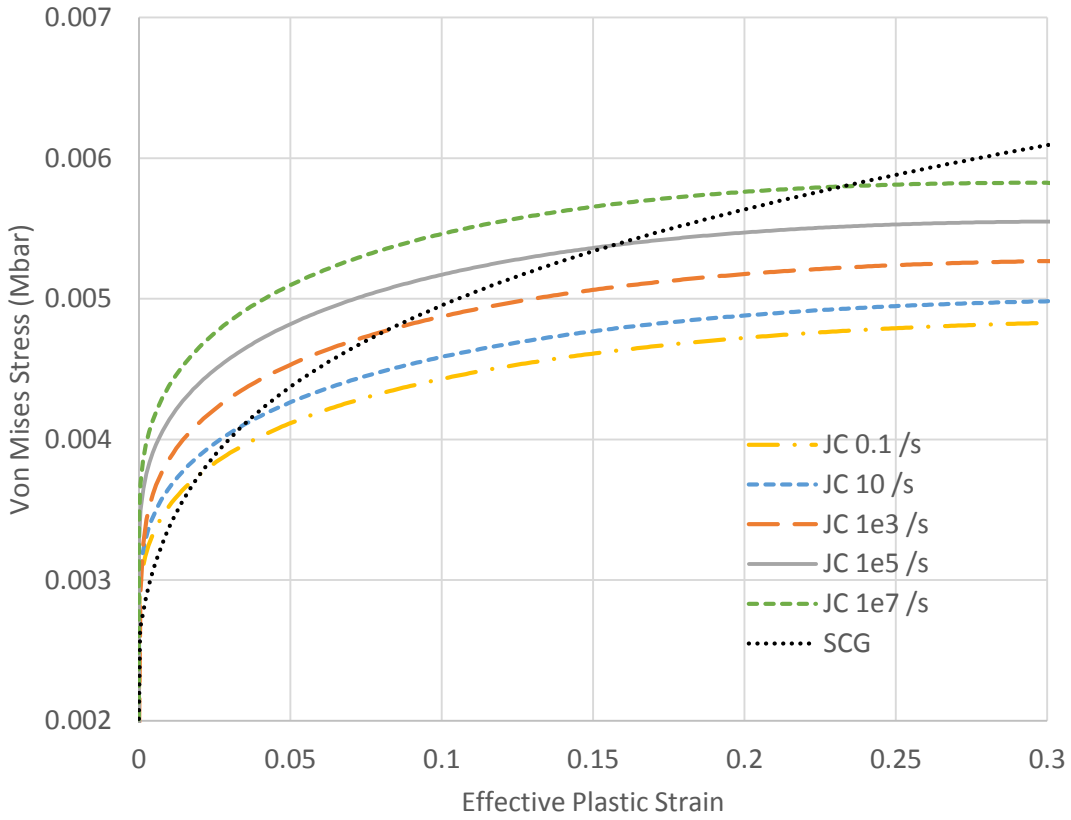

Figure 29. Strain rate dependence of von Mises stress predicted by JC and SCG models of Al 2024 at various deformation rates under pure shear.

The deviatoric stress response is thus highly dependent on the material model choice and the strain rate at which deformation occurs. The hydrostatic stress is significantly more static with respect to varying deformation rates. This is to be expected, since the flow stress relations defined by the JC and SCG model are grounded in von Mises theory, within which the total hydrostatic contribution to plastic yield stress is nonexistent for uniform stress distributions. The hydrostatic response of the material is thus dominated by the Mie-Gruneisen EOS, which was not changed between material constitutive relations. The pressure vs. strain responses of the same shear element formulation studies are plotted in Figure 30, in which it is evident that the variation among strain rates and flow stress formulations is slowly increasing with increased shear rate, but largely similar between constitutive relations.

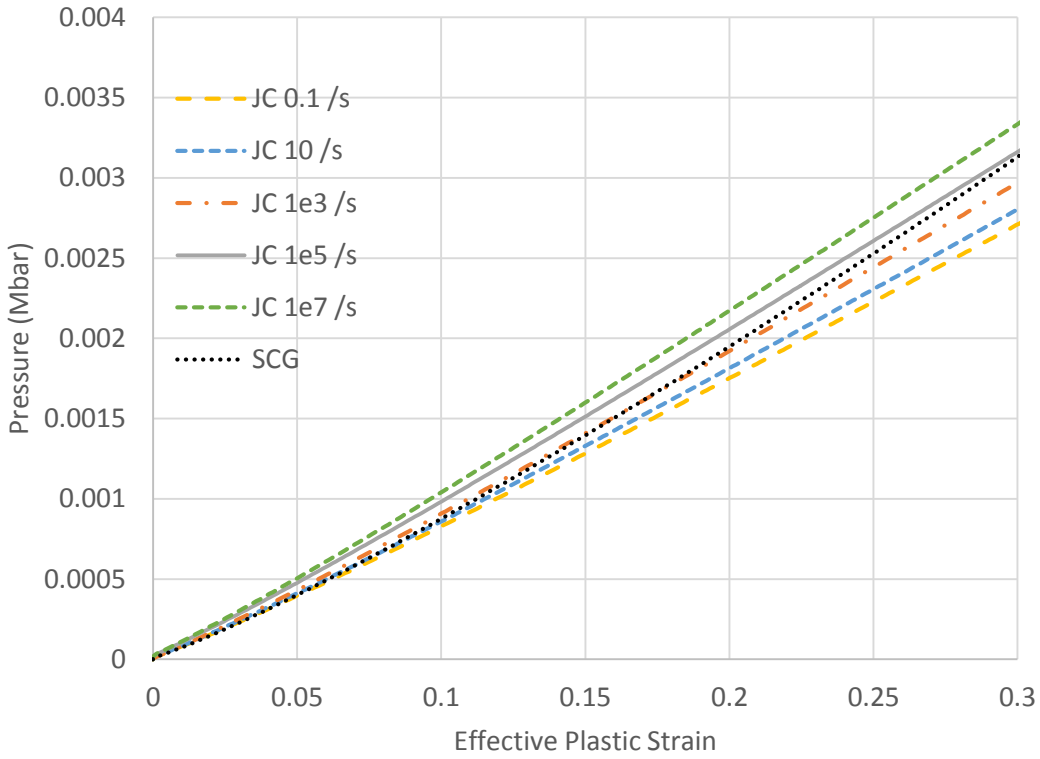

Figure 30. Strain rate dependence of pressure response predicted by JC and SCG models of Al 2024 at various deformation rates under pure shear.

It is immediately apparent from both Figure 29 and Figure 30 that the von Mises stress and pressure response increases with strain rate under the conditions of shear loading.

The level to which a material's stress increases with increased strain rate has not yet been defined. As seen in Figure 31, when values of yield stress and pressure from strain rates varying between 0.1 and 10^7 s^{-1} are fitted logarithmically, a nearly perfect fit is achieved. The higher strain rates correlate with this trend quite well, while the lower strain rates show somewhat more variance.

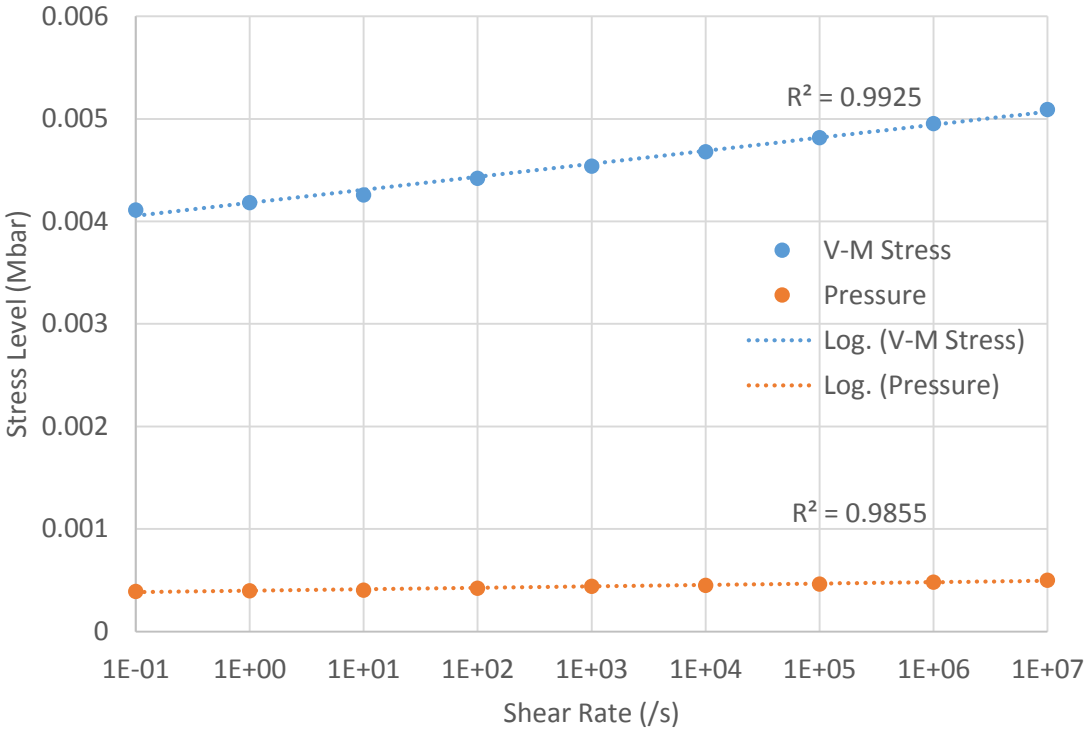

Figure 31. Yield stress and pressure vs. strain rate.

$$\sigma, p \propto ln(\dot{\varepsilon}) \tag{46}$$

Solid mechanics constitutive relations are generally relationships between stress and total strain, while fluid mechanics formulations typically define shear stress as a function of shear rate, not total shear. It is thus somewhat difficult to formulate high strain rate solid predictions in the form of an equivalent fluid model, since the traditional mechanics must be considerably modified. It is nonetheless prudent to examine the shear behavior of such solid models as a function of strain rate alone, to further quantify the role that shear stresses and strengths play in a highly rate-dependent scenario such as HVI. To do this, the same pure-shear finite element model was used, but the loading conditions were

modified; rather than using constant shear rates over multiple regimes, the same element was sheared at strain rates which were continuously increased from 0-10^7 s^{-1}. This was done for the JC and the SCG material formulations, which predicted approximately equal viscoplastic stresses at a strain rate near $5e^6$ s^{-1}. As can be seen in Figure 32, the JC model predicted an elastic region up to stresses of 0.18 GPa, followed by a plastic response which peaked near 0.33 GPa before decreasing to an ultimate stress level of 0.28 GPa at 10^7 s^{-1}, corresponding to an ultimate strain of 1.1. This decreasing stress response is not uncommon for materials under idealized circumstances, but material testing at strain rates exceeding 10^4 s^{-1} has shown that the ultimate strain of several materials shows an inverse proportionality to strain rate [144]. For many materials, total strain at failure over 0.3 can be expected in the lower strain rate tensile and compressive testing, but at shear rates over 10^4 s^{-1}, this is be an unusually high fracture criteria.

This creates two primary parameter choices when approximating the stress vs. strain rate behavior of solids: maximum predicted stress, and ultimate stress at maximum strain rate. For the SCG model, these are the same value, as stress increases monotonically both with total strain and with strain rate. But for the JC model, the maximum predicted stress is at the strain rate of $5e^6$, corresponding to a shear strain value of 0.2. Both the strain rate-dependent Johnson-Cook model and the rate-invariant Steinberg-Cochran-Guinan model have been shown to predict the behavior of metallic materials above strain rates above 10^5 s^{-1} with reasonable deviation from experimental data [145], yet an ultimate strain of 0.2 is an upper bound to be expected at such elevated strain rates; while Al 2024 has been strained to over 20% in quasistatic testing [146], increased strain rates and pressures greatly decrease the total strain at which testing can proceed in the plastic regime. Most metallic alloys will fracture or spall at significantly smaller total strains when subjected to strain rates and pressures approaching those seen in HVI [63]. Thus the stress vs. rate behavior at a strain of 0.2 is used as a baseline, with the total stress response at the ultimate rate of 10^7 s^{-1} as a lower bound. For Newtonian fluids approximating the JC model, these values correspond to a viscosity of 60 Pa-s and 28 Pa-s for the response at $5e^6$ s^{-1} and 10^7 s^{-1} rates, respectively. Using both of the two solid models' yield criteria, it is also possible to create Bingham plastic and generalized Herschel-Bulkley (shear thinning) models of Al

2024 under such constraints. The constants which were derived for these models are given in Table 3.

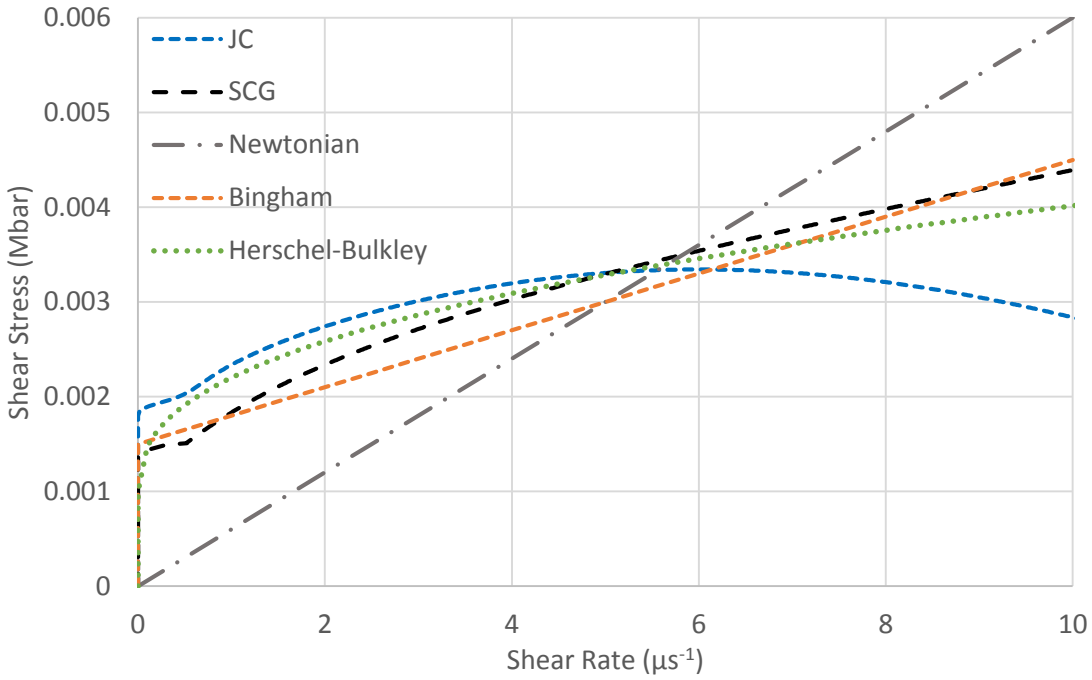

Figure 32. Shear stress vs. shear rate for the JC and SCG metal models, with a Newtonian fluid, Bingham plastic, and Herschel—Bulkley approximation to the strain rate response.

Table 3. Fluidic approximations to shear rate dependent behavior

Newtonian	$\sigma = 0.0006\dot{\varepsilon}$
Bingham Plastic	$\sigma = 0.0015 + 0.0003\dot{\varepsilon}$
Shear Thinning	$\sigma = 0.001 + 0.0012(\dot{\varepsilon})^{0.4}$

Following the work of section 5.3.3, models were constructed to compare the two Newtonian fluid predictions with 0.0006 and 0.00028 Mbar-μs viscosities, as well as the two metallic material models and the inviscid fluid. Energy histories are plotted in Figure 33, in which it is apparent that the higher viscosity formulation approximates the high strain rate SCG model more closely in internal energy, while the lower viscosity formulation approximates the JC model, toward which it was designed. As before, the strengthless fluid underpredicts the energetic response of both metallic models. In examining the kinetic

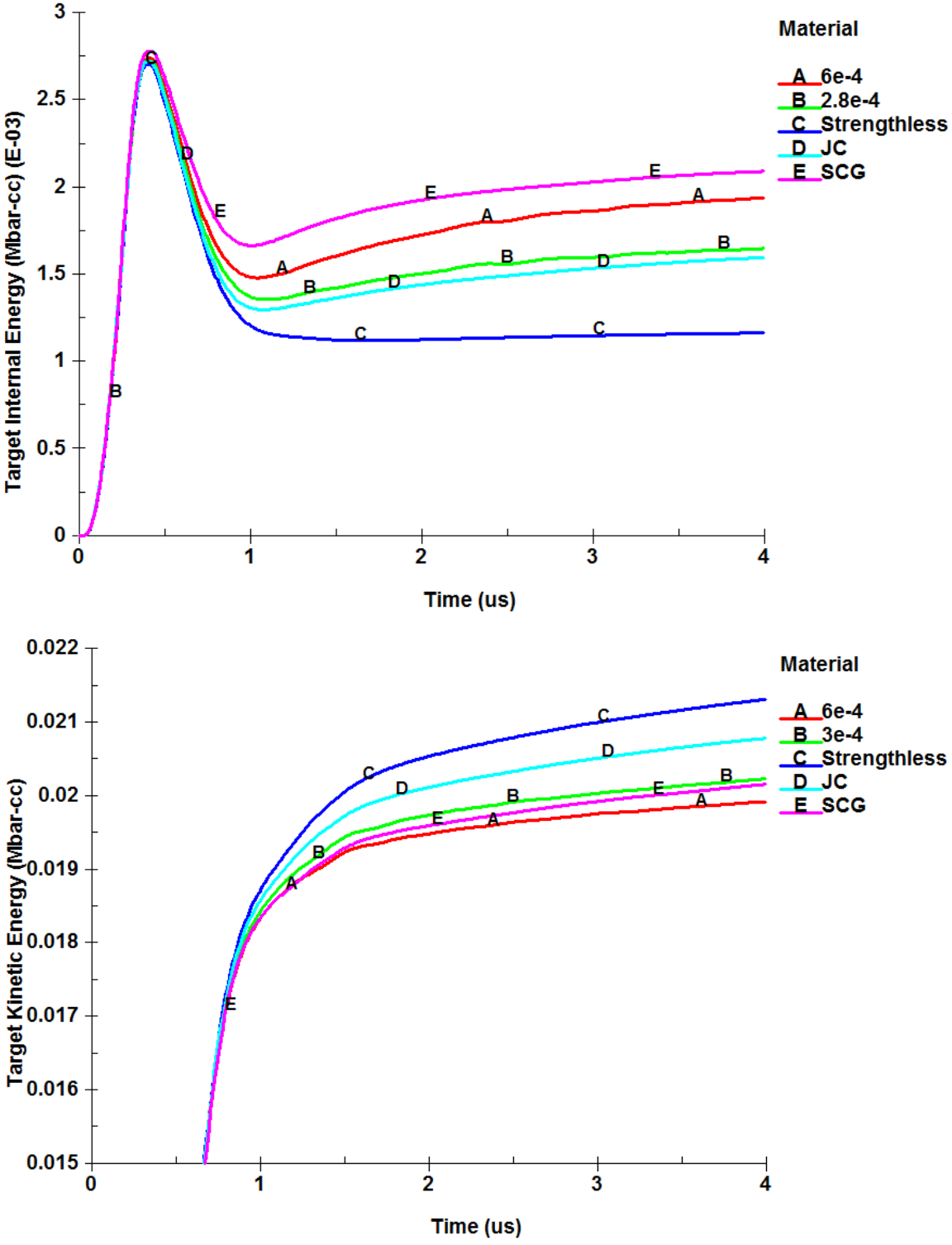

Figure 33. Internal (top) and kinetic (bottom) energy histories of the target with five different material models.

energy plot, we see that again the strengthless fluid exaggerates the motion delivered to the target by overestimating the kinetic energy, and again the higher strain rate formulation closely approximates the energetic profile of the SCG material model. However, the lower viscosity fluid does not well approximate the JC model, and is instead quite similar to the SCG metallic relation.

Non-Newtonian material algorithms have only been developed for incompressible SPH implementations [147], whereas the conditions of HVI rely on a large degree of compressibility. To model the non-Newtonian behavior predicted, an axisymmetric MMALE implementation was used, with the initial conditions for comparison again being drawn from the 6.64 km/s aluminum sphere impact. Debris cloud shapes at 6 μs are shown in Figure 34, with velocity contours for comparison. It is immediately apparent that all three fluid models fail to qualitatively model the axial spall of the impactor's rear, and instead only represent a dense portion of impactor material in the forward debris cloud. The angles of the rear ejecta are appropriately modeled by all three fluid formulations, and the general axial and lateral expansion of the debris is largely accurate. The velocities of the debris are quite close between all of the presented models, with the major exception being the aforementioned lack of rearward spall.

Comparing the projectile's energetic response predicted by the non-Newtonian fluids in Figure 35 and Figure 36, it is apparent that the addition of a viscous term dramatically increases the internal energy of the projectile after passing through the target plate. As the projectile and plate material expand, they continue to shear against one another in the fluid models, increasing the internal energy as the viscosity opposes such motion. The two solid models present very little of this effect, since the majority of projectile and plate material expanding in the debris cloud is fragmented dust with very little interaction. While this error appears quite pronounced, the total energy of the projectile is over an order of magnitude higher, and all three fluid models predict the shock response of the materials quite accurately. The projectile kinetic energy predicted by the five models is largely similar, with the largest reduction in energy predicted by the high strain rate SCG model, and the lowest predicted by the JC model. All three fluid models predict residual kinetic energies between the two metallic models.

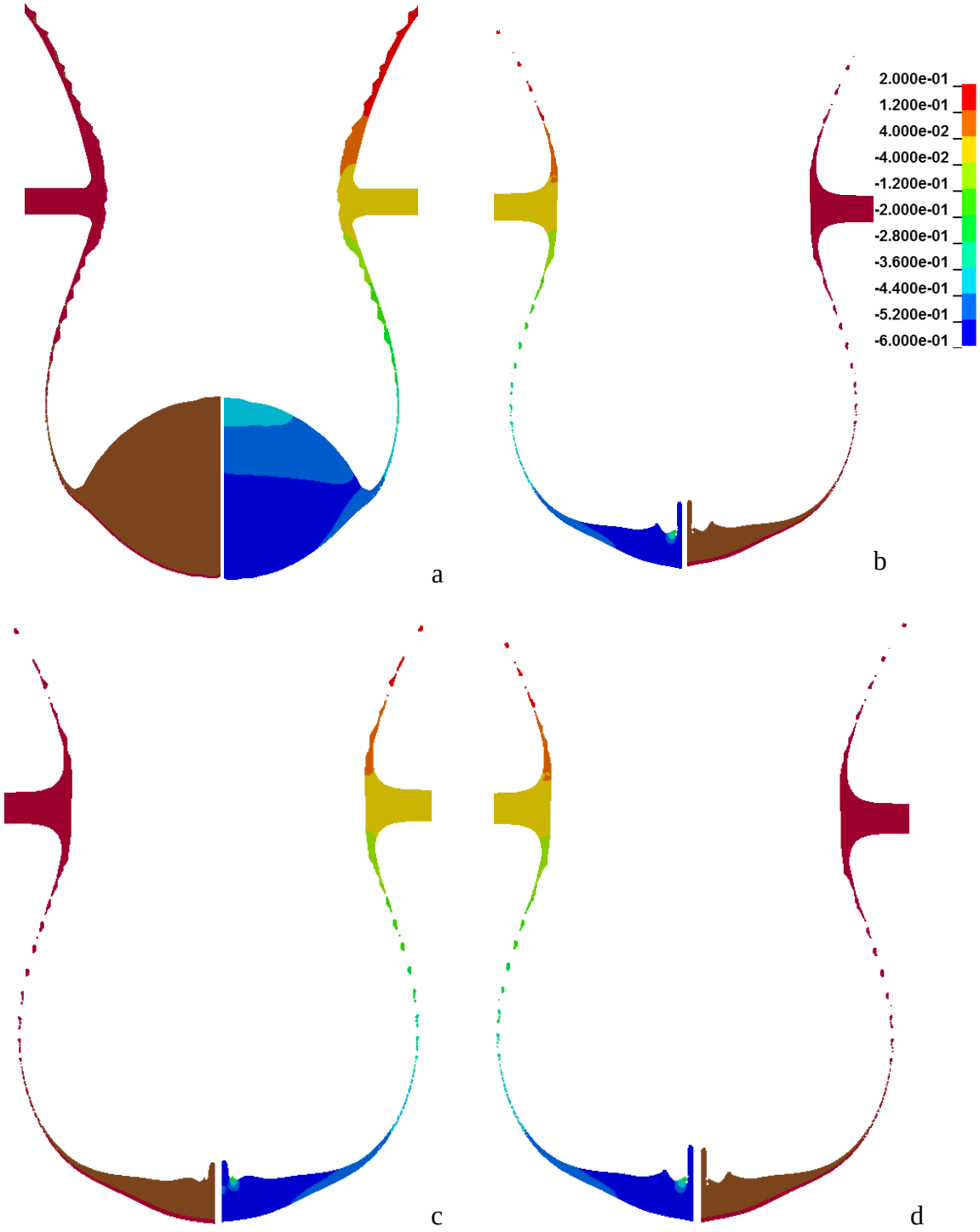

Figure 34. Johnson-Cook (a), viscous (b), shear-thinning (c), and Bingham (d) models of the 6.64 km/s aluminum impact using axisymmetric ALE. Fringes show axial velocity in cm/μs.

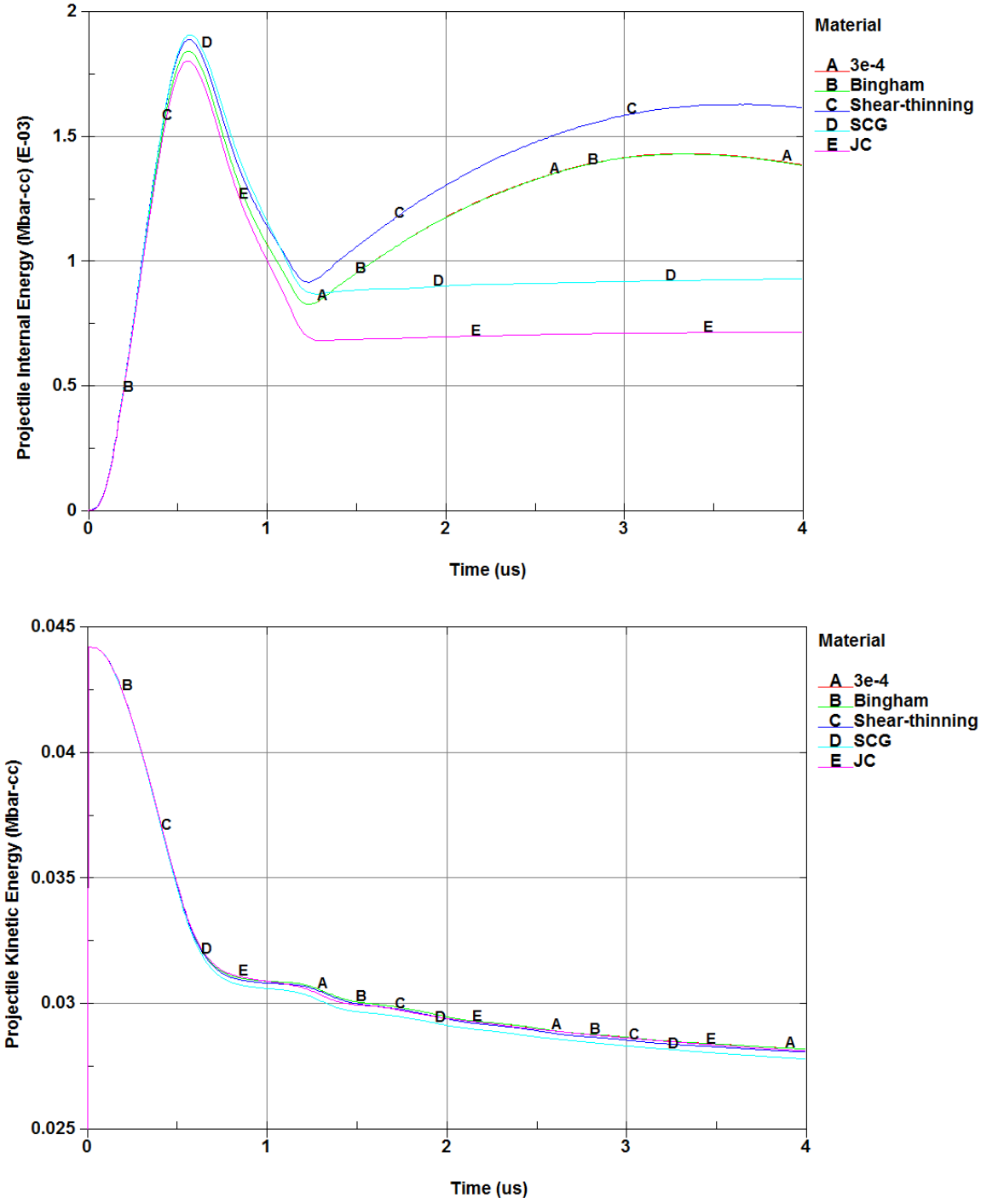

Figure 35. Projectile internal energy (top) and kinetic energy (bottom) with five ALE materials.

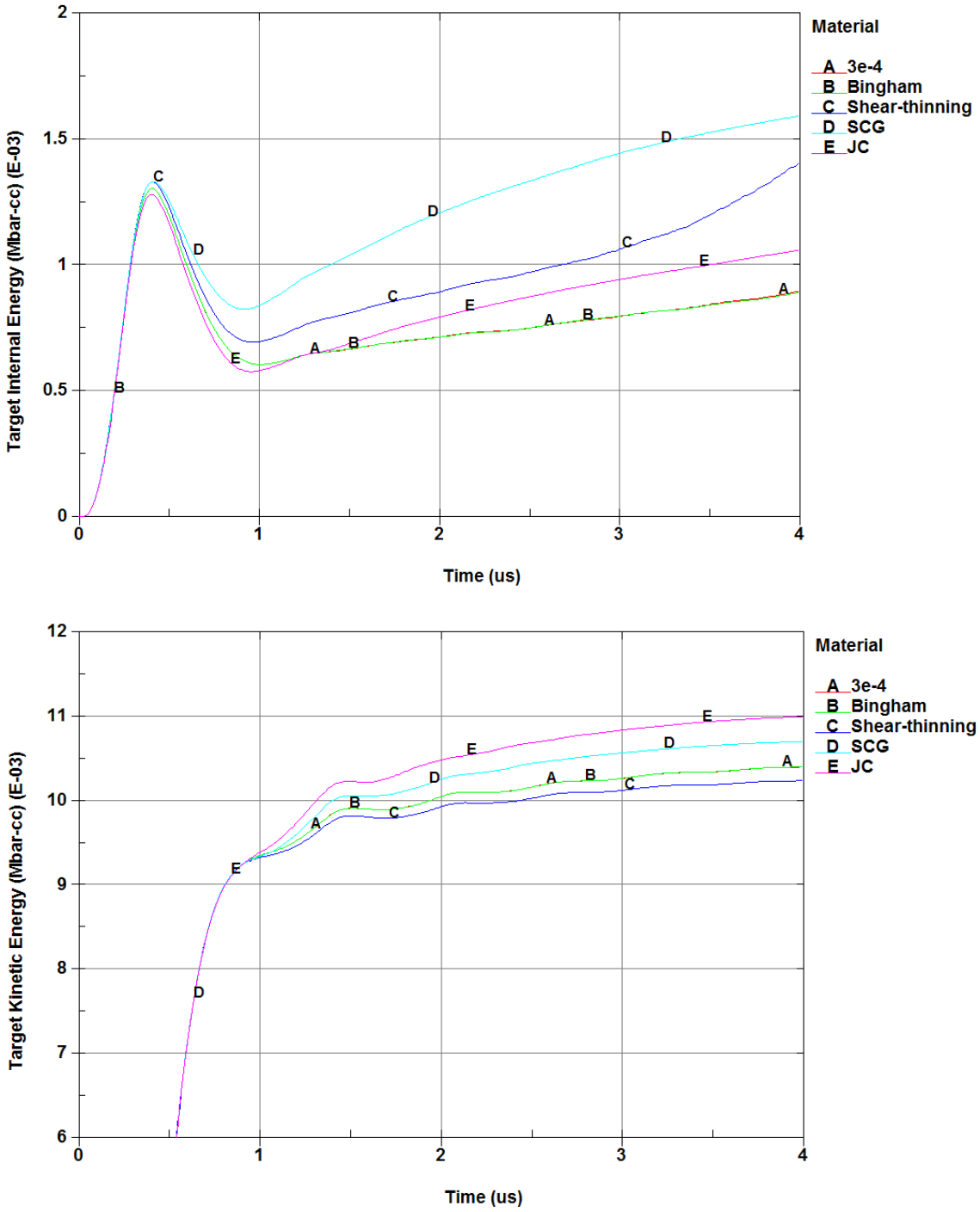

Figure 36. Target internal energy (top) and kinetic energy (bottom) modeled by five ALE material models.

Examining the internal and kinetic energy of the target, we see that the shear-thinning fluid approximates an energy response between the SCG and JC models, while the Bingham plastic and Newtonian model underpredict both metallic models after 1 μs. The target's kinetic energy history shows that all three fluid models underpredict the energy history of the metallic models. This contrasts with the earlier SPH comparison, in which the lower viscosity Newtonian fluid approximated the target energy of the JC model quite well. The poor implementation of material spall under shock loading is likely responsible for this disparity.

Across all comparisons of energy, it is obvious that the deviation between the Bingham plastic and the Newtonian fluid is negligible. This is to be expected; under the conditions of HVI, the elastic zone of material deformation is exceeded in a matter of nanoseconds. Since both fluids have the same strain rate dependency after elastic effects are considered, the initial elastic compression contributed only miniscule levels of energetic deviation.

5.3.5 Similitude

A non-dimensional analysis was initially attempted using the solid formulations directly, to ascertain a degree to which hypervelocity impacts scale physically and compare to experimental data. As can be seen in the various metallic formulations, the strain rate dependency of the high-rate models used, as well as terms capturing pressure and temperature dependency are often empirically determined and nonlinearly related to the stress response of such models. This means that while dimensionless terms can be constructed between model parameters, such as spall strength, density, impact velocity, or melting energy, such terms are ratios of these values which are inconsistent with physical relationships in the corresponding metallic model. Unfortunately, this creates highly unphysical responses when such ratios are used to scale the impacts, usually resulting in numerical divergence. The metallic models used are all approximations which were fitted to experimental data, and do not fully encapsulate the true physical relationships of the mechanisms at play in a hypervelocity impact scenario. As such, no similitude relationships were successfully constructed for solid computational models, despite the assertion by

previous researchers that HVI experiments should physically scale to some degree [148]. Instead, a scaling analysis was successfully performed by reducing the material parameters via the aforementioned fluid approximations.

Approximating the various material strengths of a solid via a fluid viscosity significantly simplifies the interaction and reduces the total number of parameters. It is prudent to use scaling relationships to analyze the fundamental values comprising the simplified model; scaling by an inaccurate level of material parameters will inevitably create defects and inaccuracies in the scaled results. Previous work in similitude analysis of impacts has been performed in which the authors posit that the size ratio between projectile and target must be constant between model and prototype [148]; this reduces the sizing of the problem to one single characteristic length. Proceeding with a determination of dimensionless terms using the Buckingham Pi methodology [149], five physical variables were determined to be essential to the impact event using a Newtonian model, seen in Table 4.

Table 4. Physical variables used for dimensionless analysis of fluid impacts.

Value	Symbol	Dimensions
Density	ρ	ML^{-3}
Impact Velocity	V	LT^{-1}
Speed of Sound	C_0	LT^{-1}
Characteristic Length	D	L
Fluid Viscosity	μ	$ML^{-1}T^{-1}$

Choosing density, speed of sound, and viscosity as the repeated variables, we derive two dimensionless quantities, which happen to correspond to forms similar to the Mach number and the Reynolds number, as seen in Eq. (48) and (47).

$$\pi_1 = V\rho^a C_0^b \mu^c = \frac{L}{T}\left(\frac{M}{L^3}\right)^0 \left(\frac{L}{T}\right)^{-1} \left(\frac{M}{LT}\right)^0 = \frac{V}{C_0} \tag{48}$$

$$\pi_2 = D\rho^a C_0^b \mu^c = D\left(\frac{M}{L^3}\right)^1 \left(\frac{L}{T}\right)^1 \left(\frac{M}{LT}\right)^{-1} = \frac{\rho C_0 D}{\mu} \tag{47}$$

Simulations were constructed to scale the fluidic impacts by the second Pi term using a factor of 5 to increase and decrease the size of the projectile and plate as well as the viscosity, while density, velocity and speed of sound were held constant at the conditions of the aforementioned strengthless impacts (ρ=2.785 g/cm^3, V=6.64 km/s, C_0=5.33 km/s). The varied properties of the three models are given in Table 5.

Table 5. Properties used for the scaled impact models

Model	Projectile Diameter (mm)	Target Thickness (mm)	Viscosity (Pa-s)
Baseline	9.53	2.225	60
5x Scale	47.65	11.125	300
1/5 Scale	1.906	0.445	12

As seen in Figure 37, the debris clouds resulting from the impacts look largely similar, with slightly more uniform droplet breakup in the larger model, as well as a larger degree of curvature and flare in the rear ejecta profile. The smaller model shows the most rounded forward debris profile, with small perturbations evident in the expanding target material of both the original and larger models.

To quantify the results of the scaling analysis, an energy comparison was performed to show deviations in the internal and kinetic energies of the models vs. time. The energy profiles of each model were scaled based on the total initial energy of the simulation, which was comprised solely of the kinetic energy in the impacting projectile. Since the velocities and densities of the incident projectiles were uniform between the three simulations, the change in kinetic energy is entirely dependent on the change in projectile diameter. The volume of a sphere (and thus the mass) scales according to r^3, such that in increase in diameter by a factor of 5 creates an increase in mass and energy by a factor of 125, and similarly, a factor of 1/125 for a five-fold reduction in size. As seen in Figure 38 and Figure 39, the energy profiles between models are remarkably close. The maximum error across all scaled values is 3% error predicted by the scaled projectile kinetic energy in the 1/5th scale model; the energy values of both the smaller and larger models are slightly overestimated throughout the simulation run time. This rather small maximum error indicates that the choice of dimensionless parameters was sufficient to create scale models

with a high degree of accuracy, indicating that the majority of the relevant physics have been scaled correctly.

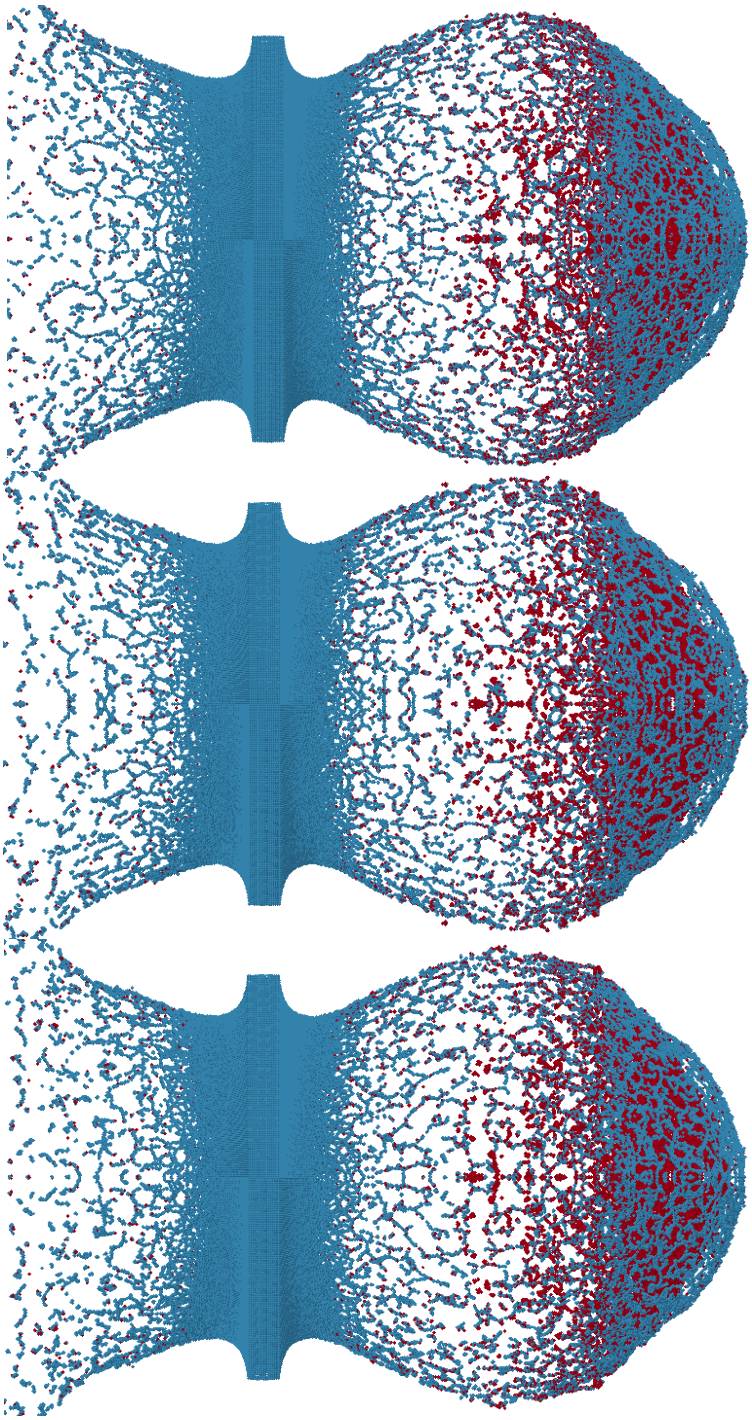

Figure 37. Original (middle), 1/5th (top) and 5x scale (bottom) debris clouds.

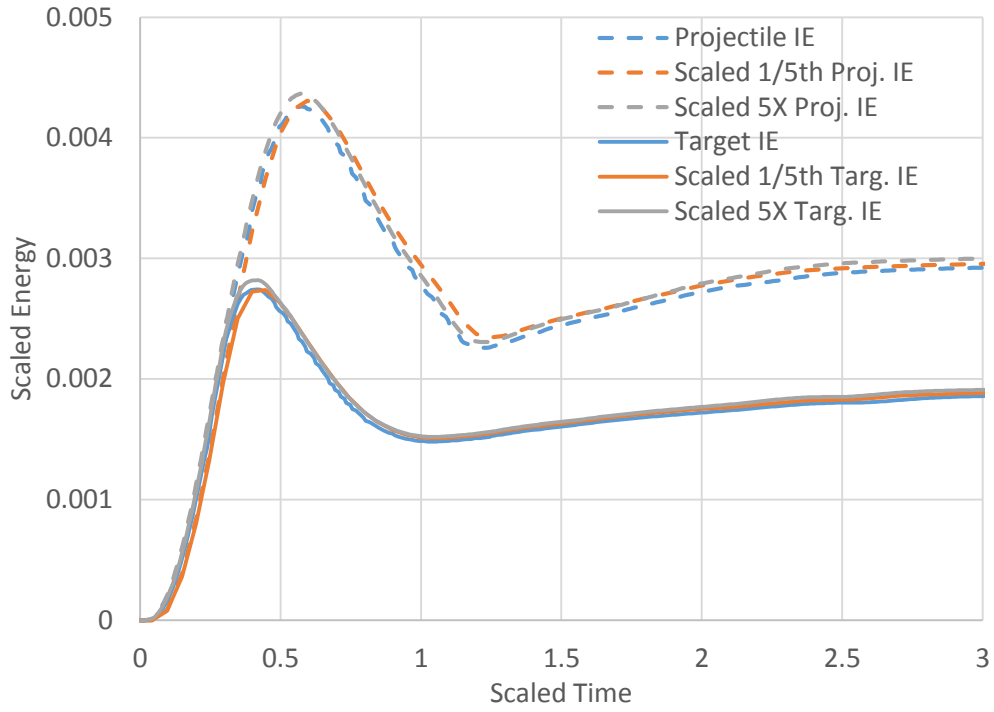

Figure 38. Internal energy of the projectile and target, scaled by initial energy.

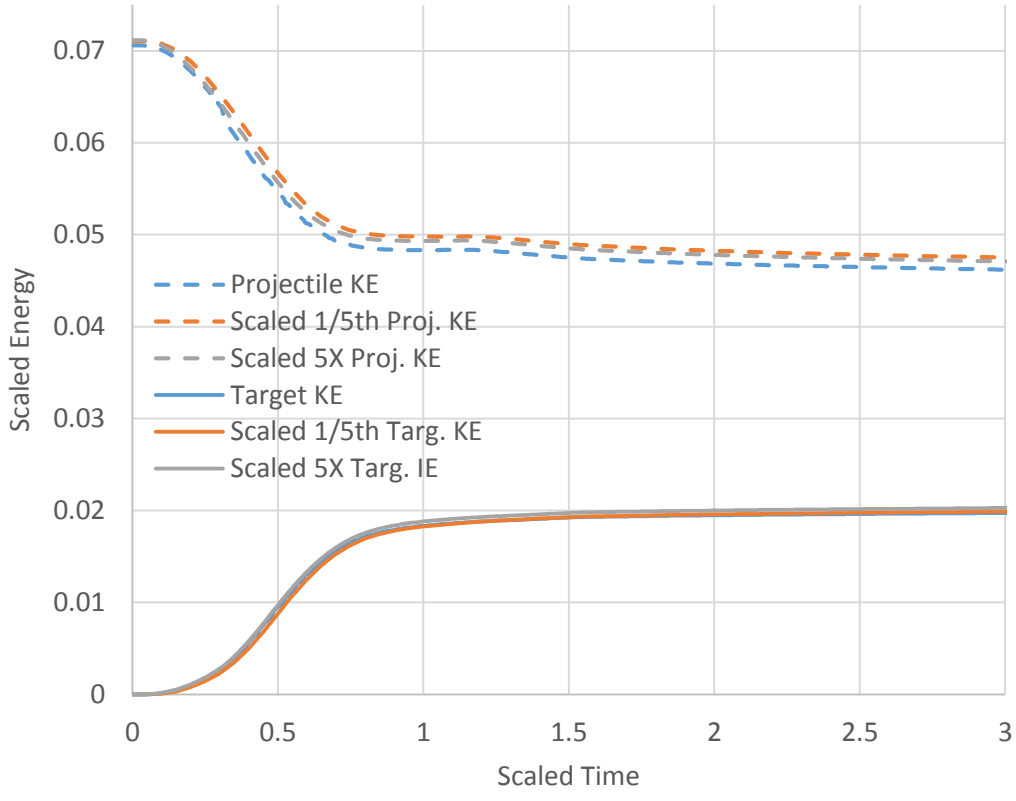

Figure 39. Kinetic energy of the projectile and target, scaled by initial energy.

Models were then created to examine similitude using the first Pi term corresponding to the Mach number. To further define the correlation between metallic HVI and a purely fluid impact, an attempt was made to identify scaling trends which occur in hypervelocity impacts between metal formulations and those which occur in water. Computational models were developed which replicate multiple impact velocities relative to each material's speed of sound, at 0.33, 0.55, 0.66, 0.85, and 1.25 *C*. At identical penetration depths corresponding to scaled time, a 2D slice was taken from the midsection for image clarity, and the angle, α, between the initial rear plume and normal was measured, as in Figure 40.

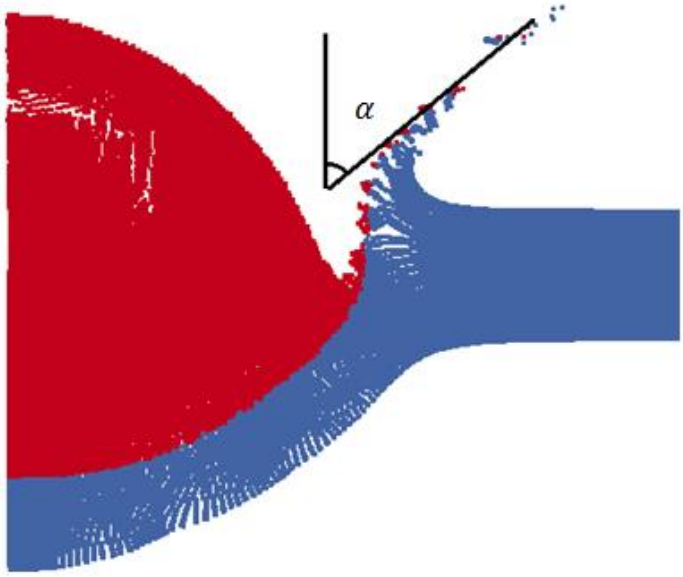

Figure 40. Definition of angle α, between normal and ejecta, seen in 500m/s Al-Al impact

As seen in Figure 41, these measurements were then plotted vs. the ratio V/C_0 to determine if any similar scaling exists between HVI and fluid-fluid impacts, dependent on velocity relative to the speed of sound. In general, α decreases as *V* increases; the trend was nearly linear for both fluid interactions and HVI. Across all values of V/C_0, there was an obvious similarity between the two modeled interactions, which can be expected. Upon initial contact with a target, a hypervelocity object experiences pressures, temperatures, and strain rates so extreme, that material strengths influence the interaction quite minimally. Being mainly pressure dominated, we can see from this analysis that the initial

stages of HVI do seem to be hydrodynamic, and would therefore be quite similar to an analogous fluidic event.

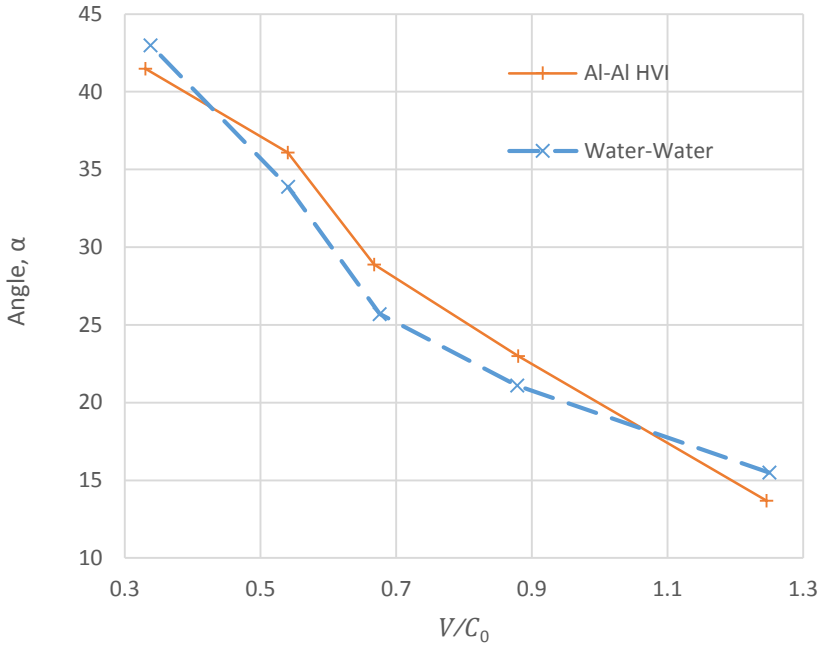

Figure 41. Rear ejecta angle α vs. V/C_0 for HVI and fluid impacts

5.4 Composite Modeling

Composite materials are being used with increasing frequency in the aerospace industry due to the possibility of improved strength to weight ratios over conventional isotropic materials. Aramid-epoxy (Kevlar) and carbon fiber reinforced polymer (CFRP) composites are already used in space applications, and the feasibility of using composites for layers of multi-bumper shielding has already been examined [136]. However, the anisotropy of composites makes closed-form predictions of their properties and dynamic response exceedingly difficult. Failure criteria and comprehensive constitutive relations have been developed with some success for quasistatic loading and low strain-rate failure [76], but near the shock pressures and strain rates seen even in the ballistic regime, these models can encounter significant difficulties reproducing an accurate response [150].

5.4.1 Full Scale Simulations with Standard Constitutive Relations

We revisit the double bumper shield configuration discussed in Section 5.1.2 with an enhanced model using solid elements and through-thickness resolution. The impacting aluminum sphere and the aluminum bumper are modeled with SPH elements, and the 18 layer Kevlar plate is modeled with solid elements and Chang-Chang failure criteria. Contact between the incident particles and the solid layers uses a penalty formulation with soft constraints.

While the solid formulation allows for visualization of delamination and more effective modeling of plane stresses, as seen in Figure 42, the Chang-Chang failure criteria was only designed at its inception to model quasistatic failure effectively. The overall level of deformation is still far below the level observed experimentally. The anisotropic stress response of the plate is seemingly correct, but the level of actual deformation and failure is largely underpredictive. The anisotropic constitutive relations discussed in Section 3.4 were designed around plane stress assumptions and low strain rates. The deviatoric stress predictions from such models may be accurate, but the hydrostatic response cannot accurately predict the shock pressures seen in HVI.

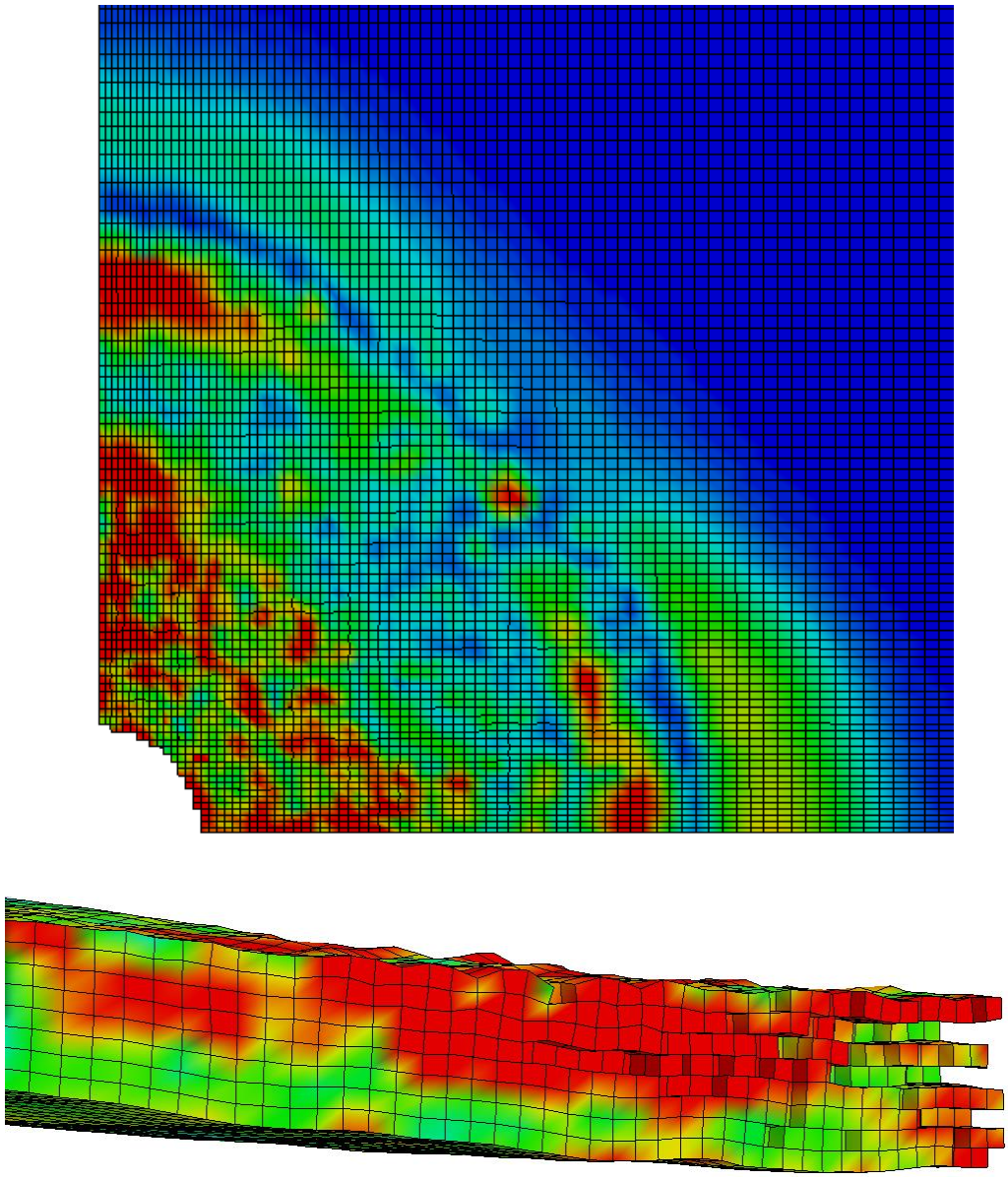

Figure 42. Damage from above (top) and from the side (bottom) of an 18 layer Kevlar plate after impact.

5.4.2 Micro-scale Modeling

In hypervelocity impact scenarios, the pressures and strain rates exceed the ranges through which lamination theory or conventional continuum damage models are valid. To this end, a micro-scale model of a composite under hypervelocity impact loading has been developed using an elastic-plastic material formulation for the constituents separately. A

40% volume fraction square packed CFRP was taken as a baseline, with a fiber diameter of 5 μm and assumptions of perfect bonding between fiber and matrix. The half-symmetry model uses 990,000 particles to represent two fiber halves 40 μm long, with a 2 μm thick Al-2024 flake impacting at 2 km/s only in the center. The Mie-Gruneisen parameters for epoxy [151] and carbon [142] are given in Table, and the elastic constants for each material's constitutive relation are from Hyer [73]. The initial geometry can be seen in Figure 43 from axial and transverse angles.

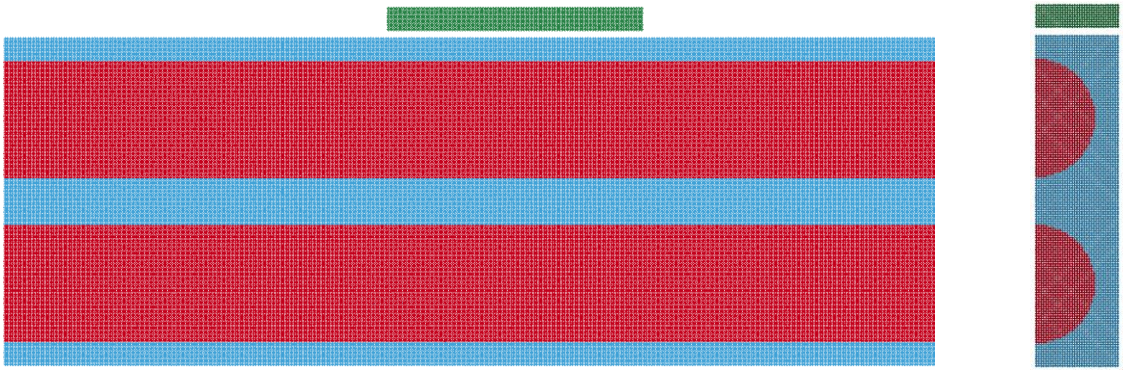

Figure 43. Initial configuration of micro-scale composite model with red fibers, blue matrix, and green impactor. Transverse view (left), axial view (right).

In a hypervelocity impact event at normal incidence, portions of a structure are damaged from the impact itself, while the shock propagation damages other portions of the structure not directly impacted by the projectile. By impacting the aluminum flake only at the center of the fibers, we can see how the microstructure of a composite affects shock propagation both in the normal and transverse directions. As seen in Figure 44, the initial impact creates a shock wave through the epoxy, which transitions into the carbon fiber within and actually increases speed. The carbon fibers are denser than the epoxy with a higher speed of sound, so even though the impact initiated at contact between aluminum and epoxy, in the transverse direction the shock wave is stronger and faster within the fiber. As expected, the shock wave is strongest closer to the normal direction at 1.5 ns, but as it begins to propagate back into the matrix from the fiber, a reflection wave is created, and the initial shock is slightly weakened. At 3 ns, the shock through the top fiber has broken into multiple successive high pressure zones due to reflections between the fiber and

matrix. The heterogeneous nature of the composite is easily identified; rather than a purely elliptical shock wave profile as seen in isotropic materials, the pressure forms two distinct curved regions of strong shock within the fibers, separated by a thinner region of weaker shock through the matrix. In the normal direction exactly under the impact zone, the shock has just transferred into the epoxy at 3 ns, and is weaker than the portion of the same shock wave which is still within the fiber.

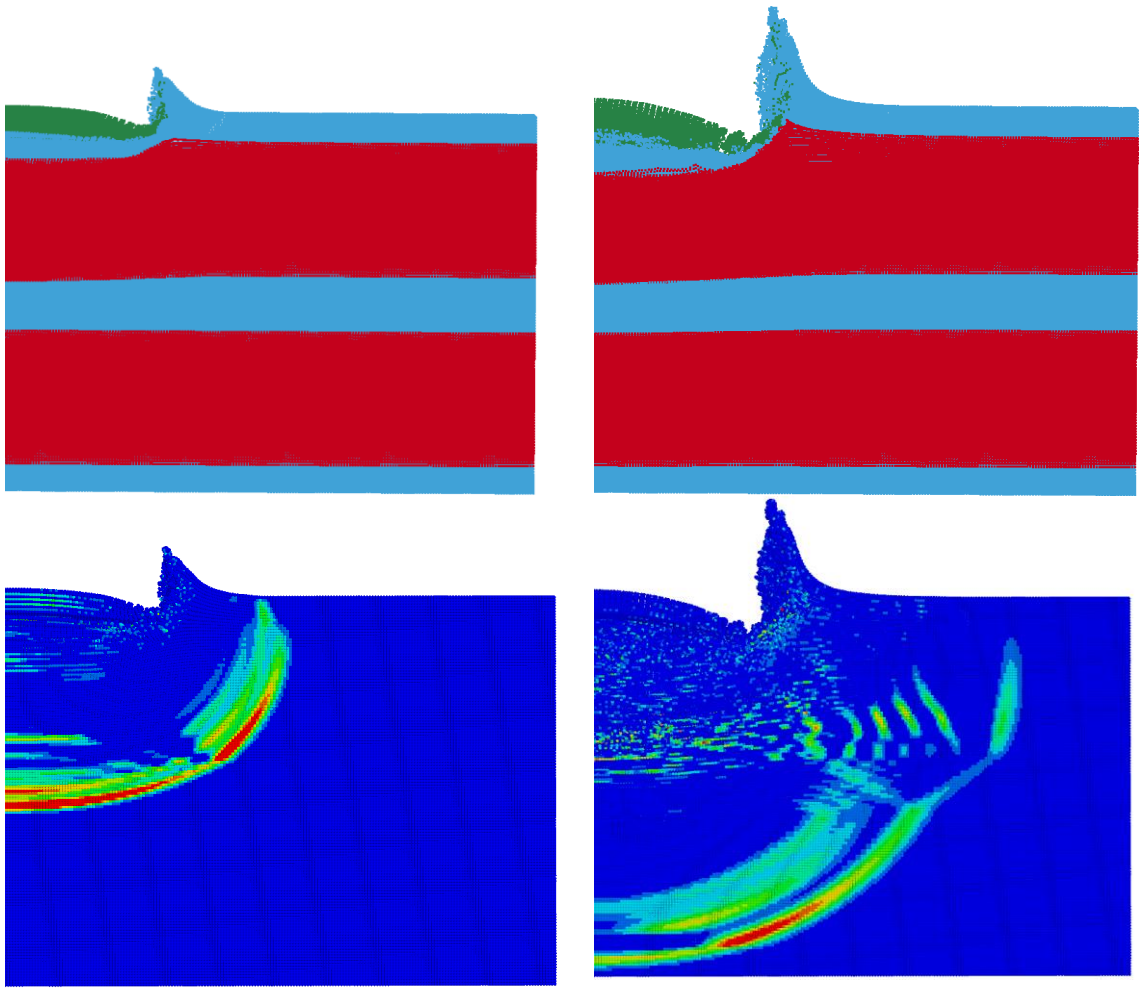

Figure 44. Impact prediction of damage to two fibers at 1.5 ns (left) and 3 ns (right), colored by part (top) and with pressure contours (bottom).

5.4.3 Modified EOS

Following the aforementioned micromechanical investigations into shock properties, macro-scale simulations were constructed in which the shock properties of the composite constituents were modeled. Including micro-scale structures in such a fully sized model is computationally prohibitive; even a resolution of 100 μm requires tens or hundreds of millions of elements for a centimeter-scale structure in 3D. Instead, the mechanical properties of the composite material were modeled with continuum approximations applicable to each lamina individually, and an equation of state was included to approximate the shock response. The appropriate shock response of a woven fiber reinforced polymer would use an anisotropic equation of state with damage criteria describing interlaminar damage and fiber-matrix interactions subject to the pressure response, but the few experimental studies which have investigated shock-induced delamination and cracking have been limited in scope and inapplicable to macro-scale shock relations [152]. Since the experimental impact attempted in 5.4.1 used multiple layers of woven 0/90° composite, the interlaminar responses are more homogeneous than in a laminate of uniaxial composites. As such, an isotropic equation of state is used to model the shock response, where the constants are determined from a volume fraction of the individual constituents. While the resulting material predicts the appropriate level of anisotropy in its stress response, seen in Figure 45, and represents the stress response in a qualitatively accurate manner, the quantitative measure of damage is still less than that seen in the experimental setting.

The predicted damage level using an equation of state improves upon the damage criteria discussed earlier, and represents a step in the right direction. However, without shock hydrodynamics testing at multiple strain rates in the axial, transverse, and through-thickness directions, the response of composite materials to HVI will continue to be incorrectly modeled.

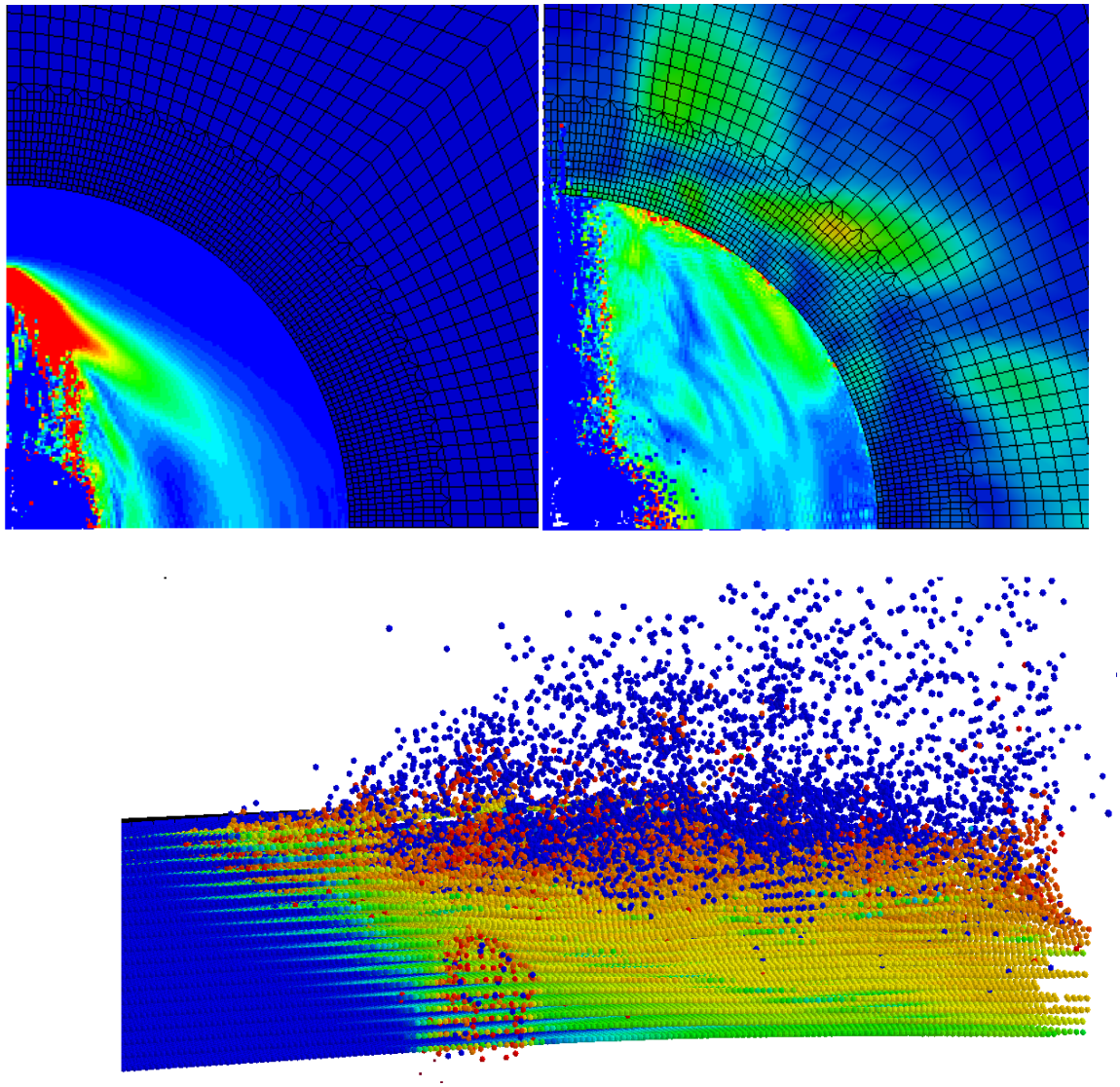

Figure 45. The anisotropic response of a 0/90 woven Kevlar plate to HVI loading after 40 and 50 μs (top), and through thickness view at 45 μs (bottom).

5.5 Plasma Generation

Several high quality tests were conducted using a van de Graff generator to expel small iron filings at speeds in excess of 40 km/s [153] with RF emissions, but as a consequence of the propulsion method, faster particles were smaller following a power law trend. As a result, the largest particles exceeding 10 km/s were on the order of 10^{-13} g, corresponding to a radius of only ~100 nm, and particles traveling upwards of 30 km/s were on the order of 30 nm in size. The interatomic spacing of iron in a bcc configuration is nearly 0.3 nm [154], meaning that modeling a spherical projectile according to the experimental conditions at 30 km/s using on the order of 100 elements through thickness will create an approximation nearing one atom per element. While extant codes have no limitations on scale and are numerically capable of modeling such sizes, the accuracy of such interactions becomes increasingly questionable, as molecular dynamics and sub-nanometer effects can become more dominant than continuum approximations [155, 156]. Such statements are not intended to mean that modeling interactions in the mass, velocity, and energy space specified are impossible; only that extant FEA codes have taken continuum approximations as first principles, which are increasingly inaccurate as nanometer-scale structures are of interest [157].

In this low-mass, high velocity regime, the sub-picogram masses mean that mechanical damage is of little concern, as the maximum penetrations will be on the order of microns. To that end, the primary focus is that of modeling the mechanical effects of plasma expansion.

5.5.1 Laser Driven Aluminum Flyer Plate

Further insight into computational modeling strategies for plasma generation and expansion can be gained from examining laser ablation processes. In such scenarios, a high energy laser is used to vaporize and ionize an initially solid surface into a plasma. The plasma generation is the primary mode of deformation and energy transfer; as such, if the mechanical effects of plasma production can be successfully modeled in laser ablation processes, it is likely that the plasma dynamics in HVI can be simulated effectively. Following experiments conducted at the PALS Laser Facility in Prague [158], several

axisymmetric MMALE models were created replicating a flyer plate driven by rapid laser ablation. The initial geometry is shown in Figure 46.

In the experiment, a 0.3 mm diameter aluminum disk with a thickness of 11 μm is exposed to a 240 J laser pulse lasting 400 picoseconds. The incident energy is absorbed with roughly 40% efficiency over an estimated depth of 6 μm, rapidly vaporizing and ionizing the surface of the aluminum plate into a hot, dense plasma. This plasma then expands violently, creating shock pressures within the solid portion of the plate and propelling it at approximately 54 km/s, as measured by the researchers.

This interaction was first modeled with the constraints of the impact simulations seen thus far: a Johnson-Cook material definition of strength and stress response, with a Mie-Gruneisen EOS for the pressure-volume relationship. This model is largely ineffective at modeling the conditions of the proposed laser ablation study, as seen in Figure 47. While the hot "gas" expands into a low density, high velocity region as expected, the material retains a uniform axial expansion trend, rather than expanding spherically as seen by the researchers. Additionally, the velocity of the expanding region only reaches a magnitude of approximately 126 km/s, while the experimentally accelerated disk had estimated plasma expansion speeds over 150 km/s. Most significantly, however, the laser ablation modeled in this way vaporizes the laser spot region and the remainder of the disk nearly

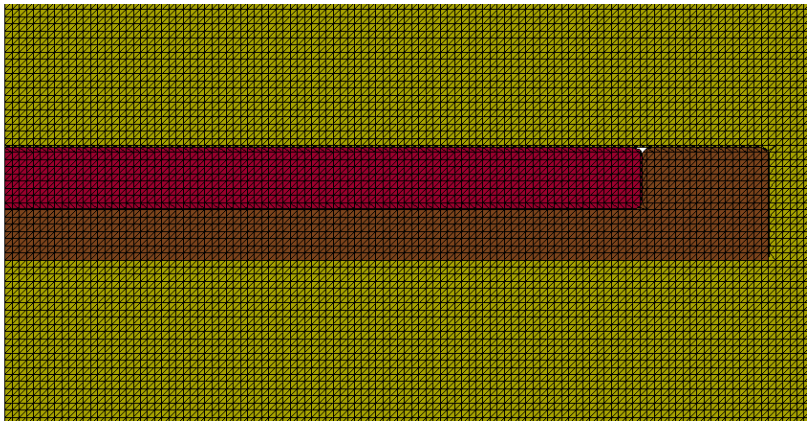

Figure 46. Initial setup of the laser ablation model, with the high energy absorption spot (red), solid aluminum plate (brown), and vacuum background mesh (yellow).

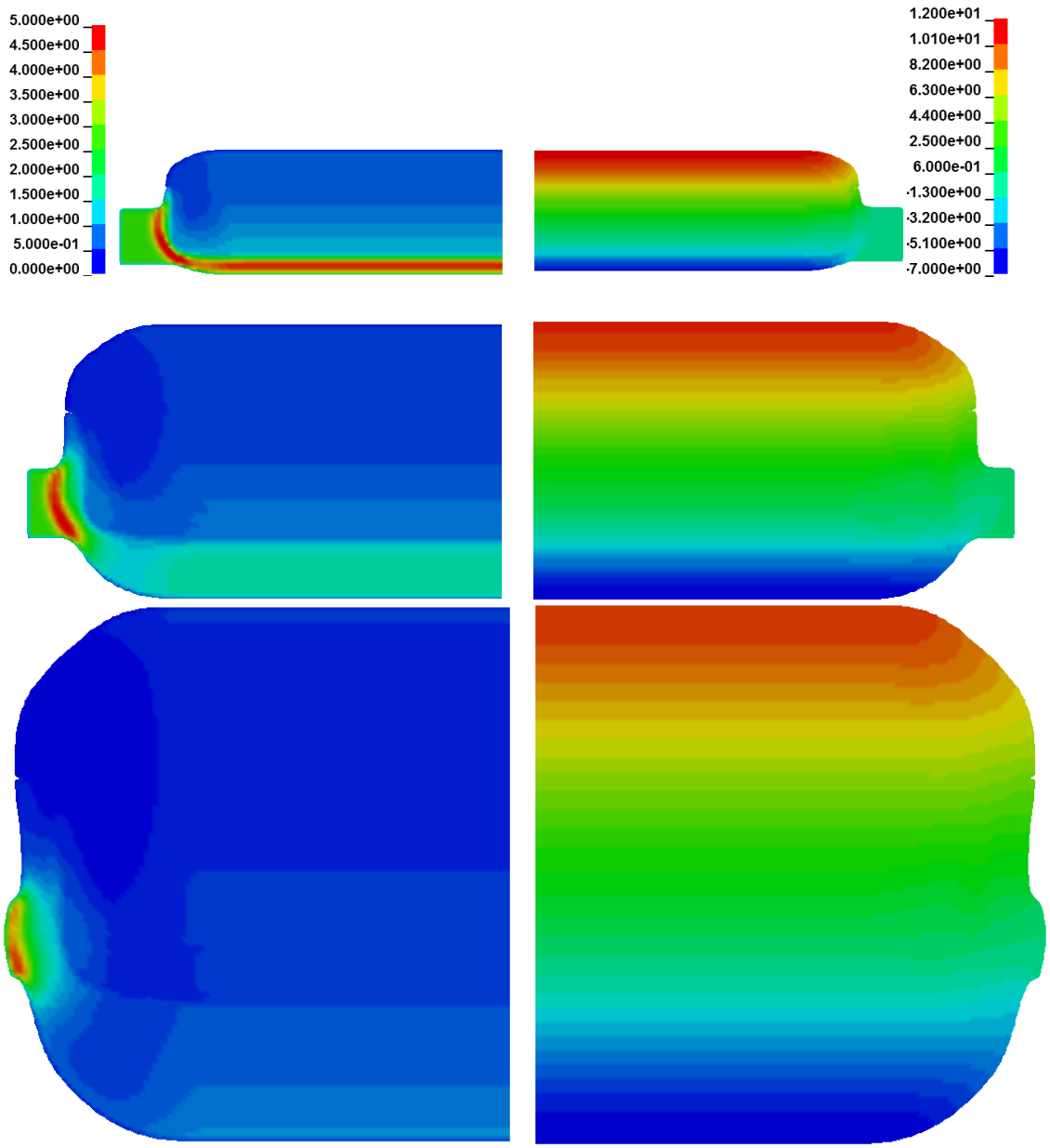

Figure 47. Density (left, g/cm^3) and velocity (right, cm/μs) of the solid formulation laser ablation study at 0.1, 0.2, and 0.4 ns.

equally. The initially solid portion of the aluminum disk which is to be accelerated reaches peak speeds of approximately 77 km/s, but the density of the material at those speeds is between 0.5 and 1 g/cm^3 at 0.4 ns, and rapidly decreasing. This is contrary to the experiment, in which a significant portion of the ablated disk remained near solid density after 3 ns.

Subsequent to the solid modeling attempt, this disk acceleration was then modeled as an interaction between two materials: a solid metal disk and a dense, energetic compressible adiabatic gas expanding within the laser irradiation diameter, as seen in Figure 48. As with the solid example, this gas was defined to be initially as dense as the remainder of the aluminum, and the physical response of the material was modeled using the isentropic gas form of the polynomial EOS. The solid portion of the disk was still modeled using the Mie-Gruneisen EOS and JC constitutive relation.

By assuming the laser-irradiated portion of the disk behaves as a gas, significantly more rapid expansion is achieved, evident in Figure 48. Not only does the expanding cloud reach velocities over 240 km/s, it begins to expand in all directions after overcoming the initial confinement of the disk walls. This propels the aluminum region immediately below the laser spot to speeds in excess of 100 km/s, but contrary to the solid expansion model, the aluminum remains relatively solid for the first few microseconds, and there are still regions over 1.3 g/cm^3 after 0.4 ns.

While the method of plasma expansion is as expected, the simulation overpredicts every measurable quantity with respect to the experimental values. By forcing the laser energy into the irradiation spot all at once, shock pressures and velocities are produced which are well in excess of those seen in the experimental setup.

To more effectively model the transient process of plasma formation and expansion, the initial laser irradiation process is allowed to occur over the first 400 picoseconds, steadily increasing the energetic content of the plasma. By doing so, the initial energy in the irradiation zone no longer vaporizes the aluminum plate, but rather accelerates it under steadily increasing expansion, seen in Figure 49.

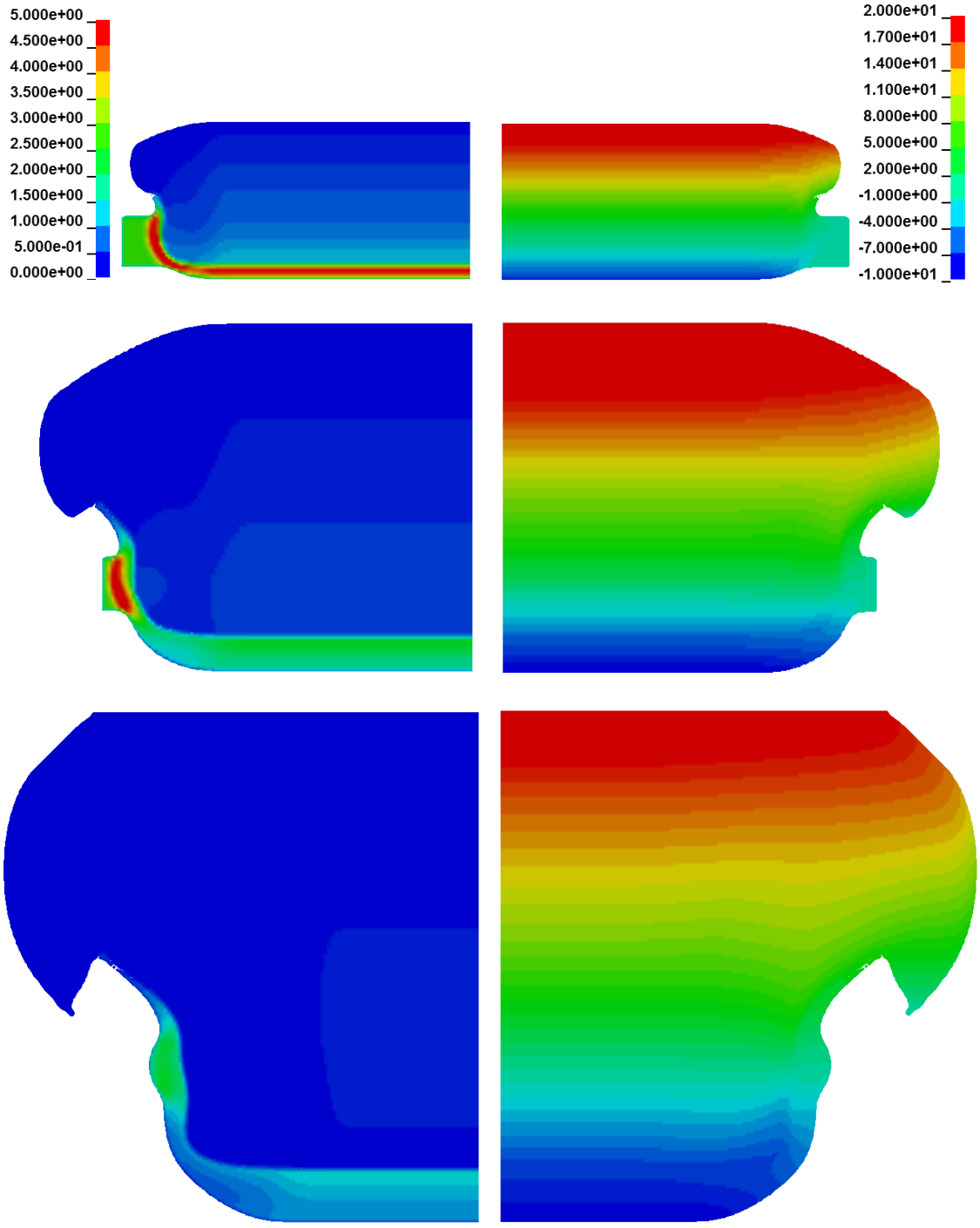

Figure 48. Density (left, g/cm^3) and velocity (right, cm/μs) of the compressible gas laser ablation simulation with lumped energy at 0.1, 0.2, and 0.4 ns.

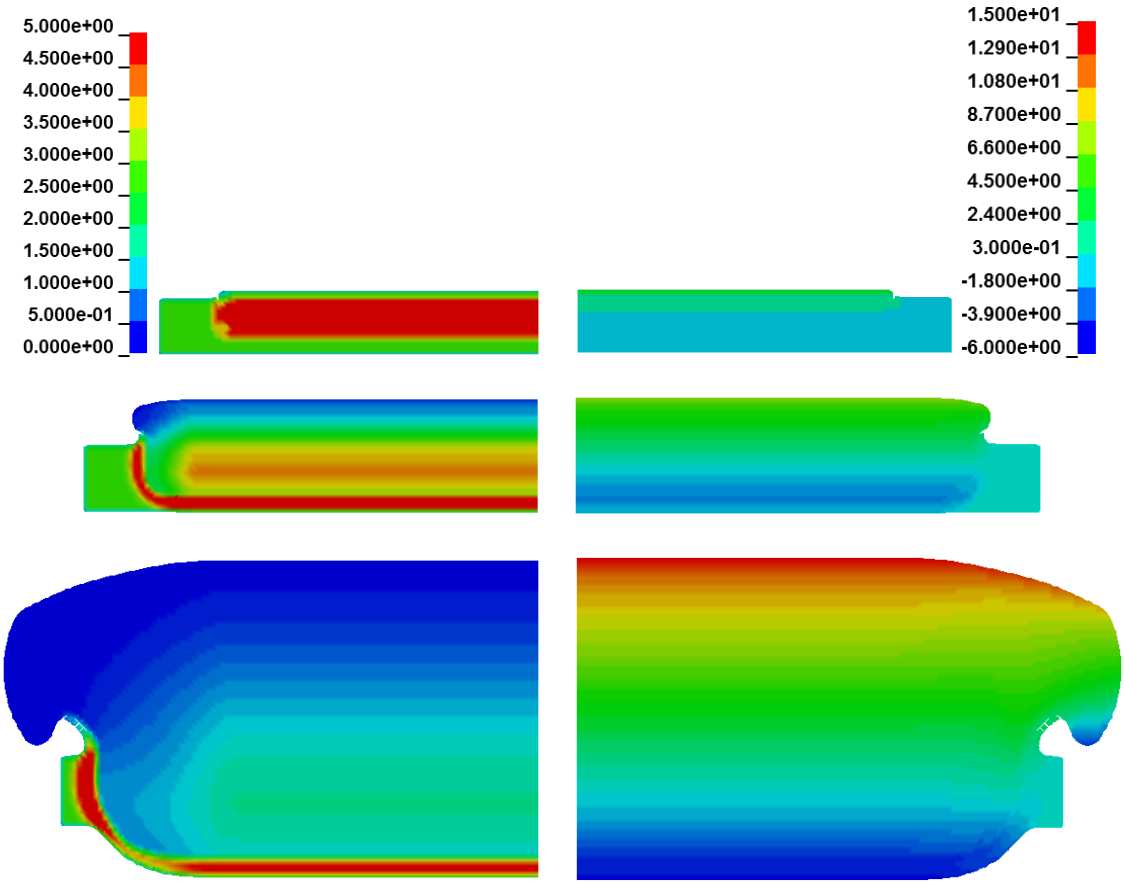

Figure 49. Density (left, g/cm^3) and velocity (right, cm/μs) of the laser ablation simulation with ramped energy at 0.1, 0.2, and 0.4 ns.

The ultimate velocity of the expanding cloud still reaches 156 km/s, but does so via an increasing ramp, rather than a sudden blast. While some shock heating inevitably occurs, this allows the majority of the solid plate material to remain at or above 4 g/cm^3, and propels it to a maximum speed of 57 km/s, which compares favorably to the experimentally reported 54 km/s.

5.5.2 Iron Particle Impact at 10 km/s

Following the laser ablation studies, simulations were constructed to analyze the plasma generation and impact behavior seen in HVI described by Lee, *et. al* [153] using iron projectiles. To alleviate concerns of scale, the impacting particle was enlarged to a radius of 1 μm, impacting at 10 km/s. While this size is an order of magnitude higher than the particles experimentally propelled to such speeds, the scaling up of the simulation decreases computational time and increases the likelihood of numerical accuracy, for the aforementioned reasons concerning sub-nanometer inaccuracies and molecular dynamics. Since the constituents and impact speeds are the same, the shock pressures generated should be sufficient for plasma production regardless of the increased projectile size.

The impact was first simulated using the high strain rate SCG constitutive relation and the Mie-Gruneisen EOS, as depicted in Figure 50. The resultant density and velocity contours are not indicative of plasma formation, due to the assumptions taken by both the material model and the equation of state. The SCG model was designed at its inception to model the stress response of materials in the primarily solid regime; similarly the Mie-Gruneisen EOS was never modified to capture energetic change primarily through phase change dynamics which are present in impacts at sufficiently elevated velocities. The resultant material response is one which approximates the mechanical deformation reasonably, but predicts little to no phase change and plasma expansion. The maximum velocity and density predictions of this impact model are a 4.8 km/s expansion of 0.5 g/cm^3 matter, which represents a significant error from the experimentally observed 31 km/s plasma speed [153].

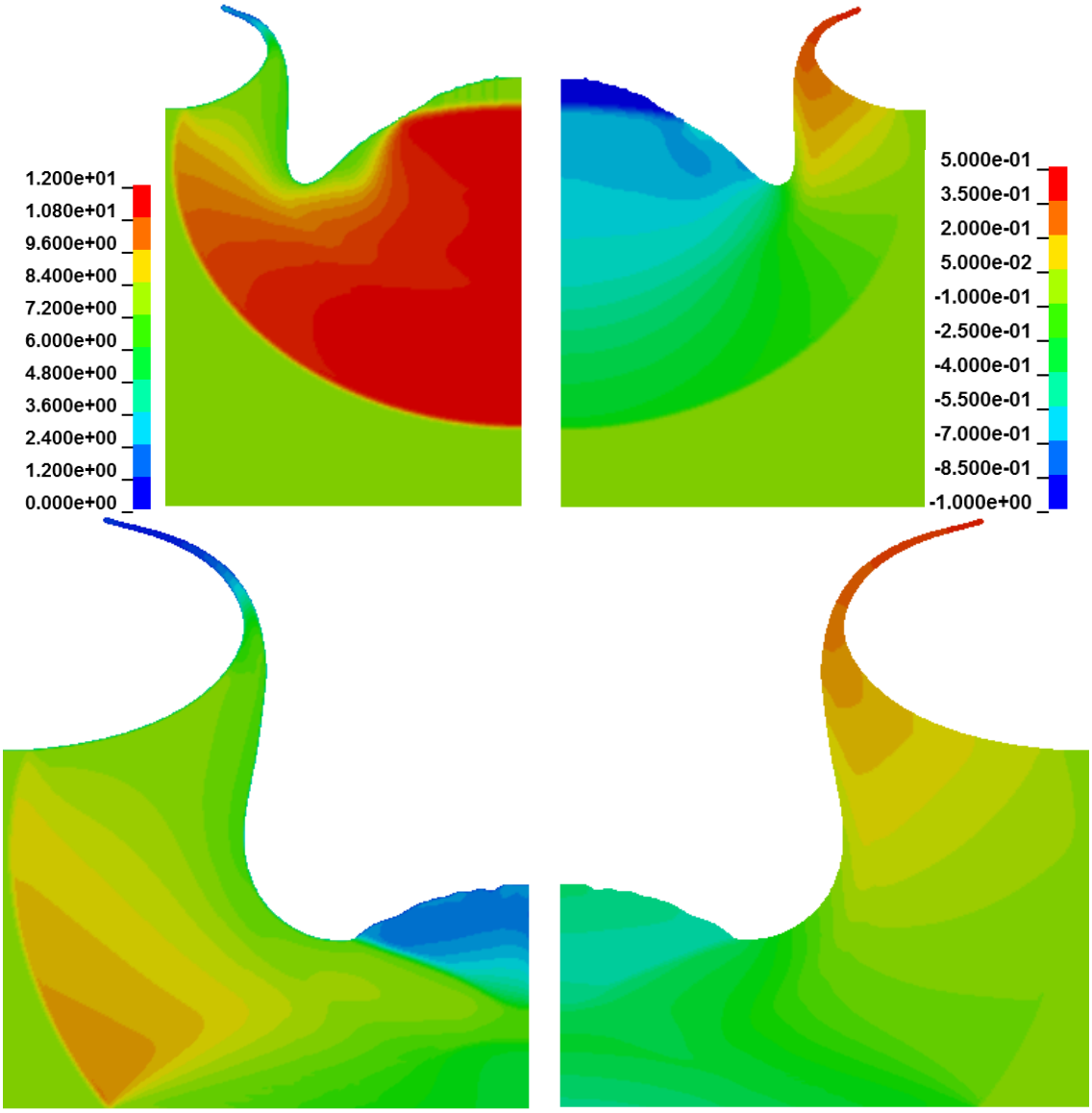

Figure 50. Density (left) and axial velocity (right) of the iron impact at 10 and 20 ns.

Pursuant to the modeling procedures of the laser ablation studies, the impact was next evaluated in a piece-wise fashion. The incident projectile and target plate were modeled as solids for the first 4 ns of interaction, at which time the peak impact pressures were seen to occur. At this point, the high-pressure, high-energy region was then converted to a hot, dense compressible gas, and allowed to mechanically interact with the plate and incident projectile.

The resultant debris shape appears odd, given the trends observed in larger interactions and predicted by solid mechanics formulations. However, the total deformation at a time of 20 ns is not entirely unphysical, and the measured speed of plasma expansion grows to a peak velocity of 33 km/s and gradually decreases to 32 km/s after the first 20 ns as the gas expands; this correlates quite well to the experimentally determined average plasma velocity of 31 km/s. Additionally, the total density and motion of the incident projectile follow the same trend seen in the solid model. The presence of the initial plasma layer induces a shock response which lowers the density of the projectile's rear hemisphere and begins to accelerate it upward; this same effect is seen after approximately 15 ns in the purely solid example. While the initiation of this effect is slightly earlier in the plasma example, the total velocity and density profiles of the projectile at 20 ns are similar (note that the velocity fringe in Figure 51 spans a significantly larger range). The effect on the target of defining a region to follow shocked gas dynamics is significantly less severe; the velocities and density changes induced by shock pressures are largely identical between the two scenarios. The only immediately obvious change on the plate response is the shape of the rear ejecta veil. The solid model predicts a thin fluid-like lateral expansion composed of projectile and plate material similar to that seen in the debris cloud images presented earlier; by contrast, the plasma model shows an extremely low density cloud expanding between the two higher density deformations composed separately of projectile and plate debris.

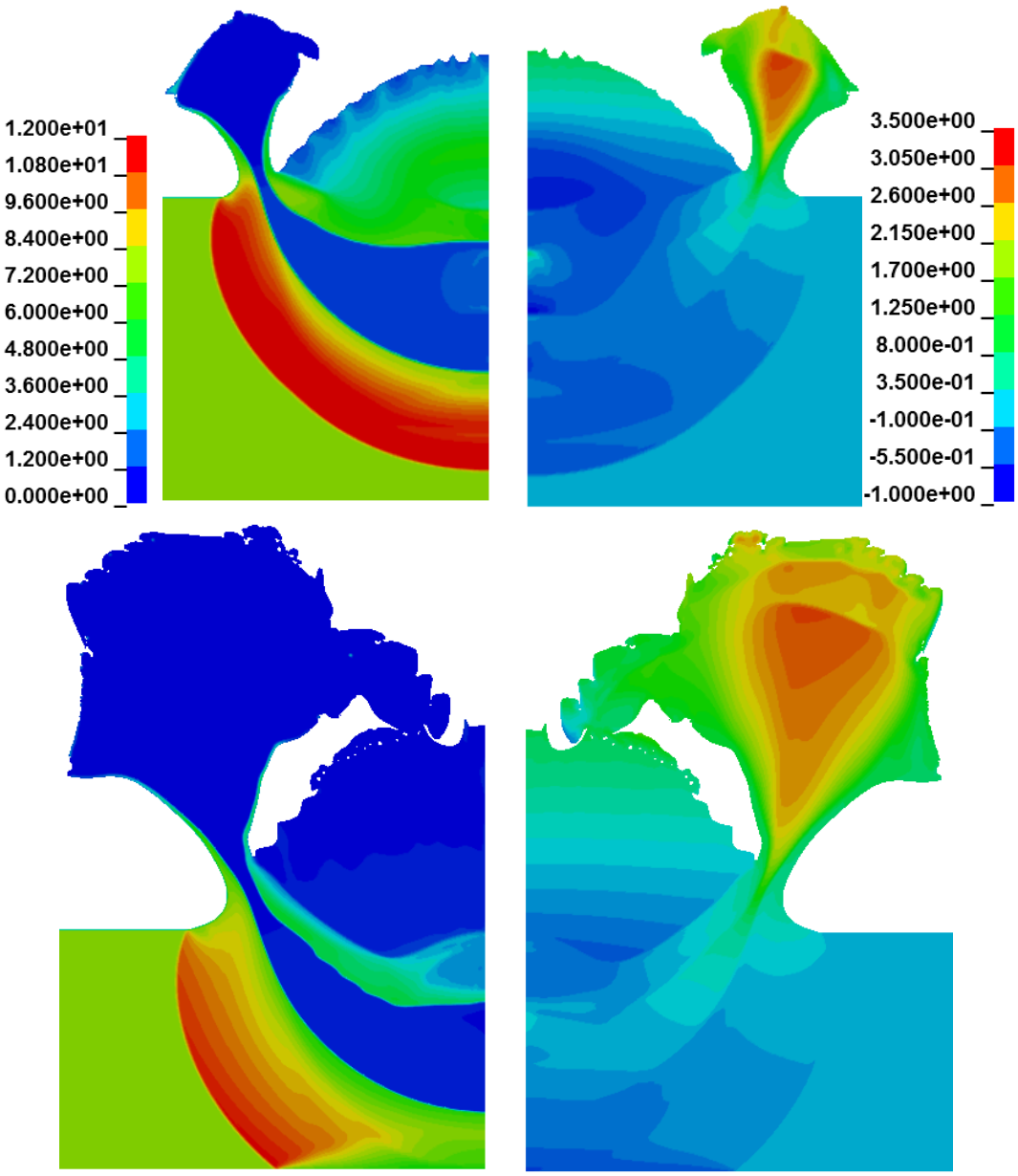

Figure 51. Density (left) and axial velocity (right) of the iron impact with gas material conversion at 10 and 20 ns.

5.5.3 Discussion and Summary

The developed techniques in the laser ablation and hypervelocity impact simulations both predict values with good correlation to experimentally provided measurements, however, the HVI model has a much higher degree of uncertainty due to the unknown mechanisms inherent to HVI plasma production. In the laser ablation study, the incident radiative energy and its time distribution were both known due to experimental procedures; the HVI model was based upon a known mass and impact velocity, but the partition of energy into shock pressures, phase change, and ionization energy is currently unknown for any HVI induced plasmas. The compressible gas model yielded results with approximately 6% error for the expansion velocity, but a single measure of validation is insufficient to conclude that an effective modeling strategy has been produced. Additionally, the time dependence of impact plasma creation during HVI is not well understood; the gas model utilized a single time of conversion where the initially solid mass was uniformly converted into a gas formulation. This method is undoubtedly a rough approximation of a continuous process over some finite time, and will thus yield inaccuracies if extended to other modeling scenarios.

Since the oscillation frequency of a plasma is directly related to its electron density [81], it is possible that an additional method of model validation can be constructed by comparing the gas cloud density with the RF signals measured at the expansion distance correlating to the measurement devices. The limited number of direct frequency measurements reported by Lee, *et al.* [153] show a significant degree of noise and are of insufficient quality for such a comparison. A larger data set may yield appropriate measurements for such validation purposes. Nonetheless, the compressible gas approximations showed a significant improvement over the purely solid formulations in both the laser ablation simulation and the HVI plasma model, and such a modeling strategy using ALE techniques could be extended to other plasma modeling scenarios, pursuant to improved validation measures and a more detailed understanding of the relevant shock-induced phase change dynamics.

5.6 Bumper Shield Evaluation

In an effort to computationally examine the performance of multi-bumper shields in defeating incident micrometeorites and orbital debris, several shielding materials and configurations were analyzed under hypervelocity impacts.

5.6.1 Honeycomb Channeling

Honeycomb sandwich panels have been used for dual functions in structural support and orbital debris shielding in several space structures, most notably on the International Space Station. The increased structural rigidity is beneficial, but early hypervelocity tests demonstrated a channeling effect, in which the debris from an incident projectile is directed down the length of the honeycomb and prevented from expanding, causing more damage than in a traditional bumper shield. Following light gas gun experiments done at the Centre d'Etudes de Gramat (CEG) [159] evaluating honeycomb sandwich panel performance under normal and oblique incidence, models were constructed to analyze the channeling effect directly. The experimentally studied honeycomb sandwich panel was composed of two 0.8 mm thick aluminum plates separated by 20 mm long honeycomb cores with 0.05 mm thick aluminum sheets and a honeycomb width of 4 mm. These plates were impacted by 7 mm spherical aluminum projectiles at velocities of approximately 5.7 km/s.

The impact at normal incidence was modeled using axisymmetric SPH, and is represented in Figure 52 and Figure 53. While the axisymmetry creates a condition of concentric circles rather than honeycombs, the distance between lateral interfaces is equivalent. As seen by the density contours in Figure 52, as the initial impact density evolves, the fastest and densest material in the center of the debris cloud is prevented from expanding. As the lateral debris impacts the honeycomb material, it is slowed while the honeycomb debris is added to the total debris field. Examining the axial velocity contours in Figure 53, it is evident that while the net axial velocity of the debris is not significantly affected in the central area, the amount of material which remains concentrated there is increased. Outside of the primary honeycomb, the barriers are somewhat effective in preventing lateral spread, and the velocity of the debris which passed through the initial

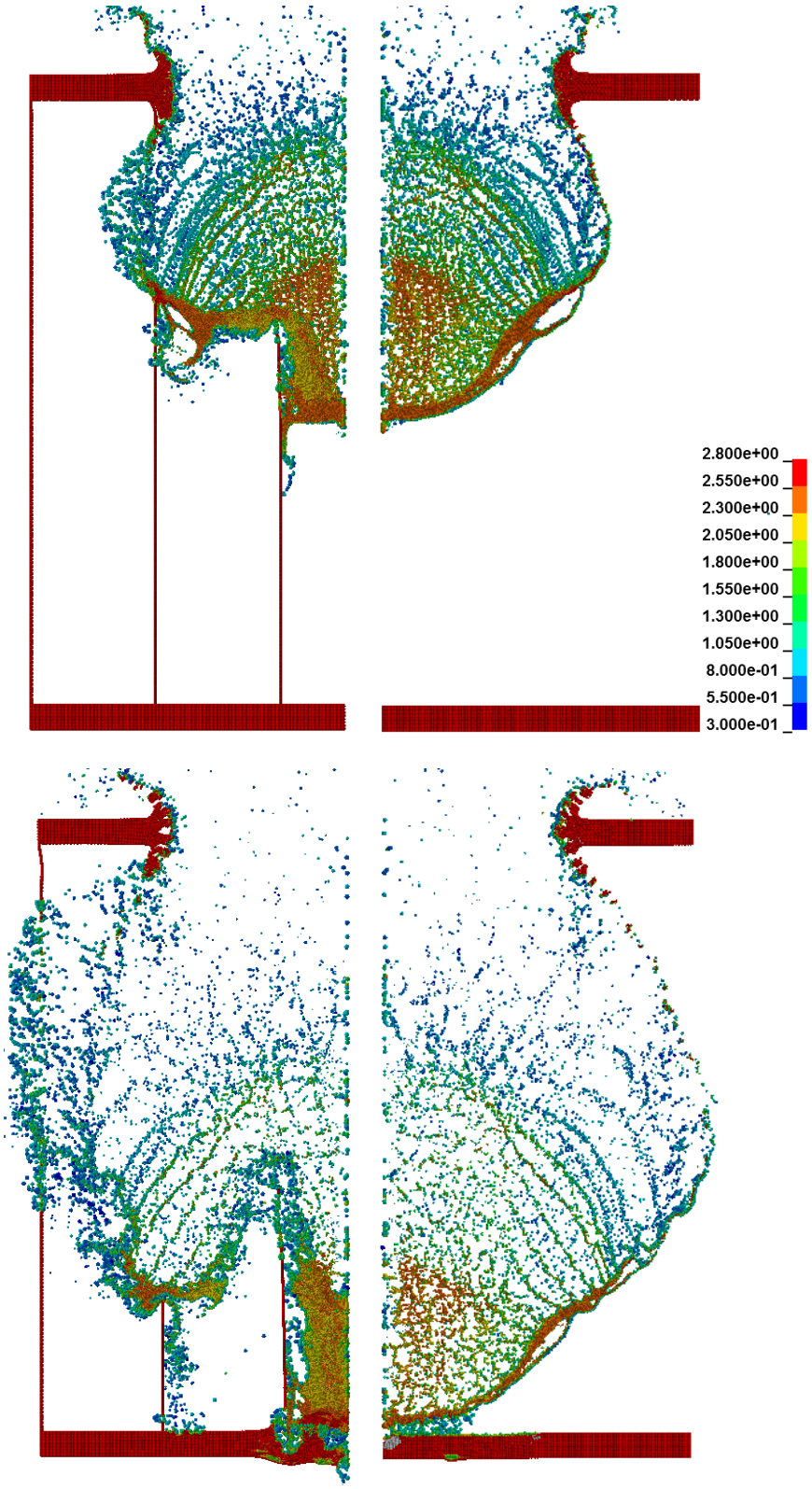

Figure 52. Comparison of debris density between a honeycomb panel (left) and a standard bumper shield (right) at 2 and 3.5 µs.

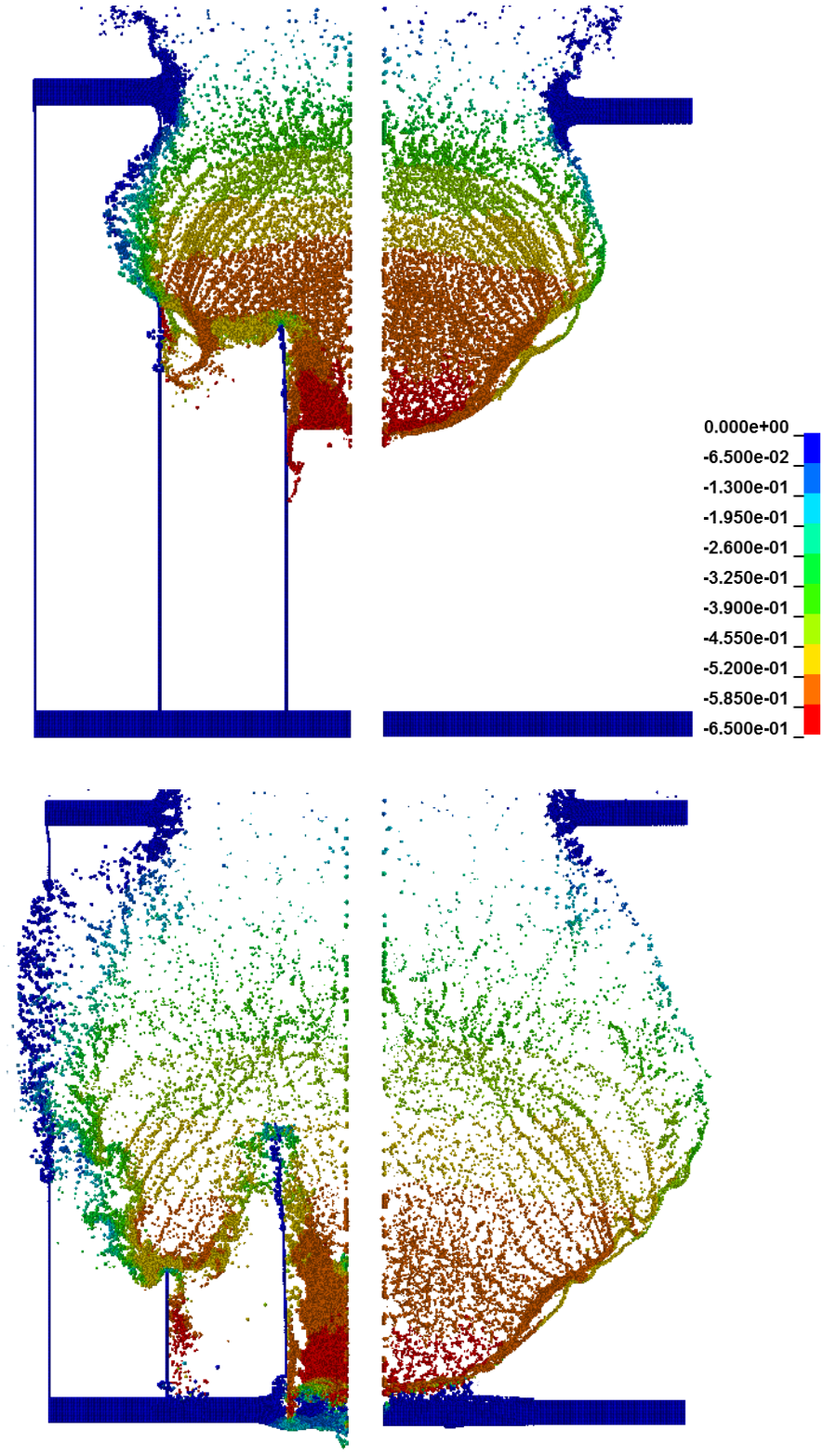

Figure 53. Velocity contours of debris impacting a honeycomb (left) and a standard bumper shield (right) at 2 and 3.5 μs.

honeycomb barrier has been evidently slowed somewhat. However, preventing lateral spread is the exact opposite of a bumper shield's purpose; the spread of debris into a diffuse cloud is what makes subsequent damage considerably minor. By concentrating the most damaging portion of debris into one area, the honeycomb virtually guarantees more significant damage in a smaller area. This effect is supported by experimental evidence [35]. Due to this effect, subsequent bumper shielding evaluations are performed on bumper materials with no honeycomb.

5.6.2 Parametric Bumper Evaluation

To evaluate the performance of various materials under HVI loading, a parametric study was performed, in which the materials of interest were varied in thickness from 1 mm to 4 mm, and their shielding efficacy evaluated as a function of residual momentum and residual kinetic energy vs. areal density. As shown in Table 6, ten metals were initially chosen for comparison, and Al 6061 was used as a baseline; the remaining nine metals represent densities, melting points, and strengths both above and below aluminum. This is shown graphically in Figure 54.

Copper, tantalum, and zinc were discarded as material choices since their properties relative to aluminum were better represented by other materials, such as tungsten and titanium. By analyzing a wide range of these property ratios, the relative role of such model parameters can be more easily analyzed. Several of the final material choices can be initially assumed to be better or worse performers than aluminum; magnesium alloy AZ31B is lower than aluminum across all properties, while 4340 steel and titanium alloy 6Al/4V are higher across all parameters. Of particular note however are beryllium and lead; beryllium is significantly lighter and stronger than aluminum, though brittle, and lead is quite dense, but has a low melting point and very low failure stress. For a parametric comparison, each of the materials was modeled in bumpers with thicknesses of 1, 2, 3, and 4 mm, and an impact event was simulated with a 1.3 cm Al 2024 projectile at 7 km/s. The resultant debris was then evaluated based on measured residual total momentum and kinetic energy.

Table 6. Selected material properties of bumper metal candidates.

Material	Density (g/cm^3)	Melting Point (K)	Shear Strength (Mbar)	Spall Strength (Mbar)
Al 6061	2.703	1220	0.276	0.012
Steel 4340	7.81	2310	0.801	0.032
Beryllium	1.85	1820	1.51	0.0035
Magnesium	1.738	1150	0.165	0.009
Lead	11.34	760	0.086	0.0006
Ti 6Al/4V	4.419	2110	0.419	0.04
Tungsten	19.3	4520	1.6	0.009
Zinc	7.139	900	0.395	0.012
Copper	8.93	1790	0.477	0.012
Tantalum	16.69	4340	0.69	0.044

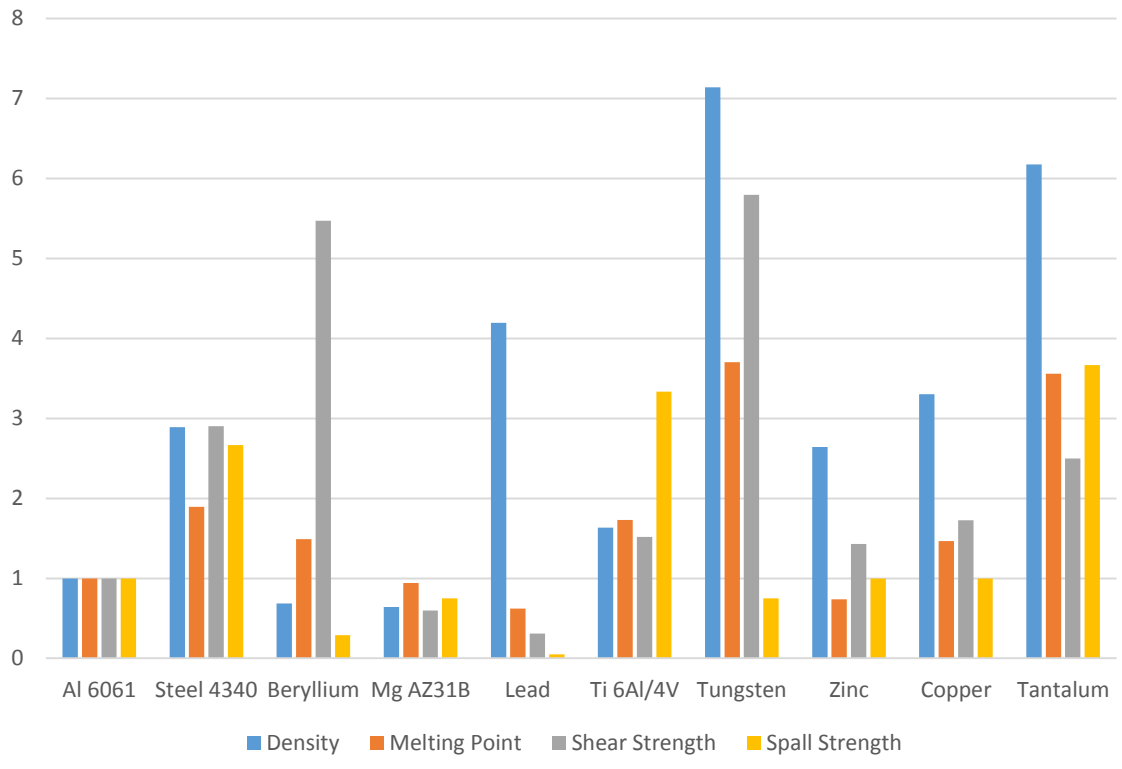

Figure 54. Selected parameters of nine metals compared to an Al 6061 baseline.

The relative performance in reducing total momentum and total kinetic energy is presented as a figure of merit shown in Figure 55 and Figure 56, respectively, where the materials are evaluated on their efficacy relative to Al 6061 of the same thickness; thus the figure of merit for Al 6061 is equal to 1, while a bumper which performs twice as well would have a value of 2. The value for 4 mm tungsten shielding was significantly higher than the other metals in both graphs, so the magnitude was reduced for clarity, and the value for tungsten is listed beside its graphical depiction. The results are obviously more dependent on density than any other factor. The lightest material, magnesium, performs poorest, followed by beryllium, while tungsten's density of 19.3 g/cm^3 yields results an order of magnitude higher than most metals, followed by lead, steel, and titanium.

However, space applications are critically weight limited, so a more relevant measure of shielding efficiency is the performance criteria relative to an Al 6061 shield of equal mass. In examining Figure 57 and Figure 58, the advantages of steel and titanium have all but disappeared, while beryllium and magnesium now have a higher figure of merit than aluminum across all thicknesses. The trend of increased performance with decreased weight has one major outlier in tungsten. While the performance at lower thicknesses is significantly reduced relative to aluminum as expected, the performance of the 4 mm plate is still by far the highest performance index. Examining the debris cloud in the Appendix reveals why: at a thickness of 4 mm, tungsten is not so much a bumper as it is armor plating. The 1.3 cm aluminum sphere is almost completely defeated, and significant portions of the incident projectile are spalled backwards or deformed laterally rather than penetrating through. By 5 μs after impact, the majority of the projectile's mass has slowed to less than 1.5 km/s. Such a method is inadvisable in space applications, however, since the increased weight is prohibitive, and multi-bumper shields can accomplish the same reduction in damage at significantly lower mass. The density profiles of the debris clouds of all studied materials and thicknesses are presented in the Appendix.

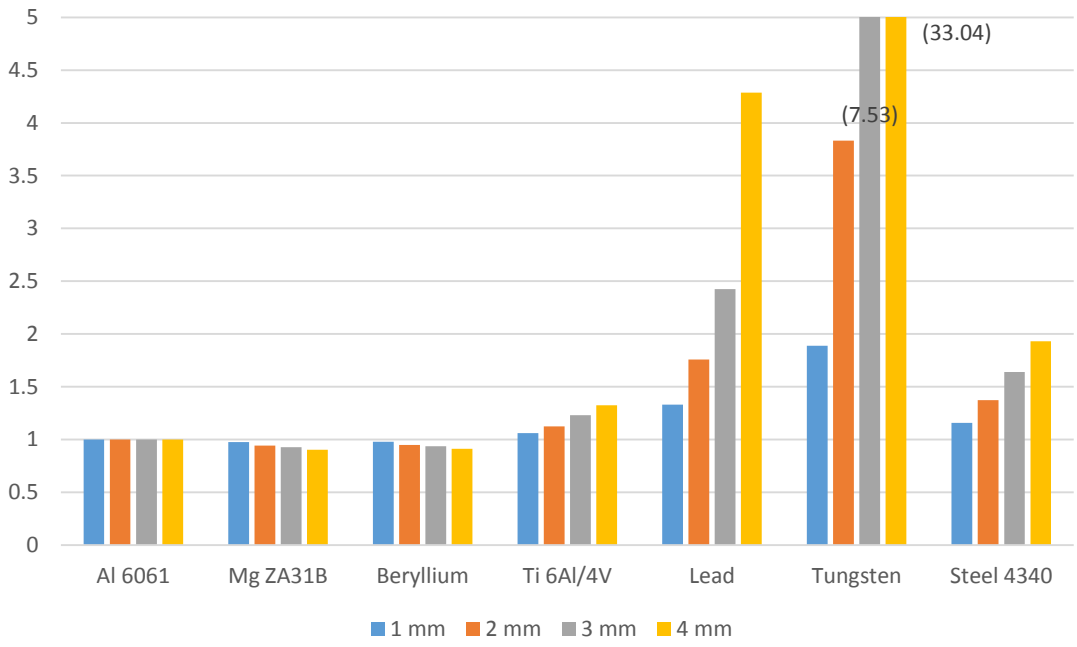

Figure 55. Figure of merit for momentum reduction, relative to Al 6061 of the same thickness

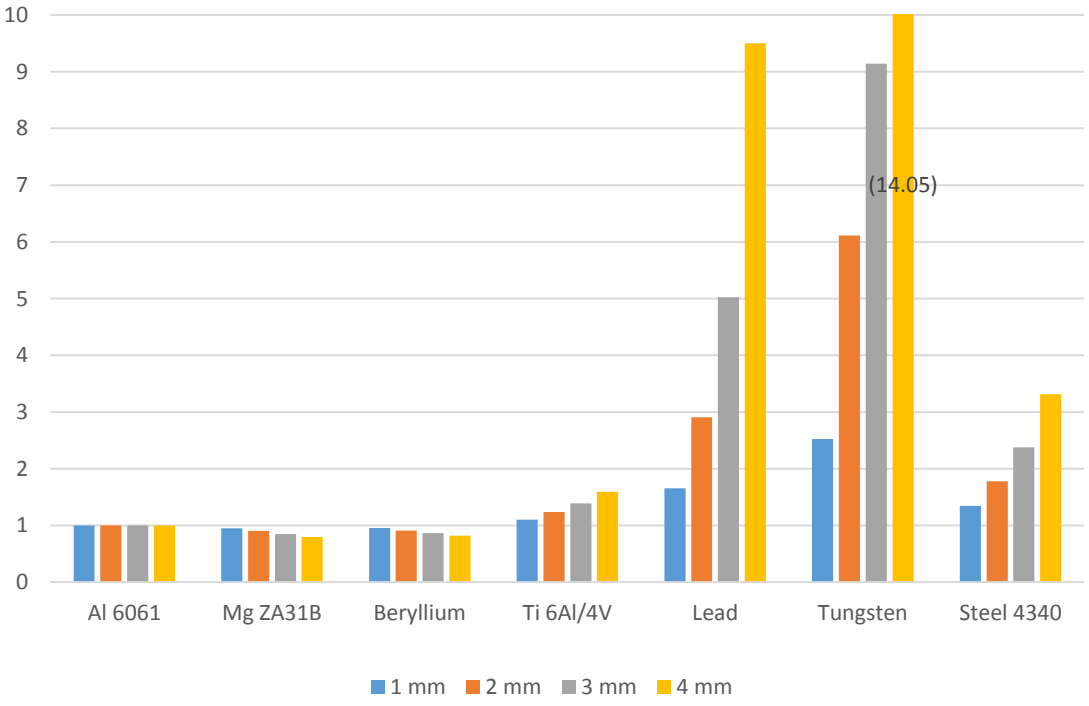

Figure 56. Figure of merit for kinetic energy reduction, relative to Al 6061 of the same thickness

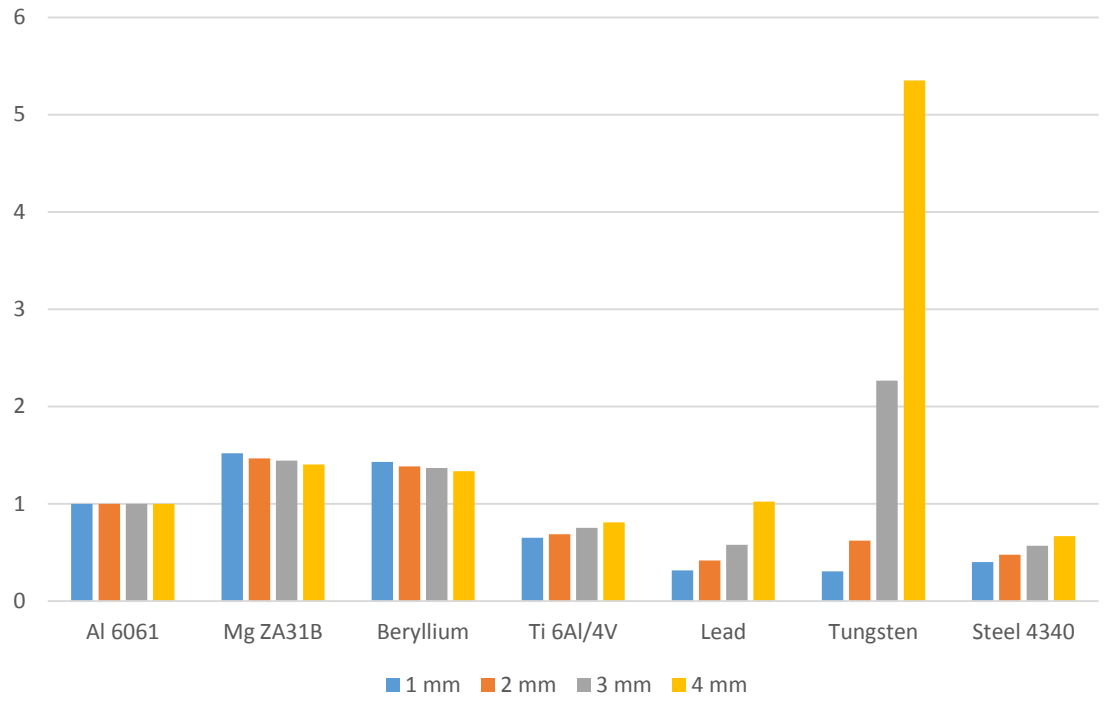

Figure 57. Figure of merit in reducing momentum, normalized by Al 6061of the same mass.

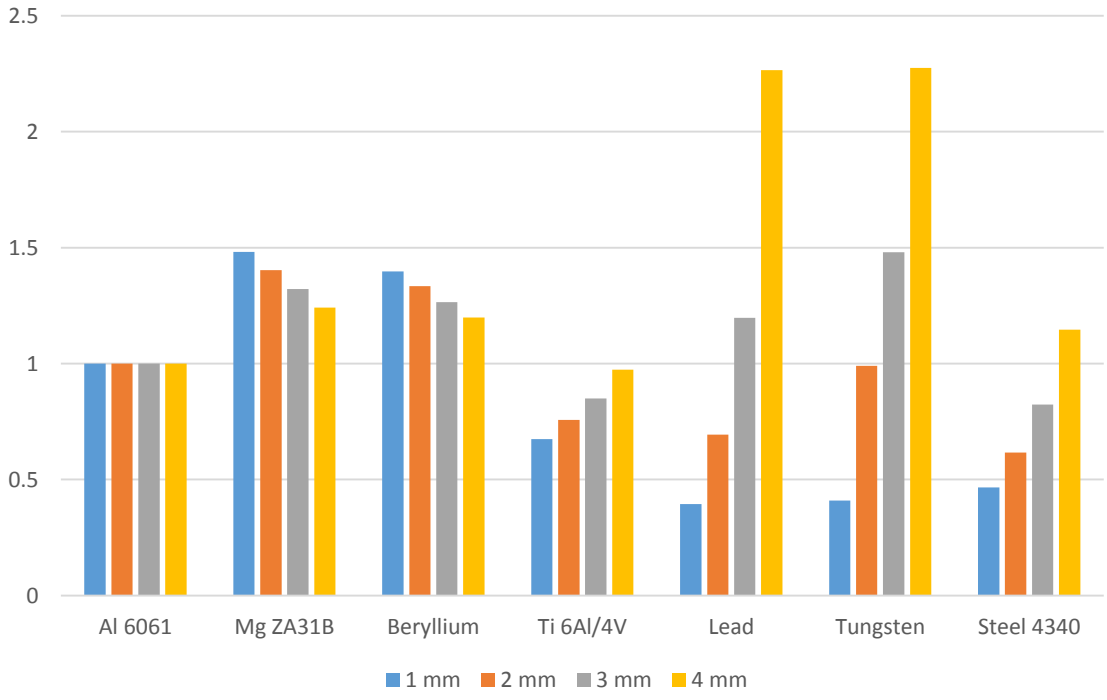

Figure 58. Figure of merit in reducing kinetic energy, normalized by Al 6061of the same mass.

5.6.3 Bumper Variations

Using traditional materials, modifications in orientation or configuration can produce increases in effective shielding. Aluminum with multiple drilled holes or voids, or an aluminum foam can induce a preferable shock response while remaining lightweight. As seen in Figure 59, the initial impact into a semi-hollow aluminum bumper creates sufficient shock pressures to spall and melt the incident projectile, as the maximum density

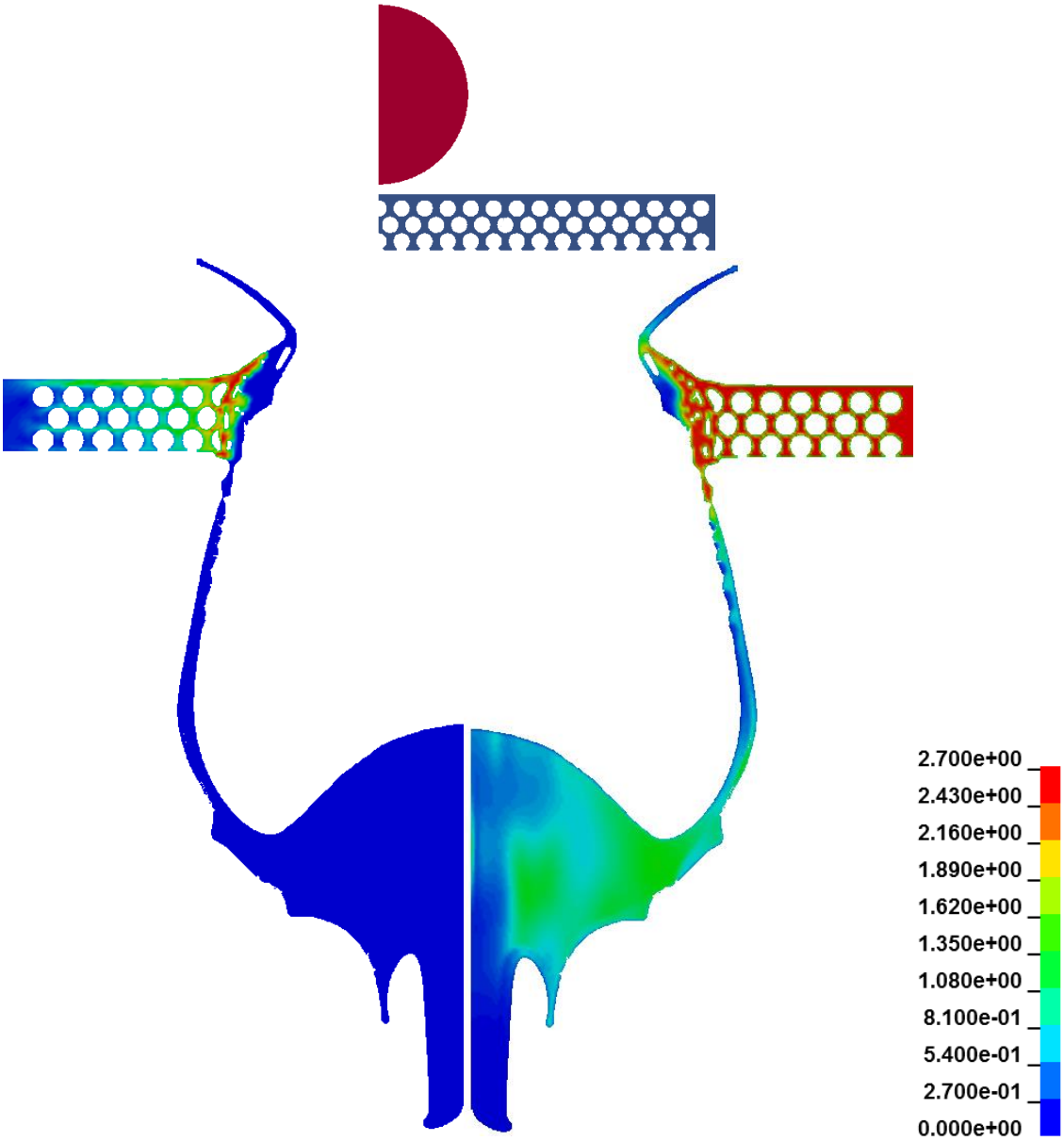

Figure 59. Initial configuration of aluminum sphere impacting aluminum "foam"(top), stress propagation (bottom left), and density (bottom right) after 4 microseconds.

after 4 μs approximately 1 g/cm^3 for the resultant debris. Additionally, the presence of micro-voids prevents the shock response from traveling as effectively through the shield structure. Most importantly, the presence of such holes represents a significant weight reduction in the shield assembly, and thicker designs using micro-voids can be utilized to further defeat incident debris.

Furthermore, combinations of materials identified in the parametric study show a reduction in energy and increase in melt over uniform shields made of one material. As seen in Figure 60, using a magnesium bumper with a thin layer of tungsten on the surface, an incident aluminum sphere is shocked to the point of complete melt. While a thick tungsten shield is too heavy for space deployment, the combined tungsten/magnesium bumper was designed to be identical in weight to a 2 mm bumper of Al 6061, but shows markedly lower density in the debris field. There are small fragments of higher density tungsten in the resultant debris, but their size is on the order of 0.02 mm after 6 μs, and they should be relatively harmless to a secondary layer.

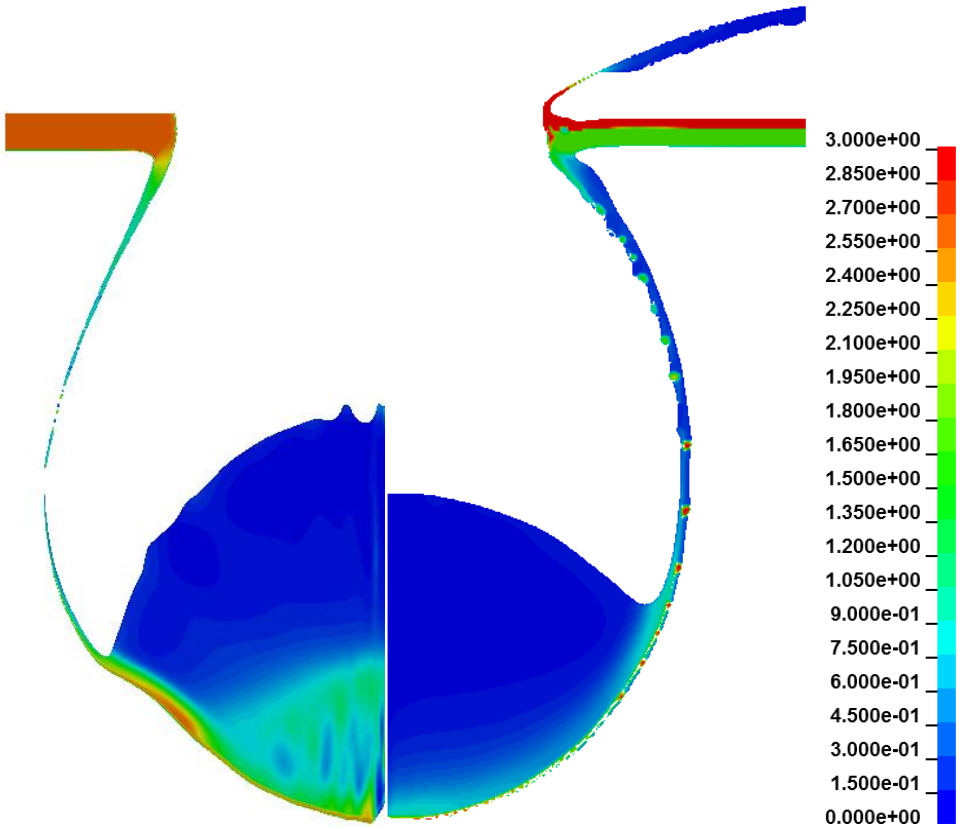

Figure 60. Density contours of a 1.3 cm aluminum sphere impacting a 2 mm thick aluminum shield (left) and a lamination of tungsten and magnesium (right) at 6 μs.

6 CONCLUSIONS

6.1 Summary of Findings

This dissertation has presented work using computational methods focused on a detailed understanding of the dynamics and physical processes underlying hypervelocity impacts. The modeling techniques introduced in this work allow for a more complete characterization of HVI physics, including structural damage, debris cloud evolution, and phase change including portions of plasma formation. This chapter reviews the analysis and contributions of preceding sections, and discusses implications for future work in this area.

Chapter 2 described the orbital debris and meteoroid environment and predictions of risk, including a literature review of the characterization of HVI and protection measures. Ballistic limit equations were discussed, and the need for further risk assessment was detailed along with physical limitations on experimental techniques. The fundamentals of shaped charges and laser ablation experiments were introduced, drawing parallels to HVI interactions.

Chapter 3 detailed the physical approximations to shock phenomena, material stress response, and possible phase changes involved in HVI. A brief comparison of such methods showed that the JC and SCG models predicted the lowest deviation from experimental results, while the Mie-Gruneisen EOS allowed for a continuous approximation of shock pressures which agreed well with direct experimental measures.

The numerical algorithms used in the current analysis were described in Chapter 4, with a focus given to recent advancements in Lagrangian and ALE algorithms. A detailed formulation of SPH mechanics was derived, and descriptions of varying formulations and boundary condition treatment were shown. The criteria for time step calculation, coupling between computational methods, and stability were introduced, as well as a discussion of numerical accuracy, convergence, and verification.

Chapter 5 contained the results of computational work in HVI analysis. Spherical aluminum impacts and non-spherical zinc experiments were used for validation purposes, with the average error predicted by numerical methods under 4%. Variations in projectile shape and material were presented and differing shock dynamics were shown to produce significant changes in debris cloud morphology. The strain rate response of metals was recast as the deformation of Newtonian and non-Newtonian fluids, with excellent correlation to the solid models. These newly developed fluid models were then used in a similitude analysis, demonstrating their capability in scaling HVI dynamics. The plasma creation and expansion in HVI was directly modeled with good correlation to experimental measurements, after laser ablation studies were used to create an effective modeling strategy. Several shielding material candidates were parametrically evaluated, and new configurations for an initial bumper were proposed which seem to improve upon traditional metallic bumper designs.

The summation of the work presented here is a multifaceted examination of hypervelocity impact physics within a computational framework, which has established new modeling strategies in the analysis of this technically challenging scenario. Significant contributions to the existing literature are detailed below.

6.2 State of the Art Contributions

In analyzing HVI computationally, the existing literature failed to adequately address several fundamental concepts which were investigated. In such cases, the concepts of interest were analyzed computationally using what experimental data was available. The work presented in this document has contributed to state of the art analysis and computational work in several ways, detailed below.

6.2.1 Fluidic Approximations to High Strain Rate Solid Behavior

The strain rate-dependent behavior of structural materials has been investigated for decades, but the deformation modes of solid materials in conditions similar to HVI have never been fully quantified. To analyze the extent to which shear deformation and strain rate-dependency influence material behavior in HVI, fluidic analogues were constructed

which replicated the stress response of strain rate-dependent material models. These models used Newtonian and non-Newtonian representations of the solid deformation to create fully fluidic impact simulations. The debris clouds generated by such impacts resembled the solid mechanics simulations using a particle approach, but differed more significantly in their qualitative impact predictions using an ALE algorithm. However, the comparison between fluid models and the solid impact simulations revealed that both Newtonian and non-Newtonian representations recreated the energy profile of the impact event with a higher fidelity that a strengthless, purely hydrodynamic material representation.

The improved accuracy shows that the assumption of a hydrodynamic material response is characteristically flawed, and that while shear forces contribute to the energetic material response in small magnitudes (3-5%), ignoring such forces creates unphysical effects. Additionally, by using a fluid description of HVI materials, a non-dimensional scaling analysis is possible which is unfeasible using high strain rate solid models. An extensive literature review has shown no other published work which attempts to describe high strain rate solid deformation through the use of a viscous fluid; to the author's knowledge, this is an entirely new technique.

6.2.2 Plasma Modeling

To simulate the shock-induced formation of plasmas in HVI, simulations were first constructed to model a laser-ablation driven aluminum flyer plate. When energy deposition was modeled using purely solid formulations, the resultant density and momentum transfer showed a large degree of inaccuracy; when the plasma zone was instead modeled as an energetic compressed gas, the model predicted the expansion and momentum transfer significantly more accurately. This method was then used in modeling a small iron particle impacting a semi-infinite target which experimentally induced plasma formation. When applied to the impact simulation, predicted plasma expansion velocities were in good agreement with the experimentally measured values. While the exact mechanism for such conversion of solid matter into a plasma state is not fully understood, the ability to model any physical aspect of such behavior is an improvement over the current literature; previous

computational investigations into HVI behavior have attempted to model physical damage alone, neglecting all plasma effects.

6.2.3 Shielding Analysis

A parametric study was done on several material choices for usage in multi-shock bumper shields. At several thicknesses, these materials were evaluated using a figure of merit for their suitability in bumper shields based on momentum and kinetic energy criteria, normalized by weight. The results indicated that thin shields made of magnesium or beryllium could induce a reduction in damage from incident projectiles using less weight than an equivalent aluminum shield. Additionally, it was seen that tungsten, while likely too heavy for practical usage in space, could significantly reduce the momentum and energy of an incident projectile if used at thicknesses above 3 mm. New configurations to bumpers were suggested, including an aluminum plate with lateral holes, or an aluminum foam, as well as laminates of disparate materials, such as tungsten and magnesium. Both of these bumper types are relatively easy to manufacture, and offer a weight-normalized improvement over equivalent mass aluminum shields.

While previous work in HVI analysis has investigated shielding performance and weight-normalized efficacy, such work has invariably examined structural concepts on a case-by-case basis, evaluating existing designs and supplementing experimental work. By parametrically evaluating multiple candidate materials and structural configurations which are not of current experimental interest, the design process can be reversed. In this way, inexpensive computational work can identify primary candidates which are then evaluated by the significantly more resource intensive experimental studies. This allows for more rapid concept design and fewer expensive test shots.

6.3 Future Work

The work presented in this document would benefit from extended efforts in several key topics related to improvements in algorithms and model constraints, investigations into multifunction shielding designs, and new datasets from experimental studies.

6.3.1 Improved Model Characterization and Scope

The presented computational results were shown to correlate well to experimental studies, and new techniques were presented which identified previously unpublished characterization methods for the fluidic behavior in shock-dominated impact events and HVI plasma production. Nonetheless, these modeling methods can be improved upon to generate a more complete modeling methodology.

The developed reformulation of strain rate effects via a fluid dynamics description should be valid for a number of materials under high strain rate loading conditions, and is not theoretically limited to the aluminum studies presented here. As such, it should be extended to multiple materials over a greater range of strain rates and loading conditions. A more comprehensive scaling analysis should also be performed to assess the validity of such dimensionless analysis using additional materials and over larger variations in scale. A more explicit formulation of this interplay between high strain rate solid behavior and viscoplastic fluid dynamics may be achieved through a larger dataset created by such methods.

Additionally, the plasma simulation methodology adopted in this work ignored electromagnetic effects from the dense plasma since mechanical effects dominate in such a regime. However, as the plasma expands and rarifies, such electromagnetic considerations will increase in relevance, and are necessary if HVI plasma experiments are to be directly correlated with simulation results. As computational magnetohydrodynamics evolve, the coupling of these effects to mechanical pressures could yield a more complete description of this phenomenon.

6.3.2 Multifunction Shield Concepts and Analysis

The implementation of multi-bumper shields has significantly reduced the probability that orbital debris threats will cause structural failure and loss of mission in low Earth orbit. However, traditional sacrificial shields add weight to spacecraft while serving only the purpose of debris protection. If such shielding mechanisms can be integrated into existing structural components or other critical shields, such as thermal protection systems

(TPS) or radiation shields, a multifunction shield is possible which affords equal risk reduction at a reduced weight penalty.

The analysis of such a multipurpose structure using computational tools is feasible if the design constraints and mechanical properties are well characterized. Additionally, the use of computational analysis can lend additional insight into loading conditions causing multiple concurrent modes of failure. For example, the mechanical and thermal performance of carbon-carbon reusable tiles and ablative heat shields using the more recent carbon-impregnated phenolic ablator (PICA) composite is well characterized, and the impact response of such materials is currently under investigation [160]. By analyzing the thermal and structural performance of such heat shields after impact damage has occurred, design changes can be recommended for a safer and lighter multifunction shield.

6.3.3 New Physical Theories and Experimental Data

Computational models were constructed using the latest experimental studies and validated physical approximations available to the author; nevertheless, assumptions were still necessary in modeling phenomena which have not been thoroughly characterized. Improvements in experimental and theoretical descriptions of composite shock performance, HVI plasma production, and unconventional shielding materials would greatly increase predictive modeling capabilities and provide additional validation to the work presented here.

To circumvent the limitations of traditional composite failure theories, an equation of state was implemented to separate hydrostatic and deviatoric stress responses to strong shocks; however, the volume fraction shock equation used in this composite analysis still relied upon experimental studies of isotropic hydrostatic forces of each individual component. By investigating the shock response of anisotropic materials experimentally, a more complete description of this deformation can be achieved. In particular, theoretical and experimental studies of shock behavior at microscopic boundaries between constituents and macro scale transitions between lamina would greatly improve models of composite materials under HVI.

The physics of phase change in HVI creation of plasmas is currently unknown, and the presented computational models used simplified assumptions to approximate this process. Due to limitations in physical size, time scale, and the energies involved, it is unlikely that technological developments in the near future will allow for a detailed experimental resolution of the phase change process itself; however, an improved theoretical description of this multiphysics process would allow for experimental validation opportunities and provide a basis for improved HVI plasma simulation strategies. Additionally, high fidelity experimental resolution of HVI plasma measurements such as RF emissions and temperature evolution would allow for computational schemes to validate assumptions with a higher degree of confidence.

Lastly, the parametric bumper study focused on energetic contributions and comparisons directly between the shielding materials, and did not compare to experimental test shots. The preliminary findings of this analysis would benefit greatly from experimental validation of the examined materials; in particular, the proposed improvements by using multiple layered materials and aluminum foam should be experimentally examined.

REFERENCES

[1] Imburgia, J. S., 2011, "Space Debris and Its Threat to National Security: A Proposal for a Binding International Agreement to Clean up the Junk," Vand. J. Transnat'l L., 44.

[2] Technology, A. F. I. O., and Przemieniecki, J. S., 1991, *Critical Technologies for National Defense*, American Institute of Aeronautics and Astronautics.

[3] Davison, L., and Graham, R. A., 1979, "Shock Compression of Solids," Physics Reports, 55(4), pp. 255-379.

[4] Cour-Palais, B. G., 1987, "Hypervelocity Impact in Metals, Glass and Composites," International Journal of Impact Engineering, 5(1), pp. 221-237.

[5] Thurber, A., and Bayandor, J., 2014, "Fluidic Analysis of Hypervelocity Impacts," Journal of Fluids Engineering, (accepted)

[6] Amsden, A., and Ruppel, H., 1981, "Sale-3d: A Simplified Ale Computer Program for Calculating Three-Dimensional Fluid Flow," Technical Report No. Los Alamos National Lab., NM (USA).

[7] Mcglaun, J. M., Thompson, S. L., and Elrick, M. G., 1990, "Cth: A Three-Dimensional Shock Wave Physics Code," International Journal of Impact Engineering, 10(1–4), pp. 351-360.

[8] Robertson, N., Hayhurst, C., and Fairlie, G., 1994, "Numerical Simulation of Impact and Fast Transient Phenomena Using Autodyn™-2d and 3d," Nuclear Engineering and Design, 150(2–3), pp. 235-241.

[9] Hibbett, Karlsson, and Sorensen, 1998, *Abaqus/Standard: User's Manual*, Hibbitt, Karlsson & Sorensen.

[10] Hallquist, J. O., 2007, "Ls-Dyna Keyword User's Manual," Livermore Software Technology Corporation, 970.

[11] Whirley, R., Engelman, B., and Hallquist, J., 1993, "Dyna-3d: A Nonlinear, Explicit Three-Dimensional Finite Element Code for Solid Mechanics, User Manual," Lawrence Livermore National Lab, LLNL Report No. UCRL-MA, 107254.

[12] Portree, D. S., and Loftus, J. P., 1999, *Orbital Debris: A Chronology*, National Aeronautics and Space Administration.

[13] 2011, *Limiting Future Collision Risk to Spacecraft:An Assessment of Nasa's Meteoroid and Orbital Debris Programs*, The National Academies Press.

[14] Gleghorn, G., Asay, J., Atkinson, D., Flury, W., Johnson, N., Kessler, D., Knowles, S., Rex, D., Toda, S., and Veniaminov, S., 1995, "Orbital Debris: A Technical Assessment," NASA STI/Recon Technical Report N, 95.

[15] Sridharan, R., Beavers, W., Lambour, R., Gaposchkin, E., and Kansky, J., 1997, "Remote Sensing and Characterization of Anomalous Debris," eds., 393, pp. 261.

[16] Rossi, A., Pardini, C., Anselmo, L., Cordelli, A., and Farinella, P., 1997, "Effects of the Rorsat Nak Drops on the Long Term Evolution of the Space Debris Population," eds.

[17] Kessler, D. J., and Cour-Palais, B. G., 1978, "Collision Frequency of Artificial Satellites: The Creation of a Debris Belt," Journal of Geophysical Research: Space Physics (1978–2012), 83(A6), pp. 2637-2646.

[18] Levin, E., Pearson, J., and Carroll, J., 2012, "Wholesale Debris Removal from Leo," Acta Astronautica, 73, pp. 100-108.

[19] Kessler, D. J., Johnson, N. L., Liou, J., and Matney, M., 2010, "The Kessler Syndrome: Implications to Future Space Operations," Advances in the Astronautical Sciences, 137(8).

[20] Ceplecha, Z., Borovička, J., Elford, W. G., Revelle, D. O., Hawkes, R. L., Porubčan, V., and Šimek, M., 1998, "Meteor Phenomena and Bodies," Space Science Reviews, 84(3-4), pp. 327-471.

[21] Klinkrad, H., 2006, *Space Debris: Models and Risk Analysis*, Springer.

[22] Jones, J., and Brown, P., 1993, "Sporadic Meteor Radiant Distributions: Orbital Survey Results," Monthly Notices of the Royal Astronomical Society, 265(3), pp. 524-532.

[23] Mcdonnell, T., Mcbride, N., Green, S. F., Ratcliff, P. R., Gardner, D. J., and Griffiths, A. D., 2001, Interplanetary Dust, Springer, Near Earth Environment.

[24] Whipple, F., 1947, "Meteorites and Space Travel," The Astronomical Journal, 52,pp. 131.

[25] Swift, H., Preonas, D., and Turpin, W., 1970, "Dissection Methods for Measuring the Characteristics of Expanding Clouds," Review of Scientific Instruments, 41(5), pp. 746-751.

[26] Cour-Palais, B., 1969, "Meteoroid Protection by Multiwall Structures".

[27] Christiansen, E. L., and Kerr, J. H., 2001, "Ballistic Limit Equations for Spacecraft Shielding," International Journal of Impact Engineering, 26(1), pp. 93-104.

[28] Christiansen, E. L., 1993, "Design and Performance Equations for Advanced Meteoroid and Debris Shields," International Journal of Impact Engineering, 14(1), pp. 145-156.

[29] Schonberg, W. P., 2008, "The Development of Ballistic Limit Equations for Dual-Wall Spacecraft Shielding: A Concise History and Suggestions for Future Development," eds.

[30] Yew, C. H., and Kendrick, R. B., 1987, "A Study of Damage in Composite Panels Produced by Hypervelocity Impact," International Journal of Impact Engineering, 5(1), pp. 729-738.

[31] Schonberg, W. P., 1990, "Hypervelocity Impact Response of Spaced Composite Material Structures," International Journal of Impact Engineering, 10(1), pp. 509-523.

[32] Schonberg, W. P., and Walker, E. J., 1994, "Hypervelocity Impact of Dual-Wall Space Structures with Graphite/Epoxy Inner Walls," Composites Engineering, 4(10), pp. 1045-1054.

[33] Jex, D., Miller, A., and Mackay, C., 1970, "The Characteristics of Penetration for a Double-Sheet Structure with Honeycomb," NASA TM X-53974.

[34] Taylor, E. A., Glanville, J. P., Clegg, R. A., and Turner, R. G., 2003, "Hypervelocity Impact on Spacecraft Honeycomb: Hydrocode Simulation and Damage Laws," International journal of impact engineering, 29(1), pp. 691-702.

[35] Nitta, K., Higashide, M., Kitazawa, Y., Takeba, A., Katayama, M., and Matsumoto, H., 2013, "Response of a Aluminum Honeycomb Subjected to Hypervelocity Impacts," Procedia Engineering, 58(0), pp. 709-714.

[36] Stump, W., and Christiansen, E., 1986, "Secondary Impact Hazard Assessment," Eagle Engineering Inc, Houston, Texas, pp. 86-128.

[37] Christiansen, E., 2000, "International Space Station (Iss) Meteoroid," Orbital Debris Shielding, Cosmonautics and Rocket Engineering, Russian Academy of Sciences, TsNIIMASH, 18), pp. 166-180.

[38] Munroe, C. E., 1900, "The Applications of Explosives," Popular Science, (56).

[39] Walters, W., Gooch, W., and Burkins, M., 2001, "The Penetration Resistance of a Titanium Alloy against Jets from Tantalum Shaped Charge Liners," International Journal of Impact Engineering, 26(1–10), pp. 823-830.

[40] Pappu, S., and Murr, L., 2002, "Hydrocode and Microstructural Analysis of Explosively Formed Penetrators," Journal of materials science, 37(2), pp. 233-248.

[41] Phipps, C., Birkan, M., Bohn, W., Eckel, H.-A., Horisawa, H., Lippert, T., Michaelis, M., Rezunkov, Y., Sasoh, A., and Schall, W., 2010, "Review: Laser-Ablation Propulsion," Journal of Propulsion and Power, 26(4), pp. 609-637.

[42] Toro, E., 2009, Riemann Solvers and Numerical Methods for Fluid Dynamics, Springer Berlin Heidelberg, The Generalized Riemann Problem.

[43] Lax, P., and Wendroff, B., 1960, "Systems of Conservation Laws," Communications on Pure and Applied mathematics, 13(2), pp. 217-237.

[44] Lyon, S. P., and Johnson, J. D., 1992, "Sesame: The Los Alamos National Laboratory Equation of State Database," Los Alamos National Laboratory, Los Alamos, NM, LA-UR-92-3407.

[45] Rice, M., Mcqueen, R. G., and Walsh, J., 1958, "Compression of Solids by Strong Shock Waves," Solid State Physics (6), pp. 1-63.

[46] Monaghan, J. J., 1994, "Simulating Free Surface Flows with SPH," Journal of Computational Physics, 110(2), pp. 399-406.

[47] Knudson, M. D., Lemke, R. W., Hayes, D. B., Hall, C. A., Deeney, C., and Asay, J. R., 2003, "Near-Absolute Hugoniot Measurements in Aluminum to 500 Gpa Using a Magnetically Accelerated Flyer Plate Technique," Journal of Applied Physics, 94(7), pp. 4420-4431.

[48] Chhabildas, L., Reinhart, W., Thornhill, T., and Brown, J., 2006, "Shock-Induced Vaporization in Metals," International Journal of Impact Engineering, 33(1), pp. 158-168.

[49] Jones, H., and Miller, A., 1948, "The Detonation of Solid Explosives: The Equilibrium Conditions in the Detonation Wave-Front and the Adiabatic Expansion of the Products of Detonation," Proceedings of the Royal Society of London. Series A. Mathematical and Physical Sciences, 194(1039), pp. 480-507.

[50] Wilkins, M. L., Squier, B., and Halperin, B., 1965, "Equation of State for Detonation Products of Pbx 9404 and Lx04-01," eds., 10, pp. 769-778.

[51] Lee, E., Hornig, H., and Kury, J., 1968, "Adiabatic Expansion of High Explosive Detonation Products," Technical Report No. California Univ., Livermore. Lawrence Radiation Lab.

[52] Tarver, C. M., Breithaupt, R. D., and Kury, J. W., 1997, "Detonation Waves in Pentaerythritol Tetranitrate," Journal of Applied Physics, 81(11), pp. 7193-7202.

[53] Steinberg, D. J., Cochran, S. G., and Guinan, M. W., 1980, "A Constitutive Model for Metals Applicable at High-Strain Rate," Journal of Applied Physics, 51(3), pp. 1498-1504.

[54] López-Puente, J., Arias, A., Zaera, R., and Navarro, C., 2005, "The Effect of the Thickness of the Adhesive Layer on the Ballistic Limit of Ceramic/Metal Armours. An Experimental and Numerical Study," International Journal of Impact Engineering, 32(1–4), pp. 321-336.

[55] Ross, M., 1969, "Generalized Lindemann Melting Law," Physical Review, 184(1), pp. 233.

[56] Cochran, S., and Guinan, M., 1976, "Bauschinger Effect in Uranium," Technical Report No. California Univ., Livermore (USA), Lawrence Livermore Lab.

[57] Asay, J., Chhabildas, L., and Dandekar, D., 1980, "Shear Strength of Shock-Loaded Polycrystalline Tungsten," Journal of Applied Physics, 51(9), pp. 4774-4783.

[58] Steinberg, D. J., and Lund, C. M., 1989, "A Constitutive Model for Strain Rates from 10−4 to 106 S−1," Journal of Applied Physics, 65(4), pp. 1528-1533.

[59] Johnson, G. R., and Cook, W. H., 1983, "A constitutive model and data for metals subjected to large strains, high strain rates and high temperatures," Proceedings of the 7th International Symposium on Ballistics, vol. 21, pp. 541-547.

[60] Dowling, N. E., Prasad, K. S., and Narayanasamy, R., 2013, *Mechanical Behavior of Materials: Engineering Methods for Deformation, Fracture, and Fatigue*, Pearson Education, Limited.

[61] Schwer, L., 2007, "Optional Strain-Rate Forms for the Johnson Cook Constitutive Model and the Role of the Parameter Epsilon_0," LS-DYNA Anwenderforum, Frankenthal.

[62] Samantaray, D., Mandal, S., and Bhaduri, A. K., 2009, "A Comparative Study on Johnson Cook, Modified Zerilli–Armstrong and Arrhenius-Type Constitutive Models to Predict Elevated Temperature Flow Behaviour in Modified 9cr–1mo Steel," Computational Materials Science, 47(2), pp. 568-576.

[63] Johnson, G. R., and Cook, W. H., 1985, "Fracture Characteristics of Three Metals Subjected to Various Strains, Strain Rates, Temperatures and Pressures," Engineering Fracture Mechanics, 21(1), pp. 31-48.

[64] Seaman, L., Curran, D. R., and Shockey, D. A., 1976, "Computational Models for Ductile and Brittle Fracture," Journal of Applied Physics, 47(11), pp. 4814-4826.

[65] Zerilli, F. J., and Armstrong, R. W., 1987, "Dislocation-Mechanics-Based Constitutive Relations for Material Dynamics Calculations," Journal of Applied Physics, 61(5), pp. 1816-1825.

[66] Follansbee, P., and Kocks, U., 1988, "A Constitutive Description of the Deformation of Copper Based on the Use of the Mechanical Threshold Stress as an Internal State Variable," Acta Metallurgica, 36(1), pp. 81-93.

[67] Simo, J. C., and Taylor, R. L., 1985, "Consistent Tangent Operators for Rate-Independent Elastoplasticity," Computer Methods in Applied Mechanics and Engineering, 48(1), pp. 101-118.

[68] Panton, R. L., 2013, *Incompressible Flow*, Wiley.

[69] Bingham, E., 1916, "The Behavior of Plastic Materials," Bulletin of US Bureau of Standards, 13(pp. 309-53.

[70] Herschel, W., and Bulkley, R., 1926, "Konsistenzmessungen Von Gummi-Benzollösungen," Kolloid-Zeitschrift, 39(4), pp. 291-300.

[71] Mühlratzer, A., Handrick, K., and Pfeiffer, H., 1998, "Development of a New Cost-Effective Ceramic Composite for Re-Entry Heat Shield Applications," Acta astronautica, 42(9), pp. 533-540.

[72] Cunniff, P. M., 1996, "A Semiempirical Model for the Ballistic Impact Performance of Textile-Based Personnel Armor," Textile Research Journal, 66(1), pp. 45-58.

[73] Hyer, W., and White, S. R., 2009, *Stress Analysis of Fiber-Reinforced Composite Materials*, DEStech Publications, Inc.

[74] Ochoa, O. O., and Reddy, J. N., 1992, *Finite Element Analysis of Composite Laminates*, Springer.

[75] O'brien, T., 1982, "Characterization of Delamination Onset and Growth in a Composite Laminate," Damage in Composite Materials, ASTM STP, 775(2), pp. 140-167.

[76] Chang, F.-K., and Chang, K.-Y., 1987, "A Progressive Damage Model for Laminated Composites Containing Stress Concentrations," Journal of Composite Materials, 21(9), pp. 834-855.

[77] Tsai, S. W., and Wu, E. M., 1971, "A General Theory of Strength for Anisotropic Materials," Journal of composite materials, 5(1), pp. 58-80.

[78] Hashin, Z., 1980, "Failure Criteria for Unidirectional Fiber Composites," Journal of applied mechanics, 47(2), pp. 329-334.

[79] Riedel, W., Nahme, H., and Thoma, K., 2004, "Equation of State Properties of Modern Composite Materials: Modeling Shock, Release and Spallation," eds., 706, pp. 701-706.

[80] Vignjevic, R., Campbell, J., Bourne, N., Matic, O., and Djordjevic, N., 2007, "Modelling Shock Waves in Composite Materials," eds., 955, pp. 287-290.

[81] Chen, F. F., 1984, *Introduction to Plasma Physics and Controlled Fusion*, Springer,

[82] Dietzel, H., Eichhorn, G., Fechtig, H., Grun, E., Hoffmann, H.-J., and Kissel, J., 1973, "The Heos 2 and Helios Micrometeoroid Experiments," Journal of Physics E: Scientific Instruments, 6(3), pp. 209.

[83] Friichtenicht, J. F., and Slattery, J. C., 1963, "Ionization Associated with Hypervelocity Impact," NASA TN D-2091.

[84] Gault, D. E., and Heitowit, E. D., 1963, "The Partition of Energy for Hypervelocity Impact Craters Formed in Rock," eds., 2, pp. 419-456.

[85] Douglas Caswell, R., Mcbride, N., and Taylor, A., 1995, "Olympus End of Life Anomaly—a Perseid Meteoroid Impact Event?," International Journal of Impact Engineering, 17(1), pp. 139-150.

[86] Close, S., Kelley, M. C., Fletcher, A., Lee, N., and Colestock, P., 2011, "Rf Signatures of Hypervelocity Impacts on Spacecraft," 3rd AIAA Atmospheric Space Environments Conference. Honolulu, HI: AIAA.

[87] Starks, M., Cooke, D., Dichter, B., Chhabildas, L., Reinhart, W., and Thornhill Iii, T., 2006, "Seeking Radio Emissions from Hypervelocity Micrometeoroid Impacts: Early Experimental Results from the Ground," International journal of impact engineering, 33(1), pp. 781-787.

[88] Ratcliff, P., Reber, M., Cole, M., Murphy, T., and Tsembelis, K., 1997, "Velocity Thresholds for Impact Plasma Production," Advances in Space Research, 20(8), pp. 1471-1476.

[89] Burkhart, B., Falceta-Gonçalves, D., Kowal, G., and Lazarian, A., 2009, "Density Studies of Mhd Interstellar Turbulence: Statistical Moments, Correlations and Bispectrum," The Astrophysical Journal, 693(1), pp. 250.

[90] Waagan, K., Federrath, C., and Klingenberg, C., 2011, "A Robust Numerical Scheme for Highly Compressible Magnetohydrodynamics: Nonlinear Stability, Implementation and Tests," Journal of Computational Physics, 230(9), pp. 3331-3351.

[91] Close, S., Colestock, P., Cox, L., Kelley, M., and Lee, N., 2010, "Electromagnetic Pulses Generated by Meteoroid Impacts on Spacecraft," Journal of Geophysical Research: Space Physics (1978–2012), 115(A12).

[92] Cook, R. D., 2007, *Concepts and Applications of Finite Element Analysis*, John Wiley & Sons.

[93] Bathe, K. J., 2006, *Finite Element Procedures*, Prentice Hall.

[94] Wu, S. R., Saha, N., and Chen, P., 2004, "Shell Elements Performance in Crashworthiness Analysis," eds., ASME 2004 International Mechanical Engineering Congress and Exposition, pp. 43-51. American Society of Mechanical Engineers.

[95] Hughes, T. J., Taylor, R. L., Sackman, J. L., Curnier, A., and Kanoknukulchai, W., 1976, "A Finite Element Method for a Class of Contact-Impact Problems," Computer Methods in Applied Mechanics and Engineering, 8(3), pp. 249-276.

[96] Hughes, T. J. R., and Liu, W. K., 1981, "Nonlinear Finite Element Analysis of Shells: Part I. Three-Dimensional Shells," Computer Methods in Applied Mechanics and Engineering, 26(3), pp. 331-362.

[97] Hughes, T. J., and Liu, W. K., 1981, "Nonlinear Finite Element Analysis of Shells-Part Ii. Two-Dimensional Shells," Computer Methods in Applied Mechanics and Engineering, 27(2), pp. 167-181.

[98] Hallquist, J., and Benson, D., 1986, "A Comparison of an Implicit and Explicit Implementation of the Hughes-Liu Shell," Finite Element Methods for Plate and Shell Structures, TJR Hughes and E. Hinton, Editors, pp. 394-431.

[99] Belytschko, T., Lin, J. I., and Chen-Shyh, T., 1984, "Explicit Algorithms for the Nonlinear Dynamics of Shells," Computer methods in applied mechanics and engineering, 42(2), pp. 225-251.

[100] Flanagan, D., and Belytschko, T., 1981, "A Uniform Strain Hexahedron and Quadrilateral with Orthogonal Hourglass Control," International Journal for Numerical Methods in Engineering, 17(5), pp. 679-706.

[101] Zienkiewicz, O. C., and Taylor, R. L., 2000, *The Finite Element Method: Solid Mechanics*, Butterworth-heinemann.

[102] Nayroles, B., Touzot, G., and Villon, P., 1992, "Generalizing the Finite Element Method: Diffuse Approximation and Diffuse Elements," Computational Mechanics, 10(5), pp. 307-318.

[103] Belytschko, T., Lu, Y. Y., and Gu, L., 1994, "Element-Free Galerkin Methods," International Journal for Numerical Methods in Engineering, 37(2), pp. 229-256.

[104] Carter, B., Chen, C.-S., Ingraffea, A., and Wawrzynek, P., 2012, "A Topology Based System for Simulating 3d Crack Growth in Solid and Shell Structures," ICF 9-Sydney, Australia.

[105] Melenk, J. M., and Babuška, I., 1996, "The Partition of Unity Finite Element Method: Basic Theory and Applications," Computer methods in applied mechanics and engineering, 139(1), pp. 289-314.

[106] Belytschko, T., and Black, T., 1999, "Elastic Crack Growth in Finite Elements with Minimal Remeshing," International journal for numerical methods in engineering, 45(5), pp. 601-620.

[107] Godunov, S. K., 1959, "A Difference Method for Numerical Calculation of Discontinuous Solutions of the Equations of Hydrodynamics," Matematicheskii Sbornik, 89(3), pp. 271-306.

[108] Dukowicz, J. K., and Kodis, J. W., 1987, "Accurate Conservative Remapping (Rezoning) for Arbitrary Lagrangian-Eulerian Computations," SIAM Journal on Scientific and Statistical Computing, 8(3), pp. 305-321.

[109] Benson, D. J., 1992, "Momentum Advection on a Staggered Mesh," Journal of Computational Physics, 100(1), pp. 143-162.

[110] Van Leer, B., 1977, "Towards the Ultimate Conservative Difference Scheme. Iv. A New Approach to Numerical Convection," Journal of Computational Physics, 23(3), pp. 276-299.

[111] Roe, P. L., 1981, "Approximate Riemann Solvers, Parameter Vectors, and Difference Schemes," Journal of computational physics, 43(2), pp. 357-372.

[112] Van Leer, B., 1979, "Towards the Ultimate Conservative Difference Scheme. V. A Second-Order Sequel to Godunov's Method," Journal of computational Physics, 32(1), pp. 101-136.

[113] Caramana, E., Burton, D., Shashkov, M., and Whalen, P., 1998, "The Construction of Compatible Hydrodynamics Algorithms Utilizing Conservation of Total Energy," Journal of Computational Physics, 146(1), pp. 227-262.

[114] Burton, D., Carney, T., Morgan, N., Sambasivan, S., and Shashkov, M., 2013, "A Cell-Centered Lagrangian Godunov-Like Method for Solid Dynamics," Computers & Fluids, 83, pp. 33-47.

[115] Esmond, M. J., and Thurber, A. J., 2013, "Development of a 1D Lagrangian Hydrocode," Technical Report No. Los Alamos National Laboratory (LANL).

[116] Zukas, J. A., 1990, *High Velocity Impact Dynamics*, Wiley.

[117] Johnson, G. R., 2011, "Numerical Algorithms and Material Models for High-Velocity Impact Computations," International Journal of Impact Engineering, 38(6), pp. 456-472.

[118] Libersky, L. D., and Petschek, A., 1991, Advances in the Free-Lagrange Method Including Contributions on Adaptive Gridding and the Smooth Particle Hydrodynamics Method, Springer, Smooth Particle Hydrodynamics with Strength of Materials.

[119] Lucy, L. B., 1977, "A Numerical Approach to the Testing of the Fission Hypothesis," Astronomical Journal, 82, pp. 1013-1024.

[120] Gingold, R. A., Monaghan, J. J., 1977, "Smoothed Particle Hydrodynamics - Theory and Application to Non-Spherical Stars," Monthly Notices of the Royal Astronomical Society, 181, pp. 375-389.

[121] Gingold, R., and Monaghan, J., 1982, "Kernel Estimates as a Basis for General Particle Methods in Hydrodynamics," Journal of Computational Physics, 46(3), pp. 429-453.

[122] Thurber, A., and Bayandor, J., 2013, "Unlocking the Physics of Hypervelocity Impact." ASME 2013 Fluids Engineering Division Summer Meeting, June 7-13, 2013, Incline Village, NV, FEDSM2013-67584, American Society of Mechanical Engineers.

[123] Monaghan, J., and Gingold, R., 1983, "Shock Simulation by the Particle Method Sph," Journal of Computational Physics, 52(2), pp. 374-389.

[124] Liu, G. G. R., and Liu, B., 2003, *Smoothed Particle Hydrodynamics: A Meshfree Particle Method*, World Scientific Publishing Company, Incorporated.

[125] Swegle, J. W., Hicks, D. L., and Attaway, S. W., 1995, "Smoothed Particle Hydrodynamics Stability Analysis," Journal of Computational Physics, 116(1), pp. 123-134.

[126] Randles, P., and Libersky, L., 1996, "Smoothed Particle Hydrodynamics: Some Recent Improvements and Applications," Computer methods in applied mechanics and engineering, 139(1), pp. 375-408.

[127] Bajer, C., and Bohatier, C., 1995, "The Soft Way Method and the Velocity Formulation," Computers & Structures, 55(6), pp. 1015-1025.

[128] Sauer, M., Hiermaier, S., and Scheffer, U., 2001, "Modeling Penetration Events Using Fe/Mlsph Adaptive Coupling," Sixth US National Congress on Computational Mechanics, pp. 1-4.

[129] VonNeumann, J., and Richtmyer, R. D., 1950, "A Method for the Numerical Calculation of Hydrodynamic Shocks," Journal of Applied Physics, 21(3), pp. 232-237.

[130] Courant, R., Friedrichs, K., and Lewy, H., 1928, "Über Die Partiellen Differenzengleichungen Der Mathematischen Physik," Mathematische Annalen, 100(1), pp. 32-74.

[131] Steinberg, D., 1996, *Equation of state and strength properties of selected materials*, Livermore, CA: Lawrence Livermore National Laboratory.

[132] Kanel, G., Razorenov, S., Zaretsky, E., Herrman, B., and Meyer, L., 2003, "Thermal “Softening” and “Hardening” of Titanium and Its Alloy at High Strain Rates of Shock-Wave Deforming," Physics of the Solid State, 45(4), pp. 656-661.

[133] Kanel, G. I., Razorenov, S. V., Bogatch, A., Utkin, A. V., Fortov, V. E., and Grady, D. E., 1996, "Spall Fracture Properties of Aluminum and Magnesium at High Temperatures," Journal of Applied Physics, 79(11), pp. 8310-8317.

[134] Groenenboom, P. H. L., 1997, "Numerical Simulation of 2d and 3d Hypervelocity Impact Using the Sph Option in Pam-Shock™," International Journal of Impact Engineering, 20(1–5), pp. 309-323.

[135] Cykowski, E., 1994, "Hydrocode Modeling of Cadmium and Aluminum Projectile Impacts into Whipple Shields in the Velocity Range of 4.7 Km/S–14.5 Km/S," NASA Johnson Space Center Report, 32311.

[136] Riedel, W., Nahme, H., White, D. M., and Clegg, R. A., 2006, "Hypervelocity Impact Damage Prediction in Composites: Part Ii—Experimental Investigations and Simulations," International Journal of Impact Engineering, 33(1–12), pp. 670-680.

[137] Dal Santo, M., and Bayandor, J., 2010, 48th Aiaa Aerospace Sciences Meeting Including the New Horizons Forum and Aerospace Exposition, American Institute of Aeronautics and Astronautics, Explosion Damage Prediction of Advanced Space Structures Subject to Hypervelocity Impact.

[138] Piekutowski, A. J., 1993, "Characteristics of Debris Clouds Produced by Hypervelocity Impact of Aluminum Spheres with Thin Aluminum Plates," International Journal of Impact Engineering, 14(1), pp. 573-586.

[139] Johnson, G. R., and Holmquist, T. J., 1989, "Test data and computational strength and fracture model constants for 23 materials subjected to large strains, high strain rates, and high temperatures." Los Alamos National Laboratory, Technical Report No. LA-11463-MS.

[140] Piekutowski, A. J., 2001, "Debris Clouds Produced by the Hypervelocity Impact of Nonspherical Projectiles," International journal of impact engineering, 26(1), pp. 613-624.

[141] Konrad, C., Chhabildas, L., Boslough, M., Piekutowski, A., Poormon, K., Mullin, S., and Littlefield, D., 1994, "Dependence of Debris Cloud Formation on Projectile Shape," eds., 309, pp. 1845-1848.

[142] Steinberg, D. J., 1991, *Equation of State and Strength Properties of Selected Materials*, Lawrence Livermore National Laboratories.

[143] Banerjee, B., Guilkey, J. E., Harman, T. B., Schmidt, J. A., and Mcmurtry, P. A., 2012, "Simulation of Impact and Fragmentation with the Material Point Method," preprint arXiv:1201.2452.

[144] El-Magd, E., and Abouridouane, M., 2006, "Characterization, Modelling and Simulation of Deformation and Fracture Behaviour of the Light-Weight Wrought Alloys under High Strain Rate Loading," International Journal of Impact Engineering, 32(5), pp. 741-758.

[145] Dykhuizen, R., Smith, M., Gilmore, D., Neiser, R., Jiang, X., and Sampath, S., 1999, "Impact of High Velocity Cold Spray Particles," Journal of Thermal Spray Technology, 8(4), pp. 559-564.

[146] Khan, A. S., and Liu, H., 2012, "A New Approach for Ductile Fracture Prediction on Al 2024-T351 Alloy," International Journal of Plasticity, 35, pp. 1-12.

[147] Shao, S., and Lo, E. Y., 2003, "Incompressible Sph Method for Simulating Newtonian and Non-Newtonian Flows with a Free Surface," Advances in Water Resources, 26(7), pp. 787-800.

[148] Jones, B. H., 1971, "A Brief Study of the Possibility of Using Partial Similitudes to Estimate the Level of Impact Damage," No. ARAP-165. AERONAUTICAL RESEARCH ASSOCIATES OF PRINCETON INC NJ.

[149] Buckingham, E., 1914, "On Physically Similar Systems; Illustrations of the Use of Dimensional Equations," Physical Review, 4(4), pp. 345-376.

[150] Gower, H., Cronin, D., and Plumtree, A., 2008, "Ballistic Impact Response of Laminated Composite Panels," International Journal of Impact Engineering, 35(9), pp. 1000-1008.

[151] Austin, R. A., Mcdowell, D. L., and Benson, D. J., 2006, "Numerical Simulation of Shock Wave Propagation in Spatially-Resolved Particle Systems," Modelling and Simulation in Materials Science and Engineering, 14(4), pp. 537.

[152] Ecault, R., Boustie, M., Touchard, F., Pons, F., Berthe, L., Chocinski-Arnault, L., Ehrhart, B., and Bockenheimer, C., 2013, "A Study of Composite Material Damage Induced by Laser Shock Waves," Composites Part A: Applied Science and Manufacturing, 53, pp. 54-64.

[153] Lee, N., Close, S., Lauben, D., Linscott, I., Goel, A., Johnson, T., Yee, J., Fletcher, A., Srama, R., Bugiel, S., Mocker, A., Colestock, P., and Green, S., 2012, "Measurements of Freely-Expanding Plasma from Hypervelocity Impacts," International Journal of Impact Engineering, 44(0), pp. 40-49.

[154] Pauling, L., 1947, "Atomic Radii and Interatomic Distances in Metals," Journal of the American Chemical Society, 69(3), pp. 542-553.

[155] Luan, B., and Robbins, M. O., 2005, "The Breakdown of Continuum Models for Mechanical Contacts," Nature, 435(7044), pp. 929-932.

[156] Odegard, G. M., Gates, T. S., Nicholson, L. M., and Wise, K. E., 2002, "Equivalent-Continuum Modeling of Nano-Structured Materials," Composites Science and Technology, 62(14), pp. 1869-1880.

[157] Sysoev, A., Ivanov, V., Surkov, Y. A., and Vysochkin, V., 1997, "Mass Spectra Formation from Charged Microparticles," Nuclear Instruments and Methods in Physics Research Section B: Beam Interactions with Materials and Atoms, 122(1), pp. 79-83.

[158] Gus'kov, S. Y., Borodziuk, S., Kalal, M., Kasperczuk, A., Kondrashov, V., Limpouch, J., Pisarczyk, P., Pisarczyk, T., Rohlena, K., and Skala, J., 2005, "Investigation of Shock Wave Loading and Crater Creation by Means of Single and Double Targets in the Pals-Laser Experiment," Journal of Russian Laser Research, 26(3), pp. 228-244.

[159] Sibeaud, J.-M., Thamie, L., and Puillet, C., 2008, "Hypervelocity Impact on Honeycomb Target Structures: Experiments and Modeling," International Journal of Impact Engineering, 35(12), pp. 1799-1807.

[160] Grujicic, M., Pandurangan, B., Zhao, C., Biggers, S., and Morgan, D., 2006, "Hypervelocity Impact Resistance of Reinforced Carbon–Carbon/Carbon–Foam Thermal Protection Systems," Applied Surface Science, 252(14), pp. 5035-5050.

[161] Taylor, G., 1948, "The Use of Flat-Ended Projectiles for Determining Dynamic Yield Stress. I. Theoretical Considerations," Proceedings of the Royal Society of London. Series A. Mathematical and Physical Sciences, 194(1038), pp. 289-299.

[162] Nemat-Nasser, S., Isaacs, J. B., and Liu, M., 1998, "Microstructure of High-Strain, High-Strain-Rate Deformed Tantalum," Acta Materialia, 46(4), pp. 1307-1325.

[163] Brünig, M., and Driemeier, L., 2007, "Numerical Simulation of Taylor Impact Tests," International Journal of Plasticity, 23(12), pp. 1979-2003.

[164] Maudlin, P. J., Bingert, J. F., and Gray Iii, G. T., 2003, "Low-Symmetry Plastic Deformation in Bcc Tantalum: Experimental Observations, Modeling and Simulations," International Journal of Plasticity, 19(4), pp. 483-515.

[165] Furnish, M., Reinhart, W., Trott, W., Chhabildas, L., and Vogler, T., 2006, "Variability in Dynamic Properties of Tantalum: Spall, Hugoniot Elastic Limit and Attenuation," eds., 845, pp. 615-618.

[166] Ball, W. W. R., 1908, *A Short Account of the History of Mathematics*, Dover Publications.

[167] Roache, P. J., 1997, "Quantification of Uncertainty in Computational Fluid Dynamics," Annual Review of Fluid Mechanics, 29(1), pp. 123-160.

APPENDIX A: ALGORITHM AND MATERIAL MODEL EVALUATION

In the scientific communities of dynamic testing and shock physics characterization, the Taylor bar impact test [161] is used as a standard method of determining shock induced deformation and plastic flow in metals. In this test, a cylindrical metallic bar is propelled at a rigid surface at speeds exceeding a few hundred meters per second, and as the impact compresses the material, the impact end deforms radially outward. The Taylor bar was used as a baseline comparison of element formulations and material models with a tantalum bar impact.

Tantalum is a dense, hard, ductile metal with high corrosion resistance, relatively low reactivity, and an extremely high melting point. These properties mean that extremely pure specimens of tantalum can remain unreacted in a laboratory setting and allow for a uniquely large range of temperatures, strain rates, and pressures over which to conduct dynamic testing while remaining primarily within the solid state [162]. Additionally, its high density, high ductility, and high melting point have made tantalum an excellent candidate for explosively formed penetrator and shaped charge liners, making the pressure, temperature, and strain rate dependent properties of tantalum a subject of interest for the weapons design community [39]. As a result, extensive studies have been performed regarding the material's response to a variety of loading conditions, and tantalum deformation is often used as a benchmark in validation of constitutive relations and hydrocodes [163].

To that end, comparative simulations have been constructed replicating an experimental Taylor bar impact test [164] of tantalum on a rigid surface to illustrate the strengths and weaknesses of the element formulations discussed in Section 4, as well as the material models discussed in Section 3. Additionally, the high strain rate behavior of Section 3's constitutive models are investigated using a model of a tantalum shaped charge penetrating a semi-infinite titanium target [39]. Some material constants were modified in accordance with recent studies [165]. The material constants used in all facets of the preceding analysis are given below.

Table A.1. Mie-Gruneisen EOS Parameters for Selected Materials

Constant	Al 2024	Al 6061	Water [124]	Ti 6Al/4V	Steel 4340	Ta
ρ_0 (g/cm^3)	2.77	2.70	1	4.419	7.81	16.69
C_0 (m/s)	5328	5240	1480	5130	4578	3410
γ_0	2	1.97	0.5	1.23	1.67	1.67
a	0.48	0.48	0	0.17	0.43	0.42
S_1	1.338	1.40	2.56	1.028	1.33	1.2
S_2	0	0	1.986	0	0	0
S_3	0	0	1.2268	0	0	0

Table A.2. Constants for the rate-independent SCG model

Constant	Al 2024	Al 6061	Ti 6Al/4V	Pb	Zn	Mg AZ31B
ρ (g/cm^3)	2.785	2.703	4.419	11.34	7.139	1.738
G_0 (Mbar)	0.286	0.276	0.419	0.086	0.395	0.165
σ_0 (Mbar)	.0026	0.0029	0.0133	0.00008	0.0015	0.0019
A (Mbar^{-1})	6.52	6.52	1.15	11.63	5.95	10.3
B (K^{-1})	6.16E-04	0.000616	0.000644	0.00116	0.00076	0.000509
β	310	125	12	110	100	1100
n	.185	0.1	0.1	0.52	0.2	0.12
σ_{max} (Mbar)	.0076	0.0068	0.0212	0.001	0.0092	0.0048
C_p (Mbar *cm^3/g*K)	8.63E-06	8.85E-06	5.25E-06	1.24E-06	3.89E-06	9.99E-06
γ_0	2.0	1.97	1.23	2.74	2.24	1.54
a	1.5	1.5	1	2.2	1.7	1.2
T_{melt} (K)	1220	1220	2110	760	900	1150
G_1 (Mbar)	.286	0.276	0.419	0.086	0.395	0.165
G_2 (Mbar)	.286	0	0.419	0.086	0.395	0.165
Σ_{spall} (Mbar)	.012	0.012	0.04	0.0006	7.139	0.009
D_0 (cm)	.0045	0.0045	-	0.0025	0.395	1.738

Table A.3. Constants for the rate-dependent SCGL model

Constant	Cu	4340 Steel	Ta	W	Be
ρ (g/cm^3)	8.93	7.81	16.69	19.3	1.85
G_0 (Mbar)	0.477	0.801	0.69	1.6	1.51
σ_0 (Mbar)	0.0012	0.012	0.0077	0.022	0.0033
A (Mbar^{-1})	2.83	2.06	1.45	0.938	1.54
B (K^{-1})	0.000377	0.0003	0.00013	0.000138	0.000258
β	36	2	22	24	26
n	0.45	0.5	0.283	0.19	0.78
σ_{max} (Mbar)	0.0064	0.025	0.011	0.04	0.0131
C_p (Mbar*cm^3/g*K)	3.83E-06	4.48E-06	2.35E-06	1.29E-06	1.82E-05
γ_0	2.02	1.67	1.67	1.67	1.11
a	1.5	1.2	1.3	1.3	1
T_{melt} (K)	1790	2310	4340	4520	1820
G_1 (Mbar)	0.477	0.801	0.69	1.6	0.61
G_2 (Mbar)	0	0	0	1.6	0
Σ_{spall} (Mbar)	0.012	0.032	0.044	0.009	0.0035
D_0 (cm)	0.007	0.003	.011	0.001	0.002
C_1 (cm^{-1})	0.71	3.6	0.71	0.71	400
C_2 (Mbar-μs)	0.12	0.024	0.024	0.12	0.12
U_k (eV)	0.31	0.31	0.31	0.31	0.31
σ_p (Mbar)	0.0002	0.007	0.0082	0.016	0.003
σ_z (Mbar)	0.00125	0.01	0.00375	0.011	0.0028
σ_{max*} (Mbar)	0.0064	0.025	0.000045	0.015	0.0131

Table A.47. Constants for the JC model.

Constant	Al 2024	Al 6061	Cu	4340	Ta	Ti 6Al/4V
A (Mbar)	0.00265	0.00324	0.0009	0.00792	0.00611	0.0088
B (Mbar)	0.00465	0.001138	0.00292	0.0051	0.00704	0.00695
n	0.34	0.42	0.31	0.226	0.608	0.36
C	0.015	0.002	0.025	0.014	0.015	0.8
m	1	1.34	1.09	1.03	0.251	0.04
D1	-0.77	-0.77	0.54	0.05	-	-
D2	1.45	1.45	4.89	3.44	-	-
D3	-0.47	-0.47	-3.03	-2.12	-	-
D4	0	0	0.014	0.002	-	-
D5	1.6	1.6	1.12	0.061	-	-

Element Comparison Using the Taylor Bar Impact Test

The actual deformation of the experimentally studied tantalum Taylor Bar [164] was somewhat asymmetric, yielding a deformed footprint measuring 1.41 cm by 1.28 cm; the majority of the deformed footprint had a 1.28 cm diameter, which was used for comparative purposes, but the Euclidean sum [166] of these values could also be used, yielding an averaged footprint radius of 1.346 cm.

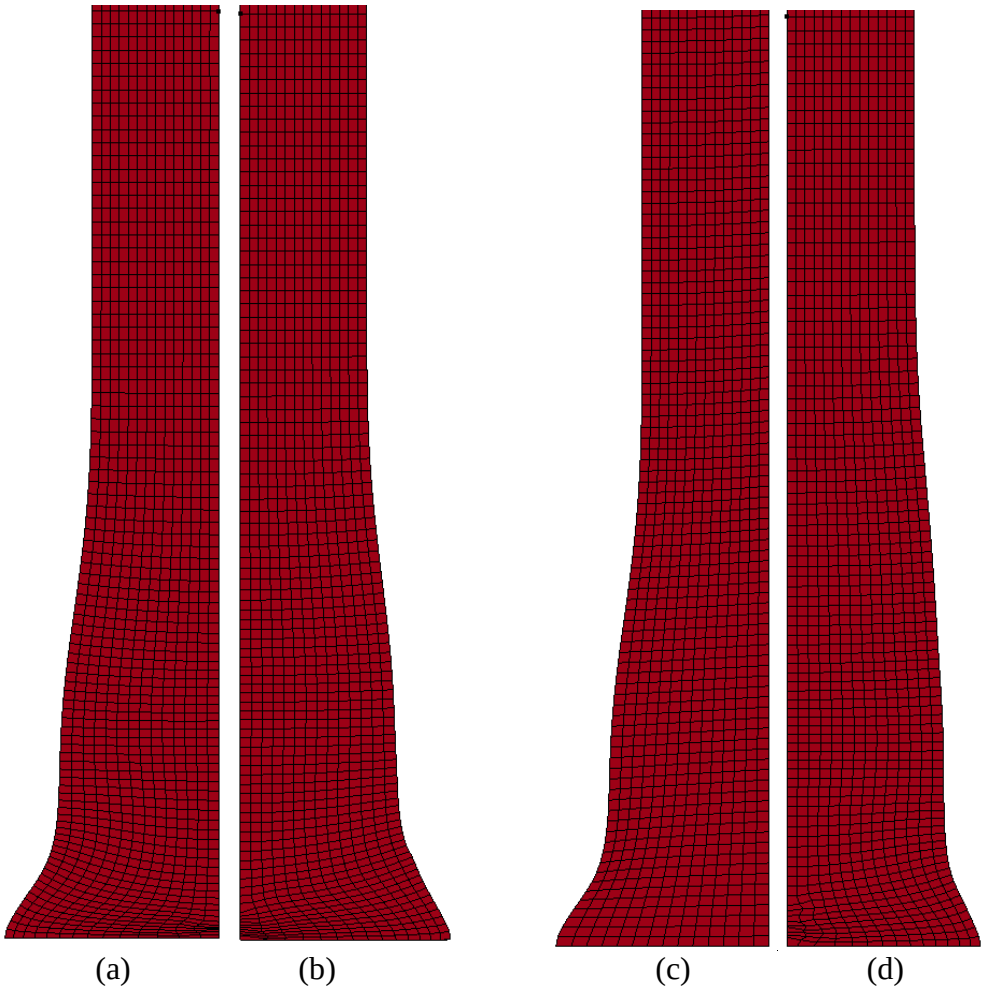

Figure A.1. Solid elements with (a) single point integration, (b) 8 noded quadrature, (c) ALE mesh smoothing, and (d) EFG approximation modeling the 139 m/s impact of a tantalum Taylor bar against a rigid surface.

Table A.58. Comparison of solid element formulations for Ta impact test

Measurement	Experiment	1 Node	8 Noded	ALE	EFG
Radius (cm)	1.28	1.2887	1.2673	1.2824	1.1584
Height (cm)	4.37	4.281	4.278	4.282	4.316
Minimum Timestep (μs)	-	6.26E-03	5.64E-03	1.17E-02	1.00E-02
Runtime (s)	-	68	469	544	441
% error in radius	-	0.682812	-0.9875	0.1875	-9.5
% error in height	-	-2.03661	-2.10526	-2.01373	-1.2357

As evidenced by Figure A.1, the single point integration, 8 noded quadrature, and EFG approximations show excessive deformation of the mesh near the central impact point, while the ALE remeshing strategy effectively prevents such mathematical anomalies. Interestingly, the single point integration technique predicts a lower error than the significantly more expensive 8 noded integration technique. The EFG technique yields the worst results in deformed radius, as well as the stiffest response overall.

SPH Comparison Using the Taylor Bar Impact Test

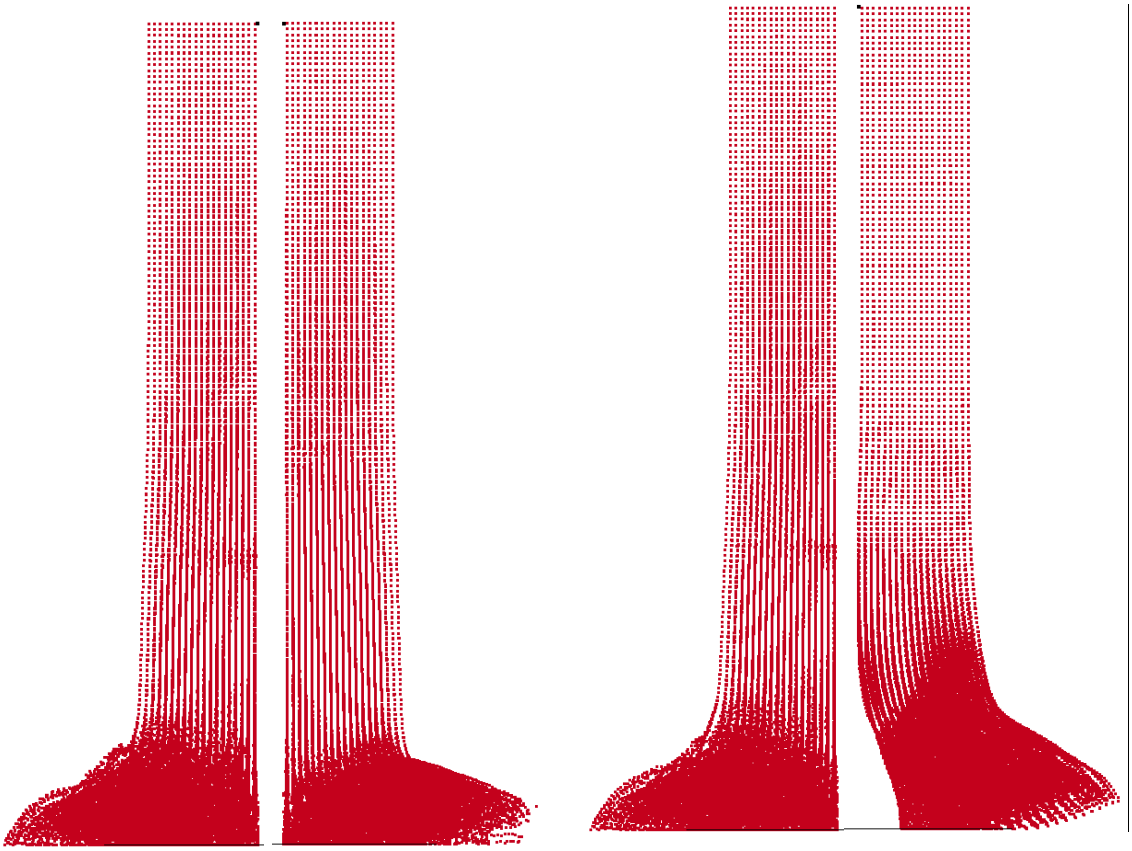

Figure A.261. SPH formulations using (a) generalized particle approximation, (b) default with renormalization, (c) symmetric approximation, and (d) total Lagrangian approximation modeling the 139 m/s impact of a tantalum Taylor bar against a rigid surface.

Table A.69. Comparison of SPH formulations for the Ta impact test

Method	Exp.	Default	Renormalization	Symmetric	Total Lagrangian
Radius (cm)	1.28	1.722	1.6768	1.7064	1.7628
Height (cm)	4.37	4.257	4.261	4.258	4.256
Min. Timestep (μs)	-	3.86E-02	3.62E-02	3.86E-02	1.50E-02
Runtime (s)	-	1034	1204	876	1947
% error in radius	-	34.53	31.00	33.31	37.71
% error in height	-	-2.58	-2.49	-2.56	-2.60

Moderate Strain Rate Comparison: Taylor Bar Impact Test

The same Taylor bar tests using tantalum were used to compare the constitutive relations described in Section 3.2. Since the ALE mesh smoothing algorithm provided the most accurate results, this method was used between all material models. The results of the material comparison are given in Table A.710A.7; the Johnson-Cook model yielded the lowest overall error, with the rate-invariant Steinberg-Cochran-Guinan model recreating the impact with the second least error. The Elastic-Plastic-Hydrodynamic model yielded the highest errors and actually began to diverge with time, while the Zerilli-Armstrong and MTS models showed moderate levels of error. Selected images of the overpredicted and underpredicted material response are shown in the following figures.

Table A.710. Comparison of constitutive models for Ta impact test

Method	**Exp.**	**SCGL**	**SCG**	**JC**	**ZA**	**MTS**	**EPH**
Radius (cm)	1.28	1.612	1.125	1.282	1.737	1.046	1.825
Height (cm)	4.37	4.201	4.419	4.282	4.174	4.554	4.087
Min. Timestep (μs)	-	.0117	.0117	.0117	.0117	.0119	.00169
Runtime (s)	-	536	566	544	560	567	>600
% error in radius	-	25.94	-12.11	0.188	35.71	-18.26	42.60
% error in height	-	-3.86	1.12	-2.01	-4.48	4.21	-6.47

Figure A.3. Reasonably accurate Taylor bar predictions from the JC model (left) and SCG (right).

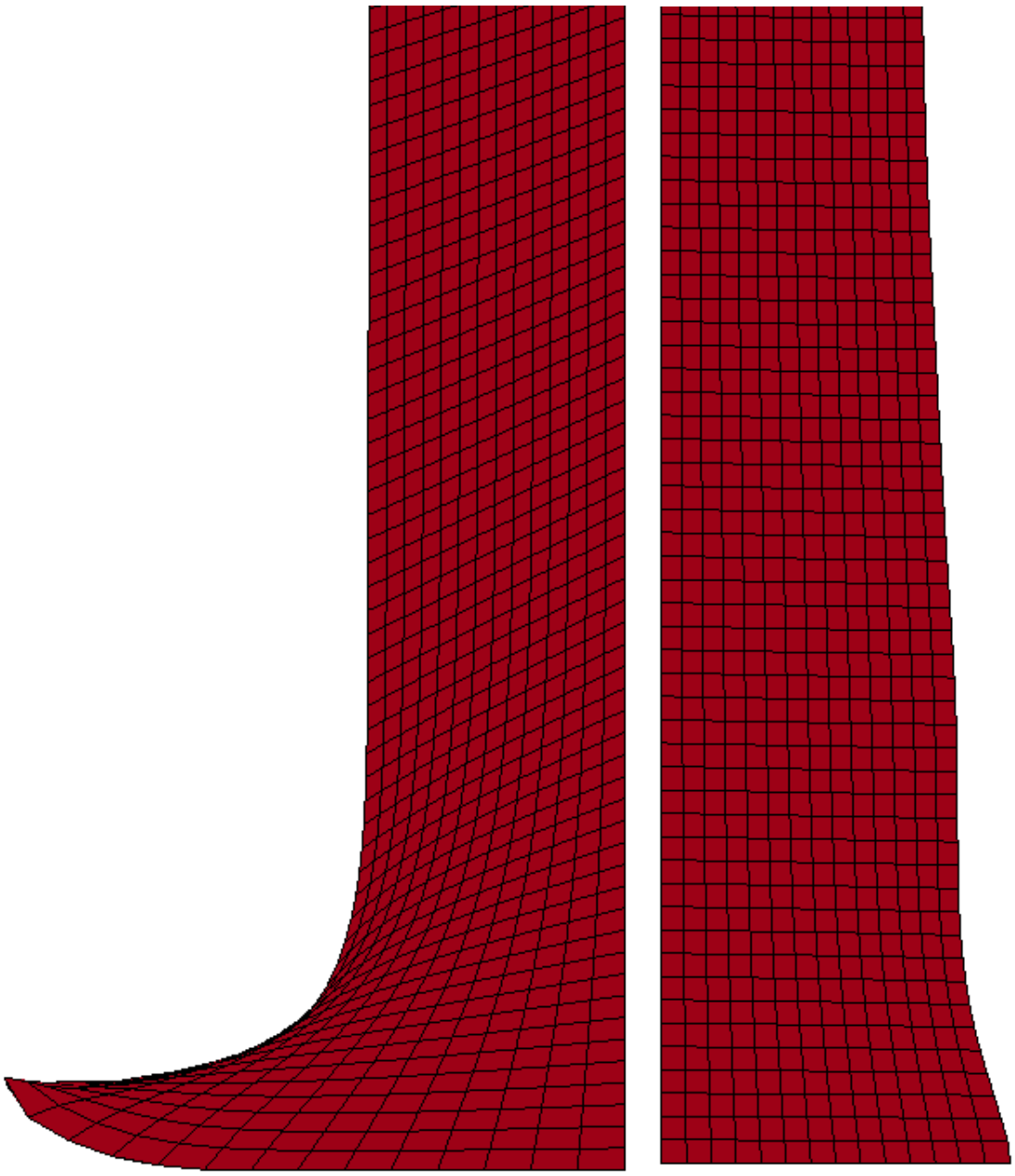

Figure 62. Inaccurate Taylor bar deformations predicted by the EPH (left) and MTS model (right).

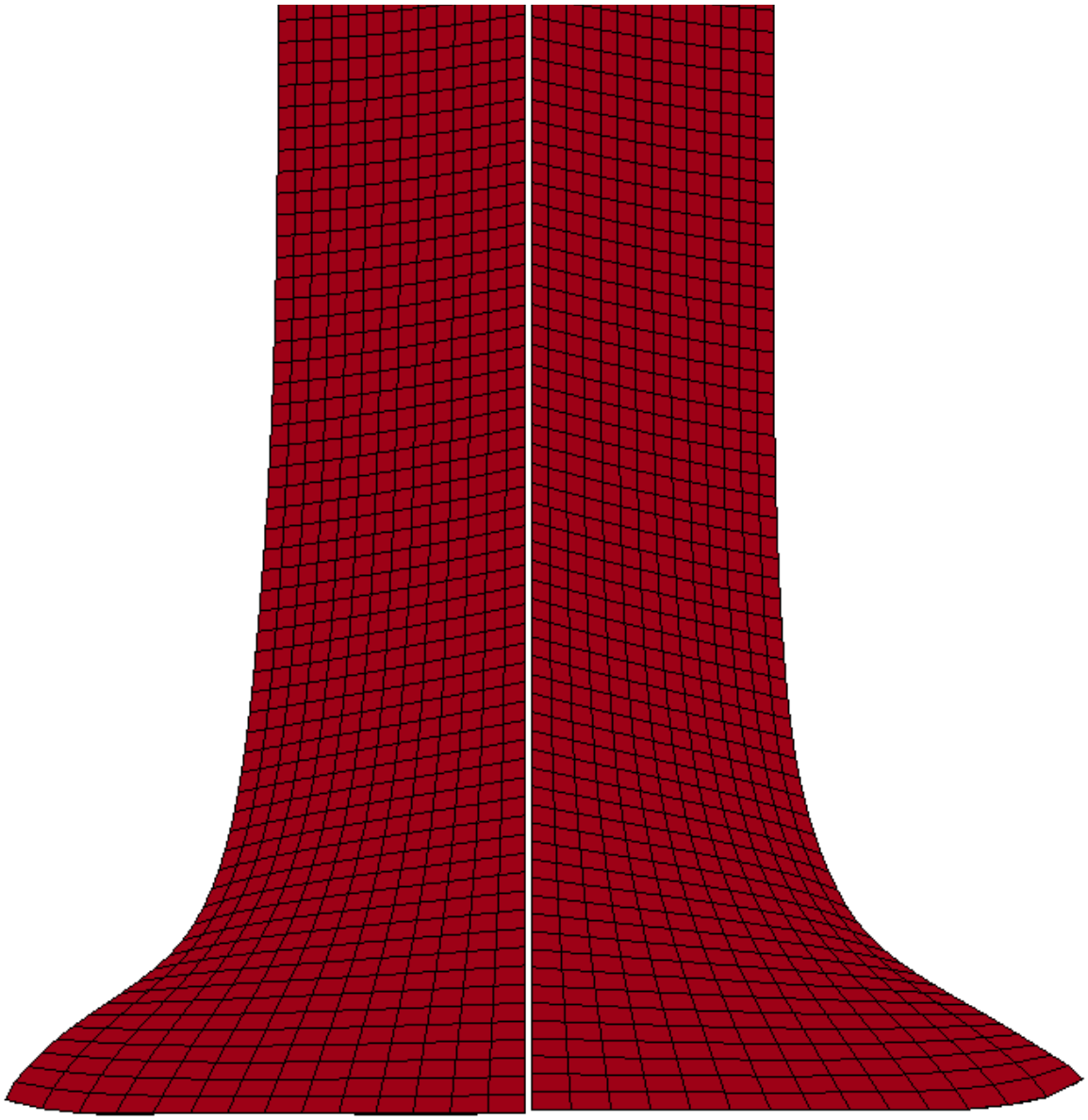

Figure 63. Overpredictions of Taylor bar deformation by the SCGL (left) and ZA models (right).

High Strain Rate Material Comparison: Tantalum Shaped Charge

As the primary damage mechanisms in HVI occur at strain rates exceeding 10^5 s^{-1}, an investigation was performed into the high strain rate performance of the aforementioned material models. To do this, several simulations were created to represent a tantalum shaped charge impacting a titanium armored plate billet, recreating the conditions of tests performed at the US Army Research Lab [39]. All of the discussed material models underpredicted both tip velocity and penetration depth, except for the ZA model, which overpredicted both. The best results were predicted by the JC, SCG, and SCGL models, and the worst predictions were given by the EPH model, as seen in Table A.8.

Table 11.8. Shaped charge performance by various material models.

Model	Exp.	SCGL	SCG	JC	ZA	MTS	EPH
Jet Velocity (km/s)	8.2	7.95	8.01	7.72	8.62	7.53	6.92
Penetration Depth (cm)	79	77.8	75.1	78.5	84.2	73.4	72.5
Velocity Error	-	3.04878	2.31707	5.85366	5.121951	8.17073	15.6098
Depth Error	-	1.51899	4.93671	0.63291	6.582278	7.08861	8.22785

APPENDIX B: CONVERGENCE ANALYSIS

SPH

A convergence analysis was done by measuring pressure, velocity, and acceleration of particles in the baseline metallic model at a time of 0.5 μs after initial contact of projectile and target. This impact window represents some of the most severe pressures and inertial changes, and thus one of the most severe case with which to measure convergence. Because each particle in the model has mass but is essentially without volume, selecting a single particle upon which to measure these quantities across three levels of particle spacing can lead to highly variant results, due to local interactions of neighboring particles. Instead, to approximate a volume which is identical across all studies, the average of these values was taken within a small region of the impact study and compared. The aforementioned values were averaged within a 1.5 mm sphere centered 1 mm below the initial top surface of the plate, which includes particles of both the projectile and plate deforming, seen in FigureB.1 for the coarsest mesh. In accordance with the methods proposed by Roache [167], Equation (49) is used as

$$p = \left(\frac{f_3 - f_2}{f_2 - f_1}\right) / \ln(r) \tag{49}$$

where f is any measured value of interest, r is the ratio of particle spacing between finer and coarser studies, the subscript 1 denotes the finest particle spacing, and 3 the coarsest.

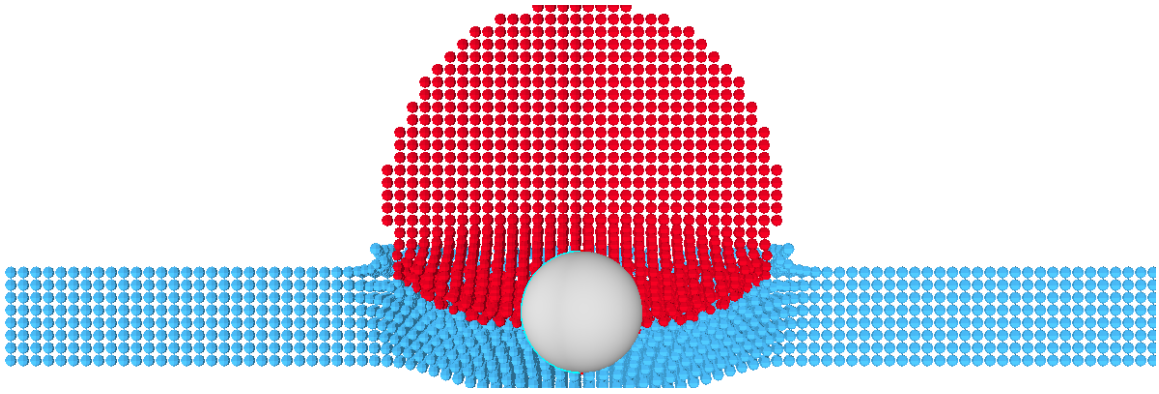

Figure B.1. The volume used for convergence analysis, encompassing multiple particles under high deformation.

As seen in Table B.1, a ratio of 1.5 was used, and while the numerical method does converge through all cases, the order can vary considerably between measured values.

Table B.1. Observed order of convergence in SPH

Particle Spacing (mm)	**Pressure (Mbar)**	**Velocity (cm/μs)**	**Acceleration (cm/μs^2)**
0.031	0.52438	0.41854	0.43289
0.020667	0.50787	0.42126	0.55721
0.013778	0.49744	0.41926	0.57853
Observed Order	1.132724	0.758351	4.348619

MMALE

Axisymmetric ALE simulations were constructed of the same impact event, with seven mesh refinement levels. The initial mesh level used 56 elements and 57 nodes in the axial direction, with 24 elements along the width, for a total of 1344 elements. These were divided by two in each direction for the subsequent mesh levels, with the highest mesh refinement containing 3584 axial and 1536 lateral, for a total of 5,505,024 elements in mesh level 7. The first three mesh refinement levels were far too coarse for any measure of convergence to be apparent, so mesh levels 4, 5, 6, and 7 are shown with convergence measures in Table B.2. The properties in the table were measured at the coordinate 0, 0, 0 at 1 μs after impact, which corresponds to the initial coordinate of the plate's upper surface during an extreme impact event. Overall convergence is good, with pressure showing the largest variance.

Table B.2. Convergence measures of axisymmetric MMALE simulations.

Mesh Level	Axial Nodes	Nodal Spacing (cm)	Velocity (cm/ μs)	Pressure (Mbar)	Density (g/cm^3)	Internal Energy (Mbar-cc)
4	449	0.015625	-0.51789	0.209344	3.288794	2.14E-04
5	897	0.007813	-0.51233	0.223666	3.334561	1.17E-04
6	1793	0.003906	-0.51007	0.226577	3.324774	5.87E-05
7	3585	0.001953	-0.50917	0.224857	3.321735	2.90E-05
4-5-6	-	Observed	1.295116	2.298735	2.225369	0.748704
5-6-7	-	Order	1.333408	0.759091	1.68727	0.960931

Appendix C: Selected Debris Clouds

Parametric Bumper Analysis

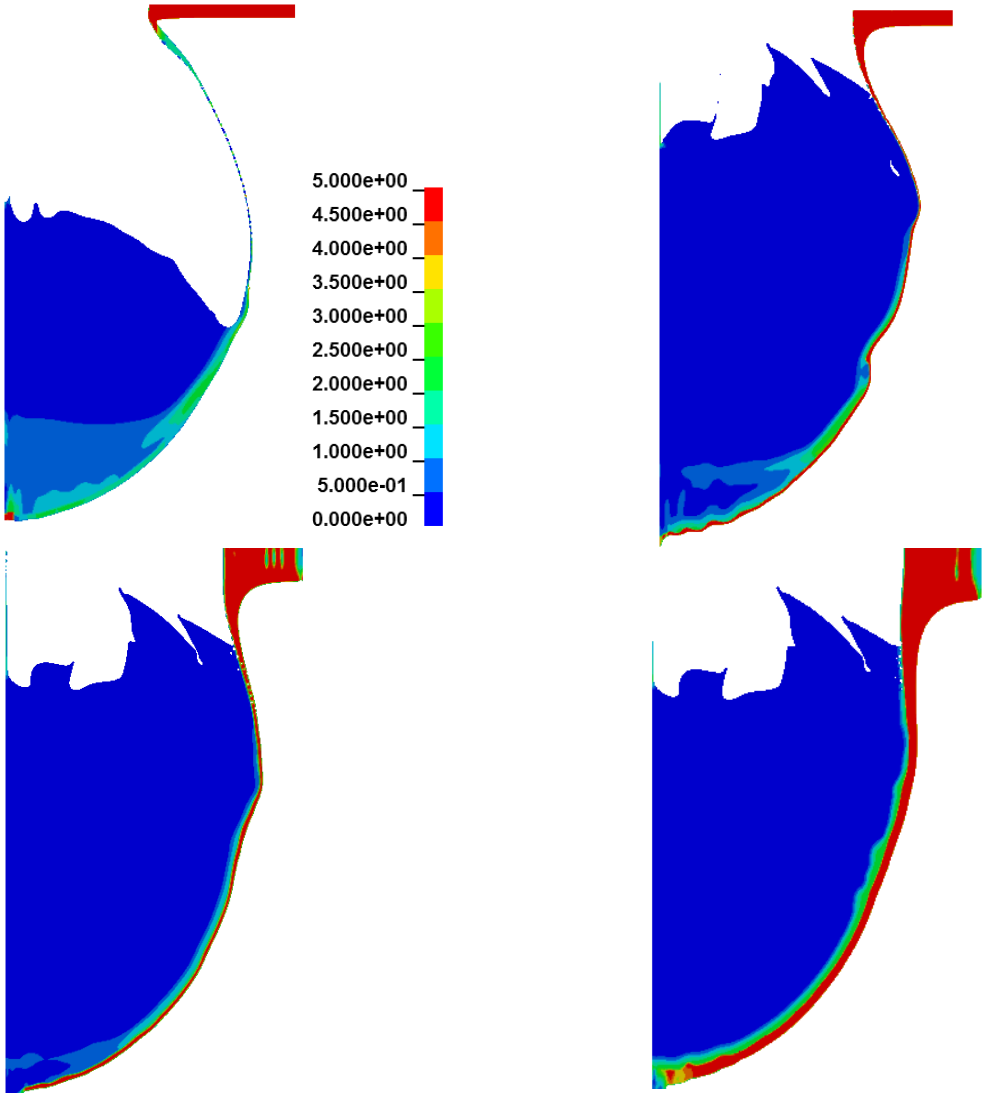

Figure C.164. Density contours of a 1.3 cm Al sphere impacting 1, 2, 3, and 4 mm thick plates of 4340 steel.

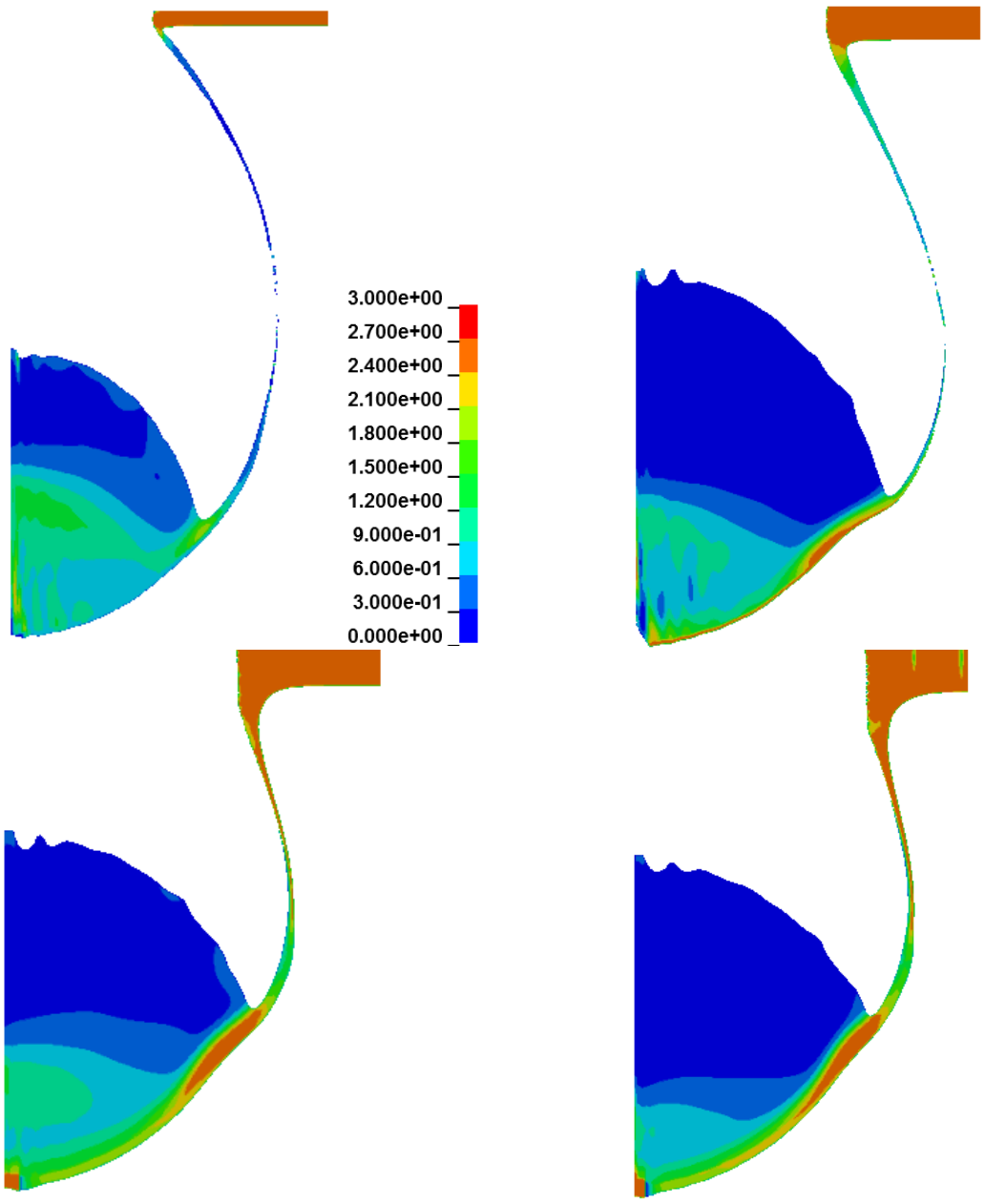

Figure C.265. Density contours of clouds from impacts into 1, 2, 3, and 4 mm thick Al 6061 plates.

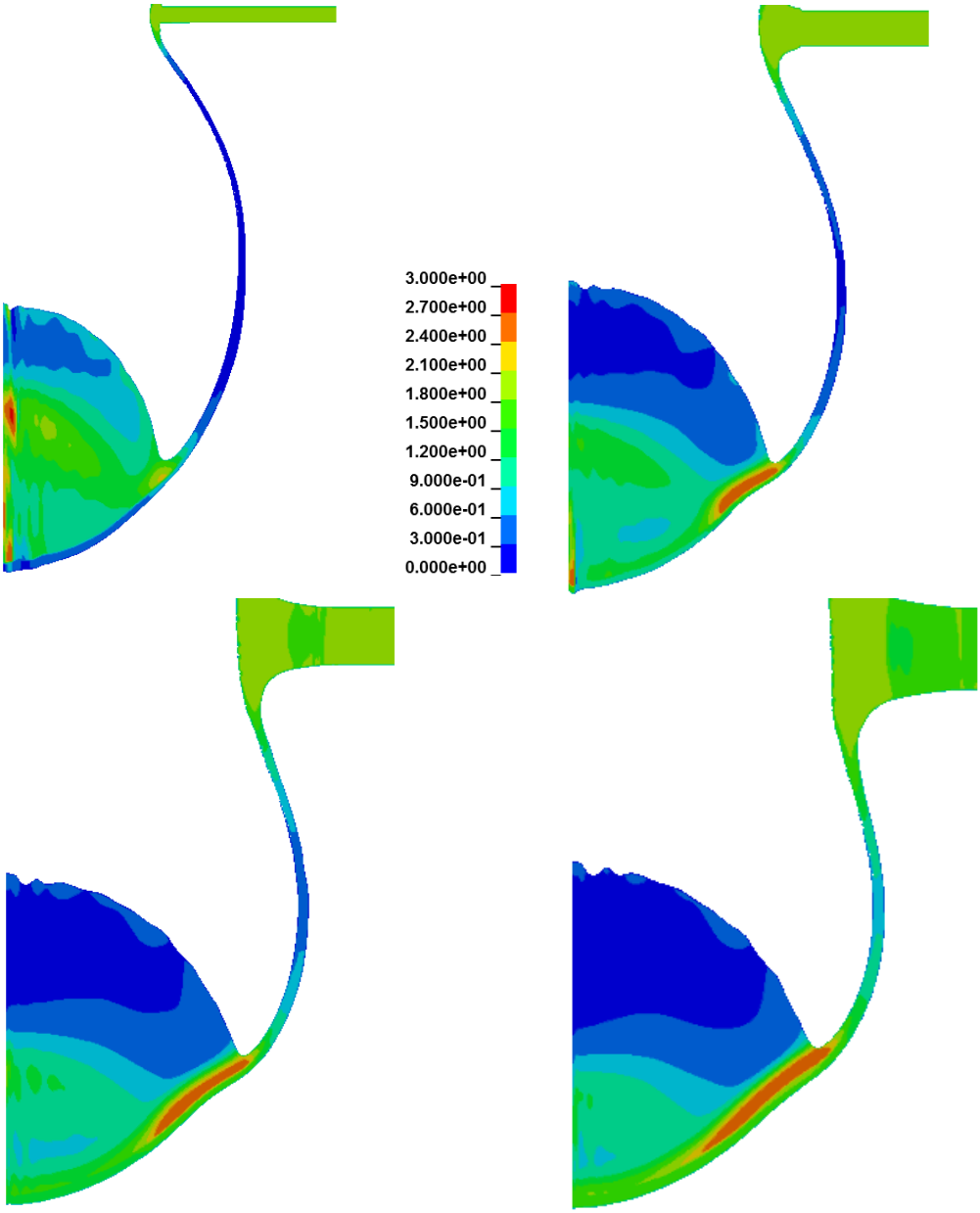

Figure C.366. Beryllium plates at 1, 2, 3, and 4 mm thickness under 1.3 cm aluminum sphere impacts at 7 km/s.

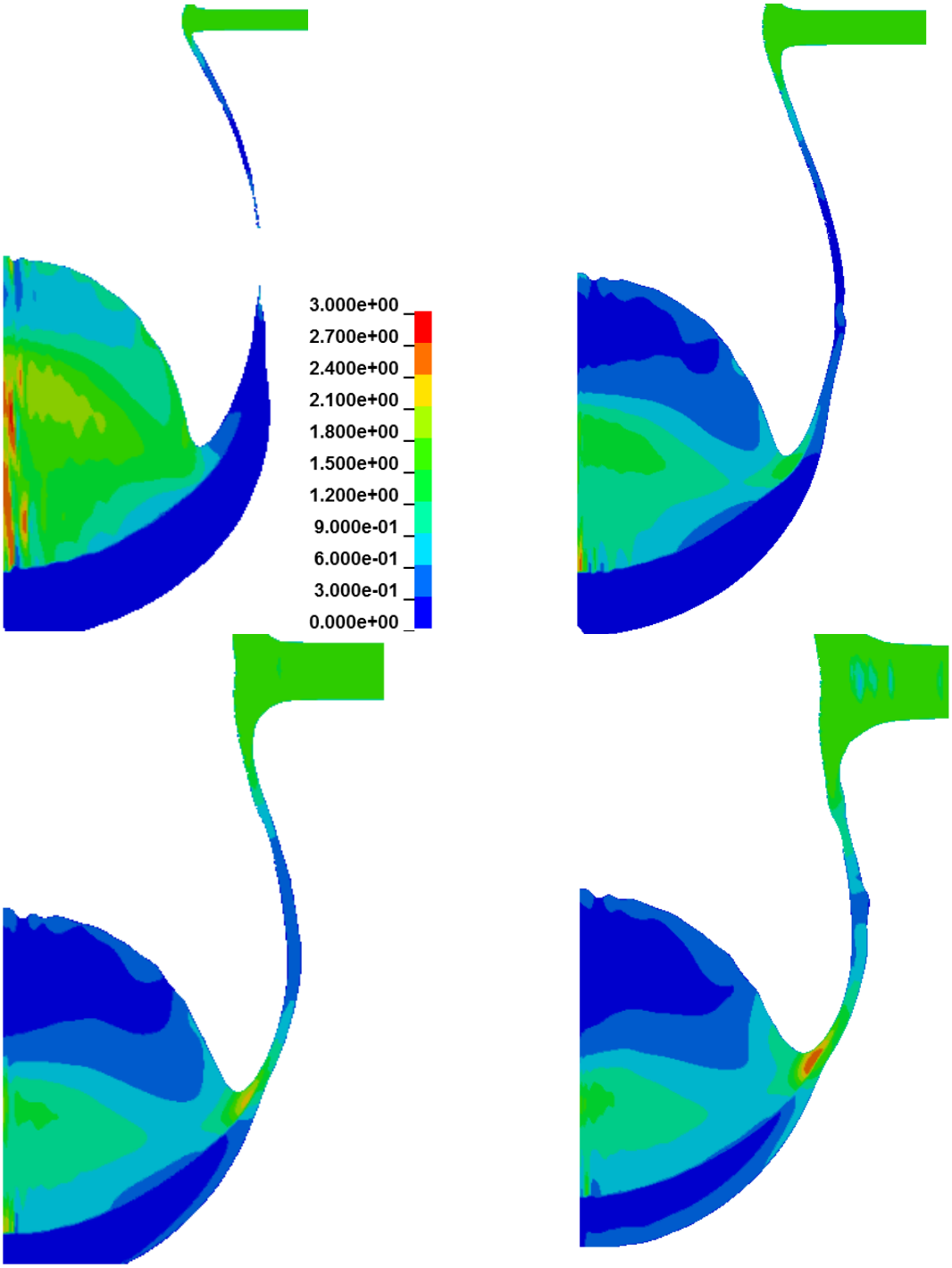

Figure C.4. Magnesium densities from parametric study.

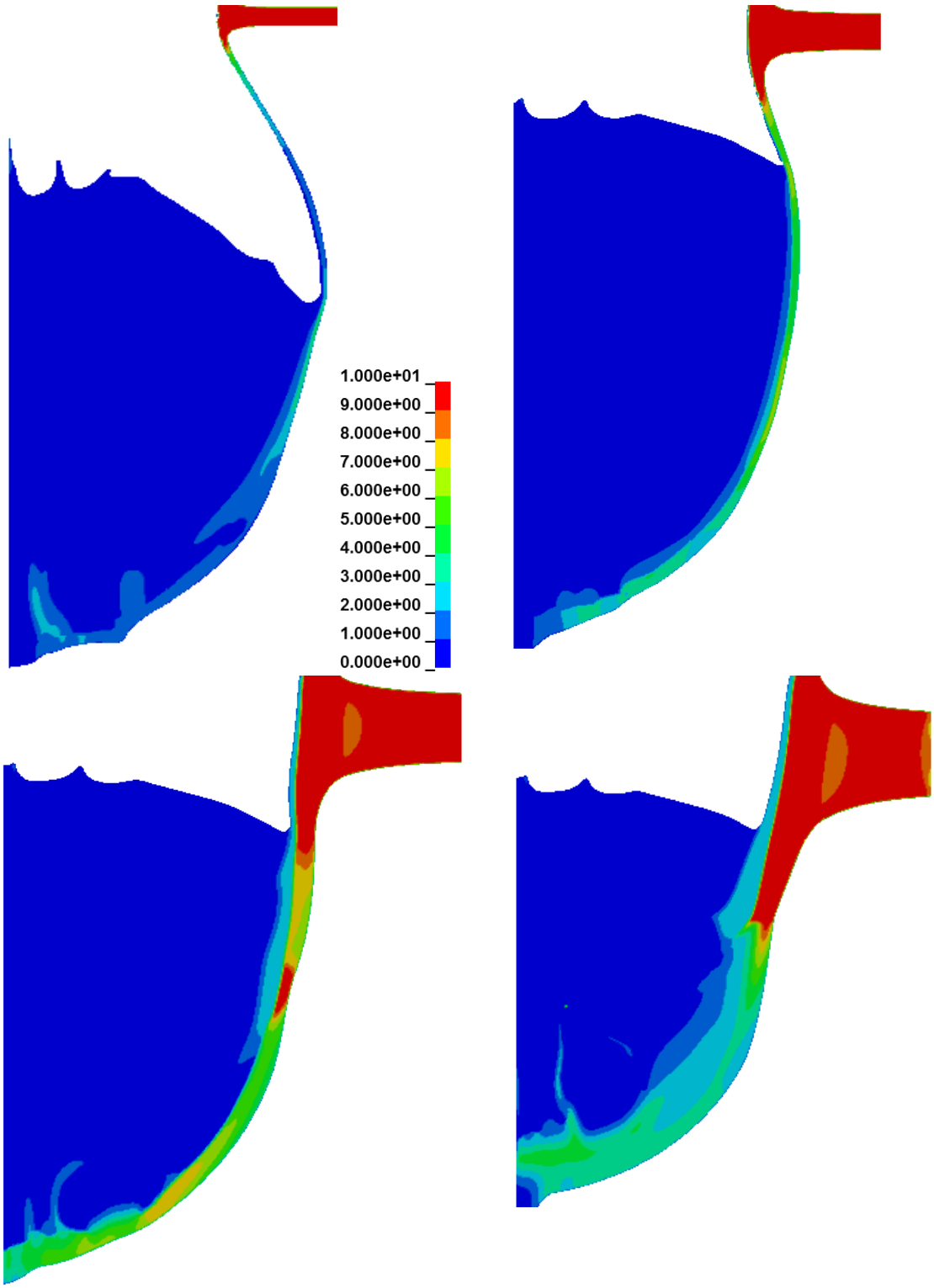

Figure C.567. Lead parametric study densities.

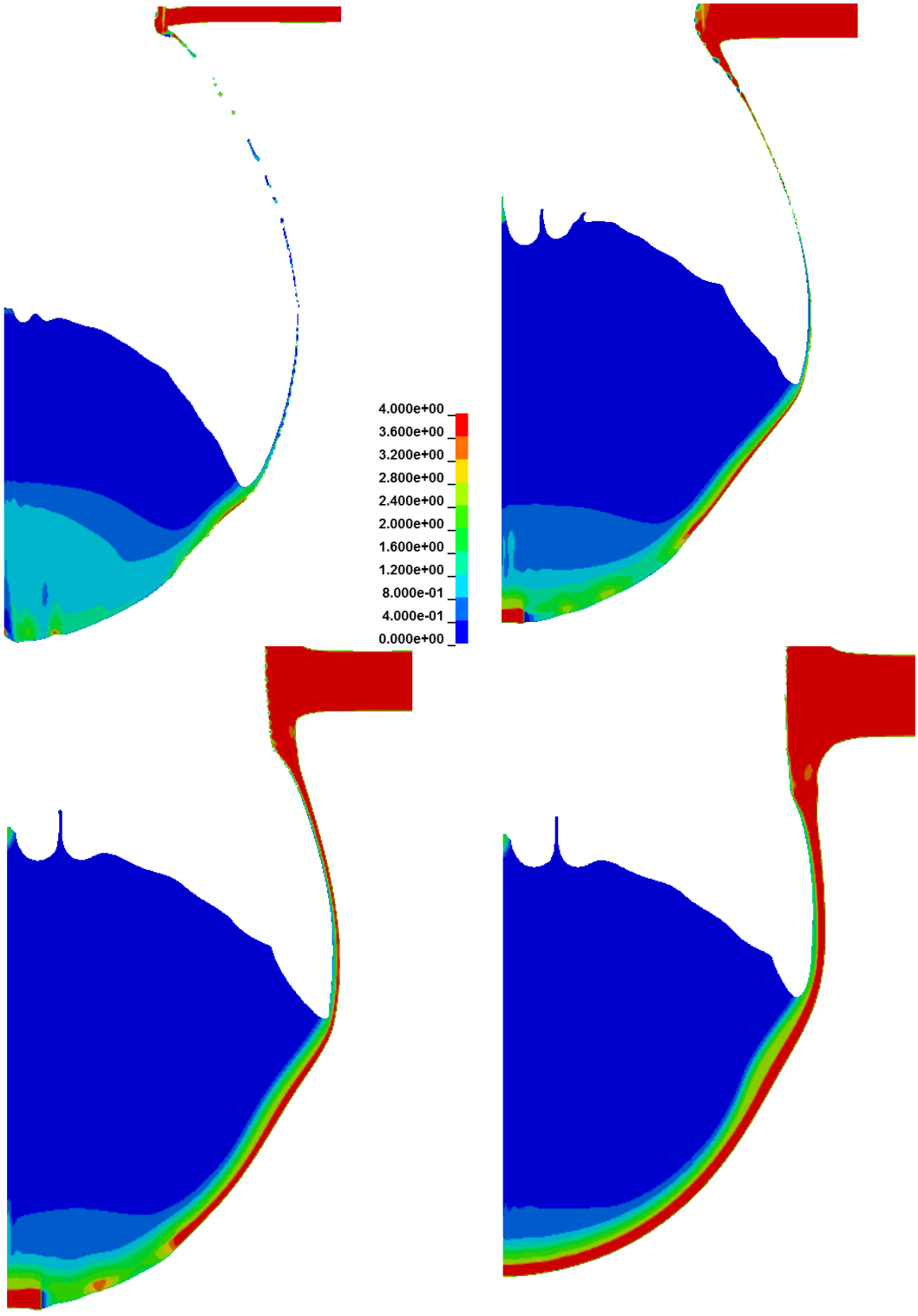

Figure C.668. Titanium densities from parametric study.

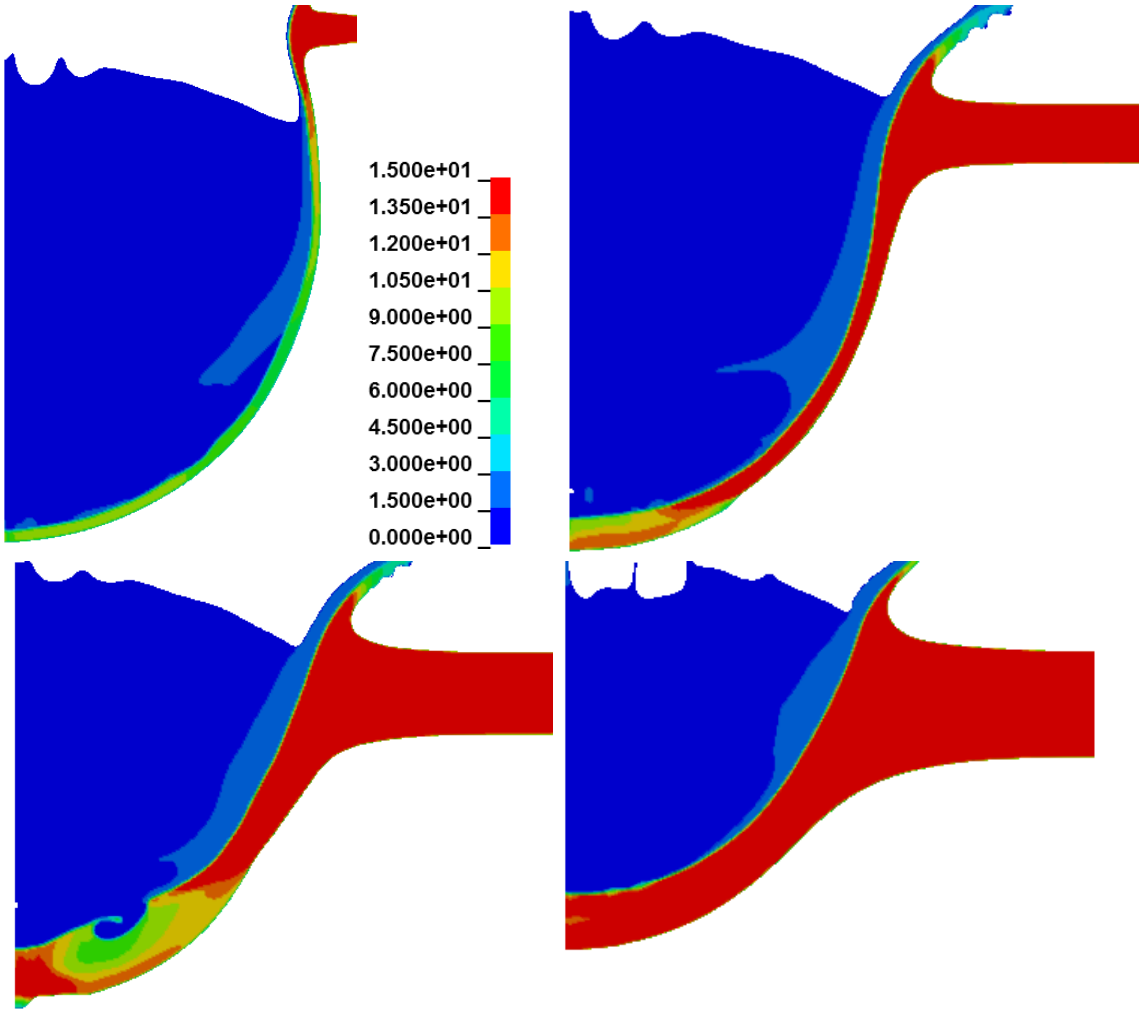

Figure C.769. Tungsten parametric study densities.

Massive Aluminum Block

The European Space Agency conducted a test in which a 1 cm aluminum sphere was propelled into a 7.5 cm thick solid block of aluminum at 7 km/s. As seen in Figure C.870, the resultant shock pressures induced massive spall on the rear free surface as well as creating a deep crater of mixed projectile and target material. This was simulated using MMALE and SPH discretizations.

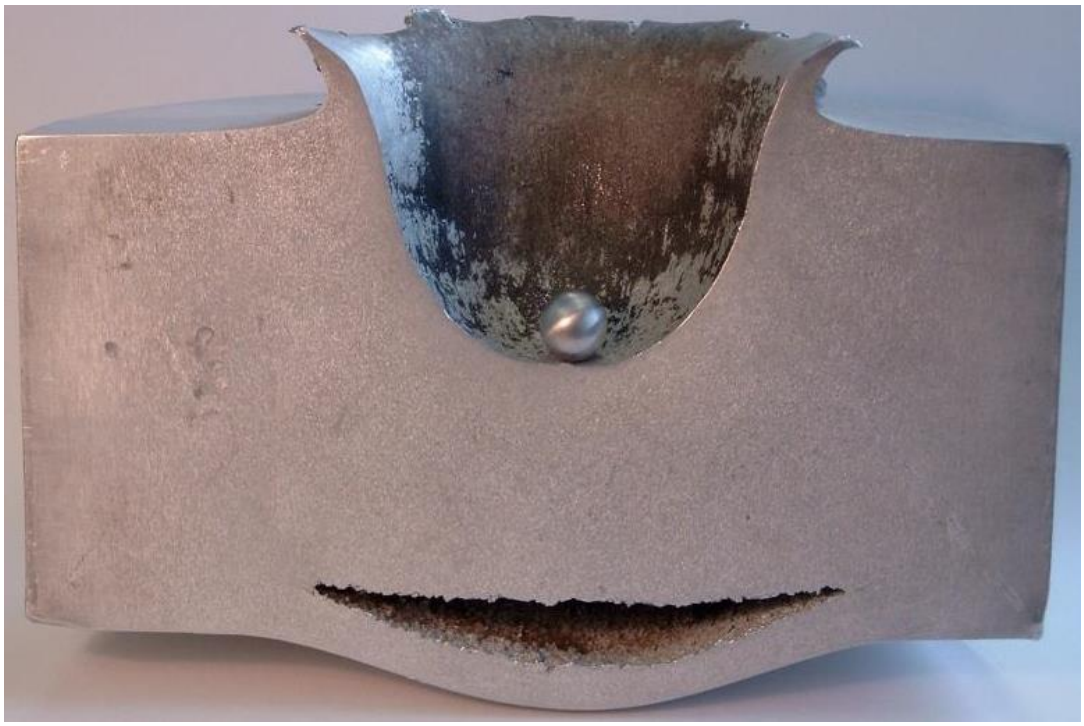

Figure C.870. Experimental ESI aluminum block HVI result.

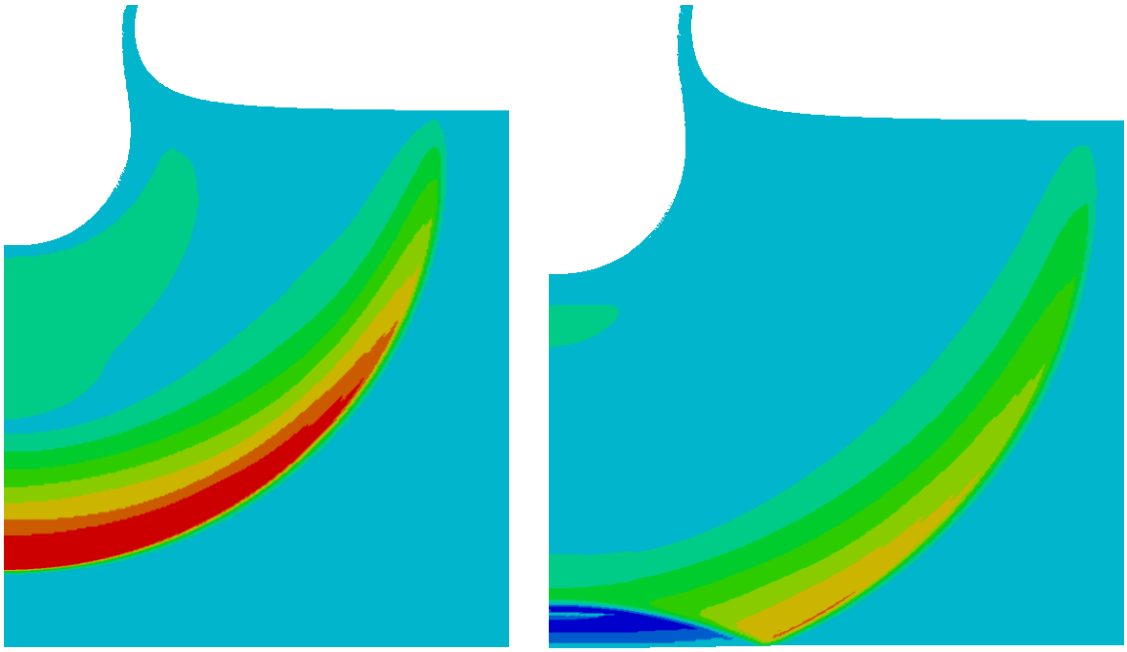

Figure C.971. Pressure contours at 10 and 13 μs showing tensile forces upon free surface shock reflection.

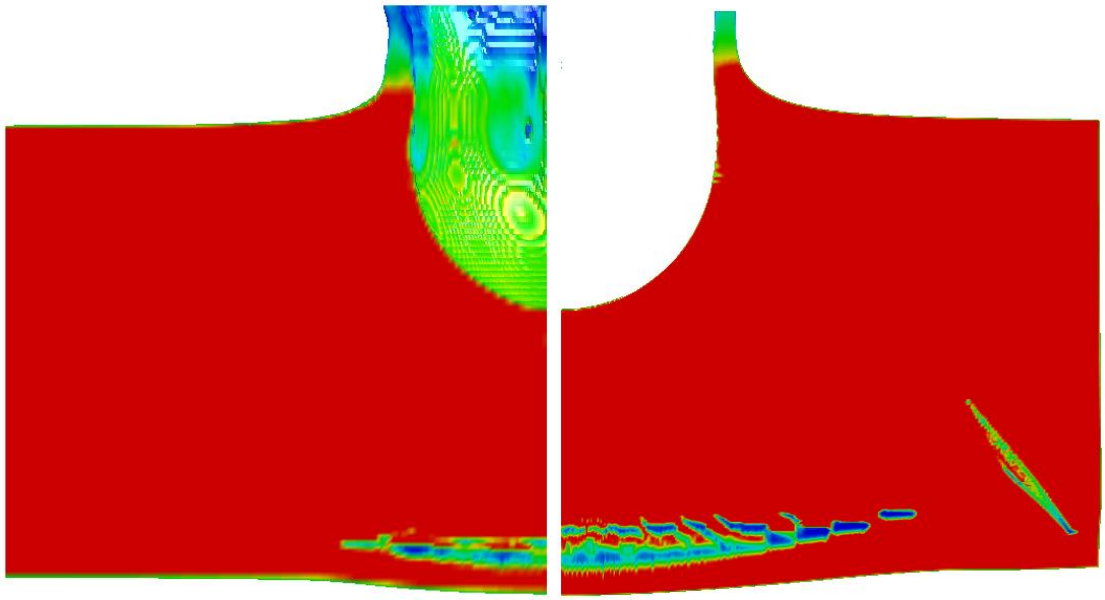

Figure C.1072. Density contours of ALE 3D (left) and axisymmetric (right) results of the Al block impact.

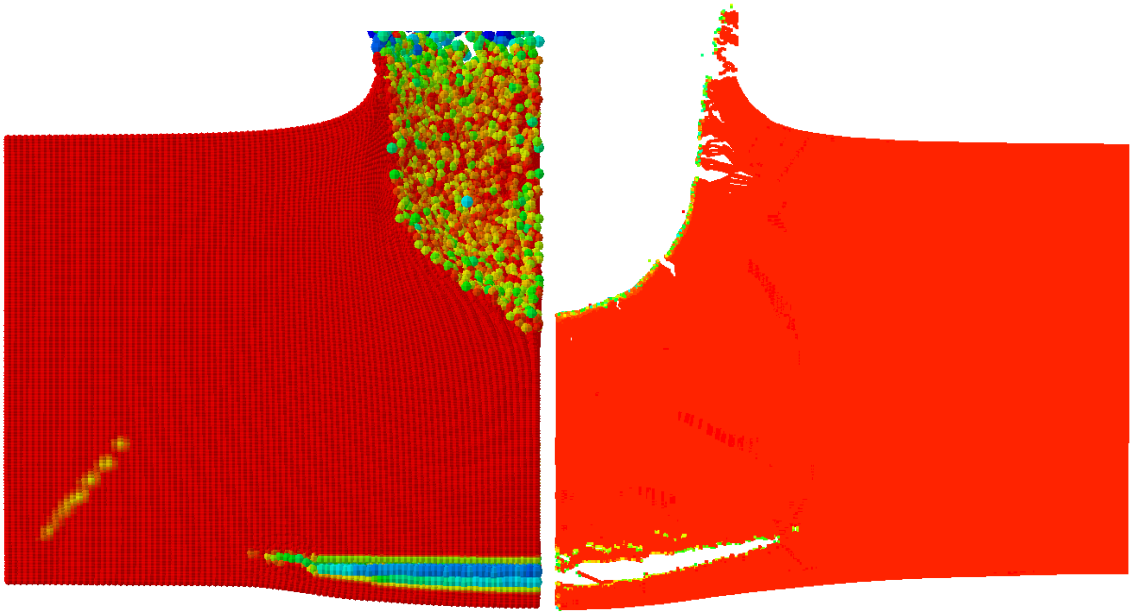

Figure C.1173. Density contours of axisymmetric SPH (left) and 3D SPH (right) predictions of damage to the Al block.